



UNIVERSITY OF
BIRMINGHAM

**Advanced Manufacture Methods for Form Stable Composite
Phase Change Materials (FSCPCMs) for Thermal Energy Storage
Applications**

By

Zhu Jiang

Thesis submitted to the University of Birmingham for the
Degree of Doctor of Philosophy

School of Chemical Engineering
College of Engineering and Physical Sciences
University of Birmingham
Edgbaston, Birmingham, UK
March 2020

UNIVERSITY OF
BIRMINGHAM

University of Birmingham Research Archive

e-theses repository

This unpublished thesis/dissertation is copyright of the author and/or third parties. The intellectual property rights of the author or third parties in respect of this work are as defined by The Copyright Designs and Patents Act 1988 or as modified by any successor legislation.

Any use made of information contained in this thesis/dissertation must be in accordance with that legislation and must be properly acknowledged. Further distribution or reproduction in any format is prohibited without the permission of the copyright holder.

ABSTRACT

With the annually increasing worldwide energy consumption and carbon emissions, there is an urgent need to enhance overall energy utilisation efficiency and improve renewable energy penetration. Thermal energy storage (TES) is considered as an effective method to effectively recover industrial waste heat and to address the intermittency of renewable energy. Large-scale deployment of TES technology, however, requires the use of a massive amount of high-performance and cost-effective TES materials. This PhD study concerns the form stable composite phase change material (FSCPCM), which is a composite phase change material that can maintain structure stable during phase change. It is one of the most promising types of TES materials for their favourable thermal properties. However, only a few FSCPCMs are currently at an early stage of commercialisation, owing to low production yield, high costs, and lack of large-scale manufacturing methods and associated expertise. This forms one of the reasons for a slow rate of FSCPCM deployment and the motivation of this research.

This PhD study aims to address the gaps in FSCPCM manufacturing. The focus is on the advanced manufacturing technologies for the FSCPCMs. The investigations include a mix-sintering method and a continuous hot-melt extrusion method. The two methods are scalable, flexible, easy-controllable and potentially very cost-effective. For the mix-sintering method, a modified mix-sintering method with an additional preheating process is proposed and compared with the traditional fabrication route. The microstructure development of the FSCPCM is studied and the criteria for using the modified mix-sintering method to produce high-quality products are investigated and verified. With the hot-extrusion method, a novel HDPE-pentaerythritol (PE)-graphite FSCPCM was firstly extruded by a single screw extruder. Effects of different processing

parameters on the extrusion operation stability and rheological behaviour were studied. These include optimal particle loading, particle size and processing temperature. The particle dispersion of the extruded FSCPCM was correlated with different processing parameters. Finally, thermal properties and thermal cycle stability of the extruded FSCPCMs were investigated to assess their suitability for TES applications.

The work on the mix-sintering method shows that both the physical and thermal properties of the diatomite-KNO₃ FSCPCM have been improved significantly with the use of the preheating process. The modified mix-sintering method contributes to the formation of a denser structure of the FSCPCM with an increment of ~20% in density and a reduction of up to ~14.67% in the porosity. The thermal conductivity has also been enhanced up to 54.91%. It is found that the melted salt KNO₃ is absorbed into the porous structure of diatomite as well as the interparticle voids during the preheating process, leading to a less porous structure of the FSCPCM after compression and sintering. Moreover, a better wettability between the liquid phase and solid surface is found to be an important criterion to capture the benefits of the use of preheating process, while the porous structure is not an essential condition. This finding is verified by both a graphite-KNO₃ composite and a SiO₂-KNO₃ composite.

A novel HDPE-pentaerythritol (PE)-graphite FSCPCM was successfully extruded. The work on the continuous hot-melt extrusion of the HDPE-pentaerythritol (PE)-graphite FSCPCM shows that the particle loading, particle size, processing temperature strongly affect the extrusion stability and rheological behaviour of mixtures for making the FSCPCM. Two extrusion instabilities were observed during the process: sharkskin defect and oscillating defect. A periodic pressure oscillation phenomenon along with surface distortion evolution is found in the unstable extrusion process. The stable and continuous extrusion can be achieved by reducing the mass ratio of particle loading,

decreasing the particle size and increasing the processing temperature. Besides, the particle dispersion of the FSCPCM is found to be related to the extrusion conditions. The particle dispersion increases with the extrusion speed until a certain value before it starts to decrease. This is because the particle dispersion is affected by the shear stress and the mixing time, with the former increasing with increasing extrusion speed and the latter showing the opposite trend. The porosity of the FSCPCM is found to increase when the processing temperature increases due to PE vaporisation. The extruded FSCPCM is found to have an energy density as high as 426.17 kJ/kg from 100 °C to 200 °C. Thermal cycling of the CPCM shows a slight decrease of latent heat of the CPCM by 5.72% after 100 cycles.

ACKNOWLEDGEMENT

I would like to express my greatest gratitude to my lead supervisor, Professor Yulong Ding, for his guidance, motivation and encouragement throughout my study. His immense knowledge and unlimited enthusiasm towards research have inspired me to strive for the new knowledge generation persistently. His modest and patient attitude will affect me in my whole life, guiding me to be a better person. It is a great honour and an unforgettable experience to be his student.

I would like to express my sincere thanks to Dr. Zhenyu (Jason) Zhang as my second supervisor, and also Dr. Yongliang Li, Dr. Helena Navarro for giving me invaluable advice on my research. Their suggestions and supports are essential for the completion of my PhD.

I also greatly appreciate the assistance from Ms. Jie Chen, Mr. Chyntol Kanhimbe and Dr. Mark Duffield. Their technical support on my experimental work has made my study much easier and smoother. Besides, I am very grateful for every member in Birmingham Centre Energy Storage (BCES) at the University of Birmingham. They are like my families overseas, supporting me both in life and study.

I would also like to express a special appreciation to my parents. Their selfless love and support is the greatest treasure to me, making me feel fearless whatever happens.

Lastly, I would like to thank China Scholarship Council (CSC), UK Engineering and Physical Sciences Research Council (EPSRC), and State Grid Corporation of China (SGCC) for their financial support on my PhD study.

PUBLICATIONS

A. Journal papers

1. **Jiang, Z.**, Palacios, A., Lei, X., Navarro, M. E., Qiao, G., Mura, E., Xu, G., Ding, Y. (2019). Novel key parameter for eutectic nitrates based nanofluids selection for concentrating solar power (CSP) system. *Applied energy*, 235, 529-542.
2. **Jiang, Z.**, Jiang, F., Li, C., Leng, G., Zhao, X., Li, Y., Zhang, T., Xu, G., Jin, Y., Yang, C., Ding, Y. (2019). A Form Stable Composite Phase Change Material for Thermal Energy Storage Applications over 700° C. *Applied Sciences*, 9(5), 814.
3. **Jiang, Z.**, Leng, G., Ye, F., Ge, Z., Liu, C., Wang, L., Huang, Y., Ding, Y. (2015). Form-stable $\text{LiNO}_3\text{--NaNO}_3\text{--KNO}_3\text{--Ca}(\text{NO}_3)_2$ /calcium silicate composite phase change material (PCM) for mid-low temperature thermal energy storage. *Energy Conversion and Management*, 106, 165-172.
4. Palacios, A., Navarro, M. E., **Jiang, Z.**, Avila, A., Qiao, G., Mura, E., & Ding, Y. (2020). High-temperature corrosion behaviour of metal alloys in commercial molten salts. *Solar Energy*, 201, 437-452.
5. Yu, Q., **Jiang, Z.**, Cong, L., Lu, T., Suleiman, B., Leng, G., Wu, Z., Ding, Y., Li, Y. (2019). A novel low-temperature fabrication approach of composite phase change materials for high temperature thermal energy storage. *Applied energy*, 237, 367-377.
6. Zhang, Y., **Jiang, Z.**, Zhang, Z., Ding, Y., Yu, Q., & Li, Y. (2019). Polysaccharide assisted microencapsulation for volatile phase change materials with a fluorescent retention indicator. *Chemical Engineering Journal*, 359, 1234-1243.
7. Jiang, F., Zhang, L., **Jiang, Z.**, Li, C., Cang, D., Liu, X., Xuan, Y., Ding, Y. (2019). Diatomite-based porous ceramics with high apparent porosity: Pore structure modification using calcium carbonate. *Ceramics International*, 45(5), 6085-6092.
8. Leng, G., Qiao, G., **Jiang, Z.**, Xu, G., Qin, Y., Chang, C., & Ding, Y. (2018). Micro encapsulated & form-stable phase change materials for high temperature thermal energy storage. *Applied energy*, 217, 212-220.

B. Conference papers

1. **Jiang, Z.**, Leng, G., & Ding, Y. (2018). A Large-Scale Manufacturing Method to Produce Form Stable Composite Phase Change Materials (PCMs) for Thermal Energy Storage at Low and High Temperatures. In *Advances in Green Energy Systems and Smart Grid* (pp. 214-221). Springer, Singapore. (oral presentation).
2. **Jiang, Z.**, Ding, Y. (2019). X-Ray tomographic analyses of a composite phase change material (PCM). *UK-China International Particle Technology Forum VII*, 28–31 July 2019, Edinburgh, UK. (poster).
3. **Jiang, Z.**, Ding, Y. (2019). Study of processing conditions on the microstructure of mid-temperature composite PCM prepared by a one-step manufacturing method, *UKES 2019 Energy Storage Conference*, 3-5 September 2019, Newcastle, UK. (poster).

CONTENTS

1	Introduction.....	18
1.1	Background of Thermal Energy Storage (TES).....	18
1.2	Research gaps in latent heat storage based technologies.....	20
1.3	The objectives and motivations	21
1.4	Thesis outline	22
2	Literature review	25
2.1	Introduction to phase change materials (PCMs).....	25
2.2	Form-stable composite phase change materials (FSCPCMs)	29
2.2.1	Introduction.....	29
2.2.2	Classifications of FSCPCMs	31
2.2.3	Challenges and innovation needs for FSCPCMs	36
2.3	Fabrication methods for FSCPCMs	37
2.3.1	Classifications of fabrication methods	37
2.3.2	Impregnation method	38
2.3.3	Mix-sintering.....	51
2.3.4	Extrusion.....	64
2.3.5	Other methods	69
2.4	Summary	72

3	Materials and methodologies	75
3.1	Materials	75
3.2	Fabrication equipments and methods	76
3.2.1	Mix-sintering.....	76
3.2.2	Extrusion method	77
3.3	Characterization devices and methods.....	80
3.3.1	Differential scanning calorimeter (DSC)	80
3.3.2	Thermogravimetric Analysis (TGA).....	83
3.3.3	Laser flash apparatus (LFA).....	83
3.3.4	Rheometer	85
3.3.5	Scanning electron microscope (SEM) and energy-dispersive x-ray spectrometer (EDS)	85
3.3.6	Mercury porosimetry	86
3.3.7	Compressive strength.....	87
3.3.8	XRT	87
3.3.9	Thermal cycling.....	88
3.3.10	Infrared microscopy (IR)	89
3.3.11	Helium pycnometer	90
3.3.12	Contact angle.....	90
3.3.13	Mastersizer	91

4	Results and discussion (I): a modified mix-sintering fabrication method with a preheating process	92
4.1	Introduction.....	92
4.2	Fabrication and characterisations	93
4.2.1	FSCPCM formulations	93
4.2.2	Fabrication method	93
4.2.3	Characterisation methods	95
4.3	Results and discussion.....	97
4.3.1	Characterisation of physical properties;	97
4.3.2	Thermal properties.....	103
4.3.3	Thermal cycling stability	110
4.3.4	Criteria of the preheating process for the FSCPCM	114
4.4	Summary	124
5	Results and discussions (II): a continuous hot-melt extrusion method – the effects of processing conditions on flow stability and rheological behaviour	127
5.1	Introduction.....	127
5.2	Fabrication.....	128
5.2.1	Sample formulations	128
5.2.2	Processing conditions	129
5.2.3	Characterisation methods	131

5.2.4	Effect of the mass ratio of the PE fillers on the extrusion and rheological behaviour	131
5.2.5	Size effect of particle fillers on the extrusion and rheological behaviour.....	150
5.2.6	Effect of operation temperature on the extrusion properties and rheological behaviour.....	158
5.3	Summery	164
6	Results and discussion (III): a continuous hot-melt extrusion method – the study of structural and thermal properties of the FSCPCM	167
6.1	Introduction.....	167
6.2	Characterisation methods.....	167
6.3	Results and discussion.....	169
6.3.1	Structural characteristics.....	169
6.3.2	Thermal properties.....	178
6.3.3	Thermal cycling stability	190
6.3.4	Chemical compatibility	193
6.4	Summary	196
7	Conclusions and future work	198
7.1	Conclusions.....	198
7.2	Future work	200
	References.....	203

List of Tables

Table 1 Requirements for an ideal PCM.....	27
Table 2 Comparison between organic and inorganic PCMs [21]	28
Table 3 Review on remarkable works of preparing FSCPCMs by impregnation method	40
Table 4 Review on remarkable works of preparing composite PCMs by mix-sintering	53
Table 5 State of art of the composite PCM prepared by extrusion	65
Table 6 Basic information about the raw materials.....	75
Table 7 Mass ratio of the PCM and Diatomite	93
Table 8 Measurement methods and repetitions	96
Table 9 True density and calculated porosity (with SD).....	99
Table 10 Melting point and latent heat of KNO_3 and the formulated FSCPCMs (with SD).....	105
Table 11 Specific heat of the composite PCMs with SD.....	107
Table 12 Fitting curve of specific heat and calculated energy density	108
Table 13 Average of the thermal conductivity for the FSCPCMs.....	110
Table 14 Average of the thermal conductivity for samples with 50 times thermal cycling (with SD)	114
Table 15 Pore size geometry of the diatomite and mixed powders	116
Table 16 Formulation of the composite PCM for extrusion.....	128
Table 17 Particle size distribution of the PE particles with different size of sieves	129
Table 18 Measurement methods and repetitions	131
Table 19 Measurement methods and repetitions	168
Table 20 Melting point and latent heat of the composite PCM	180
Table 21 Melting point and latent heat of sample S50 at different extrusion speeds with SD	181
Table 22 Melting point and latent heat of sample S50 at different heating rates	183

Table 23 Specific heat of the composite PCMs	184
Table 24 Fitting curve of specific heat and calculated energy density	185
Table 25 Average and enhancement of the thermal conductivity	187
Table 26 Thermal degradation properties at N ₂ and Air atmosphere	190
Table 27 Melting point and latent heat of sample S50 after different thermal cycling times	192

List of Figures

Figure 1 Technology readiness level of different energy storage technologies	19
Figure 2 Thermal energy at the heart energy chain [8]	20
Figure 3 Diagram of the thesis structure.....	23
Figure 4 Melting temperature and enthalpy range of different PCMs [23].....	29
Figure 5 Components and advantages of FSCPCMs.....	30
Figure 6 The microstructure of the diatomite/ Na_2SO_4 composite PCM [38].....	32
Figure 7 The SEM and EDS images of a paraffin/vermiculite composite [35].....	33
Figure 8 SEM images of the paraffin-HDPE CPCMs: (a) 75 wt.% Paraffin + 25 wt.% HDPE; (b) 75 wt.% Paraffin + 22.5 wt.% HDPE+ 2.5 wt.% OMT (organophilic montmorillonite, fire retardant); (c) 75 wt.% Paraffin + 20 wt.% HDPE + 5 wt.% OMT; (d) 75 wt% Paraffin + 15 wt.% HDPE + 10 wt.% OMT;....	36
Figure 9 Fabrication methods based on the ingredients of FSCPCMs	38
Figure 10 Percentage of different impregnation method used in literature	47
Figure 11 Static and dynamic vacuum impregnation device	48
Figure 12 Schematics of the mechanism for microstructure development of FSCPCMs [43]	57
Figure 13 Images of a graphite/salt composite obtained by two cold-compression routes at the macroscopic (left) and microscopic (centre and right) scales.....	59
Figure 14 SEM images for hot compressed and cold compressed FSCPCM before and after one thermal cycling.....	60
Figure 15 Schematic diagram showing the cold sintering process for $\text{NaNO}_3/\text{Ca}(\text{OH})_2$ FSCPCM	61
Figure 16 Multi-layer paraffin/EG composite in a square shape (a) and in a star shape (b)	62
Figure 17 Laser sintering process for fabrication paraffin wax/EG FSCPCM	62
Figure 18 Schematic of the melt coaxial electrospinning setup used for fabricating paraffin- TiO_2 -PVP FSCPCM fibres	71

Figure 19 SEM image of diatomite particles	76
Figure 20 Facilities used in the mix-sintering process.....	77
Figure 21 Shear mill used for grinding the PE granules	78
Figure 22 Brabender® Plastic-Corder® Labstation extruder	79
Figure 23 Mettler Toledo DSC2	81
Figure 24 Resolution and sensitivity obtained by TAWN method of this DSC.....	81
Figure 25 Schematic diagram of the conventional mix-sintering method without preheating process	94
Figure 26 Schematic diagram of the modified mix-sintering method with the preheating process	95
Figure 27 Bulk Density of the green and sintered FSCPCMs prepared by different processes	98
Figure 28 SEM and EDS images of the green and sintered FSCPCM prepared by different methods	101
Figure 29 Compressive strength of the FSCPCM with or without preheating process.....	103
Figure 30 DSC curves of pure KNO ₃ and the formulated FSCPCMs.....	105
Figure 31 Thermal conductivity of the preheated and not-preheated FSCPCMs	109
Figure 32 SEM and EDS images of sample N70 with different thermal cycles	112
Figure 33 SEM and EDS images of sample P70 with different thermal cycles.....	113
Figure 34 Thermal conductivity of the preheated/non-preheated sample before and after 50 times thermal cycling	114
Figure 35 Pore size distribution of diatomite and mixed powders.....	115
Figure 36 Schematic of the structure formation mechanism of FSCPCM without preheating process	117
Figure 37 Schematics of the structure formation mechanism of FSCPCM with preheating process	118

Figure 38 Contact angle of KNO_3 salt with different supporting materials.....	119
Figure 39 SEM images of sample $\text{SiO}_2\text{-KNO}_3$ with/without preheating	121
Figure 40 SEM and EDS images of sample graphite- KNO_3 with/without preheating	122
Figure 41 Densities of KNO_3 salt compound with different supporting materials.....	123
Figure 42 Compressive strength of KNO_3 salt compounded with different supporting materials .	124
Figure 43 Schematic of the extrusion process	130
Figure 44 Pressure profile when extruding the neat HDPE at different extrusion speeds	132
Figure 45 Averaged pressure and output at different extrusion speeds of neat HDPE.....	133
Figure 46 Pressure profile when extruding composite PCMs at different extrusion speeds	135
Figure 47 Throughput of the CPCMs (S30-S60) at different extrusion rates	137
Figure 48 Discontinuous flow curve and characteristic defects of a linear polymer (HDPE) [168]	138
Figure 49 Surface morphology of different samples at different extrusion rates	141
Figure 50 Schematic diagram showing the development of sharkskin defect [171]	143
Figure 51 Evolution of the surface in a single pressure for sample S50 (1mm).....	144
Figure 52 Velocity profile at different boundary conditions [177]	145
Figure 53 Storage and loss moduli of neat HDPE and composite PCMs (S30-S60).....	148
Figure 54 Apparent shear viscosity of the neat HDPE and composite PCMs (S30-S60)	150
Figure 55 Pressure profile when extruding sample S50 with different sizes of particles	152
Figure 56 Surface morphology of sample S50 with different particle size	155
Figure 57 Storage and loss modulus of sample S50 with different particle size.....	157
Figure 58 Pressure profile for sample S50 (0.25mm) with different processing temperatures at 30 rpm	159
Figure 59 Surface morphology of sample S50 (0.25 mm) at different temperatures.....	161
Figure 60 Storage and loss moduli of sample S50 (0.25 mm) at different temperatures	163

Figure 61 Apparent shear viscosity of composite PCM S50 (0.25 mm) at different temperatures	164
Figure 62 Computed 3-D structure of the FSCPCM.....	170
Figure 63 (a) A sliced cross-section image of the specimen, consisting of polymer, particles and pores; (b) and (c) are binarised images correspond to (a) with different greyscale threshold: (b) selects the particles and (c) selects both the particles and the polymer matrix.	171
Figure 64 Particle dispersion efficiency at a different extrusion speed.....	172
Figure 65 Particle size distribution of sample S50 (0.25 mm) at different extrusion rates	173
Figure 66 Porosity of Sample S50-0.25mm prepared at different processing temperatures.....	175
Figure 67 Pore size distribution of Sample S50-0.25mm at 150°C and 180°C	176
Figure 68 SEM images of sample S30 and S50 in the extrusion direction and cross-section direction (5 rpm).....	178
Figure 69 DSC curves of the HDPE-PE-graphite composite PCMs.....	179
Figure 70 DSC curves of sample S50 at a different extrusion speed.....	181
Figure 71 DSC curves of the sample S50 at different heating rate	183
Figure 72 Thermal conductivities of the composite PCMs and HDPE.....	187
Figure 73 TGA curves of the composite PCMs and the components at N ₂ and Air atmosphere....	189
Figure 74 DSC curves of sample S50 after different thermal cycling times	191
Figure 75 TGA curves of Sample S50 with and without 100 thermal cycles in the N ₂ atmosphere	193
Figure 76 Chemical compatibility between components of the FSCPCM.....	194
Figure 77 Chemical compatibility of the FSCPCM after thermal cycles	195

1 Introduction

1.1 Background of Thermal Energy Storage (TES)

The rate of the worldwide energy consumption increase in 2018 was almost twice the average growth rate since 2010 [1]. This is driven by the continuous global economic growth and the rising population of the middle class. The statistic shows that industrial activities including the energy sectors (e.g. power generation, coke production, etc.) are mainly responsible for the energy consumption [2]. However, the energy utilisation efficiency has not been improved significantly, leading to a vast amount of industrial waste energy unused. Therefore, one of the greatest challenges is to enhance the energy utilisation efficiency. On the other hand, carbon emissions reached a historically high in 2018 due to the use of fossil fuels, with coal-fired power plant being the largest contributor to the carbon emission growth [1]. Clearly, the use of renewable energy to replace fossil fuels is one of the most promising approaches to reduce the carbon emission. However, the intermittency and fluctuating nature of renewable energy are the roadblocks to the large-scale deployment of renewable energy. As a result, resolving the intermittency of the renewable energy sources has become a hot topic of the research community in recent decades.

Energy storage technology provides an effective approach to address the aforementioned challenges. Such a technology can enhance the energy utilisation efficiency by recycling waste energy, address the intermittency of renewable energy and help make the energy demand meet the energy supply [3]. Various energy storage technologies has been developed, which have different technology readiness levels (TRLs, 0-9); see Figure 1. Pumped hydroelectric storage (PHS, TRLs=9), compressed air (CA, TRLs=9), and Li-ion batteries (TRLs=9) are regarded as the developed energy storage technologies [4], whereas thermal energy storage (TES) and cryogenic energy storage (CES) are less developed (TRLs=6-7) [5], [6]. Thermal energy storage is regarded as one of the most

important storage technologies, because thermal heat is at the heart of the energy supply chain as shown in Figure 2. In addition, the TES has an economic advantage compared with other technologies [2]. The importance of thermal energy and the TES is also reflected by the following aspects: approximately 50% of the energy demand in UK is in the form of heat [7]; thermal energy is an intermediate product and/or by-product of many industrial processes; global energy budget centres around heat conversion, transmission and storage [8]; and indeed TES has found a diverse range of applications, e.g. combined heat and power system, passive heat/cold buffer system in food industry and thermal protection in electronics, etc. [9]–[11].

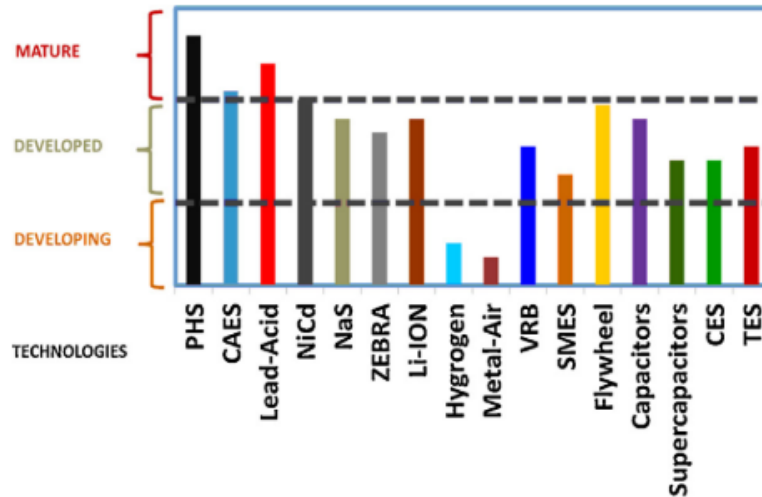


Figure 1 Technology readiness level of different energy storage technologies

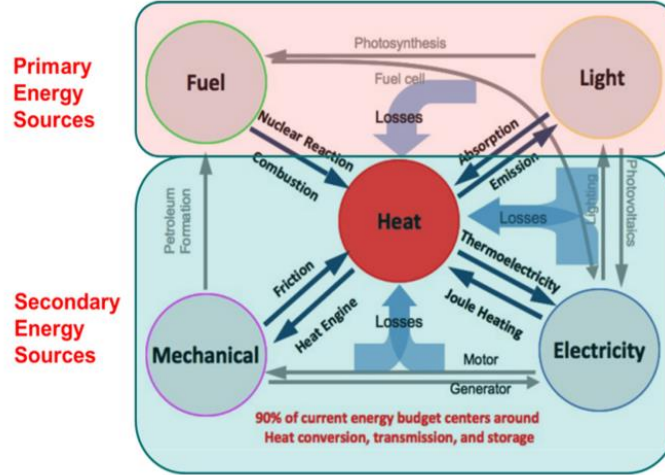


Figure 2 Thermal energy at the heart energy chain [8]

1.2 Research gaps in latent heat storage based technologies

TES technology can be classified into sensible heat based thermal energy storage (SH-TES), latent heat based thermal energy storage (LH-TES), and thermochemical heat based thermal energy storage (TCH-TES). The SH-TES is highly developed and has been used for many decades. The TCH-TES utilises reversible chemical reactions or sorption processes to store and release heat, and it is the least developed that requires significant fundamental research before any substantial industrial applications [12]. The LH-TES is less developed compared to the SH-TES, but has a high energy density with an isothermal charging/discharging process. The LH-TES has therefore been a hot topic in recent years. Despite significant progress in the LH-TES, there are still a number of challenges. This work is therefore concerned with the LH-TES technology, with a specific focus on the material's manufacture.

The LH-TES material, also termed as phase change material (PCM), has been studied intensively over the past few decades, with an aim to enhance energy density, durability, lifespan, thermal properties and cost-effectiveness. However, pure PCMs can hardly meet all these

requirements. Examples of key problems include low thermal conductivity, supercooling, corrosion, low chemical or thermal stability, and phase segregation, etc. A main approach to address these technological challenges is the modification of pure PCMs with additives. For examples, thickening and nucleation agent have been used to reduce the phase segregation; thermally conductive materials (e.g. carbons, metals, and carbides) have been used to enhance the overall thermal conductivity; the formation of structures/composites/microcapsules has been adapted to deal with the corrosive PCMs; These approaches have improved the performance of the PCMs. However, they have also complicated the manufacturing process of the LH-TES materials and increased the costs, and reduced the scalability of the material's production.

Currently, only a few PCMs are at their early stage of commercialization. The lack of cost-effective large-scale production technologies presents another challenge in the deployment of PCM. The department for Business, Energy & Industrial Strategy (BEIS, UK) has highlighted that the key for commercialising PCMs is to reduce the cost of PCM to a price of 50 €/kWh [12]. The cost reduction can be done by reducing the cost of the raw materials and low-cost large-yield manufacturing processes. There is therefore an urgent need to develop technologies for CPCMs which is easily scaled up at a low cost. In addition, our understanding of the relationship between the manufacturing process and PCM product performance is lacking.

1.3 The objectives and motivations

Developing a manufacturing process for CPCMs could help to improve the production yield and cut down the cost of PCMs. However, few studies have considered how to improve the manufacturing skills and thus to facilitate the commercialization of CPCMs. Most studies focus on the property optimisation through formulation design. Therefore, this forms the motivation of this study, which is to reduce the unbalanced development between the material formulation design

and manufacturing skills. This PhD work focuses on the development of scalable manufacturing methods for PCMs to contribute to the commercialiation of CPCMs, and also understanding the underlying physics, particularly how the manufacturing process affects the CPCM structures and hence their properties.

1.4 Thesis outline

In this thesis, the focus is on the advanced manufacturing technologies for the FSCPCMs. The investigations include a mix-sintering method and a continuous hot-melt extrusion method, as shown in Figure 3. The two methods are scalable, flexible, easily-controllable and potentially cost-effective.

For the mix-sintering method, a modified mix-sintering method with an additional preheating process is proposed and compared with the traditional fabrication route in chapter 4. For the hot-extrusion method, effects of processing conditions on the novel HDPE-pentaerythritol (PE)-graphite FSCPCMs were discussed in chapter 5. Chapter 6 is to investigate the thermal and physical properties of the extruded FSCPCMs, and to evaluate their thermal performance for TES applications.

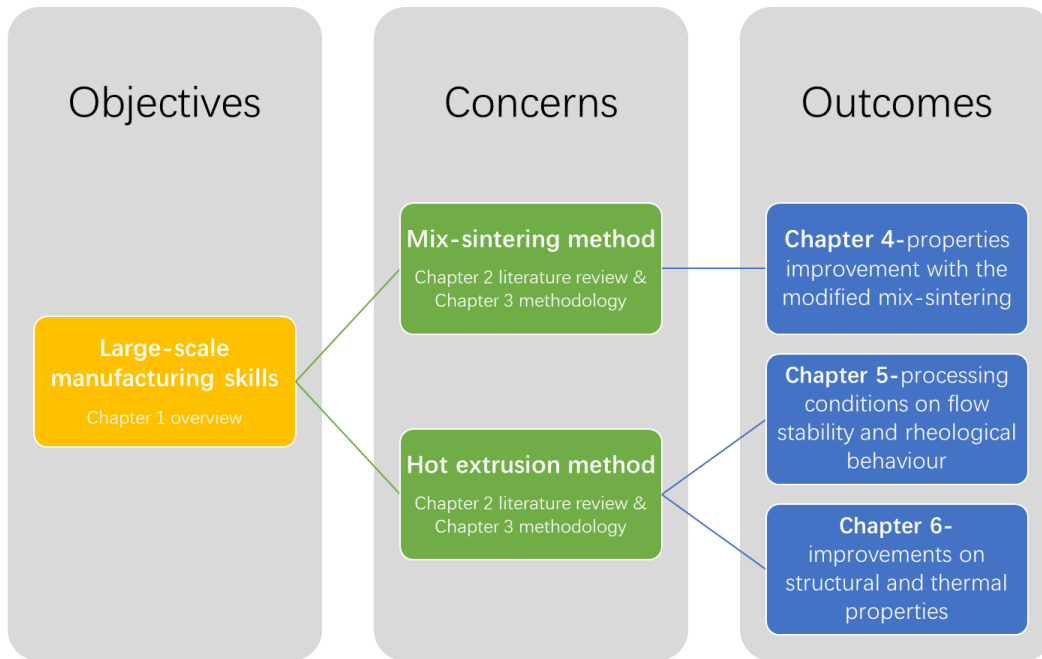


Figure 3 Diagram of the thesis structure

In detail, the thesis is divided into seven chapters as outlined in the following:

Chapter one gives a brief introduction to the current energy scenarios, showing the importance to develop large-scale TES technologies. Current challenges in the deployment of TES technologies are highlighted, including barriers of commercialising the LH-TES materials. Finally, the aims and specific objectives are described.

Chapter two summarises the literature related to the focus of this work, particularly the manufacturing methods for the FSCPCMs. Different manufacture methods and processing conditions are reviewed. Knowledge gaps in different manufacturing methods are also highlighted.

Chapter three presents the materials and methodology, explaining the experimental techniques and instruments used in the work.

Chapter four will be on the newly developed mix-sintering method with a preheating process integrated into the conventional process. The effects of the preheating process on the

microstructure development and the thermal properties of the FSCPCM are investigated. Besides, criteria are also discussed for the use of the modified mix-sintering method.

Chapter five explains the use of the continuous extrusion method for preparing a novel polymer-based FSCPCM. Effects of particle content, particle size, and temperature on the extrusion stability are studied, and the rheological behaviour of the polymer melt is also investigated.

Chapter six characterises the extrudates, where an attempt is also made to correlate the structural properties with the extrusion conditions. The thermal physical properties and thermal cycling stability of the FSCPCM are also analysed.

Chapter seven summarises the main conclusions of this work where recommendations for future work are also given.

2 Literature review

2.1 Introduction to phase change materials (PCMs)

Latent heat storage materials, also termed as phase change materials (PCMs), have attracted wide attention due to their high energy density, isothermal phase change process, long-term thermal cycling stability, and cost-effectiveness. For low-temperature thermal energy storage applications, they can be built into building insulation materials for thermal mass enhancement [13], used for domestic space heating [14], weave into fabric textile for thermal comfort [15], etc. For high-temperature applications, they can be used in the solar power generation system [16], waste heat recovery from industrial processes [17], shifting the peak heating load [18], etc. An ideal PCM should have properties such as high heat of fusion, no supercooling or phase segregation, non-corrosive, non-flammable, non-toxic, and chemically and thermally stable; see in Table 1 [19], [20]. Figure 4 shows the melting temperature and the heat of fusion of some representative PCMs. One can see that there are many PCMs, covering a wide temperature range from -100°C to 1000°C and a large range of latent heat from ~ 100 kJ/L to 1000 kJ/L. According to the melting temperature, the PCMs can be classified into low-temperature PCMs ($< \sim 100^{\circ}\text{C}$), mid-temperature PCMs (~ 100 – 200°C), and high-temperature PCMs ($> \sim 200^{\circ}\text{C}$) [9]. In terms of the chemical composition, the PCMs can be classified into organics and inorganics [21]. Table 2 also shows the advantages and disadvantages of organic and inorganic PCMs.

Although there are numerous PCMs, only a few have been commercialised [12], [22]. The low extent of commercialisation is associated with unsuitable thermal and chemical properties of most pure PCMs for practical applications. Almost every single PCM has its disadvantage which can prevent its wide deployment. The most commonly occurred disadvantages of pure PCMs include:

1. **Low thermal conductivity.** Most PCMs have low thermal conductivities. For instance, organic PCMs typically have a heat conductivity below $0.4 \text{ W/(m}\cdot\text{K)}$, while most inorganic PCMs have a heat conductivity below $1.0 \text{ W/(m}\cdot\text{K)}$ [23]. Such a thermal conductivity can affect the energy charging and discharging rates, leading to a low energy efficiency of TES system, and an inability to maintain constant temperature [23].
2. **Chemical/physical compatibility.** Many inorganic PCMs are corrosive to metals and alloys [24], [25]. Organic PCMs are less corrosive but there have been observations of interactions between organic PCMs and plastic containers, leading to the deformation and failure of plastic containers [26].
3. **Supercooling.** Almost every PCM has a certain degree of supercooling ranging from few degrees (e.g. paraffin) to tens of the degrees (e.g. water-based PCMs, sugar alcohols). The crystallisation process always happens when the temperature below its melting point, therefore supercooling exists for almost every material to a different degree [23]. However, severe supercooling can cause problems in practical applications, as supercooling gives a metastable phase [27]–[29].
4. **Volume variation.** Phase change often induces a volume change. A considerable volume variation during phase change often makes the design of a TES system complicated, leading to a significant cost increase. Moreover, the volume change of PCMs affects heat transfer, and hence changes the charging and discharging kinetics.

To overcome the problems outlined above, the use of composite PCMs has been proposed and practised in recent years. Such an approach uses various additives in pure PCMs creating structured PCMs. For examples, the introduction of thickening and nucleation agents to reduce phase segregation; the addition of highly thermally conductive materials (e.g. carbons, metals, and carbides) to enhance the thermal conductivity; and the use of matrixes or capsules to prevent PCM

corrosion. In this work, we focus on the form-stable composite PCMs, which are essentially a PCM compounded with a physically and chemically compatible matrix and sometimes a heat conduction enhancement additive. Such materials behave like a solid-solid phase change material. The composite PCMs have benefits of negligible volume changes, little corrosion, as well as high thermal conductivity. However, due to the use of non-phase change materials, the overall heat storage capacity is reduced owing to the reduced content of PCM. Hence, a compromise between thermal performance and energy storage density should be considered for the optimization of composite PCM formulation. In the following section, current achievements in the form-stable composite PCMs are discussed.

Table 1 Requirements for an ideal PCM

Categories	Requirements
Thermal	<ul style="list-style-type: none"> • Suitable phase change temperature; • High phase change enthalpy and high specific heat; • High thermal conductivity; • Negligible supercooling and phase segregation; • Long-term thermal stability; • Small volume variation and small vapour pressure;
Chemical	<ul style="list-style-type: none"> • Non-corrosive and chemically compatible with constructive materials; • Long-term chemical stability without degradation; • Nontoxic, non-flammable, non-explosive, environmental-friendly;
Economic	<ul style="list-style-type: none"> • Cost-effective ; • Large-scalable fabrication;
Kinetic	<ul style="list-style-type: none"> • High nucleation and crystallisation rate; • Reproducible melting/solidification process;

Table 2 Comparison between organic and inorganic PCMs [21]

	Advantages	Disadvantages
Organics	<ul style="list-style-type: none"> • Non-corrosive; • Chemically stable • Negligible phase separation; • Good nucleation rate; 	<ul style="list-style-type: none"> • Low thermal conductivity; • Supercooling (sugar alcohols) • Relative low phase change enthalpy; • Flammable; • Cost-intensive;
Inorganics	<ul style="list-style-type: none"> • Large phase change enthalpy; • Relative high thermal conductivity; • Cost-effective; • Non-flammable; • High-temperature stability 	<ul style="list-style-type: none"> • Supercooling (salt-water solution and salt hydrates); • Phase separation(salt-water solution and salt hydrates); • Corrosive;

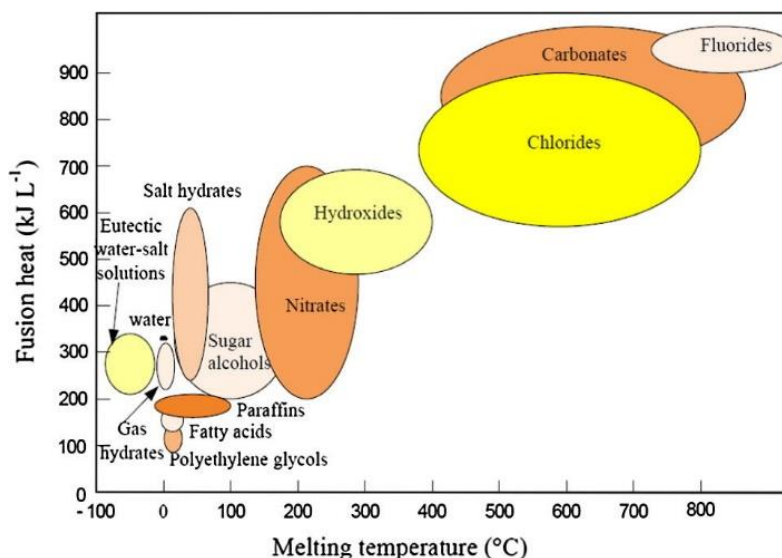


Figure 4 Melting temperature and enthalpy range of different PCMs [23]

2.2 Form-stable composite phase change materials (FSCPCMs)

2.2.1 Introduction

As mentioned in section 2.1, a CPCM can maintain shape stability and prevent PCM leakage during melting. It is also called form-stable composite PCMs (FSCPCMs) or shape-stabilized composite PCMs (SSPCMs). An FSCPCM typically consists of a PCM for heat storage, a supporting material (matrix) to maintain the overall structure stability, and/or an additive to enhance the overall thermal conductivity; see Figure 5. The supporting materials are structurally and chemically compatible with the PCM under the working conditions. Some of the supporting materials are highly thermally conductive (e.g. carbon), which can act both as a structural stabilisation and thermal conductivity enhancement materials. Other supporting materials are less thermally conductive (e.g. polymers), thermal conductivity enhancers are therefore often used in the formulation. Besides, additives can be used to overcome the shortages and enhance the thermal performance of the CPCM. Some additives could act as a nucleation agent to reduce supercooling, and a fire retardant to reduce flammability, etc. As a result, an optimized FSCPCM requires considering lots of formulation studies.

A properly formulated FSCPCM has a number of advantages including:

- 1) The ability to keep shape stable, with no need for an extra package. Heat sources can be directly in contact with the composite PCM, thus minimising heat transfer resistance.
- 2) As the PCM is confined in a chemically stable matrix, corrosion is greatly reduced.
- 3) The supporting matrix material can form a heat conduction network to enhance the overall heat conductivity.
- 4) Phase separation of the composite is greatly reduced due to the confinement of the PCM in the supporting matrix material.

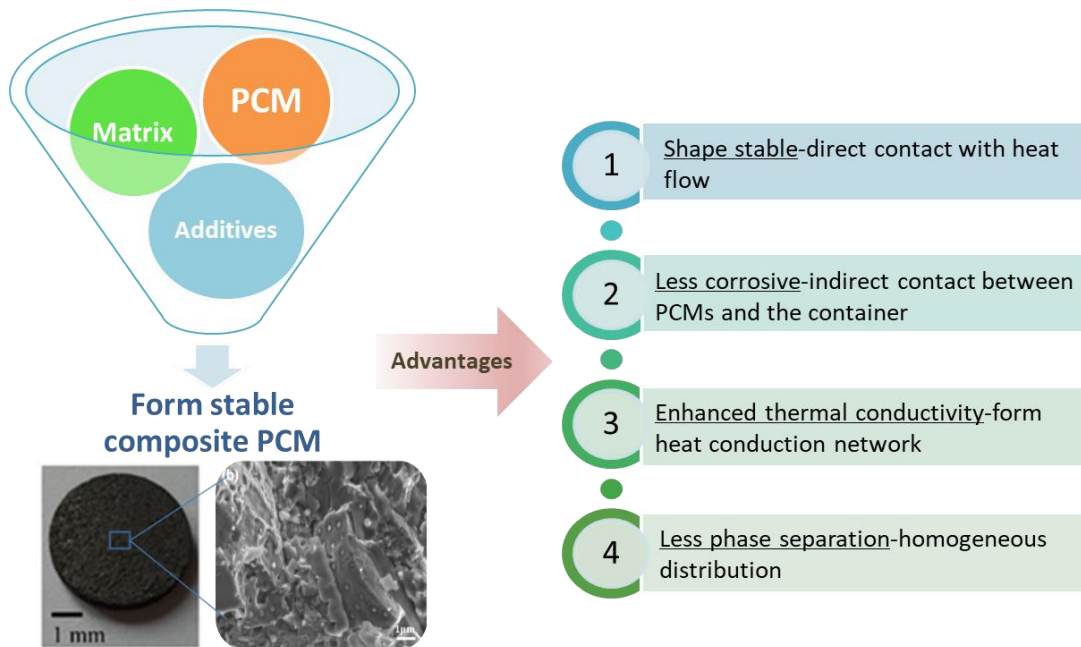


Figure 5 Components and advantages of FSCPCMs

2.2.2 Classifications of FSCPCMs

Diverse FSCPCMs have been investigated. According to chemical species of the supporting materials, they can be broadly classified into polymer-based, ceramic-based, and carbon-based FSCPCMs. They are reviewed in the following.

2.2.2.1 *Ceramic-based FSCPCMs;*

Ceramics as a structural supporting material often offers great chemical compatibility, thermal stability and absorbability [30]–[32]. Raw materials for making the ceramic materials are often plenty so their prices are highly competitive. There are both porous and non-porous ceramic minerals. Porous ceramic minerals give a high specific surfaces area and desirable absorbability. Examples include diatomite (specific surface area: ~ 1717.11 to ~ 4250.96 m²/g [33]), vermiculite (~ 672 m²/g [34], [35]), sepiolite (~ 900 m²/g [36]), expanded perlite (~ 13500 m²/g [37]), and attapulgite (~ 300 to ~ 600 m²/g [36]). Numerous studies have been carried on the use of these porous ceramic materials with both organic and inorganic PCMs. These studies have shown that the porous structure and interlayer spaces of the porous structure can contain the melted PCM (see Figure 6 [38] and Figure 7 [35]), even at a high PCM loading without leakage. Nomura et al. [39] used expanded perlite as a supporting material which could take up to 83 wt.% of erythritol without leakage. The use of non-porous ceramic minerals has also been studied as supporting materials. Examples include MgO and Kaolin [40][41]. These non-porous materials can contain the PCM within the interparticle voids due to the capillary forces [36]. Ge et al. [42][43] formulated a Na₂CO₃-Li₂CO₃/MgO/graphite composite PCM with a mix-sintering method and showed shape stability with a salt loading up to ~ 50 wt.%.

A high porosity of the supporting materials is clearly desirable to contain a high PCM loading. Various modification methods have been studied to enlarge the porosity and increase the absorbability of ceramic materials. These include: high-temperature calcination, acid/alkali

treatment, ionic exchange, and hydrothermal processing [36]. Different ceramic materials often require different treatment methods according to the physical properties and crystal structure. Jiang et al. [44] modified diatomite and observed a porosity increase by 67.53%. Pore size enlargement from ~ 0.7 to $\sim 26.6 \mu\text{m}$ with 40 wt.% CaCO_3 . Qian et al. [45], [46] used calcination, acid treatment, alkali leaching and nano-silica decoration methods to modify the pore structure of diatomite, showing alkali leaching is the most-effective method with an increase of pore volume from 0.0241 ml/g to 0.0718 ml/g by 5 wt.% NaOH.

Lv et al. [36] reviewed recent studies on the ceramic-based composite PCMs and summarised the advantages of ceramic materials as a matrix material for high-temperature PCMs such as nitrates [47], [48], carbonates[40], sulfates[38], [49] due to their excellent chemical and thermal stability at high temperatures. Qin et al. [38], [49] successfully formulated diatomite/ Na_2SO_4 composite PCMs for high-temperature applications (up to 980°C) and showed an excellent high-temperature thermal stability of the CPCM. The study used the mix-sintering method, which is more commonly used for preparing high-temperature ceramic-based CPCMs, as the (vacuum) impregnation method is limited by the maximum working temperature of the devices [47], [40]. Some ceramic materials have a relatively low thermal conductivity [36]. Thermal conductivity enhancers (e.g. graphite, metal, carbon nanotubes, etc.) are often added to address the issue.

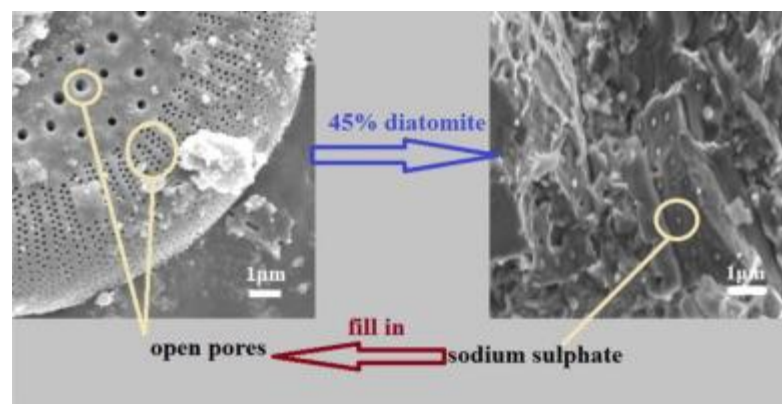


Figure 6 The morphology of the diatomite/ Na_2SO_4 composite PCM [38]

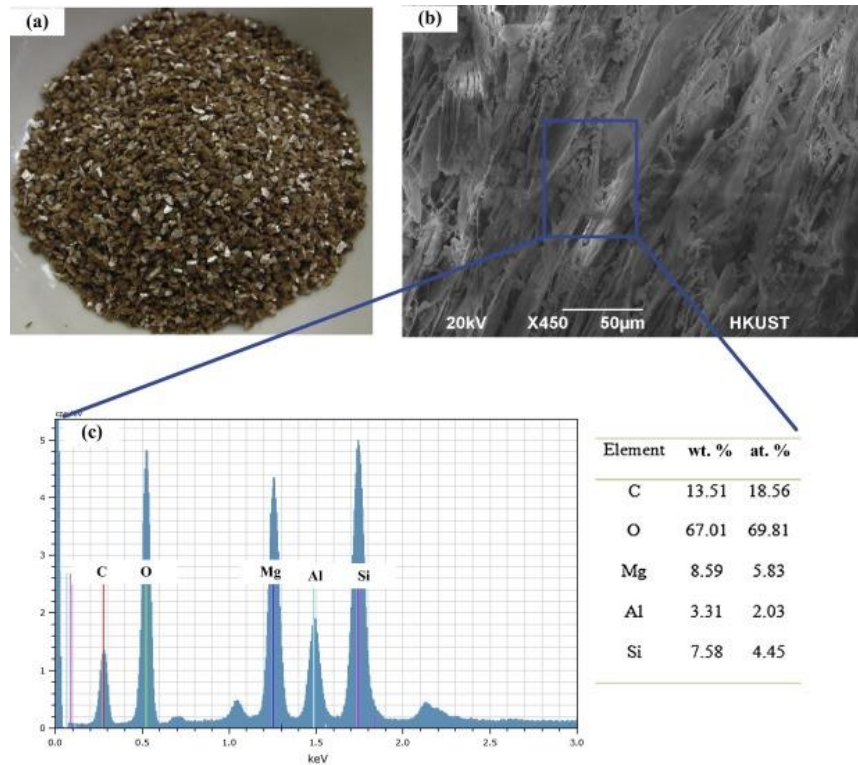


Figure 7 The SEM and EDS images of a paraffin/vermiculite composite [35]

2.2.2.2 Carbon-based FSCPCMs;

Carbon materials are highly thermally conductive and are therefore used in formulating FSCPCMs with low thermally conductive PCMs. In such cases, carbon materials also act as a structural skeleton for the composite. These materials can be broadly grouped into two: 1) microstructural carbon materials, such as expanded graphite, graphite flakes, carbon fibres, etc.; and 2) nanostructural carbon materials, for instance, single-/multi-wall carbon nanotubes (SWCNTs/MWCNTs), graphene, graphene nanoplatelets (GNPs), etc. Expanded graphite (EG) is one of the most popular microstructural carbon materials as a supporting matrix due to its highly porous structure and effective thermal conductivity enhancement. Zhang et al. [50] impregnated 80 wt.% of RT100 (paraffin) into expanded graphite and showed a good structural stability after 200 thermal cycles and good thermal conductivity (6.8 W/m·K). EG has also been used to compound with inorganic PCMs, particularly salts. Wu et al. [51] prepared a salt hydrate/EG CPCM, and concluded

that the EG could not only enhance the thermal conductivity (up to 3.643 W/m·K) but also reduce greatly the phase segregation and supercooling of the hydrated salt.

Comparative studies have been performed on the effects of particle size and type of carbon materials on the thermal conductivity enhancement. Gilart et al. [52] found that 25 wt.% EG particles impregnated with paraffin give a higher heat conductivity enhancement (by 576%) than that using the same amount of MWCNTs (by 41%), although MWCNTs have a higher thermal conductivity up to 650-830 W/m·K [53]. Xiang et al. [54] found that a larger size (15 μm) of graphene nanoplatelets (GNPs) as a supporting material could obtain a higher heat conductivity enhancement than smaller ones (1 μm). The reason for such a finding was interpreted as that larger carbon particles could form a more effective heat conduction network with lower interparticle heat conduction resistance. Although particles with smaller sizes could have more interparticle contacts, the heat conduction resistance is high due to low thermal conductivity of the PCM at the interface.

2.2.2.3 Polymer-based FSCPCMs;

Polymer-based FSCPCMs use self-reinforced polymers as the structural supporting material. Experimental work has shown that polyethylene, polyurethane, acrylic resin, and polyolefin are promising supporting material candidates. High/low-density polyethylene (HDPE/LDPE) is one of the most popular polymer candidates due to cost-effectiveness, good chemical stability, and durability. Through physical mixing and/or chemical cross-linking and blocking, these polymer materials are commonly compounded with low and medium temperature organic PCMs, including paraffin and fatty acids, owing to the maximum working temperature of the polymers (normally less than 300°C). Additionally, polymers have some drawbacks such as low thermal conductivity and flammability. Therefore, thermal conductivity enhancers are often required to formulate these composites. Besides, flame retardants such as magnesium hydroxide and microencapsulated red phosphorus are also added to reduce the flammability of the composite PCMs [55].

Kaygusuz [56] and Sari [57] prepared paraffin/HDPE/graphite FSCPCM by mixing and blending in a molten state. The mass ratio of the paraffin could reach 76 wt.% without any leakage during phase change. The overall thermal conductivity enhanced by 33.3% and 52.3% with an addition of expanded and exfoliated graphite, respectively. Cai et al. [58][59] fabricated a paraffin/HDPE composite PCM using a twin-screw extruder and showed that the HDPE formed a three-dimensional structure with paraffin embedded inside the structure (Figure 8). Chen [60] prepared several paraffin-polymer (HDPE, LDPE, LLDPE) FSCPCMs and studied the miscibility between the paraffin and the polymers. They found that the degree of the miscibility between the paraffin and the polymer affected the phase change enthalpy of the paraffin. An intermediate phase was observed because of the partial miscibility between the paraffin and the polymer, which reduces the heat that can be stored by the paraffin. They concluded that paraffin is less miscible with HDPE than that with LDPE or LLDPE, but the heat enthalpy of paraffin showed the highest with HDPE. Therefore, the miscibility between PCM and matrix material should be avoided for the formation of polymer-based FSCPCMs.

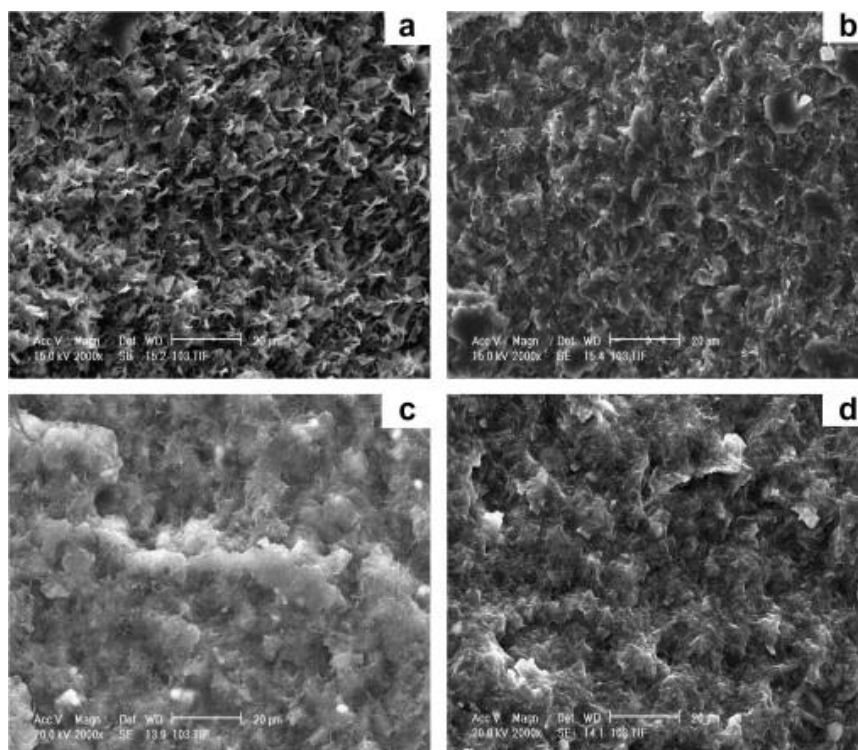


Figure 8 SEM images of the paraffin-HDPE CPCMs: (a) 75 wt.% Paraffin + 25 wt.% HDPE; (b) 75 wt.% Paraffin + 22.5 wt.% HDPE + 2.5 wt.% OMT (organophilic montmorillonite, fire retardant); (c) 75 wt.% Paraffin + 20 wt.% HDPE + 5 wt.% OMT; (d) 75 wt.% Paraffin + 15 wt.% HDPE + 10 wt.% OMT;

2.2.3 Challenges and innovation needs for FSCPCMs

Although both the academic and industrial communities have shown a strong interest in developing FSCPCMs due to the benefits aforementioned, only a few products have so far been in the early stage of commercialization. Key challenges for large-scale deployment of FSCPCMs include: high cost, low production yield, and lack of skills for large-scale manufacturing. As reported by the UK Department of Business, Energy & Industrial Strategy (BEIS), the UK manufacturers are targeting a price of 50 €/kWh for latent heat storage [12]. Such cost reduction requires the reduction of price of raw materials as well as the manufacturing processes. Meanwhile, the performance and quality of the materials should be maintained while reducing the cost. Therefore, the first task is to screen and select cost-effective raw materials that have the potential to formulate commercial FSCPCMs.

Currently, there is a vast knowledge base in both academic and industrial communities in the materials formulation design and selection, in the forms of academic papers and patents. Translating these into real industrial practice requires further and substantial efforts and investment. Another task is to develop cost-effective and scalable manufacturing processes for the FSCPCMs. The productivity and production yield should be highly competitive and meet the demand for the application. Besides, as FSCPCMs commonly consist of multi-species and/or multi-phases, the process parameters can significantly affect the properties and performance of the final products. Understanding fabrication-structure-property relationships are essential for the development of manufacturing technologies. However, there have been very few studies on these two aspects and hence clear gaps existed. The next section will provide a state-of-art summary of the manufacturing methods for FSCPCMs, where innovation needs are also identified.

2.3 Fabrication methods for FSCPCMs

2.3.1 Classifications of fabrication methods

A fabrication process is often designed according to the materials to be fabricated, their technical specifications, the scale and requirements for energy & water, etc.. For an FSCPCM fabrication, Figure 9 summarizes the processes used for the fabrication. One can see that the impregnation method has been widely used for both ceramic-based and carbon-based FSCPCMs. This is particularly applicable for porous materials. The mix-sintering method is extensively used for preparing high-temperature FSCPCMs and non-porous structural materials, which typically involves shaping and sintering. For polymer-based FSCPCMs, the preparation methods reported so far are hot-melt extrusion, mix-blending and electrospinning. The mix-blending method introduced in the literature is simply mixing the melted mixture in a lab-scale by hand or by a stirrer, which often does not provide detailed technical information of the processing conditions. This method is therefore not summarised nor compared, and state-of-art development of other fabrication methods are

discussed according to the method as classified in Figure 9: (1) impregnation method; (2) mix-sintering; (3) hot-melt extrusion (4) other methods (electrospinning, sol-gel process).

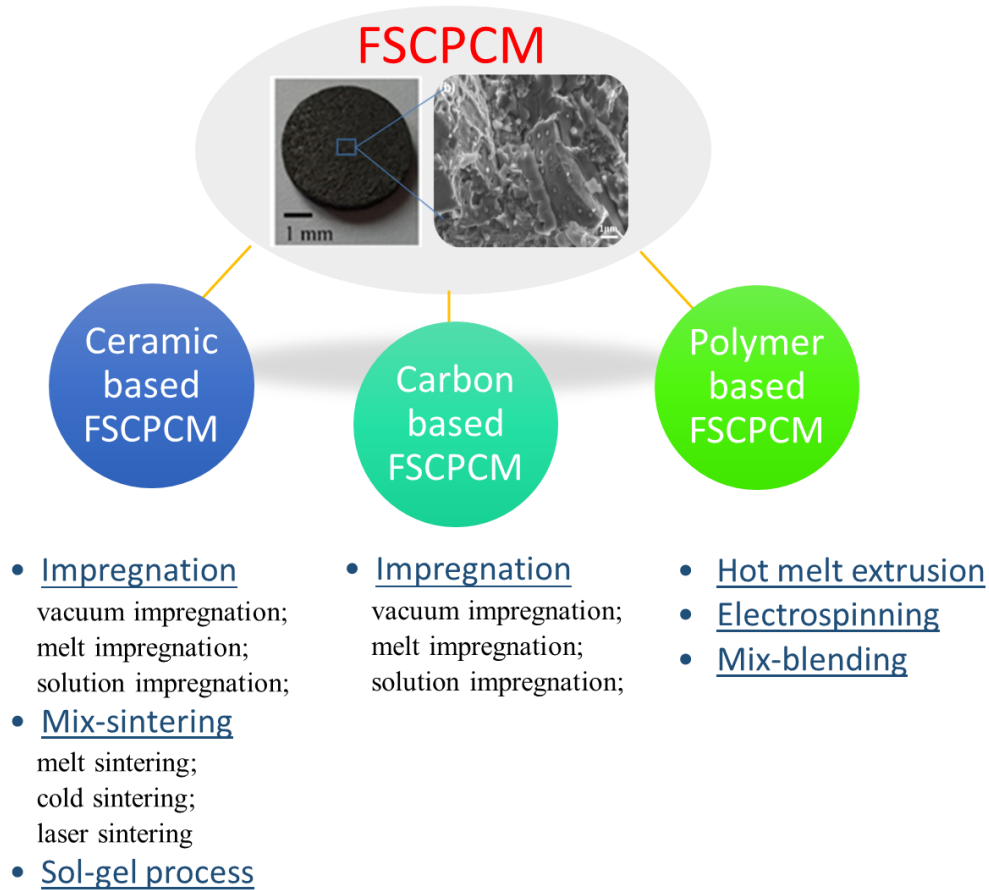


Figure 9 Fabrication methods based on the ingredients of FSCPCMs

2.3.2 Impregnation method

A wide range of FSCPCMs have been prepared by impregnating porous structural materials (e.g. diatomite, expanded graphite, vermiculite, expanded perlite) with liquid PCMs in a liquid state. The liquefied PCMs are absorbed and retained in the pore structure due to the capillary actions. The absorption ratio of the PCM is a key factor that directly influences the energy storage capacity of the composite. The absorption ratio is also closely related to the pore geometry and particle size of the matrix materials. Lv et al. [61] developed a mathematical model to predict the amount of

moisture absorbed in pores of iron ores through investigating the effects of physical parameters such as pore geometry, particle size, specific surface area, and the contact angle; see Eq. 1 below. In their model, both the water retained in interparticle voids and that inside the pores of the matrix materials are taken into account. Subsequently, Li et al. [62] applied the mathematical model to predict the theoretical absorption ratio of PCMs (paraffin) in a porous matrix (diatomite).

$$m = a + \rho \times b \times S + \rho \times V - c \frac{\rho_b}{\rho_p} \quad \text{Eq. 1}$$

where m represents the absorption ratio, %; S and V denote respectively the specific surface area ($\text{cm}^2/100 \text{ g}$) and the pore volume of the porous matrix ($\text{cm}^3/100 \text{ g}$); ρ is the density of PCM, g/cm^3 ; and ρ_b and ρ_p are the bulk density and particle density of matrix, g/cm^3 ; $b=2.2 \text{ cm}$; constant a , c are given as 10, and 40 in Li's work [62]. By comparing the experimental results and theoretical results obtained, Li et al. [62] found that the mathematical model agreed with experimental data in terms of the absorption ratio of PCM in diatomite.

In addition to the physical parameters of raw materials, e.g. pore geometry and particle size, process-related factors also have significant impacts on the absorption ratio and impregnation efficiency. These include the preparation temperature (that affects the viscosity of the PCM), time of immersion, residual moisture in the pores, and vacuum degree, etc. Table 3 summarises the state-of-art development in the impregnation method.

Table 3 Review on remarkable works of preparing FSCPCMs by impregnation method

Method description	No.	Matrixes	PCMs	Additives	Method details	Impregnation temperature (°C)	Vacuum degree	Impregnation time	PCM ratio	Sample scale (g) or size	Ref.
melt impregnation	1.	diatomite	fatty acids	/	magnetic stirring at 300 rpm for 10 min, then cleaned in ultrasound for 30 min	70	/	40min	up to 40%	/	[63]
	2.	diatomite	Paraffin (RT21)	/	/	60	/	/	up to 50%	/	[62]
	3.	diatomite	PEG4000	EG	/	65 –105	/	15 to 180 min	55%	/	[64]
	4.	diatomite	paraffin	/	/	60	/	30 min	32%	/	[65]
	5.	EG	CaCl ₂ ·6H ₂ O	surfactant OP-10	ultrasound applied	80	/	2h		/	[66]
	6.	EG	stearic acid	/	magnetic stirring at a rate of 500 rpm, dried at 60 °C for 3h after impregnation	70	/	40min	83%	3 g	[67]
	7.	EG	LiNO ₃ /KCl	/	roll mixer applied	200	/	/	90%	/	[68]
	8.	EG	N-octadecane	/	magnetic stirring at a rate of 500 rpm, dried at 40°C for 4 h after impregnation	40	/	1h	83%	/	[69]
	9.	EG	Paraffin (RT44HC)	/	/	60	/	/	75%	/	[70]
	10.	EP, MWCNTs	paraffin(RT-50 and RT-60)	/	raw material mixed and heated directly in an oven	150	/	1h	75%	/	[71]
	11.	exfoliated graphite nanoplatelets (xGnP)	paraffin	/	/	75	/	/	93%	/	[72]
	12.	expanded perlite (EP)	paraffin	/	mixed every hour	90 ±5	/	/	60%	/	[73]
	13.	expanded vermiculite (EV)	Sodium nitrate	Silicon carbide	direct mixing, then melt impregnation in muffle furnace	350	/	2h	88%	/	[74]
	14.	graphene coated nickel foam (GcN)	paraffin wax	/	/	/	/	/	83%	/	[75]
	15.	modified cellulose acetate nanofelts	Capric–myristic–stearic acid (CMS)	/	dried at 60°C for 10 h after impregnation	60	/	1h	83.3%	/	[76]
	16.	modified diatomite	PEG 6000	SWCNs	dried at 80°C for 12 h after impregnation	/	/	/	60%	/	[77]

Method description	No.	Matrixes	PCMs	Additives	Method details	Impregnation temperature (°C)	Vacuum degree	Impregnation time	PCM ratio	Sample scale (g) or size	Ref.
	17.	polyamide 6 (PA6)/EG nanofibers	fatty acids	/	/	60	/	10h		/	[78]
	18.	ultrathin graphite foams	paraffin, erythritol	/	/	/	/	/	97.3%	/	[79]
vacuum impregnation	1.	active carbon granule (ACG), EG	Polyethylene glycol (PEG)	/	dynamic impregnation under vacuum; dried in an electric vacuum oven at 40°C for 6h	90	0.05 MPa	30 min	88%	/	[80]
	2.	bentonite clay (BC), pumice sand (PS)	octadecane; capric (CA)–myristic acid (MA);PEG1000	EG	/	above the melting temperature	70 kPa	60 min	42%	/	[81]
	3.	compressed expanded natural graphite (CENG)	paraffin wax	/	EG is compressed to discs before impregnation	70	vacuum	3 h	74% to 92%	/	[82]
	4.	diatomite	PEG 1000	EG	/	/	65 kPa	90 min	50%	/	[83]
	5.	EG, bentonite (BT), diatomaceous earth (DE), zeolite Y (ZY)	hexadecane (HE), octadecane (OC), fatty acids, butyl stearate (BE)	/	placed on filter paper at 30°C for 24h after impregnation	30	30 kPa	15 min	30%-81%	/	[84]
	6.	expanded fly ash (FL), expanded clay of small size(SZ), expanded clay of large size(SL), expanded perlite (PE)	Paraffin and fatty acid, (viscosity 2 and 10mPa)	polymer coating	/	/	88.1kPa; vacuum 30 minutes before impregnation	1 h	Up to 65%	/	[85]
	7.	expanded perlite (EP), diatom earth (DE), and gamma alumina (GA)	erythritol	/	/	150	vacuum	10 to 60 min	83%	/	[39]
	8.	modified diatomite (alkali-leaching, nano-silica decorated)	PEG4000	/	/	70-120	vacuum	10 to 120 min	70%	/	[46]
	9.	modified expanded perlite (EP)	paraffin (RT-27)	/	/	60	vacuum	/	35%, 50%	/	[86]
	10.	modified expanded vermiculite (EV)	Stearic acid (SA)	/	placed on filter paper at 80°C after impregnation	80	vacuum	30 min	63.12%	2 g	[87]

Method description	No.	Matrixes	PCMs	Additives	Method details	Impregnation temperature (°C)	Vacuum degree	Impregnation time	PCM ratio	Sample scale (g) or size	Ref.
	11.	Porous Al ₂ O ₃ @Grapite Foam pumice	Paraffin	/	dried at 80 °C until no leakage	80	vacuum	3h	66%	/	[88]
	12.		capric (CA)–palmitic acid (PA); heptadecane (HEPD); dodecanol (DD)	/	/	/	0.1 MPa	30 min	34% (CA–PA), 32% (HEPD), 31% (DD)	/	[89]
	13.	radial mesoporous silica (RMS)	PEG (4000)	/	/	60 -90	/	50 min	79%	/	[90]
	14.	SiC ceramic honeycomb (SCH)	KNO ₃ /NaNO ₃	/	/	325	below 20 Pa	4h	70%	34.3*34.3*150 mm ³	[91]
	15.	two species of expanded graphites (EG): EG flakes and EG matrix	MgCl ₂ ·6H ₂ O and Mg(NO ₃) ₂ ·6H ₂ O	/	Vacuum impregnation (vacuum rotary evaporator);ultrasound impregnation; direct impregnation	/	vacuum	0.25 h to 24 h	vacuum90.7%; ultrasound 93.8 ;immersion96.1%	/	[92]
	16.	vermiculite (VMT)	capric acid (CA)–myristic acid (MA)	EG	/	RT	vacuum	/	80%	/	[93]
	17.	zeolite (ZSM-5)	ethylene glycol (PEG4000)	/	with magnetic stirring , dried at 60°C for 24 h after impregnation	70	/	2h	50%	/	[94]
solution impregnation	1.	EG	LiNO ₃ –KCl, LiNO ₃ –NaNO ₃ , LiNO ₃ –NaCl	/	/	30 over melting point	/	6 to 9h	72.8% to 78.8%	/	[95]
	2.	EG	Na ₂ SO ₄ ·10H ₂ O, Na ₂ HPO ₄ ·12H ₂ O	paraffin wax coating	dissolved in deionized water, and dried at 10°C until no weight change	40	/	10 h	87.36%	4.5 g	[51]
	3.	Meso-structured onion-like silica (MOS)	stearic acid (SA)	/	dissolved in ethanol, and stirred at 1000 rpm; dried at 75°C for 24 h to evaporate ethanol	75	no vacuum	4 h	70%	0.17g	[96]
	4.	MWCNTs	lauric acid (LA)	/	dissolved in the ethanol, and impregnate with sonication; then heated at 180°C for 1 h (build up pressure to 1MPa) to fully filled the matrix		vacuum	1h	54.8%	6g	[97]

Method description	No.	Matrixes	PCMs	Additives	Method details	Impregnation temperature (°C)	Vacuum degree	Impregnation time	PCM ratio	Sample scale (g) or size	Ref.
other impregnation method	1.	radiata pine wood	paraffin (octadecane)	/	impregnate under high pressure (0, 1, 2, and 3 ± 0.1 bar)	50	0-3 bar	15 to 750 min	~66%	25mm* 25mm* 100mm	[98]
	2.	two species of carbon foams (CF-20 and KL1-250)	paraffin wax (RT65) as	MWCNT	the liquid PCM is forced through the carbon foam by a piston with ~6 bar pressure under vacuum	120	vacuum	/	96%	/	[99]

According to Table 3, different FSCPCMs have been prepared successfully by impregnation. By the gathered data, current outcomes can be classified into the materials, the impregnation methods, the processing conditions, and the scalability. The detailed outcomes are discussed in the following subsections.

(1) Materials prepared by impregnation method

The materials used for incorporating CPCMs are summarised in Table 3, including the PCMs, structural supporting matrixes and additive materials. It can be found that porous materials, such as EG, diatomite, expanded perlite (EP), zeolite, MWCNTs, have been intensively used as the structural supporting matrix. Among them, EG and diatomite are most studied matrixes due to their extremely high porosity. The EG could absorb the amount of PCM ranging from 72.8% to 96.1%. Wu et al. [51] reported that the porosity of EG could reach as high as 92.78%, and there is a hierarchical pore size distribution from 2 nm to 100 μm . Comparatively, diatomite has a relatively low impregnation ratio ranging from 32% to 70%. Some studies modified diatomites (alkali leaching, calcination, etc.) to increase its porosity, achieving an absorption ratio up to 70% [46].

Nomura et al. [39] also found that matrix with larger pores would present a higher impregnation ratio, but this also along with a higher risk of leakage due to smaller capillary force. Goitandia et al. [84] studied the structural stability of different porous matrix with a wide range of pore sizes from micropores (>0.6 nm) to macropores (<200 nm), including EG, bentonite (BT), diatomaceous earth (DE), and zeolite Y (ZY). After these composites underwent 450 times of thermal cycling, different degree of leakage was observed for all the composites. Matrixes with macroporous structure present serious PCM leakage, such as bentonite (BT), diatomaceous earth (DE). The exudation was found from their macropores and the inter-granular space. For a matrix with microporous pores, e.g. zeolite Y, which has a pore size of ~ 0.6 nm. The leakage is found attributed

to the PCM is not able to infiltrate into the micropores of zeolite even under vacuum. As a result, the PCM is absorbed in intergranular voids or just covered on its surface. For the mesoporous matrixes (EG, mesoporous silica), they present the lowest risk of leakage. Therefore, they are regarded as more suitable to impregnate with PCM to form FSCPCMs.

In terms of the PCMs studied, one can see that organic PCMs are most studied according to Table 3. For instance, paraffin, PEG and fatty acids, etc., which often have a relatively low melting point ($<150^{\circ}\text{C}$) are widely used for the impregnation. These mid-low temperature PCMs are easy to be heated to the liquid state, such as using a hot plate or putting them into the oven until melt before impregnation. For some high-temperature inorganic PCMs, like carbonate salts, chloride salts, they are more challenging to be prepared by melt impregnation due to the limitation of the devices and the risk of manipulation at high temperature. Therefore, as can be found from Table 3, high-temperature salt is much less studied by melt (direct) impregnation.

Moreover, the wettability between the liquid PCM and the solid matrix is another important factor that affects the impregnation efficiency and the structural stability, as capillary force is determined by the contact angle between the solid material and the liquid phase. Pincemin et al. [100] found that salt PCMs (NaNO_3 , KNO_3) show very limited infiltration ratio (about 40%) in the carbon matrix, owing to the low wettability between salt PCM and carbon matrix. Inversely, a good wettability between graphite and organic PCMs (e.g. paraffin) results in a good impregnation ratio. Hence, coating unwetted inorganic salts/EG composite with a wetted organic PCM is a good method to enhance the impregnation efficiency and prevent the leakage. Wu et al. [51] impregnated inorganic salts ($\text{Na}_2\text{SO}_4 \cdot 10\text{H}_2\text{O}$ and $\text{Na}_2\text{HPO}_4 \cdot 12\text{H}_2\text{O}$) into EG matrix firstly and then impregnated with paraffin as a coating. In this FSCPCM, the paraffin can form a solid layer outside, which could hold the structure stable without any leakage.

(2) Impregnation methods

Classifications of the impregnation methods

As shown in Table 3, impregnating matrix with PCMs is mainly obtained through three approaches: melt (direct) impregnation, vacuum impregnation, and solution impregnation. Melt (direct) impregnation is simple, which impregnate the matrix with liquid PCM either in room temperature or using a heating unit. The melt PCM can infiltrate into the matrix easily by capillary force if the matrix and the PCM are wettable. To prevent leakage, the excessed PCM on the matrix surface should be removed. The vacuum impregnation is similar to the melt impregnation but is under vacuum. The solution impregnation is to dissolve the PCM in a solvent before infiltration. Usually, water and ethanol are used as solvents. After the matrix has been fully impregnated with the PCM solution, the solvent has to be removed (eg. By heating) before use. Figure 10 shows the percentage of each impregnation method from the reviewed studies, as well as its advantages and disadvantages. One can see that melt (direct) impregnation method and vacuum impregnation method are equally used. The melt (direct) impregnation is simple, while the vacuum impregnation method sometimes can obtain a higher absorption ratio. However, the solution impregnation method is much less considered mainly due to the low absorption ratio and the additional process of removing the solvent, which accounts for only 10% of the reviewed papers. In addition, it is found that mechanical stirring and ultra-sonication are often applied in the infiltration process to obtain a uniform absorption.

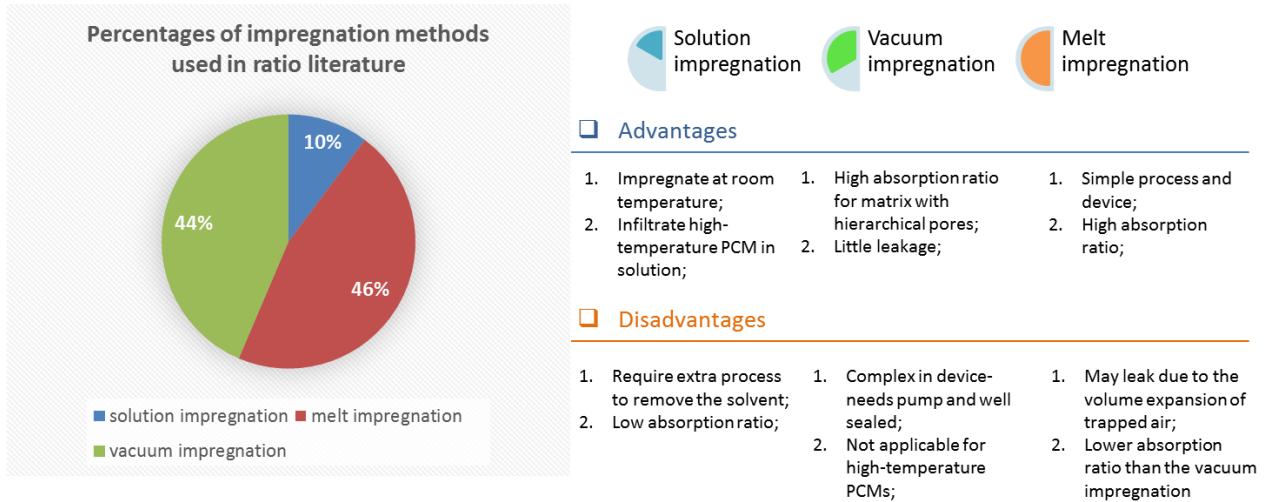


Figure 10 Percentage of different impregnation method used in literature

Novel impregnation methods and devices

Besides the three most used impregnation methods discussed above, several novel methods have been developed to enhance the impregnation efficiency. Alshaer et al. [99] used a piston to compress the melted paraffin through a carbon foam under 6 bar pressure. The carbon foam was firstly vacuumed and heated to remove the air and the moisture. By this preparation method, the infiltration efficiency can reach as high as 96 wt.%. Vasco et al. [98] used a similar method by forcing paraffin at four manometric pressures (0, 1, 2, and 3 bar) through the tangential direction of radiata pine wood. The author found that this process does not require an initial vacuum treatment due to the high compression pressure. The study also investigated the kinetics of impregnation progress, indicating that the absorption ratio is proportional to the compression pressure. The loading ratio has increased from 50% to 66% while the pressure increases from 1 to 3 bars. Wang [80] et al. has designed a dynamic impregnation device which can provide continuous ultrasonication energy under vacuum condition. The conventional static impregnation process is shown in Figure 11 (a), which firstly uses a vacuum pump to get rid of the air and then let the liquid

PCM flow inside the flask for impregnation. In Figure 11 (b), Wang [80] et al. designed a compact device consists of a vacuum pump and an ultrasonicator, which allows for impregnation under vacuum and ultrasonication simultaneously. The authors used this tailored device to impregnate active carbon granular (ACG) and expanded graphite (EG) with PEG, resulting in an absorption ratio up to 88% without any leakage.

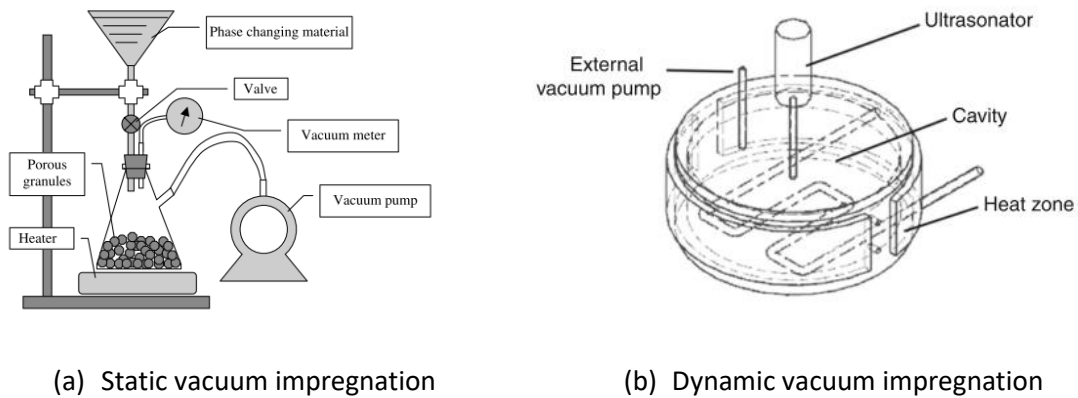


Figure 11 Static and dynamic vacuum impregnation device

(3) Impregnation processing conditions

Effect of vacuum treatment on the impregnation efficiency

Absorption ratio of the PCM is an important parameter that affects the energy storage capacity of the CPCM. However, it is affected not only by the pore geometry but also the processing condition. Hence, the impacts of the vacuum degree during preparation on the absorption ratio of different materials are studied.

Min et al. [90] compared the absorption ratio by direct impregnation and vacuum impregnation, using a mesoporous silica matrix (pore size ~ 7.62 nm) impregnated with polyethylene glycol (PEG). The results show a significant difference between these two preparation methods. The absorption ratio of vacuum impregnation ($\sim 80\%$) is almost twice as high as that of the natural immersion ($\sim 40\%$). Qian et al. [46] infiltrated PEG into a modified diatomite (pore size of $5\sim 10$ nm),

finding that the absorption ratio has been improved significantly with vacuum applied. Zhang et al. [85] studied the impregnation method, phase change behaviour and the sealing performance of a PCM infiltrate in an inorganic porous matrix. The authors also find that the loading ratio of PCM with vacuum can be four times as high as that without vacuum. Moreover, the authors compared the pore size distribution of porous matrixes, e.g. expanded perlite, expanded clay, and expanded fly ash, and the authors found that expanded clay with finer pores shows a higher enhancement of absorption ratio with vacuum impregnation than other porous materials. Qian et al. also regarded that porous materials with fine pores will need vacuum treatment to enhance the absorption ratio [46]. Nomura et al. [39] verified that the enhancement obtained by vacuum treatment is varying with the matrix pore geometry. The authors explained that the air trapped inside the pores prevents the impregnation of liquid. The loading ratio is decided by the capillary forces and the air and liquid pressure within the pores, which can be expressed as follows (Eq. 2):

$$P_{liquid}\pi D^2 + 4\pi D\gamma\cos\theta > P_{air}\pi D^2 \quad \text{Eq. 2}$$

Where P_{liquid} and P_{air} represent the pressure of the liquid PCM and air trapped inside the pores respectively; D is the pore diameter; γ denotes the surface tension of the PCM; θ represents the contact angle.

However, some authors also found that there is a negligible difference in the absorption ratio by vacuum impregnation compared with direct impregnation. Qian et al. [64] compared the vacuum impregnation and natural impregnation method by infiltrating PEG into diatomite, showing no significant difference. Galazutdinova et al. [92] also observed that different preparation methods (vacuum, direct, sonication, etc.) show similar loading ratios when impregnating EG with eutectic $\text{MgCl}_2 \cdot 6\text{H}_2\text{O}$ and $\text{Mg}(\text{NO}_3)_2 \cdot 6\text{H}_2\text{O}$. Generally, it can be concluded that the absorption ratio cannot be

enhanced consistently by the vacuum treatment, the enhancement is found related to the pore geometry of the matrix.

Effect of temperature and time on the impregnation efficiency

Temperature is an important processing parameter for impregnation method, as the viscosity of the liquid is temperature-dependent. The viscosity needs to be low to achieve a high infiltration ratio for impregnation. For melt impregnation, the temperature has to be above melting point. Min et al. [90] studied the loading ratio of PEG at different temperatures when infiltrating into the mesoporous silica matrix. The melting temperature of PEG is $\sim 57^{\circ}\text{C}$, so the studied temperatures are 60°C , 70°C , 80°C , 90°C . It was found that the absorption ratio increases significantly when the temperature rises from 60°C to 70°C , but levels off when the temperature is over 70°C . Qian et al. [64] [46] immersed the diatomite into PEG and studied the temperature effect on the impregnation efficiency. Results show a remarkable increment of the absorption ratio when the temperature increases from 65°C to 75°C , and then remain unchanged when the temperature is over 75°C . Therefore, one can see that increasing temperature could have a positive impact on the impregnation ratio, but the effect turns to indistinctive when the temperature is over a certain value.

In terms of the processing time, most studies immerse the matrix in PCM for adequate time and have not considered the minimal time required for the completion of impregnation. From Table 3, one can see that the impregnation time used in current studies has a very wide range, which varies from 0.25 h to 24 h. Vasco et al. [98] studied the kinetics of impregnation when immersing the *Pinus radiata* wood into paraffin. The results show that the absorption rate increases very fast in the first 2 hours, then slows down and reaches stable. This result is in agreement with other authors' finding [39], [46], [64], [90]. For different matrixes, the time to reach stable is also different.

Besides, it is found that the vacuum treatment can reduce the impregnation time required to reach the maximum absorption ratio.

(4) Scalability

The amount of materials prepared in each study is also displayed in Table 3. One can see that most of the samples prepared are at a laboratory level (several grams). For the industrial application of FSCPCM, a scalable, controllable, and continuous fabrication process are required for large-scale fabrication. Konuklu et al. [65] regarded that any pretreatment of the raw material, such as modification of the diatomite, will complicate the fabrication process and restrict the feasibility of large-scale fabrication. Besides, the authors regard that melt impregnation without any pre-treatment is the most promising method to scale up than other impregnation methods. As can be found in Figure 10, melt impregnation accounts for the highest percentage among all the impregnation methods. Vacuum impregnation needs an additional vacuum pump and a well-sealed system. Solution impregnation has a low impregnation efficiency and needs additional process (drying) to remove the solvent. Therefore, direct impregnation is the most practical method in the large-scale application. However, the uniformity of the samples prepared by melt impregnation need to be considered for large-scale fabrication

2.3.3 Mix-sintering

Mix-sintering fabrication method often consists of mixing, shaping and sintering processes. In the shaping process, the CPCM mixture is compressed to a compact structure under the high pressure. Then, the shaped samples are heated over the PCM melting temperature to obtain a rigid structure, which is called sintering process. In the sintering process, the liquid PCM can be absorbed into the porous structure of matrixes (e.g. diatomite, vermiculite, EG, etc.) or the interparticle voids of the non-porous matrixes (e.g. MgO, SiO₂, etc.) by capillary force. When the FSCPCM cools down,

the solidified PCM could act as a binder which can glue the grains of the supporting materials together, so the sintered FSCPM has a certain mechanical strength.

The mix-sintering method was firstly applied in the preparation of FSCPCMs in the 1980s. Randy and Terry [101]–[103] used 80wt.% NaCO_3 - BaCO_3 as phase change material and 20wt.% MgO as supporting material to prepare FSCPCMs. In the 1990s, Gluck [104] and Hame [105] compressed Na_2SO_4 and silica mixtures under a pressure of 70 MPa and then sintered to 1000°C for 2 hours to obtain high-temperature heat storage bricks. In the 21st century, the mix-sintering process is widely used to prepare FSCPCM. Gokon [106] used the mix-sintering method to fabricate alkali-carbonate/ MgO FSCPCM. The authors used the prepared FSCPCM in the catalyst bed, showing that the cooling time of the bed has been prolonged successfully.

Although the mix-sintering method has been developed for a long time, some processing parameters such as particles size, compression strength, sintering time and temperature have not been studied thoroughly. These processing parameters directly affect the quality of the product. Most of the current studies are focusing on formulation optimisations and aiming to improve the thermal properties, such as energy density, thermal conductivity, and thermal stability, etc. No study can be found that reviewed the process-related parameters regarding the preparation of FSCPCM by mix-sintering. The relationship between the processing parameter and the product property has not been revealed yet. Therefore, we have gathered the process-related parameters in Table 4, including all the studies that used mix-sintering method to prepare FSCPCMs. This can provide guidance for future study on improving the mix-sintering method for high-quality FSCPCMs.

Table 4 Review on remarkable works of preparing composite PCMs by mix-sintering

No.	Matrixes	PCMs	Additives	Particle size	Pressure	Compression method	Melting point	Sintering temperature	PCM ratio	Scale (g) , diameter	Ref.
1.	Ca(OH) ₂	NaNO ₃	/	NaNO ₃ : 350 µm and 500 µm; Ca(OH) ₂ : 50 µm	500 MPa	hot compression at 120 °C for 10 min	306 °C	/	60%	discs (Ø: 15 mm, h: 2-4 mm)	[107]
2.	calcium silicate	LiNO ₃ – NaNO ₃ – KNO ₃ – Ca(NO ₃) ₂	graphite	/	15 MPa for 1 min	uniaxial cold compression	103.5°C	150°C for 2 h	80%	discs (Ø: 15 mm, h: 3 mm)	[108]
3.	Cu, Al	In, Bi	/	<40µm and <10µm	/	/	157 °C, 270 °C	160°C and 300°C for 30-60s	30% - 40%	discs (Ø: 5 mm, h: 2 mm)	[109]
4.	diatomite	Na ₂ SO ₄	/	/	10 MPa	uniaxial cold compression	/	900°C for 1h	55%	discs (Ø: 13 mm, h: 3 mm)	[38], [49]
5.	diatomite	NaNO ₃	graphite	120-mesh	10 MPa	/	330 °C	370°C for 1h	70%	50 g, discs (Ø: 50 mm)	[110]
6.	diatomite	NaCl-KCl	/	salt: 200–400 µm; diatomite : 3-5µm	40 MPa for 1 min	/	661 °C	680 °C for 1 h.	70%	/	[111]
7.	diatomite	KNO ₃	/	/	45 MPa	uniaxial cold compression	330.23 °C	350 °C for 2 h	65%	Ø: 26 mm and h: 4.5 mm	[112]
8.	EG	NaNO ₃ – KNO ₃	/	Graphite (500 µm) KNO ₃ /NaNO ₃ (0.5-3 mm)	5-10 MPa	Uniaxial and isostatic compression	220.2 °C	/	95%	/	[113], [114]
9.	EG	MgCl ₂ -KCl	graphite paper (GP)	EG (mesh 100); GP (0.5mm*30mm*3 mm)	/	/	424 °C	500°C for 3h	<80%	discs (Ø: 60 mm, h: 15 mm)	[115]
10.	EG	Ca(NO ₃) ₂ – NaNO ₃	/	80 mesh	8 MPa for 80s	uniaxial cold compression	280 °C	300 °C for 3 h	93%	>130 g	[116]

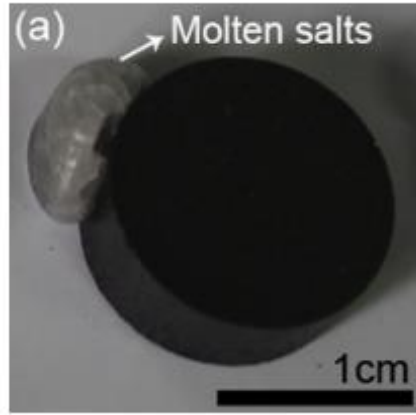
No.	Matrixes	PCMs	Additives	Particle size	Pressure	Compression method	Melting point	Sintering temperature	PCM ratio	Scale (g) , diameter	Ref.
11.	EG	paraffin wax	/	50 -200 µm	/	/	/	power of laser sintering 5.5w; scan speed: 1.5 ~ 50 mm/s	80%	discs (Ø: 70 mm, h: 5 mm)	[117]
12.	Graphite flake, Expanded natural graphite, Expanded graphite powder	NaNO ₃ /KNO ₃	/	Graphite flake (6-400 µm), Expanded natural graphite (50 µm), Expanded graphite powder (500 µm)	/	Hot compression	~210 °C	/		/	[100]
13.	magnesium oxide	Na ₂ CO ₃ -Li ₂ CO ₃	natural graphite flakes, carbon nanotubes (CNTs)	/	/	uniaxial cold compression	~500 °C	25 to 400°C at 5°C/min, 400 to 550°C at 1°C/min, and holding at 550°C for 90 min	~50%	/	[43], [32]
14.	MgO	K ₂ CO ₃ -Na ₂ CO ₃	SiC	/	40 MPa	uniaxial cold compression	710.1 °C	750 °C for 30 min;	~60%	15 mm	[118]
15.	MgO	Na ₂ CO ₃	MWCNTs	/	8 MPa for 2 min	/	851 °C	900°C under N ₂ for 2 h	60%	discs (Ø: 11 mm)	[119]
16.	MgO	Na ₂ CO ₃ , K ₂ CO ₃ , and Li ₂ CO ₃	/	50 nm	/	/	723 °C, 898 °C	950 °C for 2 h	65% 80%	/	[120]
17.	MgO	Na ₂ CO ₃ -Li ₂ CO ₃ , Na ₂ CO ₃	graphite flake	MgO: ~400-600 µm; ~90-110 µm, ~30-50 µm; ~3-5 µm.	30 MPa	uniaxial cold compression	500.35 °C	550 °C for 90 mins	50%	discs (Ø: 30 mm, h: 15 mm)	[121] – [123]
18.	MgO (huntite)	NaNO ₃	graphite	graphite (500 µm)	/	/	318.4 °C	/	70%	discs (Ø: 13 mm, h: 2 mm)	[124]

No.	Matrixes	PCMs	Additives	Particle size	Pressure	Compression method	Melting point	Sintering temperature	PCM ratio	Scale (g) , diameter	Ref.
19.	modified diatomite	LiNO ₃ , Na ₂ SO ₄	/	/	/	/	255 °C, 887.61°C	300°C (LiNO ₃), 900°C(Na ₂ SO ₄) for 2h	60%(LiNO ₃), 65% (Na ₂ SO ₄)	/	[45]
20.	vermiculite	erythritol	graphite	graphite (0.5-1mm); erythritol (30-50µm);	40 MPa	/	18.6 °C ¹	150°C for 1 h	70%	/	[125]
21.	α-alumina, diatomite, mullite	Na ₂ SO ₄ -NaCl	/	/	~176 MPa for 3 min	uniaxial cold compression	624 °C	680 °C for 2 h	50%	discs (Ø: 12 mm)	[126]

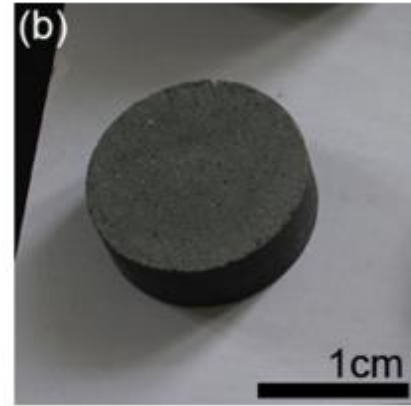
According to Table 4, the outstanding outcomes are concluded from the aspects of the materials used, the preparation methods, the processing conditions, and the scalability.

(1) Materials prepared by the mix-sintering method

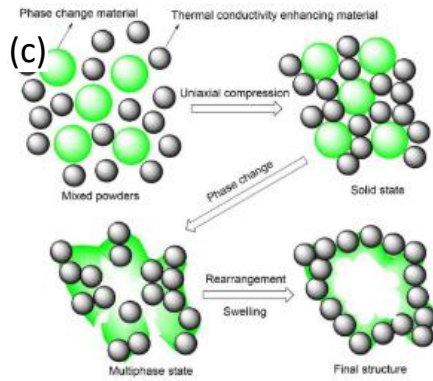
As shown in Table 4, the temperature range of the PCMs fabricated by mix-sintering is varying from 103.5°C to 898°C, indicating that the mix-sintering method is more applicable for preparing high-temperature PCMs. The mostly used PCMs are high-temperature salts, such as carbonates, nitrates and sulfates. In terms of the matrixes, as most of the high-temperature salts are corrosive and reactive at high temperature, the selection of supporting materials is very important. Chemical compatibility between the PCMs and the supporting materials has to be studied carefully. In Table 4, one can see that ceramic materials are mostly used due to high-temperature stability and good corrosion resistance, such as MgO, diatomite, vermiculite, etc.. Besides, a good wettability between the PCM and supporting materials is essential to obtain a stable physical structure. Ge et al. [43] found that the microstructure development is different when using eutectic carbonate ($\text{Li}_2\text{CO}_3\text{-Na}_2\text{CO}_3$) to compound with wettable (MgO) and non-wettable (graphite) structural supporting materials (see Figure 12). Cross-section of the graphite/salt composite showing that graphite particles are dispersed only on the tablet surface, which cannot prevent the molten salt from leakage; see Figure 12(a)(c). However, the MgO/salt composite is uniformly distributed, which could hold the structure stable over melting temperature (see Figure 12(b)(d)). A further study on contact angle [127] [128] confirmed that $\text{Li}_2\text{CO}_3\text{-Na}_2\text{CO}_3$ salt is wettable with MgO but not wettable with graphite. Therefore, the wettability between liquid PCM and structural supporting materials has a significant impact on the structural stability of FSCPCM. A good wettability is essential to form a stable and rigid structure.



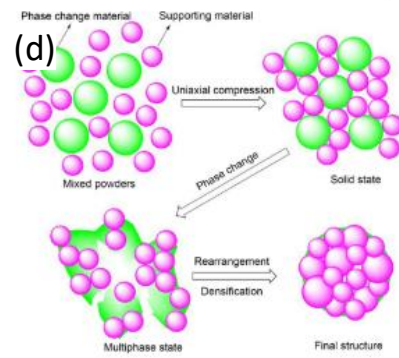
(a) $\text{Li}_2\text{CO}_3\text{-Na}_2\text{CO}_3/\text{graphite}$ CPCM shows a leakage after sintering



(b) $\text{Li}_2\text{CO}_3\text{-Na}_2\text{CO}_3/\text{MgO}$ CPCM shows a stable structure after sintering



(c) Microstructure development of $\text{Li}_2\text{CO}_3\text{-Na}_2\text{CO}_3/\text{graphite}$ CPCM



(d) Microstructure development of $\text{Li}_2\text{CO}_3\text{-Na}_2\text{CO}_3/\text{MgO}$ CPCM

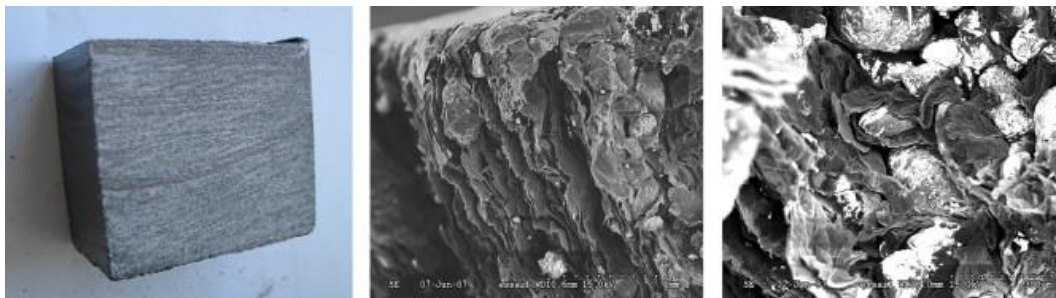
Figure 12 Schematics of the mechanism for microstructure development of FSCPCMs [43]

(2) Different methods used for mix-sintering

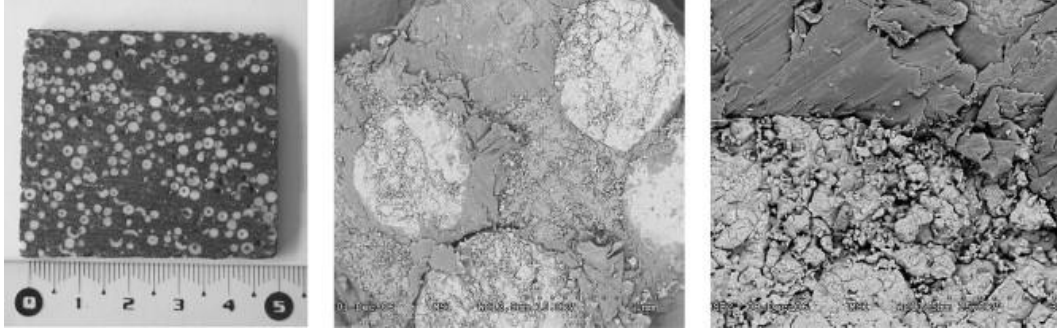
Comparison between different compression methods

There are different compression methods used for mix-sintering in Table 4, including hot compression, cold compression, uniaxial compression and isostatic compression. Among them, cold uniaxial compression is the most widely used. Acem [113] and Lopez et al. [114] compared two cold compression routes, cold uniaxial compression and isostatic compression, to prepare $\text{KNO}_3\text{-NaNO}_3/\text{expanded graphite}$ FSCPCM. Its cross-section structure is displayed in Figure 13. One can see

that the FSCPCM prepared by uniaxial compression presents a parallel layered structure (Figure 13 (a), left) with alternate “graphite dominant” layers (Figure 13 (a), middle) or “salt dominant” layers (Figure 13 (a), right). The “graphite dominant” layer is compact, while the “salt dominant” layer presents a deformation of graphite due to salt particles partially occupy the pores. In terms of the sample prepared by isostatic compression, it displays a structure that salt particles and graphite are homogeneously distributed as shown in Figure 13 (b). Besides, an interface between the salt and graphite can be obtained at the microscopic scale; see Figure 13 (b), right. The authors found that the isostatic compressed sample has a leakage issue during thermal cycling, owing to its extremely rigid structure can not provide enough voids and space for the volume expansion (10%) of the molten salt. However, the uniaxially compressed sample can work correctly due to its layered structure. Study on the thermal conductivity also shows different results between uniaxial compressed and isostatic compressed FSCPCMs: the uniaxially compressed FSCPCM displays an anisotropic thermal conductivity, while the isostatic compressed sample shows an isotropic thermal conductivity. For the uniaxial-compressed sample, its radial-directional thermal conductivity can be 20 times as high as its axial direction, which could be used for orientated efficient heat conduction. Generally, the authors regarded that the uniaxially compressed FSCPCM is more suitable for fabrication due to its good structural stability and high radial-directional heat conduction.



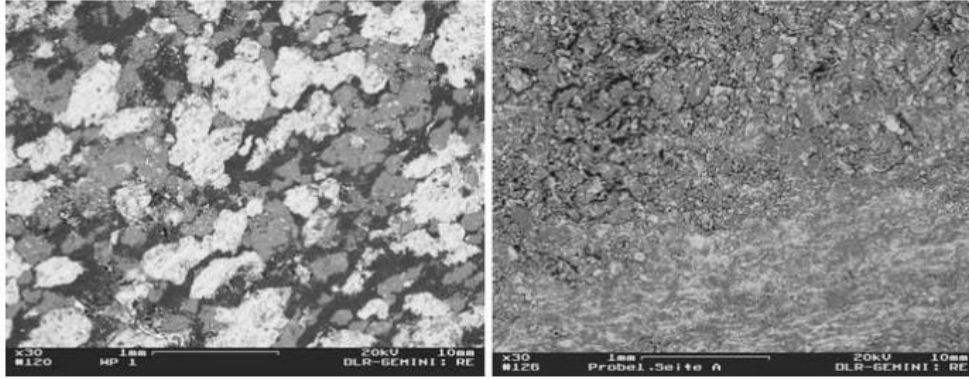
(a) Graphite/salt FSCPCM prepared by uniaxial compression



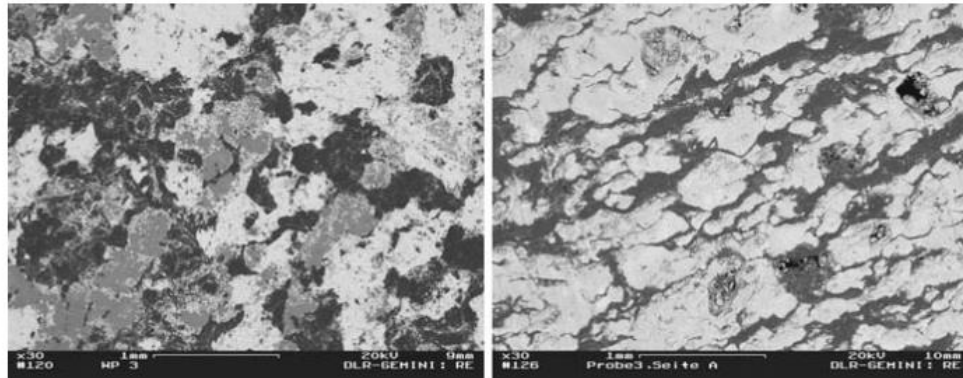
(b) Graphite/salt FSCPCM prepared by isostatic compression

Figure 13 Images of a graphite/salt composite obtained by two cold-compression routes at the macroscopic (left) and microscopic (centre and right) scales.

The compression methods mentioned above is conducted at room temperature, termed as cold compression. Most of the studies used the cold compression method as shown in Table 4, owing to its easy-achievable device and simple manipulations. Do et al. [129] compared the cold and hot (at 180°C) compression method for $\text{NaNO}_3\text{-KNO}_3/\text{EG}$ FSCPCM. Figure 14 displays the microstructure of the cold and hot compressed FSCPCM before and after one thermal cycling. Before thermal cycling, the microstructure of the cold and hot compressed composite is similar: both the salt (white) and graphite (black) components are observable. However, there is a significant difference after one thermal cycling. The salt phase cannot be observed in the cold-compressed FSCPCM, indicating the melted salt has been absorbed in the micropores of EG. Whereas, the microstructure of hot-compressed sample remains unchanged. We can also find that the EG component is less interconnected for hot-compressed sample after thermal cycling, which results in a lower thermal conductivity compared with the cold compressed sample. However, some small pores and voids can be observed after thermal cycling for both samples. This study revealed the impact of hot and cold compression method on the microstructure development and the thermal conductivity of the FSCPCM.



(a) SEM images of the cold compressed composite PCM: before (left) and after one thermal cycling (right)



(b) SEM images of the hot compressed composite PCM: before (left) and after one thermal cycling (right)

Figure 14 SEM images for hot compressed and cold compressed FSCPCM before and after one thermal cycling

Novel sintering methods

Most of the sintering process is conducted in a furnace under a certain heating route. In the conventional routes, the sintering step is the most energy-consuming and time-consuming step. Besides, this step needs to be controlled carefully to avoid cracking. Hence, some researchers have come up with new routes for sintering. Yu et al. [107] used a new method, named 'cold sintering process (CSP)', to obtain sintered FSCPCM at a low temperature. The authors successfully fabricated the $\text{NaNO}_3/\text{Ca}(\text{OH})_2$ FSCPCM for high-temperature application over 300°C , where NaNO_3 is used as the PCM and $\text{Ca}(\text{OH})_2$ is used as the supporting material. The sample is cold-sintered at 120°C for 10 minutes but could achieve a great mechanical property with a compressive strength over 100 MPa. Figure 15 displays the cold sintering mechanism of the $\text{NaNO}_3/\text{Ca}(\text{OH})_2$ FSCPCM. In this process,

the solvent (e.g. water or aqueous solutions) is an essential medium to complete the dissolution-precipitation process. The surface of the raw materials (NaNO_3 and Ca(OH)_2) are wetted and partly dissolved in the water firstly. With the aid of a high temperature (120°C), an epitaxial precipitation process on the surfaces of Ca(OH)_2 particles is carried out efficiently, and resulting in a bond between the particles. Meanwhile, the Ca(OH)_2 particles are rearranged and the pores are removed by the external high pressure. After a certain time of cold sintering, the composite has achieved a rigid structure. In terms of the cold sintering method, its overall energy consumption amount is considerably reduced, showing both environmental and economic benefits in fabrication. However, this is a new approach to prepare FSCPCM which still needs further study on the controllability of the process for large-scale deployment.

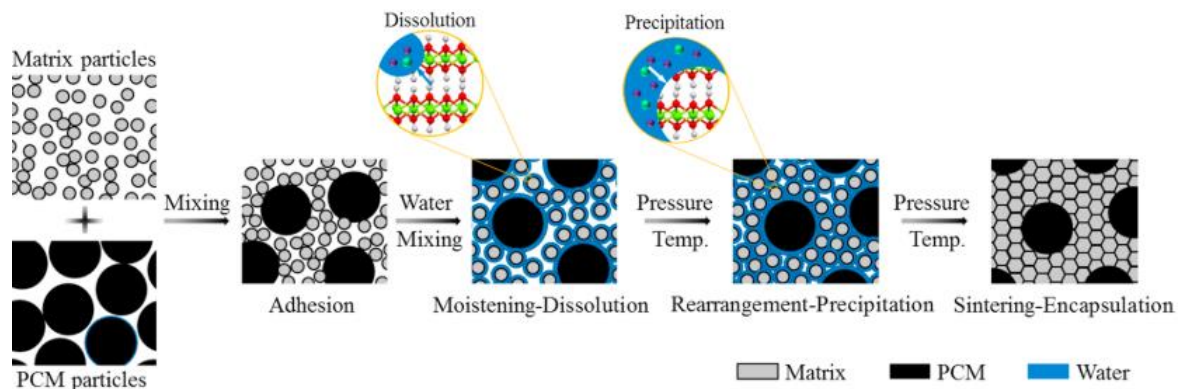


Figure 15 Schematic diagram showing the cold sintering process for $\text{NaNO}_3/\text{Ca(OH)}_2$ FSCPCM

With the development of 3D printing, selective laser sintering technique (SLS) provides an avenue to produce micro-scale functional material with zero material waste. Nofal et al. [117] firstly adopted the SLS technique to fabricate paraffin/EG FSCPCM. The prepared sample can be single-layered or multi-layered in different shapes; see Figure 16. The preparation process is firstly paving a flat layer of the CPCM mixture and then using a computer-controlled laser beam to scan through the surface. The detailed schematic process of the laser sintering is shown in Figure 17. The laser is

acting as the heat source to melt the paraffin. The melted paraffin was absorbed in the pores of EG and its interparticle voids. Besides, the melted paraffin is also acting as a binder that can glue the graphite powder together. As the laser is computer controlled, it can scan accurately at a certain spot according to the program. Therefore, it is especially suitable for fabricating delicate micro-size FSCPCM. In their work, the laser power is 5 watts and able to melt the paraffin at $\sim 56^{\circ}\text{C}$. However, the maximum temperature that the laser can achieve is still not clear. Besides, the effects of particle size, composition, scan speed and output laser power on the final product property have not been studied.

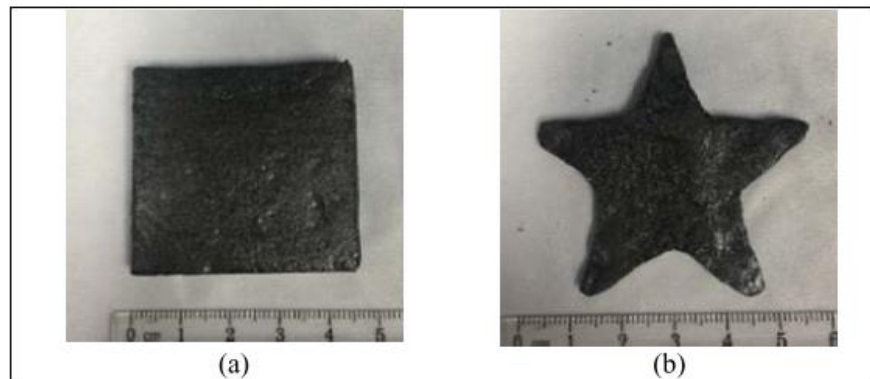


Figure 16 Multi-layer paraffin/EG composite in a square shape (a) and in a star shape (b)

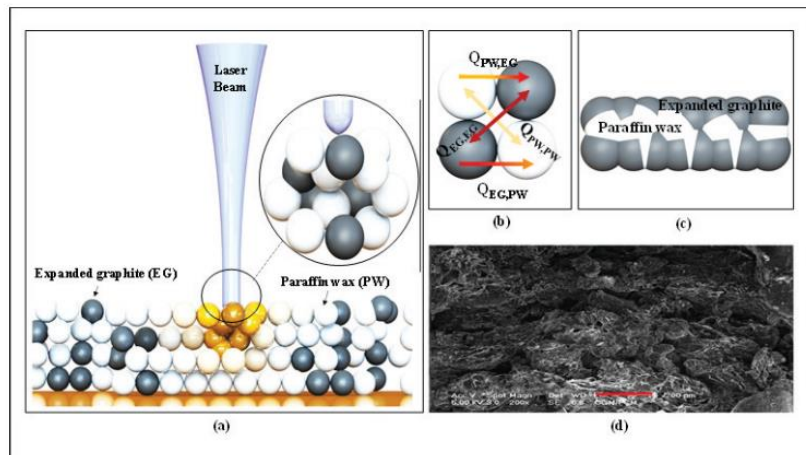


Figure 17 Laser sintering process for fabrication paraffin wax/EG FSCPCM

(3) Processing conditions for mix-sintering

By the gathered processing data in Table 4, one can see that the particles size being used for fabricating FSCPCM is ranging from 50 nm to 500 μm . Most of the raw materials are crushed and ground in a mill to obtain the required particle size. However, some materials are used as received, such as the EG. This is to keep the original worm-like porous microstructure of EG. Li et al. [121], [123] studied the effects of particle size and density of MgO on the microstructure, thermophysical and mechanical properties of the FSCPCMs. Four different sizes of MgO particles were used in their work: $\sim 400\text{--}600\ \mu\text{m}$, $\sim 90\text{--}110\ \mu\text{m}$, $\sim 30\text{--}50\ \mu\text{m}$ and $\sim 3\text{--}5\ \mu\text{m}$. The authors found that smaller MgO particles could form a more compact structure due to smaller interparticle pores generated. This rigid structure contributes to a good thermal conductivity and mechanical strength of the composite. Besides, FSCPCM prepared of light MgO displays a denser structure than the heavy MgO.

Sintering is also an important step, where PCM is fully melted and the supporting grains are rearranged. One can see from Table 4 that the sintering temperature often used is $\sim 3^\circ\text{C}$ to $\sim 76^\circ\text{C}$ higher than the melting temperature of the PCM. The sintering temperature has to above the melting point to fully melt the PCM. Meanwhile, the sintering temperature should below the decomposition temperature of the PCM to avoid degradation. Besides, the heating rate often used is $1^\circ\text{C}/\text{min}$ and $5^\circ\text{C}/\text{min}$. The fast heating could lead to the cracking of the sample, therefore it has to be controlled at a relatively low speed. In terms of the sintering time, it should allow for the completion of the particle rearrangement. A period of $\sim 0.5\text{h}$ to $\sim 3\text{h}$ is often used for sintering from literature. As can be found above, there are no common rules for preparing FSCPCMs. Most of the studies prepared the FSCPCM by trial and error method. However, to enlarge the fabrication to industrial-scale, more study should be conducted on optimizing the processing parameters.

(4) Scalability

The amount of the sample prepared by the mix-sintering method is shown in Table 4. We can see that the prepared sample is in the laboratory scale with largest amount to $\sim 100\text{g}$ and the largest dimension up to $\varnothing 70\text{ mm}$. The equipment required for mix-sintering is easily accessible, for instance, a mill for grinding and mixing, a mould and compressor for shaping, and an oven or furnace for drying and sintering. For industrial production, there is already an integrated production line for brickmaking process, which can be used for preparing FSCPCM by mix-sintering directly. Therefore, there is great potential to scale up the mix-sintering method to an industrial scale. However, as aforementioned, the processing parameter for mix-sintering is still required to be optimized for large-scale fabrication.

2.3.4 Extrusion

The hot-melt extrusion process is currently a very important method in the plastics and rubber industry, also in areas of metals, ceramics, etc.. The extrusion process was firstly developed in the late 18th century by Bramah [130]. Then, with the expansion of the thermoplastic industry, the extrusion method was rapidly developed and used in large-scale production of plastics. Meanwhile, the extrusion devices have been evolved from the ram extruder to single- or twin-screw extruders, which are able to operate continuously without replenishing process. By this continuous fabrication method, the fabrication cost can be reduced and the yield can be improved significantly. Recently, the benefits of extrusion method have attracted a lot of researchers applying this approach to produce high-performance FSCPCM, especially polymer-based FSCPCMs. A state of art of FSCPCMs fabricated by hot-melt extrusion methods is displayed in Table 5.

Table 5 State of art of the composite PCM prepared by extrusion

No.	Matrixes	PCMs	Additives	Method description	Temperature	Screw type	RPM	Melting point	PCM ratio	Ref.	
1.	HDPE	Paraffin	/	1. extruded to composite pellet; 2. Compressed to sheets (70 bar for 5 min)	120°C-170°C, (hv-HDPE/H-PW); 150°C-160°C (hv-HDPE/L-PW)	twin-screw extruder (L/D of 30:1, Collin ZK25)	175 rpm	18°C - 23°C; 56°C - 58°C	75%	[131]	
2.	HDPE	wax	EG	1. blended by twin screw extruder; 2. shaped by the injection moulding machine	180°C -200°C	180	a lab-scale Brabender twin-screw extruder (L/D of 40:1)	110 rpm	43.08°C	40%	[132]
3.	HDPE	palmitic acid	graphene nanoplatelets GNP (5-10 μm)	Blended and extruded by twin-screw extruder	160 °C	twin-screw agitator	1000 rpm for 30 min	62°C	80%(slight leakage after 150 thermal cycles)	[133]	
4.	HDPE	stearyl alcohol	EG	1. mixed EG and SAL; 2. blended with HDPE by an extruder	180 °C	twin-screw agitator	1500 rpm for 30 min	57°C		85%	[134]
5.	HDPE	Paraffin	EG (300um), Fire retardant (ammonium polyphosphate, pentaerythritol and melamine, 10um)	1. premixed in a high-speed blender; 2. extruded by a twin-screw extruder	90-160°C	twin-screw extruder (TE-35, KeYa, China)	250 rpm	51.22°C	60%	[135]	
6.	HDPE	PureTemp 42 (a commercial PCM)	/	mixed and extruded	160°C	Filabot EX extruder (Die: 1.75mm); leak during extrusion	35 rpm	42°C	21.40%	[136]	
7.	HDPE	Paraffin	/	melted and mixed, then extruded	140°C-170°C	Leistritz twin-screw extruder (ZSE-18HP)	80rpm, 100rpm, 150rpm	30°C	75%	[137]	
8.	HDPE (pellets)	Paraffin	Fire retardant (MPP<10um, PER<10	mixing and extruding	120°C- 170°C	A twin-screw extruder (TE-35, KeYa, China)	450 rpm	44°C	60%	[138]	

No.	Matrixes	PCMs	Additives	Method description	Temperature	Screw type	RPM	Melting point	PCM ratio	Ref.
			um, BPBE <5um, AO ~ 8um, MCA~ 5um)							
9.	HDPE-EVA pellets	Paraffin	Fire retardant (OMT)	1. mixed for 10 min; 2. Extruded HDPE-EVA nanocomposite pellets; 3. extruded HDPE-EVA- paraffin pellets;	180 °C for HDPE-EVA nanocomposites) 120°C -170°C for HDPE-EVA-paraffin	twin-screw extruder (TE-35, KeYa, China)	450 rpm	~42°C	75%	[59]
10.	HDPE, LDPE, LLDPE	octadecane paraffin	/	1. mixed with molten paraffin; 2. extruded;	180°C	18-mm parallel co-rotating twin-screw extruder with an L/D ratio of 40 (Leistritz ZSE-18HP).	80 rpm	24.8°C - 26.9°C	90%	[60], [139]
11.	HDPE, styrene–butadiene–styrene copolymer (SBS)	paraffin	graphite, carbon fiber	mixed and extruded	140°C	two-screw extruder	/	20°C, 60°C	80%	[140]
12.	HDPE/wood flour (WF)	Paraffin	EG	1. impregnated EG with paraffin; 2. blended with HDPE/WF by twin extruder; 3. compressed at 4 MPa and 160 °C	140°C -160°C	co-rotating twin-screw extruder (KESUN KS20, China)	180 rpm	~20°C	27%	[141]

Table 5 shows the state-of-art of the FSCPCM prepared by the extrusion method, and the main outcomes are concluded from the aspects of the prepared materials, the preparation methods, the processing conditions, and the scalability.

(1) Materials prepared by extrusion method

Due to the maximum operating temperature of extruders, organic PCMs which has relatively low melting points are widely used to compound in the extruder. Paraffin is the most studied PCM due to its high enthalpy, good chemical stability, and cost-effective price. Meanwhile, HDPE has been used as the supporting material in almost every study. The reason for using HDPE as supporting materials other than other polymers is due to its excellent processing properties, such as high-temperature stability, high chemical resistance, good mechanical properties and low cost [142]. Besides, there are studies showing that paraffin is less miscible with HDPE than LDPE and LLDPE, which could form a better skeleton structure and maintain the good thermal property of PCM [60][139].

Some studies also considered adding additives to enhance the thermal performance of FSCPCM. Carbon materials are widely used as thermal conductivity enhancers to address the low conductivity issue of polymers. Moreover, flame-retardants have been widely added to increase the flame resistance of the FSCPCM, as polymer-based FSCPCM is easily combustible. Intumescent flame retardant (IFR) is the optimal and environment-friendly flame retardant, hence different kinds of IFR have been added into the FSCPCM as shown in Table 5.

(2) Different extrusion methods

Hot-melt extruders can be classified into two groups generally: 1) single- or twin-screw extruder powered by an electric motor; 2) ram extruder driven by the hydraulic or oil pressure. Ram extruder is the earliest extruder that has been used in the plastics industry. However, single- or twin-

screw extruders are more widely used recently as the process is continuous without replenishing process. McGuire et al.[143] prepared ceramic pastes by two extrusion methods. One is using ram extruder with a pre-mixing process. The other one is by a co-rotating twin-screw extruder. The aggregates in the composite were studied by the X-ray micro-computed tomography, showing that the twin-screw extrusion process is more efficient in breaking down the agglomerates than the ram extrusion. One can see from Table 5 that almost every study used a twin-screw extruder. The principles of single- and twin-screw extruder are very similar. The twin-screw extruder has advantages of less friction heat, more uniform shearing, larger conveying capacity, and more stable process. However, single screw extruder is more easy-controllable and cost-effective.

(3) Processing conditions for extrusion

The extruder is a multi-functional processing device that can heat, mix, compress and shape simultaneously. The manipulation required for the extrusion process is also simple. Most studies premixed the solid powders manually or by a high-speed blender before loading materials into the extruder. When the mixture is fed into the extruder, it is undergoing solid-conveying, mixing and melt-conveying, and shaping processes continuously under automatic control. Study shows that processing parameters of screw speed and configuration, continuous-phase viscosity, and temperature have significant impacts on the morphology development of the extrudate [144].

Impacts of extrusion temperature on the mechanical, tensile and rheological properties of a fibre/HDPE composite were studied by Salleh et al. [145]. The result shows that the tensile modulus, complex viscosity, storage and loss modulus of the composite has increased with increasing operating temperature. However, the influence of temperature on polymer-based CPCMs might be different, as the CPCM can melt to liquid phase and behave differently from particles. One can see from Table 5, the processing temperature of extrusion is slightly above the

melting temperature of the polymer, but much higher than the melting point of PCM. This might cause some leakage issue for the extruder as reported by Benjamin et al. [136]. Besides, the viscosity of the polymer is several orders of magnitude higher than the viscosity of the melted PCM. Therefore, it is challenging to mix them uniformly. Also, the linkage between the processing temperature and the quality of the FSCPCM has not been revealed.

The rotating speed has a great impact on the chain structure and homogeneity of the FSCPCM. Estep [137] compared the HDPE/paraffin composite prepared at different rotating rates: 80, 100, and 150 rpm. Results show that the FSCPCM prepared at the lowest processing speed (80 rpm) presents the highest leakage due to poor dispersion of paraffin and large channels of the matrix that cannot encapsulate the paraffin.

(4) Scalability

Due to the benefits of continuous fabrication, extrusion is regarded as the most promising fabrication method to scale up the production of FSCPCM, especially for the polymer-based FSCPCM. Although the extrusion process has become a developed fabrication method in the thermoplastic industry, applying the extrusion process into the fabrication of FSCPCMs still faces some issues. The materials fabricated by extrusion is limited at the moment. Also, the relationship between the processing parameters and the properties of FSCPCM has not been revealed. To implement the extrusion process in fabricating FSCPCMs industrially, more specific studies on formulating new species of FSCPCMs and investigating the relationship of process-property are essential for future development.

2.3.5 Other methods

Impregnation method, mix-sintering method and extrusion method are widely studied due to its easy-controllable and large-scalable advantages. Other than those, there are also other

methods have been used to fabricate FSCPCMs. For instance, electrospinning method to fabricate nanoscale PCM fiber[146], [147], and sol-gel method [148], [149], etc.

Electrospinning is capable to process different soluble polymers with sufficiently high molecular weight, including branched copolymers. Mccann et al. [147] firstly prepared phase change nanofiber by a melt coaxial electrospinning method, which combines melt electrospinning with a coaxial spinneret (shown in Figure 18). This method allows for nonpolar solids such as paraffin to be electrospun and encapsulated by a TiO_2 -PVP (Polyvinylpyrrolidone) composite. The obtained FSCPCM displays a core-sheath structure, which consists of 45 wt.% paraffin. This study indicates that using melt coaxial electrospinning method to prepare nanoscale FSCPCM fibrous matrices is simple, useful, and feasible. Chen et al. [146] also used electrospinning method to encapsulate PEG by cellulose acetate (CA) and to obtain ultrafine FSCPCM fibres. Results show that PEG is distributed not only on the surface but also within the core of fibres. Besides, the PEG/CA composite fibres present great thermo-regulating properties and excellent reliability after 100 thermal cycles.

The sol-gel process is a wet-chemical technique used for the fabrication of both glass and ceramic materials. In this process, the colloidal sol evolves gradually to a gel-like network containing both liquid phase and solid phase. During the formation of the gel-like network, precursors were added to facilitate the hydrolysis and polycondensation reactions, such as metal alkoxides and metal chlorides, etc. [150]. Guo et al. [151] prepared the PEG/ SiO_2 FSCPCM by sol-gel method, which could encapsulate PEG up to 90 wt%. For the PEG/ SiO_2 composite, SiO_2 gel forms an interconnected network that can retain the long-chain PEG molecular inside the network by capillary force. The structure is found stable and without leakage during the phase change process. In the synthesis process, surfactants or co-solvents are always used as a homogenizing medium. Tang et al. [149], [152] used ultrasound instead of surfactant or co-solvent to homogenize the sol-gel. In their study,

the prepared PEG/SiO₂ composite presents better shape stability and larger enthalpy than other PEG/SiO₂ composites.

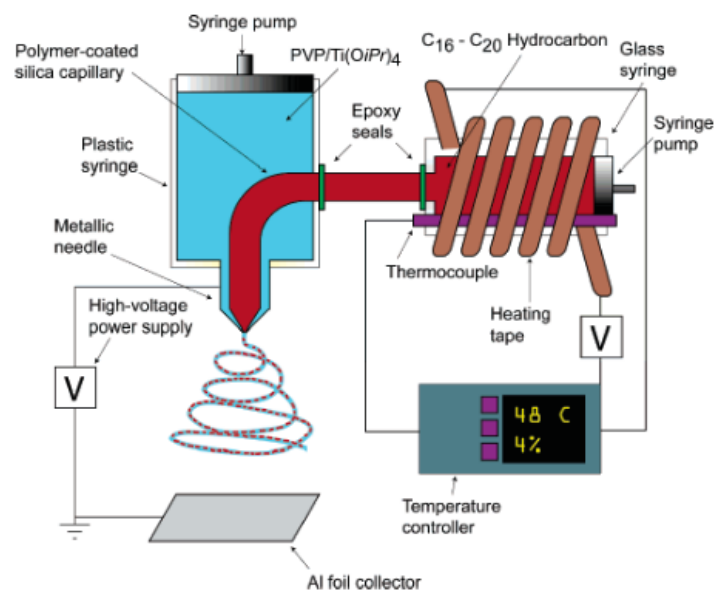


Figure 18 Schematic of the melt coaxial electrospinning setup used for fabricating paraffin-TiO₂-PVP FSCPCM fibres

2.4 Summary

The FSCPCM provides an avenue to overcome the shortages of pure PCM, such as low thermal conductivity, corrosivity, supercooling issue and volume changes. Therefore, the focus of this work is on the FSCPCMs, which consists of a PCM, a structural supporting material and/or a property enhancer. Currently, there are two challenges for the large-scale deployment of FSCPCMs: 1) relatively high cost; 2) low production yield and lack of skills for large-scale manufacturing. There are currently extensive studies focusing on formulating ideal FSCPCMs. Whereas, the manufacturing method for FSCPCM is very less studied, which has been the main challenge that drags the deployment of FSCPCMs. In this chapter, different fabrication methods for preparing FSCPCMs are investigated. There are three extensively studied and easy-accessible manufacturing methods: 1) impregnation method; 2) mix-sintering method; 3) extrusion method. This chapter has reviewed the literature to understand the state of the art, and also the knowledge gaps in each of the fabrication methods.

Impregnation method is the most studied among the reviewed studies. From Table 3, it can be found that this method is widely applied for preparing mid-low temperature FSCPCMs(<200°C) due to the limitation of devices and operational difficulties. Porous matrixes, such as EG, diatomite, expanded perlite (EP), zeolite, MWCNTs have been intensively used as the structural supporting matrix. Pore geometry of the matrixes and wettability between the liquid PCM and the solid matrix is found to affect the impregnation efficiency and the structural stability significantly. It is revealed that the mesoporous pores present the lowest risk of leakage. Besides, processing parameters, such as impregnation time, operation temperature and vacuum treatment has been correlated with the encapsulation ratio and the material properties. The vacuum treatment is found to affect the absorption ratio differently according to the matrix pore geometry. Porous matrix with fine pores is

regarded that needs vacuum treatment to enhance the absorption ratio. Besides, a relatively high processing temperature is found to have a positive impact on the impregnation ratio. The minimal time required for the impregnation process has not been investigated, but results show that the absorption rate increases very fast at the beginning, then slows down and reaches stable. The impregnation time being used in current studies has a very wide range, which varies from 0.25 h to 24 h. In addition, this study compares three different impregnation methods, which are melt impregnation, vacuum impregnation and solution impregnation. Among these methods, the direct impregnation is regarded as the most practical method in the large-scale application.

The mix-sintering method is widely used to prepare high-temperature FSCPCMs ($\sim 100^{\circ}\text{C}$ to $\sim 900^{\circ}\text{C}$) from Table 4. The mostly used PCM are high-temperature salts, such as carbonates, nitrates and sulfates. As most of the high-temperature salts are corrosive and reactive at high temperature, the selected supporting material has to present great high-temperature stability and good corrosion resistance, such as MgO, diatomite, vermiculite, etc. Besides, a good wettability between the PCM and supporting materials is essential to obtain a stable physical structure. In terms of the compression process, it is found to have a significant impact on the microstructure and thermal properties of the final products. As found in Table 4, the uniaxial cold compression method has been used mostly. Experimental findings prove that the uniaxial cold compression method could obtain a more stable and homogeneous microstructure than the isostatic compression and hot compression. For the sintering process, most studies used a conventional sintering process. Some novel sintering methods like cold-sintering method and laser sintering have been investigated and shown some advantages in specific applications, but these methods are still at an early stage that requires further studies before broad deployment. The processing parameters, such as particle sizes, compression pressure, sintering temperature and time, and heating rate also affects the property of FSCPCMs. It is reported that smaller matrix particles could form a more compact and rigid structure due to

smaller interparticle pores generated, hence contributing to a better thermal conductivity and mechanical strength of the FSCPCM. Excluding particle sizes, impacts of other processing parameters such as the compression pressure, sintering temperature and time, and heating rate on the quality of the materials have not been revealed in the reviewed studies. Most of the researcher prepared the composite by trial and error method. Therefore, one objective of this work is to carry out some experimental study on optimizing the current mix-sintering process and also providing some guidance for the future development of this fabrication method.

The hot-melt extrusion method has been widely used in fabricating plastics due to its continuous process and low-cost. In Table 5, we can see that the extrusion method has been successfully applied to prepare polymer-based composite PCMs. However, the materials being studied mostly are HDPE/Paraffin FSCPCMs. New composites processable by the extrusion method still require to be developed. Besides, only a few studies indicate that a higher processing temperature and a higher extrusion speed can help to form an HDPE/Paraffin FSCPCM with higher mechanical strength and less leakage. The relationship between processing parameters and the properties of the extrudate has not been fully revealed in the current studies. Therefore, this work aims at developing new FSCPCMs prepared by extrusion and also understanding the correlation between processing parameters and material properties.

3 Materials and methodologies

3.1 Materials

The description and manufacturer information of the raw materials used are shown in Table 6. The diatomite is a natural amorphous mineral which mainly composes of silica ($\sim 82.6\%$) and alumina ($\sim 8.2\%$) [38]. Diatomite usually has a high porosity ($\sim 80\%$ to $\sim 90\%$), its morphology is observed by SEM; see Figure 19. One can see the bar-shaped diatomite particles have a pore size of ~ 500 nm.

Table 6 Basic information about the raw materials

Materials	Purity	description	supplier
KNO₃	99.99%	powder	Sigma-Aldrich
Diatomite (ρ: 0.36 g/cm³)	98%	powder	JJS Minerals Company
HDPE (MFI: 6 g/10min, ρ: 0.955 g/cm³)	98%	powder	XSene® Company
Pentaerythritol (PE)	98%	granule	Alfa Aesar Company
Graphite powders (Cg, <300 mesh)	98%	powder	Inoxia Ltd.
SiO₂ powders (fumed, amorphous)	99.99%	powder	Sigma-Aldrich
SiO₂ substrate (quarz, single crystal)	99.99%	substrate	SITUS Technicals GmbH
Graphite substrate	99.99%	substrate	Alfa Aesar



Figure 19 SEM image of diatomite particles

3.2 Fabrication equipments and methods

In this section, the devices being used for mix-sintering and extrusion fabrication process are introduced. More information associated with the possessing conditions are explained detailed in corresponding chapters (chapter 4 and 5).

3.2.1 Mix-sintering

The basic process for mix-sintering includes grinding, mixing, compression and sintering. The facilities being used for mix-sintering is shown in Figure 20 and described as follows. However, the detailed processing parameters are explained in Chapter 4.

- **Step 1 – grinding and mixing:** a Fritsch planetary mill which has four milling jars was used for grinding. The rotating speed is ranging from 50 rpm to 400 rpm.
- **Step 2 - tabletting:** a Lloyd X tensile/compression tester was used to compress the sample to a certain shape. The maximum compression stress is 100 kN of this device. A cylindrical mould with a diameter of 13 mm was used for shaping.

- **Step 3 - drying and sintering:** a carbolite furnace was used for drying and sintering. The furnace can be heated according to a temperature program. For the furnace, the maximum working temperature is 1600°C and the highest heating rate is 50 K/min.



Figure 20 Facilities used in the mix-sintering process

3.2.2 Extrusion method

The extrusion method is a one-step method, which just needs loading the powder mixture into the extruder. Before loading the sample, there is a simple process to prepare the powder mixture. These processes are introduced as follows.

(1) Preparation of powder mixtures

The raw materials used to prepare composite PCM by extrusion are HDPE, PE, and graphite. HDPE and graphite are used directly, because the as-received graphite powders are fine and HDPE will be heated to melting phase in the extruder. PE granules were ground into certain particle sizes to study the size effect on the fabrication process. A shear mill shown in Figure 21 was used to grind the sample. A series of sieves (0.12mm, 0.25mm, 0.5mm, 1 mm) were mounted in the shear mill to obtain different particle sizes. After the PE particles were ground into small particles, they were

mixed with graphite and HDPE by hand. Then, in the extrusion process, the powder mixture is fully mixed.



Figure 21 Shear mill used for grinding the PE granules

(2) Hot-melt extrusion for fabricating PE/HDPE composite PCM

The hot-melt extrusion fabrication method was conducted by a single-screw extruder (Brabender GmbH, Germany) in this work. The extruder is shown in Figure 22. This machine has 6 heating zones. Among them, there are 4 built-in heaters inside the barrel, and 2 heat rings at the die head to ensure the temperature stable when the materials left the die. The maximum operating temperature of all the heaters is up to 450°C. The screw has an adjustable rotating speed between 0.2 and 350 rpm. There are two optional die heads for different purposes: a round die with a diameter of 4 mm for fabrication (Figure 22 (a)) and a capillary die (H×W×L: 2 mm × 20 mm ×160 mm) for measuring viscosity (Figure 22 (b)).

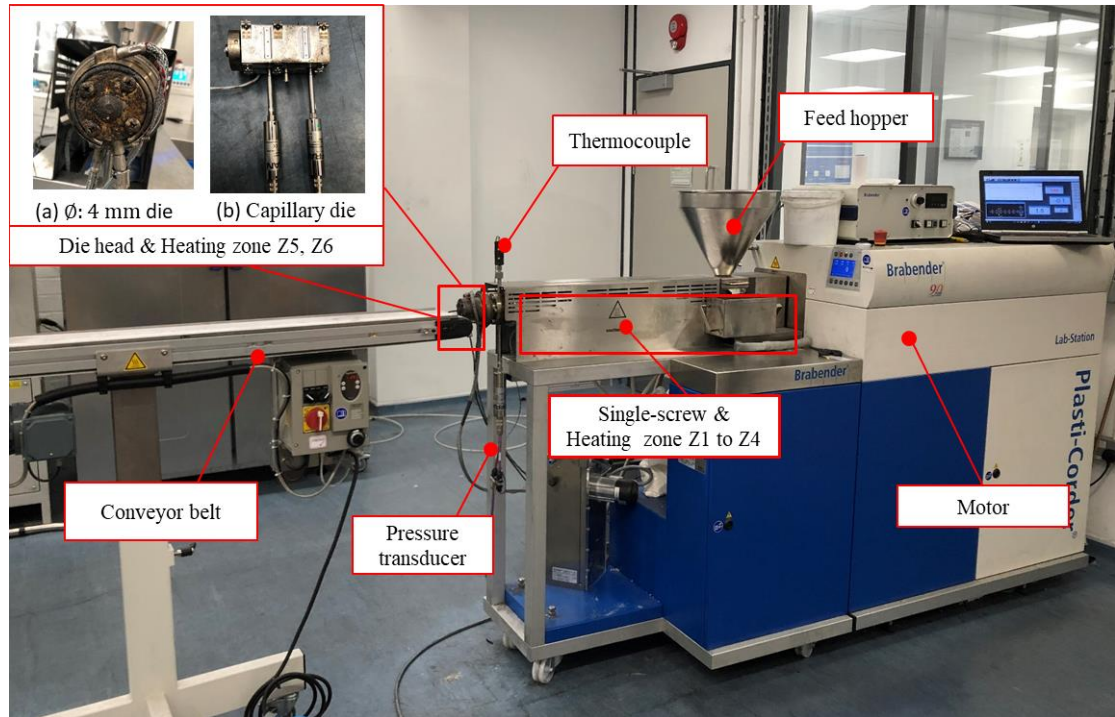


Figure 22 Brabender® Plastic-Corder® Labstation extruder

Determining the steady viscosity with a slot capillary die is using the pressure drop along the die head and the volumetric rate of the flow, by the calculation of Hagen-Poiseuille flow law shown below:

$$\tau = \frac{\Delta P \cdot H}{2 \cdot L} \quad \text{Eq. 3}$$

$$\gamma = \frac{6 \cdot Q'}{B \cdot H^2} \quad \text{Eq. 4}$$

$$\eta = \frac{\tau}{\gamma} \quad \text{Eq. 5}$$

Where τ , γ , η respects the shear stress (Pa), shear rate (s^{-1}) and viscosity ($\text{Pa}\cdot\text{s}$) respectively; ΔP (Pa) is the pressure difference between the inlet and outlet pressure of the capillary die; H (cm) is the height of the slot die; L (cm) is the distance between the pressure measuring points; B (cm) is the width of the slot die; Q (cm^3/s) is the volumetric throughput of the flow.

3.3 Characterization devices and methods

3.3.1 Differential scanning calorimeter (DSC)

3.3.1.1 Introduction to DSC

Differential scanning calorimeter is the equipment widely used to measure the thermal properties of samples (e.g. phase/glass transition temperature and enthalpy, reaction enthalpy, heat capacity, etc.) by monitoring the heat flow of the sample and the reference. When the sample undergoes a physical transformation such as phase transitions, a difference of heat flow will need to apply to the sample than the reference to maintain both at the same temperature. Therefore, DSC quantitatively and qualitatively measures the amount of energy absorbed or released by a sample during an endothermic or exothermic process. The DSC (DSC2, Mettler Toledo) used in this work can process 34 samples in a row with the sample robot, as shown in Figure 23. The working temperature range of this type of DSC is -80°C to 500°C. Heating rate is 0.02 to 300K/min. The mode of the sensor in this DSC is FRS 6 with 56 thermocouples are star-shaped arranged in one layer. The sensitivity and resolution of this DSC are 11.9 and 0.12 by the TAWN (The Dutch Society for Thermal Analysis) method, which is developed to compare the sensitivity and resolution for different DSC instruments (see Figure 24). Besides, Nitrogen gas with a flow rate of 150 ml/min is used as the protective gas inside, while Nitrogen or Air are optional environmental gases for different applications.

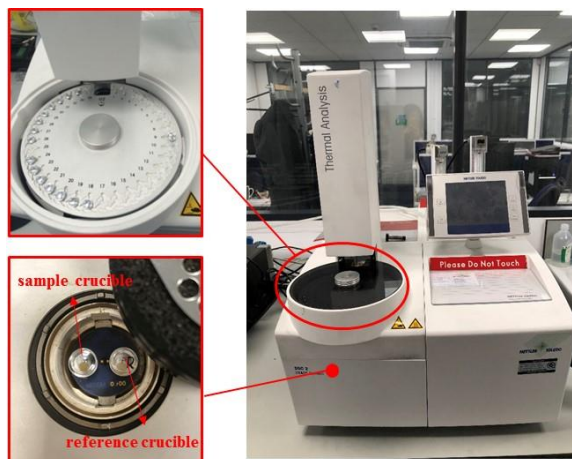


Figure 23 Mettler Toledo DSC2

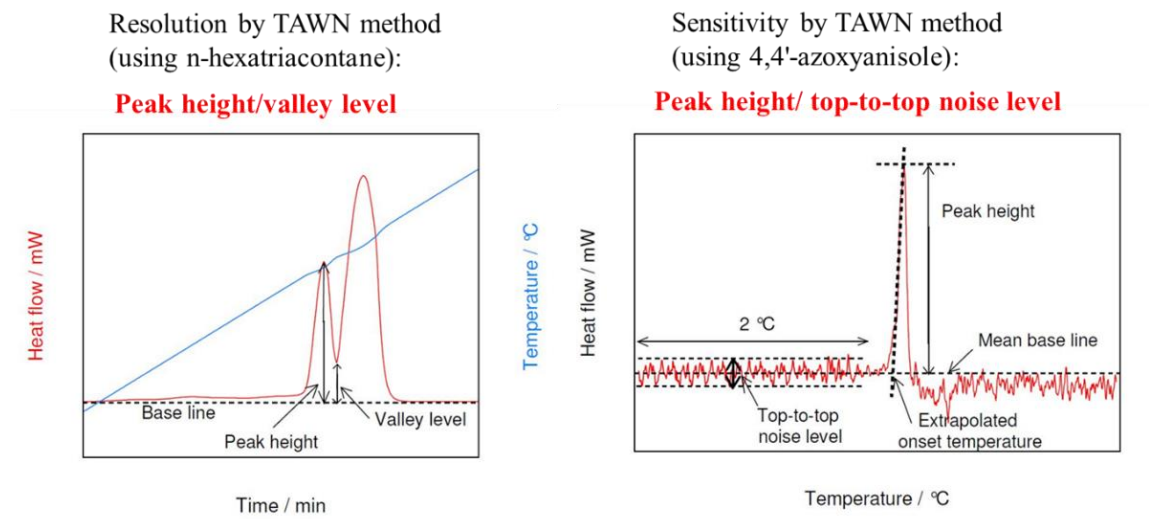


Figure 24 Resolution and sensitivity obtained by TAWN method of this DSC

3.3.1.2 Phase transition temperature and enthalpy measurement

In a typical measurement of phase transition temperature and enthalpy, all the samples were prepared in the Al crucibles, which allows for a maximum working temperature up to 640°C. Besides, the Al crucibles used in this work were pierced with a needle at the lids to maintain the pressure inside is consistent with the ambient pressure. The tests were conducted under a purge gas of 100 ml·min⁻¹ Nitrogen and different heating rates (e.g. 1, 5, 10 K·min⁻¹, see details in each

chapter). The temperature range of the test is according to the phase change temperature of the sample (see the details of the temperature range in the graphs). A blank curve was performed prior to the sample and it was subtracted to correct the sample curve. The Star-e software of Mettler Toledo allows for the integration of the phase transition peak, which gives the latent heat of phase change. Besides, the onset and peak points of the phase transition peak can be obtained by the software, which gives the phase transition temperature.

3.3.1.3 *Specific heat capacity measurement*

The evaluation of specific heat in this work is by comparison with the known specific heat of sapphire. Therefore, a blank curve, a sapphire standard curve and a sample curve should be obtained continuously under the same testing conditions. The calculation of the specific heat performed by the Mettler Toledo software is according to the DIN standard (DIN 51007). The equation to calculate C_p is shown below (Eq. 6):

$$C_{p_m} = \frac{\dot{Q}_m \cdot C_{p_s} \cdot m_s}{m_m \cdot \dot{Q}_s} \quad \text{Eq. 6}$$

\dot{Q}_m and \dot{Q}_s donate the heat flow of the sample and the sapphire, respectively; m_m and m_s represent the mass weight of the sample and sapphire, while C_{p_s} and C_{p_m} are the heat capacities of the sample and sapphire.

The specific heat capacity (C_p) measured in this work is in constant pressure, which is mostly concerned in literature. In a typical measurement, around 10 mg of the sample was located into a pierced Al crucible under a purge gas of 100 ml·min⁻¹ Nitrogen and a heating rate of 5 K·min⁻¹.

3.3.2 Thermogravimetric Analysis (TGA)

3.3.2.1 *Experimental technique*

Thermogravimetric analysis (TGA) is a common technique to determine the thermal stability of the sample by monitoring the mass change due to physical or chemical reactions, including decomposition, vaporization, sublimation, absorption and desorption. The temperature of the furnace can be programmed according to the requirements, either heat/cool in a constant heating/cooling rate or keep isothermal. In this work, a Netzsch STA 449 F1 assembled with the TG sample holder was used for thermogravimetric analysis. The resolution of the instrument is 0.025 μg and the DSC enthalpy accuracy is $\pm 2\%$. The operating temperature range is from RT to 1500 °C. There are two kinds of inert gas can be used as the reaction atmosphere.

3.3.2.2 *Method*

The TGA measurements were conducted at a temperature range from RT to 800°C, with a heating rate of 10 K/min. The amount of sample used was around 25 mg and the sample was located into the Pt crucibles. Nitrogen was set as protective gas with a gas flow of 20 $\text{ml}\cdot\text{min}^{-1}$, while both nitrogen and air gas has been selected as reaction gas with a flow of 50 $\text{ml}\cdot\text{min}^{-1}$. Before running the sample, a baseline was obtained by running an empty crucible under the same conditions to measure the sample.

3.3.3 Laser flash apparatus (LFA)

3.3.3.1 *Introduction to LFA*

Laser flash apparatus uses a transient technique to easily measure the thermal diffusivity and thermal conductivity of the sample in a wide temperature range. A laser pulse from the laser beam was emitted and reached the bottom surface of the sample. Then, the laser pulse leads to a temperature rise inside the sample from the bottom to the top surface where the heat rise can be observed. The time that the heat transfer from the bottom to the top is dependent on the thermal

diffusivity of the sample. By the obtained time interval, the diffusivity of the sample can be calculated by the following equation (Eq. 7):

$$\alpha = 0.1388 \frac{d^2}{t_{1/2}} \quad \text{Eq. 7}$$

Where α is the thermal diffusivity (cm^2/s), d is the thickness of the sample (cm), the $t_{1/2}$ is the time at 50% of the maximum temperature increase (s). The coupled Proteus® software is used to calculate the thermal diffusivity, which automatically compares and chooses the best correction model for the results.

The LFA (LFA427, Netzsch) used in this work allows for the measurements within a temperature from -120°C to 1575°C and a heating/cooling rate from $0.01 \text{ K}\cdot\text{min}^{-1}$ to $50 \text{ K}\cdot\text{min}^{-1}$. The detectable range of the thermal diffusivity is $0.01 \text{ mm}^2/\text{s}$ to $1000 \text{ mm}^2/\text{s}$. The accuracy of the thermal diffusivity of this instrument is $\pm 3\%$ over the entire temperature range. The form of the sample can either be in the liquid state (in a crucible) or in the solid phase (parallel-plane shape).

3.3.3.2 Method

The LFA was used to measure the thermal diffusivity of the solid samples using the one-layer method, which is widely used for the solid sample. The sample was prepared in a tablet shape with a diameter of 13 mm and a thickness of around 2 mm. Besides, the sample was coated with graphite as required by the measurement technique to improve the emission/absorption property of the sample and to reduce the signal-to-noise ratio. The tests were performed at different temperatures (see details in the results) under a heating rate of $5 \text{ K}\cdot\text{min}^{-1}$ and a flow rate of $100 \text{ ml}\cdot\text{min}^{-1}$ nitrogen. For each temperature point, 6 shots were conducted every 1 min to obtain the average thermal conductivity. The thermal conductivity (λ) was calculated from the thermal diffusivity (α), specific heat capacity (C_p) and density values (ρ) using Eq. 8 shown below:

$$\lambda = \alpha \rho C_p \quad \text{Eq. 8}$$

3.3.4 Rheometer

3.3.4.1 Introduction to Rheometer

Rheometer allows to study the viscosity and also the viscoelastic properties of polymeric materials. In this study, an MCR 502 rheometer (Anton Paar) was used to measure the dynamic moduli (elastic storage modulus and loss modulus) of the polymer-based CPCM by applying an oscillating strain as a function of frequency. The instrument has a working temperature range from -160°C to 1000 °C and a measurable shear rate from 10^{-6} to 10^3 s^{-1} . The detectable torque range of the instrument is from 10^{-9} to 0.23 N·m. The error of the equipment according to the manufacturer is $\pm 5\%$.

3.3.4.2 Method

The flow was tested from 150°C-180°C with a 10°C temperature interval due to the melting temperature of the HDPE is $\sim 130^\circ\text{C}$. The tests were performed using a parallel plate (\emptyset : 35 mm) as the measuring system with a gap (distance between the upper and the bottom plate) of 1mm and under an air flow of 1 L/min. A small amplitude oscillatory measurement is conducted to measure the viscoelastic property of FSCPCM. The amplitude is set at 1% and dynamic frequency sweeps from 0.628 to 628 rad/s.

3.3.5 Scanning electron microscope (SEM) and energy-dispersive x-ray spectrometer (EDS)

3.3.5.1 Experimental technique

Scanning electron microscope (SEM) is an electron microscope that observes the surface morphology using an electron beam to scan the surface, which gives a good resolution (normally to nanometers) of the image. There are signals of back-scattered electrons (BSE) and secondary electrons (SE) when the electrons interact with the atoms from the surface at different depth.

The secondary electron (SE) imaging normally has a higher resolution and better sensitivity of the surface roughness than the back-scattered electrons (BSE) imaging. However, back-scattered electrons (BSE) imaging is more sensitive to the distribution of different elements on the surface and providing a better contrast of different components. This work used an SEM (Hitachi TM3030, Japan) which assembled with a BSE detector to observe the surface information of composites. This SEM is assembled with an energy-dispersive x-ray spectrometer (EDS) from Bruker Inc. (Quantax 70, Bruker) with a built-in silicon drift detector (XFlash® 430 H detector). The EDS can be used for qualitative and semi-quantitative element analysis.

3.3.5.2 Method

A piece of the sample was placed on the SEM stub with circular conductive carbon tape. A gold coating (thickness of 50 nm) could be applied by a coater, which is from (Q). A voltage of 15 kV was applied for measurement and an EDX mode was used when obtaining EDS images.

3.3.6 Mercury porosimetry

3.3.6.1 Experimental technique

Mercury intrusion porosimetry (MIP) is a useful method to measure the porosity, surface area, and pore size distribution by pressurizing the mercury into the pores of the samples. The pressure required to intrude the mercury into the pores is related to the pore size. Thus, the pore size distribution could be determined by the intrusion pressure. A Mercury porosimetry instrument (Autopore IV 9500, Micromeritics®) was used in this work with two low-pressure ports and one high-pressure port. The low-pressure port is used to inject the mercury into the penetrometer (sample holder), and the high-pressure port is used to collect pore size information of the sample. Mercury could be injected into the pores with increasing pressure up to 33000 psi. This instrument allows for a detectable pore diameter range from 0.003 to 1100µm.

3.3.6.1 Method

A blank measurement (empty penetrometer) is required prior to the measurement of the sample, which will be used to compensate for the sample measurement. Then, fill 1/2 to 2/3 volume of the sample into the penetrometer (around 300 mg) and seal the sample properly. Besides, a Nitrogen gas with a pressure of 4 MPa was used for measurement.

3.3.7 Compressive strength

3.3.7.1 Experimental technique

The compressive strength test is to study the mechanical properties of the sample. It is a destructive test with increasing uniaxial stress applying to the sample gradually until the sample cracks. In this work, the tester is compressing the sample with a constant moving rate. The maximum stress that the sample could withstand without fracture could be regarded as the ultimate compressive strength of the sample. A tensile/ compression tester (Lloyd, 100LS Plus) with a capacity of 100 KN was used in this work. This instrument has a travel distance up to 1150 mm and an accuracy of 0.5% for the load.

3.3.7.2 Method

The sample was prepared by a cylinder module, which gave a tablet shape with a diameter of 15 mm and a thickness of ~ 3 mm. The measurement was set with a compressing speed of 21 mm/min and a maximum strain of 70%. Each composite was repeated for 3 times, which gives an average of three measurements. All the compressive tests of the sample were performed at room temperature (~ 20 °C).

3.3.8 XRT

3.3.8.1 Experimental technique

X-ray tomography (XRT) is a nondestructive technique using an X-ray to obtain 2-D X-ray image slices and creating a 3D virtual model of the object by the 2-D images. This technique allows

for visualizing the interior geometry features of the object and gives the density and composition information of the sample. It has been widely used for medical imaging and industrial tomography. This work used a multiscale X-ray nanotomography (SkyScan 2211, Bruker) which assembled with two X-ray detectors: a flat-panel camera for the large field of view with a micron resolution and a CCD camera for small field of view with a submicron resolution (100 nm). This machine allows for a maximum sample size with a diameter up to 204 mm and a sample height up to 200 mm. The X-ray source has an adjustable voltage from 20 kV to 190 kV. A software (NRecon) was used to reconstruct the 3D model of the object and a software (CTAn) was used for quantitatively analyzing the morphometry and densitometry results of the 2-D and 3D images.

3.3.8.2 Method

A cylindrical sample with a diameter of 5 mm was used to observe the internal morphology and of the material. This work selected a flat-field camera for scanning due to a higher sensitivity of the density. To obtain an optimal image of the specimen, a voltage of 40 kV and a current of 300 mA was applied in the scanning. The exposure time for the scan was set as 160ms. Besides, a flat-field correction was obtained and applied to reduce the noise during the scanning of the sample. For the reconstruction of the image, a threshold of 0-0.016 was used to define the object.

3.3.9 Thermal cycling

3.3.9.1 Experimental technique

Thermal cycling test is expected to determine the reliability of the sample when it undergoes continuous heating and cooling. For a phase change material, the thermal cycling test is always around the melting point. In this work, a dilatometer (DLA, TA instrument) was used to perform the thermal cycling test which could run 25 times thermal cycling in one program at a time. Continuous thermal cycles were conducted by repeating the program after 25 cycles were finished.

The instrument is assembled with an optional purge gas; N₂ or Air. The furnace has a maximum working temperature up to 1500°C.

3.3.9.2 Method

The sample underwent thermal cycling in a dilatometer (DLA, TA instrument). In this work, thermal cycles were conducted continuously. For the KNO₃/diatomite CPCM, the temperature range of the thermal cycling was set from 280 °C to 380 °C. For the HDPE-PE-Cg CPCM, the thermal cycling test was performed in the temperature range from 100 °C to 200 °C. The heating rate is 10 °C/min at dynamic segments, and the sample was kept in isothermal for 10 minutes at the maximum and minimum temperature.

3.3.10 Infrared microscopy (IR)

3.3.10.1 Experimental technique

Infrared microscopy (IR) is a non-destructive technique that can determine the materials with covalent bonds by infrared spectrum. When the frequency of the infrared spectrum is the same as the vibrational frequency of the bond, it can be detected due to the absorption of the infrared spectrum. According to the spectra obtained by scanning the entire wavelength range, the sample can be determined from the library as each material has its specific spectra. In this work, the infrared microscope (Bruker, LUMOS) allows for the observation and scanning on the surface of the sample with a high spatial resolution. It can conduct spot, line, or map scanning on the surface.

3.3.10.2 Method

There is a sample stage that can be used to locate the sample and can be adjusted to focus on the surface. The ATR mode was used in the test for its high sensitivity. Before each test, the detector has to be cleaned to get rid of the contaminations on the detector. Low pressure (default option) was applied when the detector is in contact with the sample. A blank measurement was

conducted to remove the noise from the background. In this work, each spectrum was scanned for 64 times for averaging.

3.3.11 Helium pycnometer

3.3.11.1 Experimental technique

The helium pycnometer Micro-meritics Accupyc II 1340 was used in this work. This instrument allows to evaluate the true density, determine the porous density and non-porous solids density. It measures the volume occupied by the gas to obtain the high-precision volume of the solid. The true density is determined by the weight of the dried sample and the true volume of the samples. For this technique, helium is always used as the displacement medium as its molecular is very small. It can penetrate into the material structure and completely fill the porous effectively.

3.3.11.2 Method

The samples were measured at room temperature and were located in a sample holder. Each measurement was repeated for 5 cycles for averaging. When the true density of the solid was obtained, the porosity of the sample (∂ , includes open pores and close pores) can be calculated using the true density (ρ_t) and bulk density (ρ_b):

$$\partial = 1 - \frac{\rho_b}{\rho_t} \quad \text{Eq. 9}$$

3.3.12 Contact angle

3.3.12.1 Experimental technique

The measurement of the contact angle was performed on the KRUSS (DSAHT17-2) high-temperature apparatus. The apparatus consists of a heating chamber which can be heated up to 1000°C, a type B thermocouple, a vacuum unit and a high-resolution camera which is used to record the geometry of the droplet on the substrate.

3.3.12.2 Method

The measurement of the contact angle was conducted in the air atmosphere. A small pellet of the sample was firstly prepared in a 4 mm diameter round mould and compressed at 40 MPa. Then the sample pellet was placed on the centre of the substrate (SiO₂ or graphite) and the sample with the substrate were heated up in the chamber until melt. The heating rate was set at 5 °C/min before the sample melt, after which the heating rate was set at 2 °C/min till decomposition. The geometry of the droplet at different temperature was recorded by the camera and used for the analysis of the contact angle.

3.3.13 Mastersizer

3.3.13.1 Experimental technique

The Mastersizer 2000 Particle Sizer from Malvern Panalytical Ltd. was used to measure the macroscopic particle size distribution. It has a detectable size range from 0.02µm to 2000µm. A water-based dispersing unit and an oil-based dispersing unit are available for measuring different liquid-based suspensions. The rotation speed for the rotor is ranging from 0 rpm to 3500 rpm.

3.3.13.2 Method

This work used sunflower oil as a base solution to measure the particle size distribution of PE. The solubility of PE in the sunflower oil is measured to be 0.005 g/100ml, which means PE is insoluble or practically insoluble in sunflower oil. For comparison purpose, all the measurements were conducted at a rotation speed of 2500 rpm.

4 Results and discussion (I): a modified mix-sintering fabrication method with a preheating process

4.1 Introduction

From the state-of-art summary of fabrication methods in chapter 2, we can find that mix-sintering method is extensively used for preparing high-temperature FSCPCMs (~ up to 900 °C). The mix-sintering method also presents a large-scalable potential due to its simple and controllable process. Most of the studies found are focusing on modifying the PCMs with additives to improve their thermophysical properties. However, very few studies considered the effects of the fabrication process on the thermophysical properties of materials. As mix-sintering fabrication process involves multi-species and multi-phases, the process parameters can significantly affect the properties and performance of the final products.

In this chapter, a modified mix-sintering method with an additional preheating process is proposed and compared with the conventional mix-sintering process. A diatomite-KNO₃ FSCPCM was prepared by both the modified fabrication route and the conventional fabrication route. The effects of the preheating process on the physical properties, thermal properties, and thermal cycling stability of the CPCMs were studied. Besides, the microstructure development process of the FSCPCMs prepared by different fabrication routes are investigated. Finally, the criteria for using the modified mix-sintering method to produce high-quality products are investigated and verified by two different composite PCMs (SiO₂-KNO₃ composite and graphite-KNO₃ composite).

4.2 Fabrication and characterisations

4.2.1 FSCPCM formulations

KNO_3 and diatomite were weighed according to the ratio shown in Table 7. The suppliers of these materials are reported in the chapter 3. All the FSCPCMs were prepared by two fabrication routes: conventional mix-sintering method and modified mix-sintering method. The codes of the prepared samples are also shown in Table 7. For the conventional mix-sintering fabrication method, FSCPCMs with different formulations (sample N50 to sample N70) are prepared separately following the fabrication route. About 10 tablets were prepared for each formulation to conduct different tests. Similarly, the same quantities of tablets for different formulations (sample P50 to sample P70) were prepared under the modified mix-sintering method.

Table 7 Mass ratio of the PCM and Diatomite

	No.	1	2	3	4	5
Formulations	KNO_3 (wt%)	50	55	60	65	70
	Diatomite (wt%)	50	45	40	35	30
Codes for samples	traditional mix-sintering method	N50	N55	N60	N65	N70
	modified mix-sintering method	P50	P55	P60	P65	P70

4.2.2 Fabrication method

4.2.2.1 Conventional mix-sintering process without preheating process

Figure 25 displays the schematic diagram of the conventional mix-sintering process to prepare diatomite- KNO_3 FSCPCM. The fabrication process includes three steps as follows:

- **Step 1 - mixing:** KNO_3 was ground in the ball mill at 300 rpm for 20 minutes, and then sieved to a size below ~ 500 μm . The diatomite was used as received. The KNO_3 powders and diatomite powders were weighed proportionally and then well mixed in the ball mill at 100 rpm for 10 minutes.
- **Step 2 - tableting:** ~ 1 g mixed powders were added into a module, and then compressed under a uniaxial pressure of 40 MPa and held for 1 min. The obtained pellets after compression are termed as green pellets. In the compression process, most of the interparticle voids have been removed.
- **Step 3 - drying and sintering:** the green pellets were dried and sintered as follows: 1) heated to 100°C at a rate of $5^\circ\text{C}/\text{min}$ and held at 100°C for 1 hour to get rid of the moisture inside the pellet; 2) heated to 380°C with a heating rate of $10^\circ\text{C}/\text{min}$ and held at 380°C for 2 hours. In the sintering process, the PCM melts and drags the particles together by capillary forces.

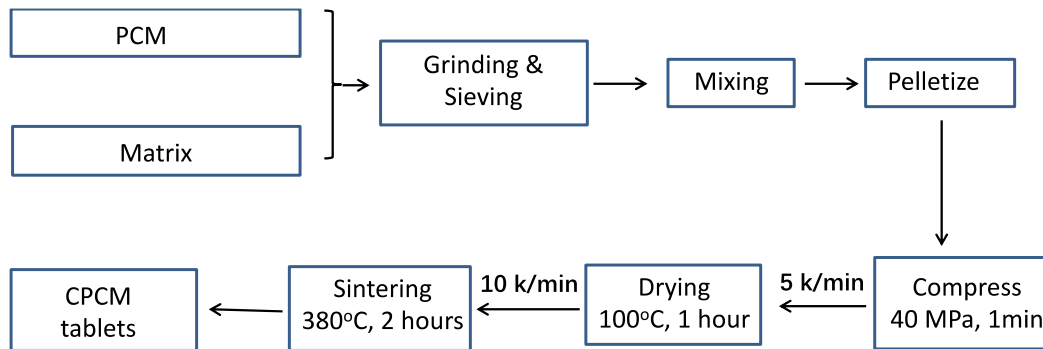


Figure 25 Schematic diagram of the conventional mix-sintering method without preheating process

4.2.2.2 Modified mix-sintering with preheating process

The modified mix-sintering process is similar to the conventional mix-sintering process. It includes a preheating process after the mixing step; see Figure 26. In the preheating process, the

powder mixture is heated above the melting temperature of KNO_3 . In this work, the mixtures were heated at 380°C for 30 minutes. There is, therefore, no need to grind the KNO_3 salt into fine powders before preheating process. After preheating, the powders might aggregate due to capillary forces which can be ground easily by mill or by mortar-pestle. Then, the preheated powders are compressed and sintered, which is the same as the conventional mix-sintering process.

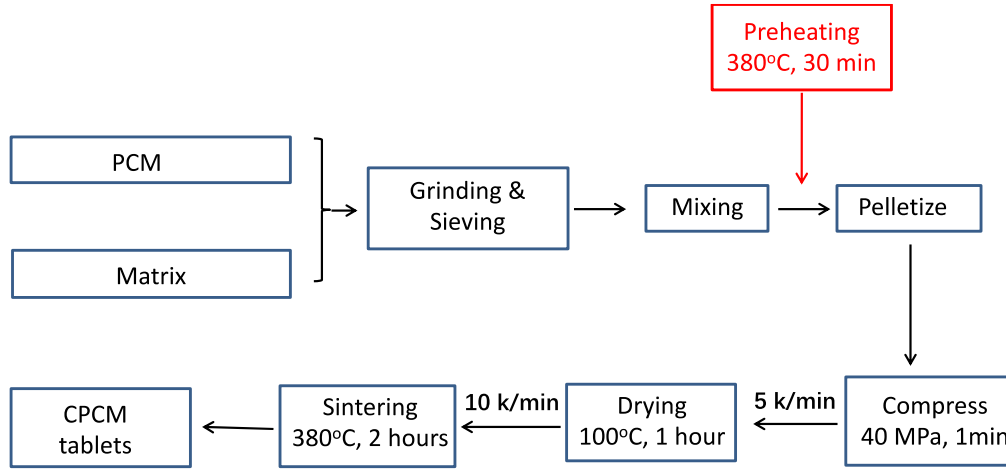


Figure 26 Schematic diagram of the modified mix-sintering method with the preheating process

4.2.3 Characterisation methods

To clarify the measurement conditions, test range and the repetitions, the details of method are shown in Table 8. Some measurements have repeated results, then the experimental

uncertainties are evaluated by the standard deviation: $SD = \sqrt{\frac{1}{N-1} \sum_{i=1}^N (x_i - \bar{x})^2}$, where x_i is the value of each test, \bar{x} is the averaged value, N is the number of the test.

Table 8 Measurement methods and repetitions

Instruments and Properties	Measurement methods	Data acquisition	Sample shape/ amount	Repetitions
Helium pycnometer True density	Default	acquire 5 results in each test	tablet: Ø: 4 mm, H: ~2 mm.	each sample conduct 1 measurement. averaged form 5 acquired results.
DSC: melting temperature/latent heat/heat capacity	25°C to 400°C at a heating rate of 5°C/min; 100ml/min Air flow.	whole range.	~10 mg powers.	each sample conduct 3 measurements. averaged form 3 measurements.
LFA: thermal conductivity	25 to 250 °C at a heating rate of 5°C/min; 100ml/min N ₂ flow.	acquire 6 results at 25°C, 100°C, 150°C, 200°C, 250°C.	tablet: Ø: 13 mm, H: ~2 mm.	each sample conduct 1 measurement. averaged form 6 acquired results
Contact angle: wettability	RT to 375 °C at a heating rate of 2°C/min.	acquire 3 results at 335°C, 345°C, 355°C, 365°C, 375°C.	tablet: Ø: 4 mm, H: ~4 mm.	each sample conduct 1 measurement. averaged form 3 acquired results.
Mercury porosimetry: Porosity and pore size distribution	Default	Whole range	~300 mg, powder or tablet	each sample conduct 1 measurement.
Dilatometer: thermal Cycling	1 cycle: a). 280 to 380 °C at a heating rate of 10°C/min; b). maintained at 380 °C for 10 minutes; b). 380 to 280 °C at a cooling rate of 10°C/min. repeat for 50 cycles. N ₂ atmosphere.	/	tablet: Ø: 13 mm, H: ~2 mm.	sample was characterized after 50 thermal cycles.

4.3 Results and discussion

4.3.1 Characterisation of physical properties;

4.3.1.1 Bulk Density

Figure 27 shows the bulk density of FSCPCMs prepared by two mix-sintering methods. The density of the green pellet and the sintered pellet is also compared. One can see that the density of FSCPCMs is increasing with the increasing proportion of KNO_3 due to high density of KNO_3 particles. The sample prepared by modified mix-sintering method presents a significantly higher density than that prepared by the conventional process, with a ~20% enhancement for all FSCPCMs. The increment of the density indicates a less porous internal structure of the FSCPCM prepared by the modified mix-sintering method. It also can be found that the density of sintered pellets is slightly higher than the green pellets, and the FSCPCM with a higher percentage of KNO_3 shows a higher enhancement in density after sintering. This is expected due to the molten KNO_3 rearranges the diatomite particles to form a denser structure after the sintering process, leading to a density increment [32], [43]. A higher percentage of KNO_3 contributes to a stronger particle rearrangement due to higher mobility of the FSCPCM composite; see detailed discussion in section 4.3.4.2. As a result, the enhancement in density after sintering is higher for the FSCPCM with a higher percentage of KNO_3 .

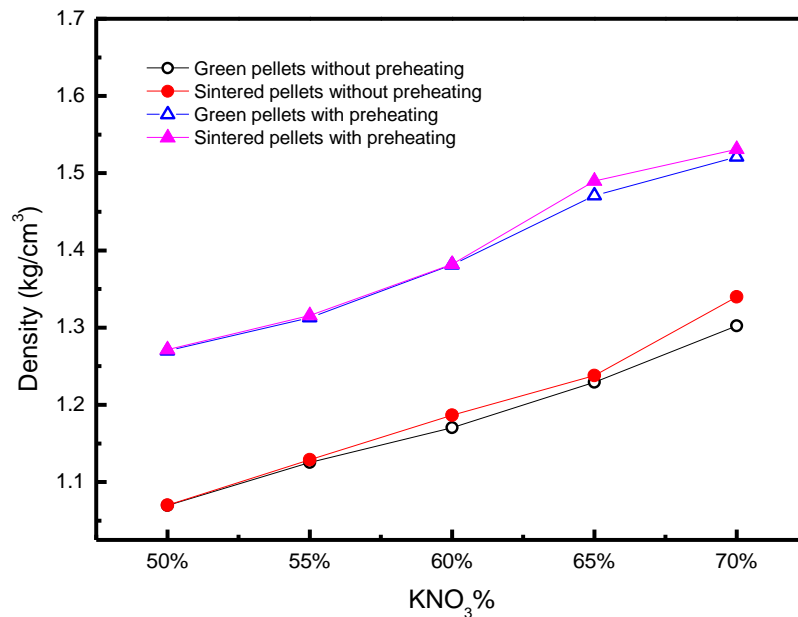


Figure 27 Bulk Density of the green and sintered FSCPCMs prepared by different processes

4.3.1.2 Porosity

The porosity of the FSCPCM is studied by its bulk density (see the previous section) and true density, with the former can determine the total volume and the later can determine the skeleton volume. The true density is measured by a Helium pycnometer. As helium can penetrate almost all the solids due to its small molecular size, the porosity measured by this method includes both open pores and closed pores. However, helium may also permeate in some low-density solids (such as polymers and cellulosic materials), giving rise to an overestimation of the pore volume. Table 9 shows the density and calculated porosity of the green and sintered pellets prepared by two methods. One can find that the true density for all the samples are similar, while the bulk density is different due to the different volume of air trapped inside. Sample (P70) with preheating process shows a lower porosity than the sample (N70) without preheating, with a decrease of 8.75% to

9.18%. Besides, the porosity has also reduced by 1.76% - 2.19% after sintering, which agrees with the increment in density after sintering.

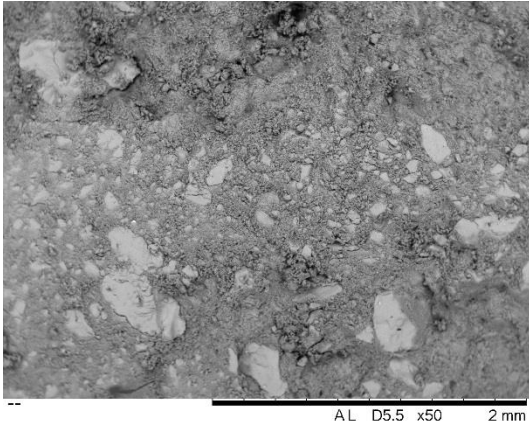
Table 9 True density and calculated porosity (with SD)

	N70 – green	N70 - sintered	P70 - green	P70 - sintered
True density (g/cm ³)	2.1348±0.0033	2.1205±0.0066	2.1673±0.0017	2.1282±0.0020
Bulk density (g/cm ³)	1.3022±0.0157	1.3399±0.0084	1.5211±0.0047	1.5311±0.0085
Porosity (%)	39.00	36.81	29.82	28.06

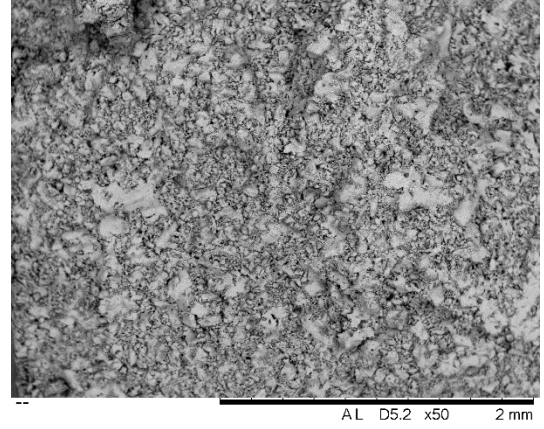
4.3.1.3 Microstructure

The morphology of the FSCPCMs with 70 wt.% KNO₃ (sample N70 and P70) is observed by SEM, and the element distribution on the surface is obtained by EDS. Figure 28 (a) & (b) display the morphology of sample N70 and P70 before sintering and Figure 28 (c)& (d) are the corresponding EDS images. In Figure 28 (a) & (c), green sample (N70) pellet has two kinds of granules observed by SEM and identified EDS: one type of particle is KNO₃ with a large particle size from ~100 um to ~500 um; another type of granule is diatomite with the particle size below ~5 um. However, the morphology of green sample pellet (P70) with preheating process is different. From Figure 28 (b) & (d), the KNO₃ granules cannot be observed. Instead, some aggregates consist of salt and diatomite can be observed after undergoing preheating process. The morphology of the sintered sample is also different from the green sample. In Figure 28 (e) (i), we can see there is a lot of interconnected pores and voids in sample N70. For the preheated sample (P70), it displays a less porous morphology after sintering although some small voids and pores are observed in Figure 28 (f) & (j). In Figure 28

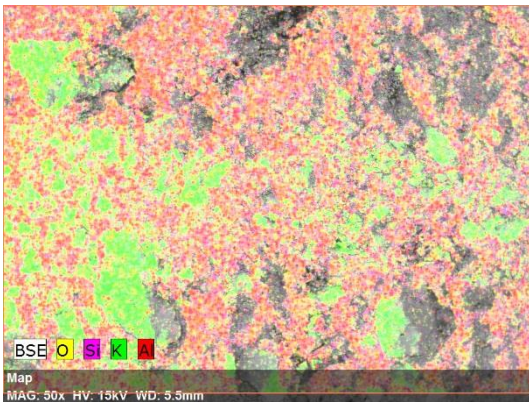
(g) & (h), one can see that all the samples are homogeneously distributed after sintering process whether the sample is preheated or not.



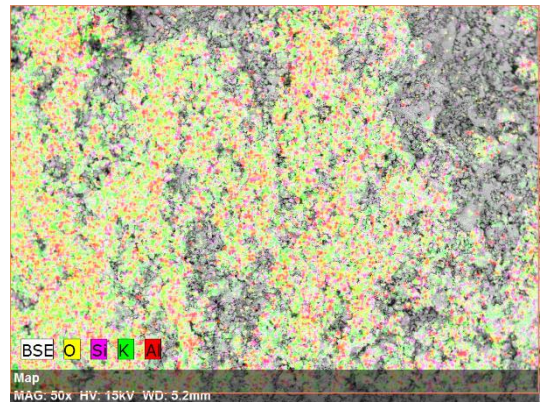
(a) SEM image of green sample N70 without preheating (X50)



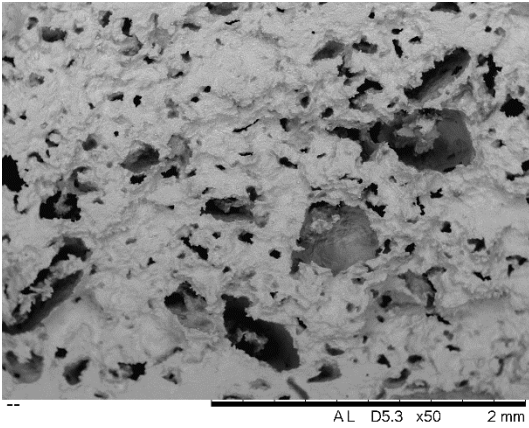
(b) SEM image of green sample P70 with preheating (X50)



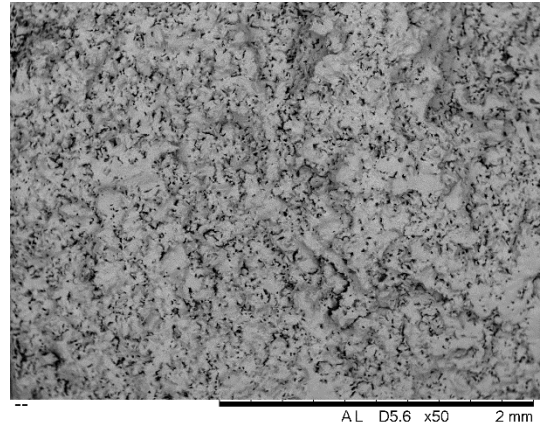
(c) EDS image of green sample N70 without preheating (X50)



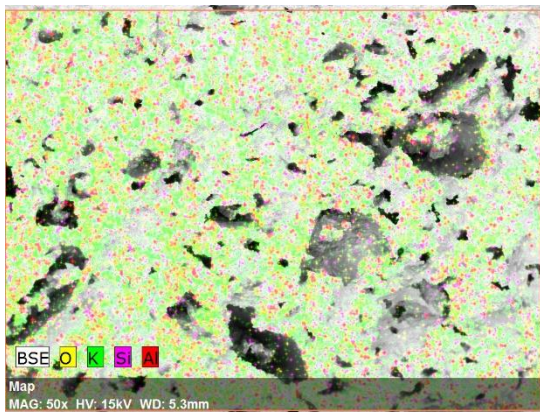
(d) EDS image of green sample P70 with preheating (X50)



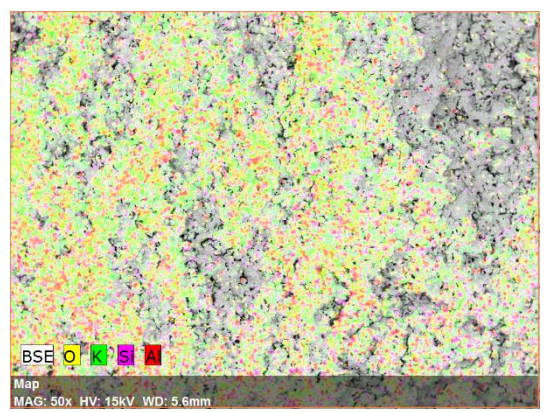
(e) SEM image of sintered sample N70 without preheating (X50)



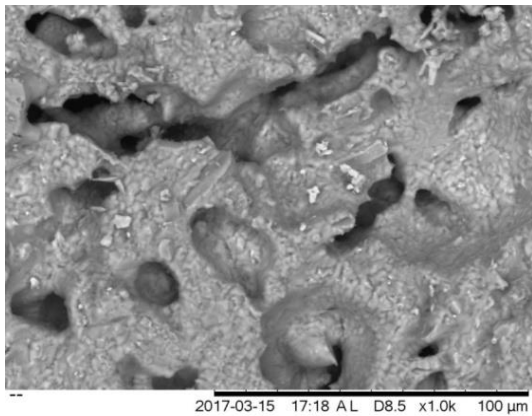
(f) SEM image of sintered sample P70 with preheating (X50)



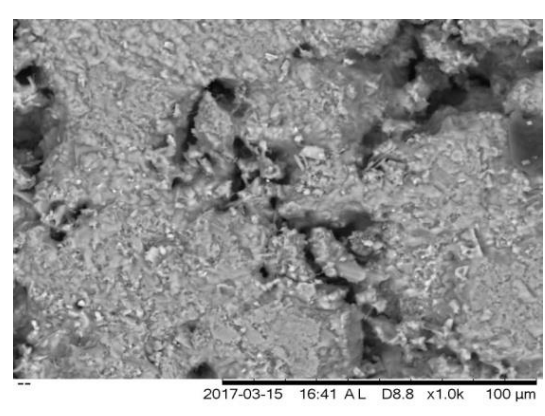
(g) EDS image of sintered sample N70 without preheating (X50)



(h) EDS image of sintered sample P70 with preheating (X50)



(i) SEM image of sintered sample N70 without preheating (X1000)



(j) SEM image of sintered sample P70 with preheating (X1000)

Figure 28 SEM and EDS images of the green and sintered FSCPCM prepared by different methods

4.3.1.4 Compressive strength

Figure 29 shows the compressive strength of the sintered FSCPCMs prepared by two processes. One can see that the sample prepared with modified mix-sintering process present a higher compressive strength compared with the sample without preheating. The improvement of compressive strength is due to the reduction of pores. Besides, we can see that the compressive strength of preheated FSCPCMs is increasing with an increasing amount of KNO_3 until KNO_3 reaches 60 wt.%, and then the compressive strength levels off. It is expected that a higher amount of KNO_3 will contribute to a less porous structure as the KNO_3 will penetrate into the pores, resulting in a higher compressive strength. However, with an increasing amount of KNO_3 , the total porosity is reaching the minimum and cannot be reduced any further. As a result, the compressive strength levels off. In terms of the sample without preheating, the lower compressive strength reveals a more porous internal structure compared with the preheated sample. Its compressive strength keeps increasing with the increasing percentage of KNO_3 . This is because the not-preheated samples are highly porous, hence their porosity can still be reduced when the percentage of KNO_3 increased to 70 wt.%.

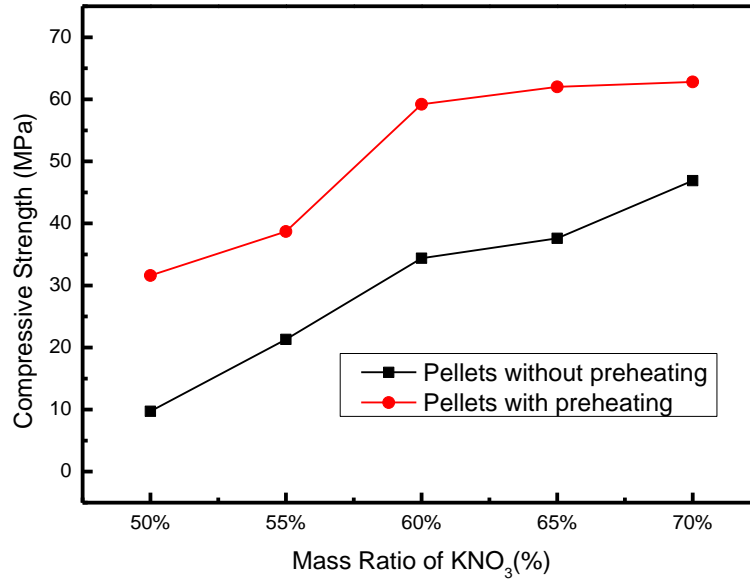


Figure 29 Compressive strength of the FSCPCM with or without preheating process

4.3.2 Thermal properties

4.3.2.1 Phase change parameters and energy density

For a PCM, phase change enthalpy is the parameter that indicates the latent heat storage capacity of the material at phase change, while specific heat determines the sensible heat storage capacity during the dynamic heating/cooling process. The total energy that can be stored per unit mass of FSCPCM includes both latent heat stored and sensible heat stored. In this section, thermal properties, such as phase change enthalpy, specific heat, and energy density are investigated.

(1) Melting point and phase change enthalpy

DSC curves of the FSCPCMs (N50, P50, N60, P60, N70, P70) are shown in Figure 30, and the inset figure shows the DSC curve of pure KNO_3 . One can find that the pure salt and the FSCPCM show similar endothermal behaviour when heated from 25°C to 400°C: two endothermal peaks observed at ~132°C and ~332°C, respectively. The first endothermal peak represents the crystal

transition of KNO_3 from aragonite phase to rhombohedral phase (solid-to-solid phase transition) [153], along with a phase change enthalpy of 45.46 kJ/kg. The second endothermal peak represents solid to liquid phase transition of pure KNO_3 with an enthalpy of 94.62 kJ/kg. It can be found that the solid-liquid transition enthalpy is nearly twice of the solid-solid transition enthalpy. The phase change enthalpies and peak temperatures are listed in Table 10. One can see that the differences in temperature ($<0.79^\circ\text{C}$) and latent heat (<1.49 kJ/kg) between preheated samples and not-preheated samples are not significant. The experimental uncertainties are shown as standard deviations (SD) in Table 10, where we can see the largest deviations for the measured phase change temperature is 0.65°C and for the latent heat is 2.94 kJ/kg. Therefore, the differences between the preheated samples and not-preheated samples is negligible compared with the experimental uncertainties. In other words, the preheating process does not affect the phase change temperature and enthalpy. One can also find that the experimental value of phase change enthalpy is slightly lower than the theoretical value. The theoretical solid-liquid transition enthalpy for FSCPCMs with 50 wt.%, 60 wt.% and 70 wt.% of KNO_3 are 47.31 kJ/kg, 56.77 kJ/kg, 66.23 kJ/kg, respectively, which is ~ 3.18 to ~ 6.06 kJ/kg higher than the experimental value of FSCPCM with or without preheating process. The slight decrease of latent heat between experimental results and theoretical results for FSCPCM was also reported by other studies [154][155]. This is likely due to the loss of PCM during the preparation of FSCPCM, such as the evaporation of melted PCM during the sintering process.

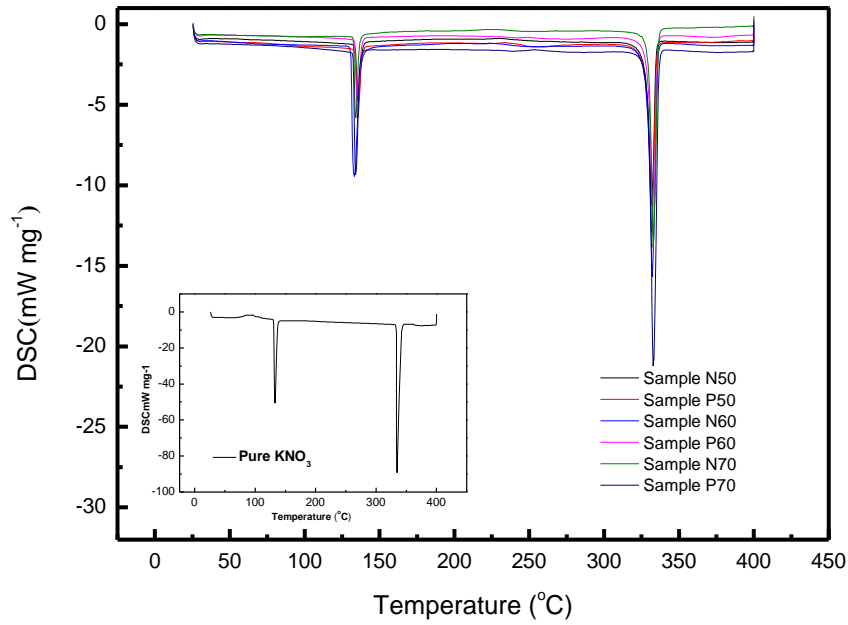


Figure 30 DSC curves of pure KNO_3 and the formulated FSCPCMs

Table 10 Melting point and latent heat of KNO_3 and the formulated FSCPCMs (with SD)

sample	$T_1(^{\circ}\text{C})$	T_{1P-} T_{1N} ($^{\circ}\text{C}$)	$\Delta H_1(\text{kJ/kg})$	ΔH_{1P-} ΔH_{1N} (kJ/kg)	$T_2(^{\circ}\text{C})$	T_{2P-} T_{2N} ($^{\circ}\text{C}$)	$\Delta H_2(\text{kJ/kg})$	ΔH_{2P-} ΔH_{2N} (kJ/kg)
KNO_3	131.18 ± 0.15	-	45.46 ± 2.66	-	332.36 ± 0.35	-	94.62 ± 2.94	-
N50	133.21 ± 0.45	-	21.29 ± 1.10	-	331.52 ± 0.12	-	41.25 ± 0.21	-
P50	132.81 ± 0.36	-0.4	21.64 ± 0.86	0.35	331.52 ± 0.28	0	42.46 ± 1.15	1.21
N60	133.10 ± 0.10	-	25.25 ± 1.15	-	332.03 ± 0.42	-	51.02 ± 1.26	-
P60	132.31 ± 0.22	-0.79	25.35 ± 0.65	0.1	332.13 ± 0.58	0.1	52.32 ± 0.95	1.3
N70	132.69 ± 0.24	-	32.22 ± 1.14	-	333.42 ± 0.65	-	63.05 ± 1.46	-
P70	132.16 ± 0.12	-0.53	30.94 ± 1.29	-1.28	332.78 ± 1.15	-0.64	61.56 ± 0.45	-1.49

(2) Specific heat

The specific heat ($\text{kJ}/(\text{kg}\cdot^{\circ}\text{C})$) of FSCPCMs, pure KNO_3 and diatomite at different temperatures are displayed in Table 11. One can see that the specific heat is generally increasing with increasing temperature, which agrees with the study by Wu et al. [156]. Also, the specific heat results at some points scattered and show high standard deviations, this is due to the difficulty of measuring the specific heat for samples with small amount. For small samples, the heat flow required for the test is also very small. Thus, the heat leak through conductive electrical connections cannot be neglected, which leads to a low accuracy of heat capacity measurement [157]. It also can be found that the pure KNO_3 presents a lower specific heat than the diatomite, leading to a decreasing specific heat of the FSCPCM with an increasing percentage of KNO_3 . Besides, we found that the FSCPCM prepared with preheating process presents a slightly higher specific heat than the sample without preheating. Etzler [158] found that the specific heat of the water has enhanced 25% when restricted in the silica pores, compared with the bulk water. The author explained that the hydrogen bonding between water molecules has been enhanced due to the confinement of silica pores [159]. A stronger hydrogen bond means a stronger restriction between the water molecules, and therefore the movement of water molecule requires more energy which is reflected by an increase in the specific heat. The specific heat increase of the preheated FSCPCMs found in this work is expected due to the movement of PCM molecules has been restricted by the porous structure of the diatomite. The preheating process contributes to the penetration of PCM into fine pores of diatomite and results in higher specific heat. Generally, it can be found that the preheating process does not affect the phase change temperature and the latent heat of the FSCPCM, but has shown some positive impacts on the specific heat of the composite.

Table 11 Specific heat of the composite PCMs with SD

T (°C)	P50	N50	P60	N60	P70	N70	KNO ₃	diatomite
25	0.85±0.10	0.78±0.02	0.86±0.05	0.82±0.04	0.88±0.05	0.85±0.01	0.40±0.09	1.03±0.04
100	1.15±0.02	0.78±0.04	1.05±0.05	1.04±0.07	1.04±0.08	1.06±0.04	0.52±0.03	1.34±0.12
150	1.25±0.09	0.95±0.08	1.31±0.11	1.19±0.10	1.18±0.02	1.00±0.08	0.76±0.02	1.34±0.13
200	1.12±0.10	1.14±0.07	1.13±0.08	0.98±0.02	1.09±0.09	0.82±0.03	0.84±0.02	1.25±0.01
250	1.2±0.03	1.13±0.10	1.13±0.10	1.09±0.20	1.1±0.05	0.9±0.05	0.95±0.03	1.38±0.01
average	1.11±0.06	0.96±0.06	1.10±0.06	1.02±0.08	1.06±0.06	0.93±0.02	0.69±0.04	1.27±0.05

(3) Energy density

By the phase change enthalpy and the specific heat of the materials obtained, the energy density of FSCPCM can be calculated. If the application temperature range is from T_0 to T_1 , then the total energy density can be calculated as follows (Eq. 10):

$$Q = \int_{T_0}^{T_1} C_p dT + \Delta H \quad \text{Eq. 10}$$

where Q is the energy density of the FSCPCM, kJ/kg; C_p denotes the heat capacity of the composite PCM, kJ/(kg·°C); T_0 and T_1 represent the lower bound temperature and upper bound temperature, respectively, °C. ΔH represents the latent heat of the FSCPCM, kJ/kg.

In this work, we consider a temperature range from 250 °C to 350 °C, which is according to the phase change temperature of this FSCPCM. As the specific heat is varying with temperature, this work uses a linear fitting of the heat capacity to estimate the sensible heat stored. It should be noted that the function of heat capacity is fitted based on the experimental results from 250 °C to 350 °C, therefore the fitted function is more precise for the calculation of heat capacity and energy density

within this temperature range. The fitting curve of heat capacity and the calculated energy density for each sample are shown in Table 12.

Table 12 Fitting curve of specific heat and calculated energy density

sample	The fitting curve of C_p (within 250 °C to 350 °C)	Sensible heat (kJ/kg)	Latent heat (kJ/kg)	total energy density (kJ/kg)
P50	$C_p = 0.0013T + 0.9234$	131.34	42.46	173.8
N50	$C_p = 0.0019T + 0.6831$	125.31	41.25	166.56
P60	$C_p = 0.0012T + 0.9206$	128.06	52.32	180.38
N60	$C_p = 0.001T + 0.8857$	118.57	51.02	169.59
P70	$C_p = 0.0009T + 0.9204$	119.04	61.56	180.6
N70	$C_p = -0.0002T + 0.9502$	89.02	63.05	152.07

One can see from Table 12 that the FSCPCM without preheating process shows a lower energy density than the preheated sample due to their lower specific heat. Sample P70 presents the highest energy density among all the samples due to its both high sensible heat storage capacity and latent heat storage capacity. Sample P70, therefore, shows optimal heat storage capacity for medium temperature TES applications.

4.3.2.2 Thermal conductivity

Thermal conductivity ($W/(m \cdot K)$) is an important parameter for the PCM as it affects the energy charging and discharging rate. The thermal conductivity of FSCPCMs prepared by different fabrication methods is shown in Figure 31. One can see that the thermal conductivity of the FSCPCM is generally decreasing with the increasing temperature, which agrees with the results reported in other studies [124], [160]. The thermal conductivity is also increasing with the increasing amount of the KNO_3 . This is because diatomite is less thermally conductive compared with KNO_3 due to its

porous structure. For the FSCPCMs with preheating process (sample P50, P60, P70), their thermal conductivities are significantly higher than the FSCPCMs prepared without preheating process (sample N50, N60, N70). The averaged thermal conductivity in the temperature range of 25 °C to 250 °C is shown in Table 13. We can find that with the modified mix-sintering process, the thermal conductivity of has enhanced by ~35.94% to ~54.91%. This is because the porosity of preheated FSCPCMs has been reduced, and the air trapped inside the pores would hinder the heat conduction inside the FSCPCM. As aforementioned, low conductivity is one of the key challenges that need to be addressed for the development of PCMs. In this work, we found that the manufacturing process could greatly improve the thermal conductivity of FSCPCM.

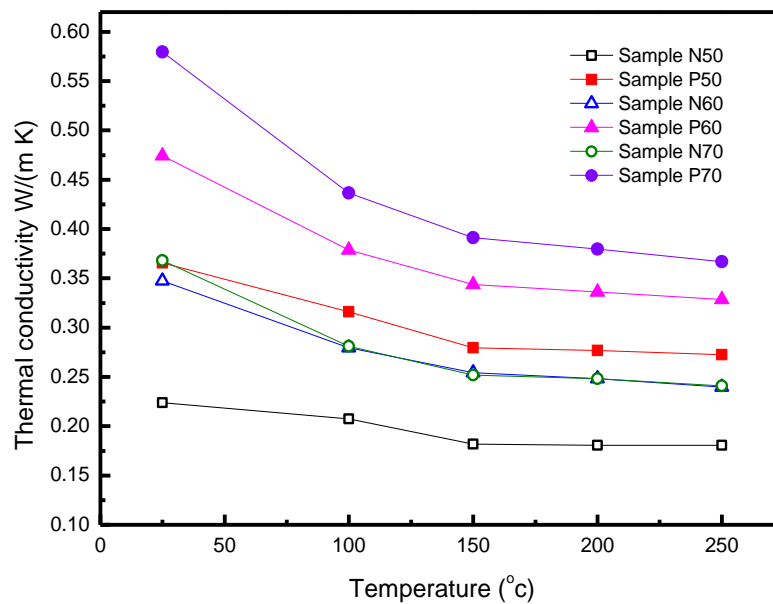


Figure 31 Thermal conductivity of the preheated and not-preheated FSCPCMs

Table 13 Average of the thermal conductivity for the FSCPCMs

sample	N50	P50	N60	P60	N70	P70
average	0.19 ± 0.005	0.30 ± 0.002	0.27 ± 0.001	0.37 ± 0.002	0.28 ± 0.002	0.43 ± 0.006
enhancement	-	54.94%	-	35.94%	-	54.91%

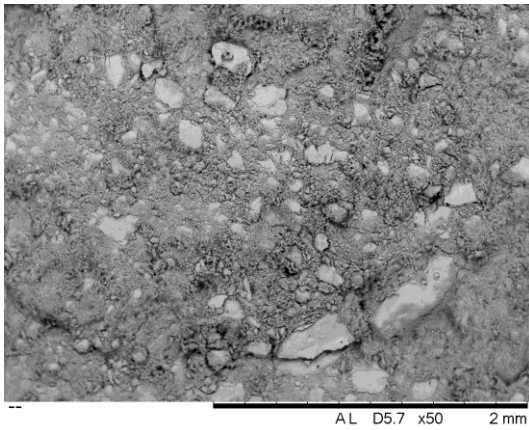
4.3.3 Thermal cycling stability

From the previous study, we can find that the dense internal structure obtained by modified mix-sintering method is the key factor for the improvement of density, compressive strength and thermal conductivity. Whether the internal structure of FSCPCM could remain unchanged after several charging/discharging cycles has not been studied. Besides, long-term stability is an essential property of FSCPCM for practical application. Therefore, this section we focus on the thermal cycling stability of FSCPCM, including structural stability and thermophysical property stability.

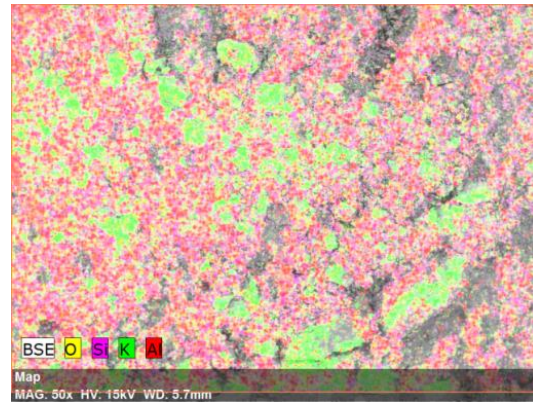
4.3.3.1 Microstructure;

Figure 32 shows the SEM and EDS images of sample N70 before sintering, after sintering (1 thermal cycle), 10 thermal cycles, and 50 thermal cycles [161], while Figure 33 shows that of sample P70. To observe the changes of microstructure after different times of thermal cycling, all the SEM and EDS images are obtained at the same place by making a mark on the sample surface. One can see from Figure 32 that the internal structure of sample N70 has changed significantly after sintering (1 thermal cycle). Then the internal structure of FSCPCM remains unchanged when undergoing thermal cycling; see Figure 32 (2-a) to (4-a). Besides, from the EDS images in Figure 32, one can find that the salt and diatomite are always homogeneously distributed. For preheated sample P70 (Figure 33), one can see that there are no observable structural changes between the green pellet and sintered pellet, which is different from sample N70. However, it is the same as sample N70 that

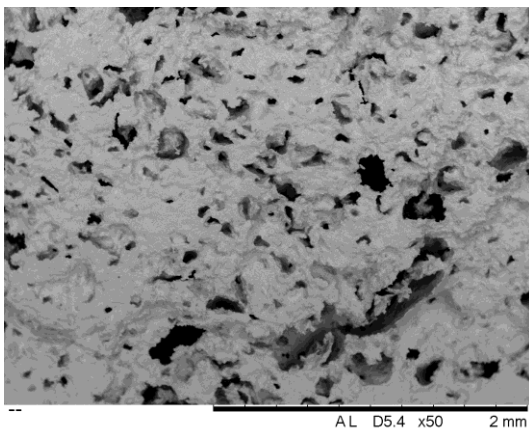
thermal cycling process does not change the internal structure of FSCPCM, and the ingredients are always uniformly distributed. Therefore, it can be concluded that the thermal cycling process does not affect the internal structure of FSCPCM significantly. The dense structure of FSCPCM needs to be obtained before thermal cycling.



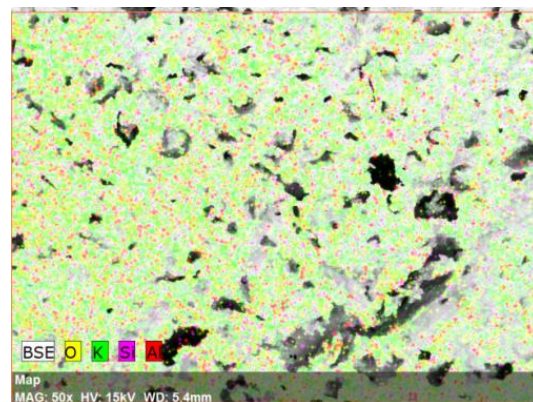
(1-a) SEM image of sample N70-green pellet



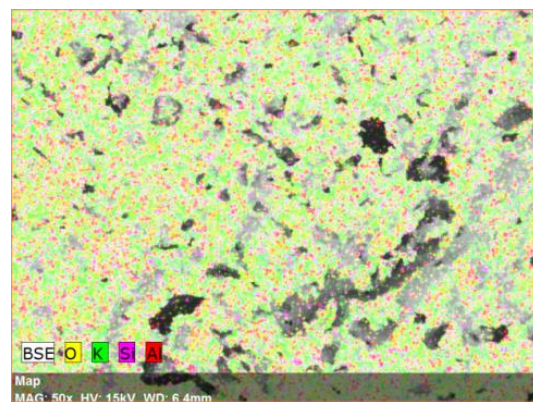
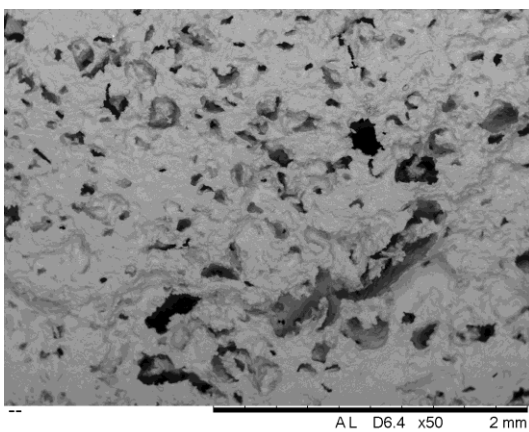
(1-b) EDS image of sample N70-green pellet



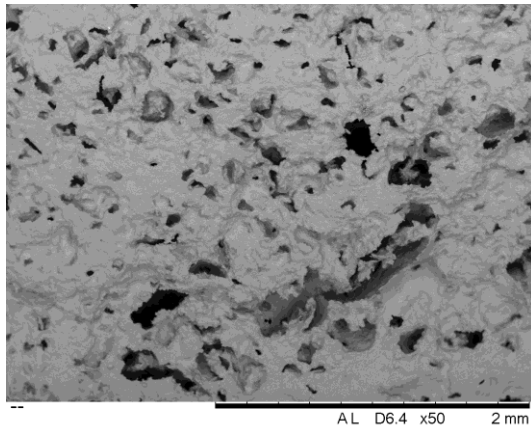
(2-a) SEM image of sample N70-sintered pellet (1 cycle)



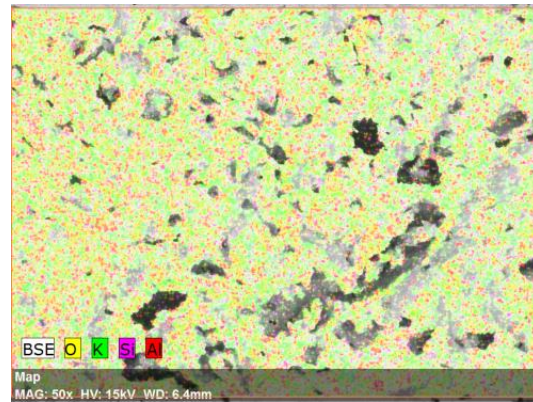
(2-b) EDS image of sample N70-green pellet (1 cycle)



(3-a) SEM image of sample N70-10 cycles



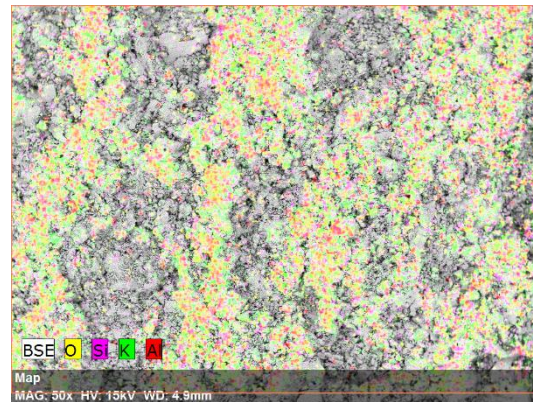
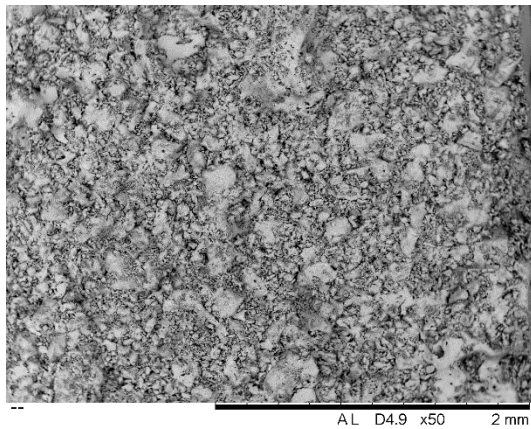
(3-b) EDS image of sample N70-10 cycles



(4-a) SEM image of sample N70-50 cycles

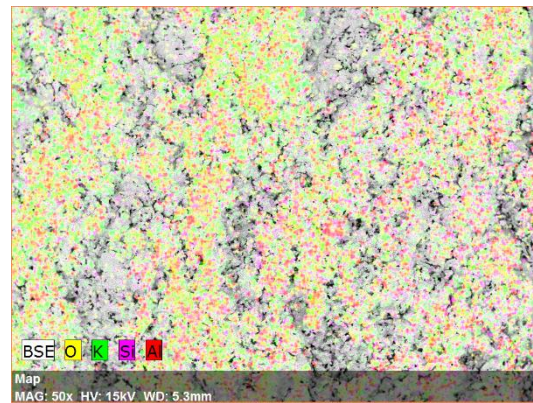
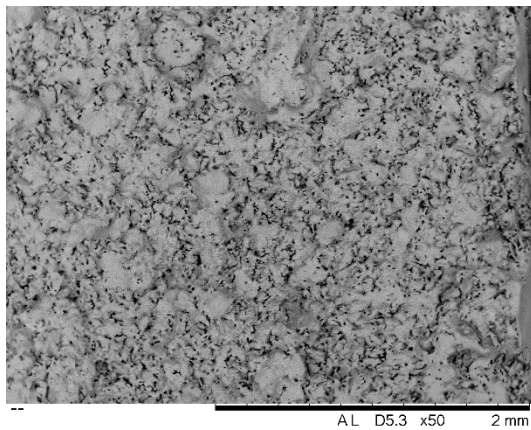
(4-b) EDS image of sample N70-50 cycles

Figure 32 SEM and EDS images of sample N70 with different thermal cycles



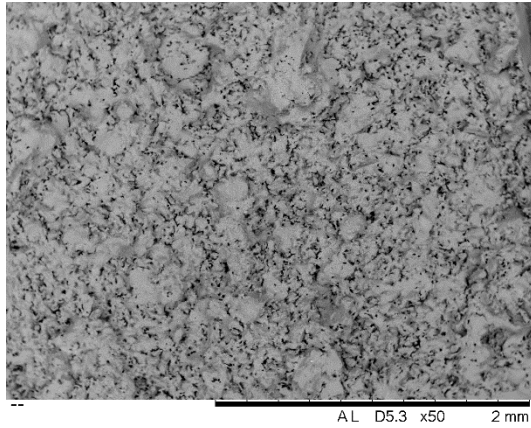
(1-a) SEM image of sample P70-green pellet

(1-b) EDS image of sample P70-green pellet

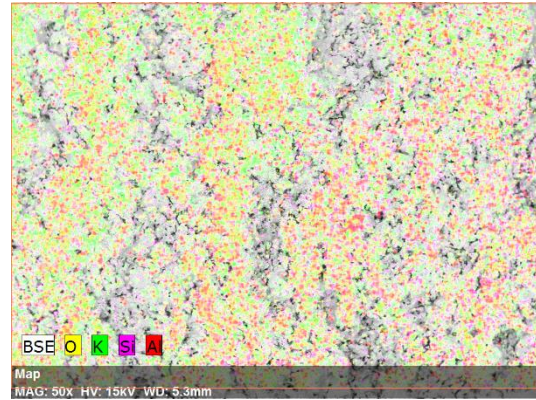


(2-a) SEM image of sample P70-sintered pellet (1 cycle)

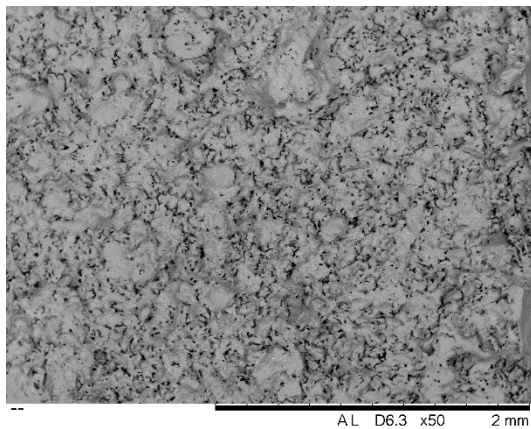
(2-b) EDS image of sample P70-sintered pellet (1 cycle)



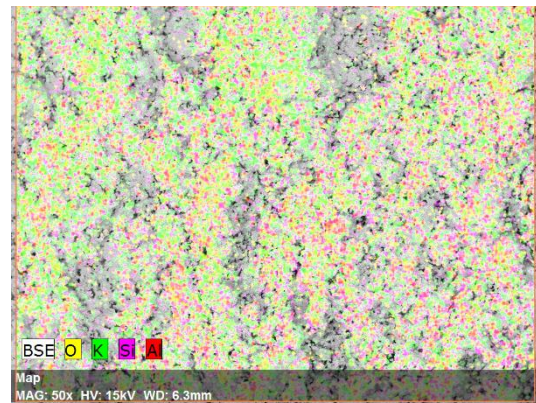
(3-a) SEM image of sample P70-10 cycles



(3-b) EDS image of sample P70-10 cycles



(4-a) SEM image of sample P70-50 cycles



(4-b) EDS image of sample P70-50 cycles

Figure 33 SEM and EDS images of sample P70 with different thermal cycles

4.3.3.2 Thermal conductivity

Figure 34 displays the thermal conductivity (λ) of the thermal cycled FSCPCMs. One can see that the thermal conductivity of the FSCPCM is dependent on the temperature and the amount of KNO_3 salt, which has been discussed in section 4.3.2.2. Table 14 shows the averaged thermal conductivity after 50 thermal cycles. One can see that the average thermal conductivity has been enhanced for all the FSCPCMs after 50 thermal cycles, with the increments from 0.38% to 4.85%. Therefore, the thermal cycling process does not degrade but slightly improve the thermal conductivity of FSCPCM. The slight improvement of thermal conductivity is likely attributed to the structural rearrangement during thermal cycling, which contributes to a denser and more homogeneous structure.

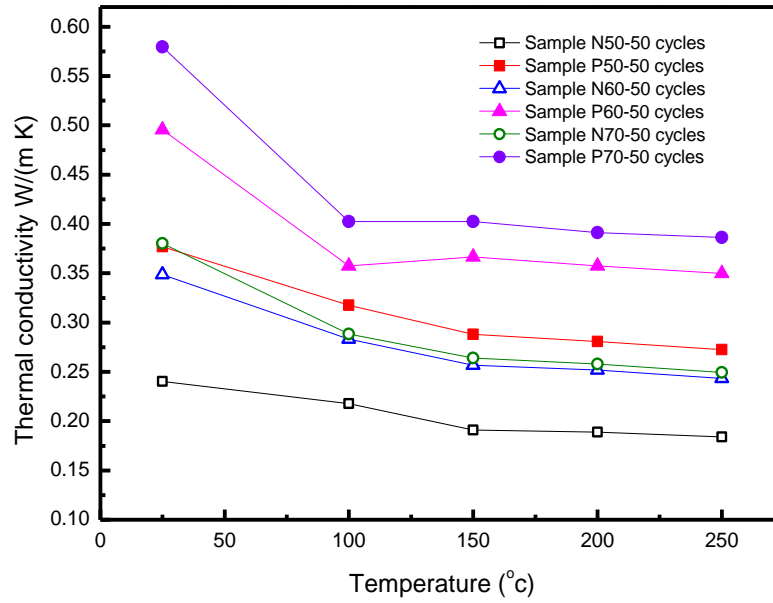


Figure 34 Thermal conductivity of the preheated/non-preheated sample before and after 50 times thermal cycling

Table 14 Average of the thermal conductivity for samples with 50 times thermal cycling (with SD)

sample	N50	P50	N60	P60	N70	P70
before cycling	0.19±0.005	0.30±0.002	0.27±0.001	0.37±0.002	0.28±0.002	0.43±0.006
after 50 times cycling	0.20±0.002	0.31±0.002	0.28±0.002	0.39±0.001	0.29±0.001	0.43±0.005
enhancement	4.85%	1.68%	1.06%	3.51%	3.57%	0.38%

4.3.4 Criteria of the preheating process for the FSCPCM

4.3.4.1 Infiltration of PCM during the preheating process

As discussed previously, the preheating process can contribute to a denser internal structure of the FSCPCM and an improvement in the physical and thermal properties. This section compares the porosity and pore distribution of FSCPCM powders that with and without preheating

process, to see if the melt PCM has been absorbed into the pores of the diatomite during the preheating process. Figure 35 displays the pore size distribution and Table 15 shows the pore geometry parameters. One can see that raw diatomite has a high porosity of 75.02% with a median pore diameter of 958.00 nm. When the raw diatomite is mixed with KNO_3 powders, the total porosity has been reduced due to the addition of non-porous content. From Figure 35, one can see that the pore size distribution of the sample without preheating (sample N60 and N70) is similar to that of diatomite. For the samples with preheating process (sample P60 and P70), their total porosity is less (3.12% - 10.06%) than that of the sample without preheating process. Besides, we cannot observe a large number of pores at $\sim 1,000$ nm (where the peak of diatomite is), but we can find a peak at $\sim 15,000$ nm. This indicates that the pores of diatomite have been occupied by melt salt during the preheating process. The pores at $\sim 15,000$ nm are generated during the preheating process, which is likely to be the voids inside the aggregates of FSCPCM powders. Therefore, we can confirm that the liquid PCM has been absorbed into the natural pores of diatomite during preheating, resulting in an overall porosity reduction.

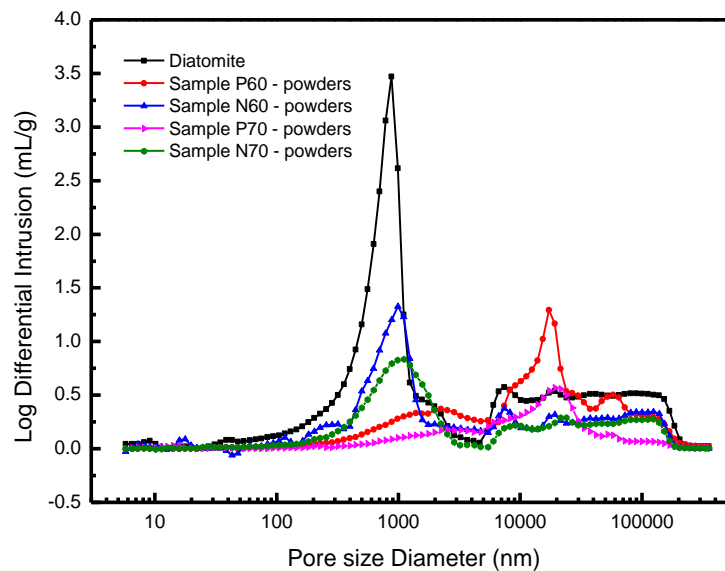


Figure 35 Pore size distribution of diatomite and mixed powders

Table 15 Pore size geometry of the diatomite and mixed powders

sample	Diatomite	P60	N60	P70	N70
Total Pore Area (m ² /g)	20.51	2.12	9.64	2.36	5.00
Median Pore Diameter (Volume, nm)	958.00	14526.60	1273.20	14174.40	1502.90
Average Pore Diameter (4V/A, nm)	411.60	2116.60	458.30	874.90	692.40
Porosity (%)	75.02	65.43	68.55	49.47	59.53

4.3.4.2 *Microstructure development of FSCPCM prepared by different fabrication methods*

(1) Conventional mix-sintering method without preheating

In the conventional mix-sintering process, powders of diatomite and salt are mixed and then compressed to pellets. The voids are reduced significantly during cold uniaxial compression, but cannot be eliminated completely; see Figure 36. When the green FSCPCM pellets are heated over the melting temperature of PCM, the melt PCM starts to spread and occupy the pores and interparticle voids due to capillary force. However, the melt PCM tends to occupy the small pores first, as this can reduce most of the overall interfacial energy of the composite. With the migration of the liquid PCM into small pores and voids, the places where solid PCM particles occupied are empty as shown in Figure 28 (e). In the liquid sintering process, the particle-liquid FSCPCM behaves like a highly viscous slurry which is rearranging gradually by the surface tension. Besides, the higher concentration of the particle content, the higher viscosity and lower rearrangement rate of the FSCPCM [162]. During the structural rearrangement, some small pores are eliminated and the total porosity has been reduced. However, some large pores cannot be eliminated at a low rearrangement rate. With the elimination of small pores, the viscosity of FSCPCM composite will increase further. This leads to a decrease in the rearrangement rate and a less possibility to eliminate large pores [162]. As observed in Figure 28 and Figure 32, some large pores still exist after

the FSCPCM undergoes sintering and thermal cycling processes. Therefore, the density and compactness of the FSCPCM are improved slightly after sintering due to the elimination of small pores, but the increase is not significant as large pores can hardly be removed due to low rearrangement rate.

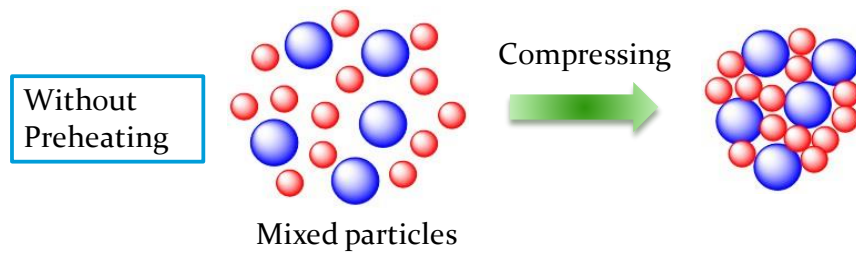


Figure 36 Schematic of the structure formation mechanism of FSCPCM without preheating process

(2) The modified mix-sintering method with preheating

In the modified mix-sintering method, the powder mixture of the FSCPCM is heated over the melting temperature of the salt before being sintered, which is the preheating process. In the preheating process, the melted PCM was absorbed into the porous structure or the interparticle voids of the supporting materials as discussed in section 4.3.4.1. Besides, the melted PCM spreads on the particle surface and behaves like a glue that can gather the particles into small aggregates; see Figure 37. When the preheated powders are compressed into a pellet, large voids are eliminated and the aggregates are compacted as shown in Figure 37. Only some small voids and pores are left. In the sintering process, the liquid PCM is trapped inside the pores of the supporting materials, which avoids the formation of large pores; see Figure 33. The small voids and pores inside the FSCPCM can be reduced by the structural arrangement during the sintering process, resulting in a slight reduction in porosity. Generally, with the additional preheating process, a dense structure can form and remain compacted after the sintering process.

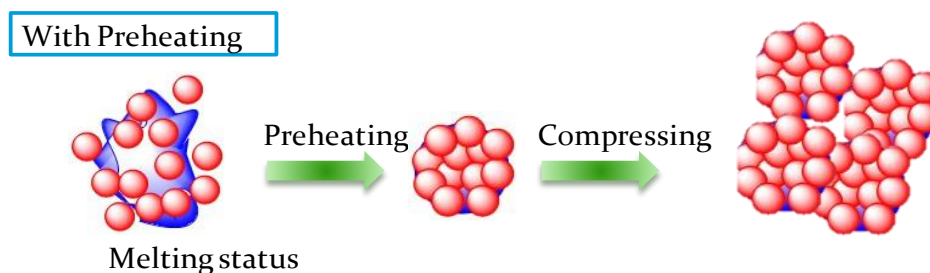


Figure 37 Schematics of the structure formation mechanism of FSCPCM with preheating process

4.3.4.3 Impacts of wettability, porosity on the effectiveness of the preheating process.

(1) The contact angle between the PCM and the supporting material

In previous discussions, it can be found that capillary force and surface tension play important roles in the structure development of FSCPCM during preparation. Capillary force is the intermolecular forces between the liquid phase and solid surface, which could either be an opposing or a driving force for fluid transportation according to the wettability between the liquid and the solid phase. Therefore, wettability is expected to affect the capillary force and hence the effectiveness of the preheating process. To study the impact of wettability, materials (substrates) have different wetting behaviour with KNO_3 are studied in this section. Ge et al. [32], [43] reported that graphite is not wettable with the carbonate salts. Hence, graphite is selected to study the wetting behaviour with salt KNO_3 . Besides, pure SiO_2 is selected as another material to study its wetting behaviour with KNO_3 , as diatomite is mainly consist of SiO_2 and they have similar chemical properties.

Figure 38 shows the contact angle between the graphite, SiO_2 substrates and molten KNO_3 . The tested temperature range is from 335°C to 375°C , which is above the melting point of KNO_3 . One can see that the contact angle of both substrates is decreasing with increasing temperatures due to the increase of the thermal motions of the liquid phase [163], [164]. This indicates that molten KNO_3 is more wettable at higher temperatures. Besides, we can see from Figure 38 that

graphite and SiO_2 present different wetting behaviours with molten KNO_3 . Graphite is considerably less wettable than SiO_2 with a contact angle from $\sim 80^\circ\text{C}$ to $\sim 100^\circ\text{C}$ (when contact angle $> 90^\circ$, it is regarded as not wettable). However, SiO_2 displays a good wettability with KNO_3 salt, showing a contact angle less than 60° and it has decreased to 26.86° when the temperature increases to 375°C .

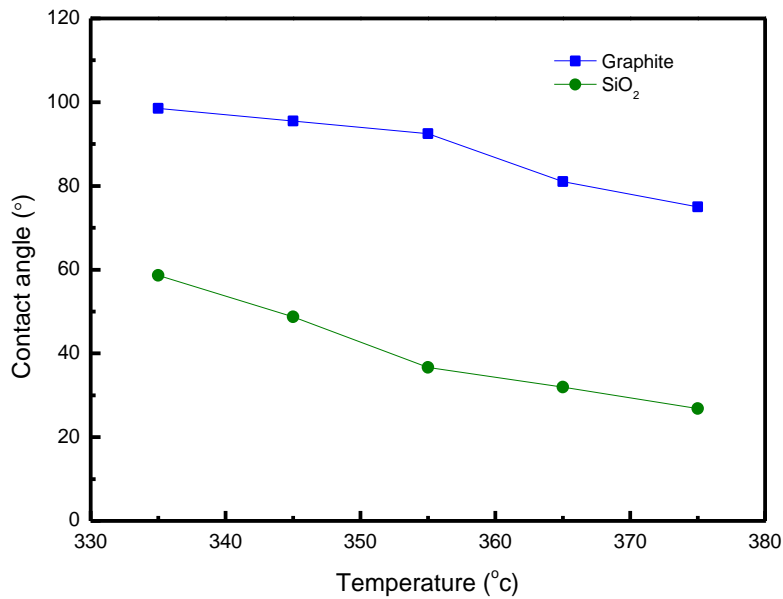


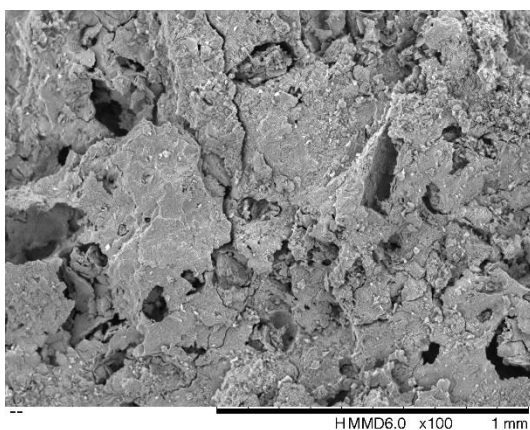
Figure 38 Contact angle of KNO_3 salt with different supporting materials

(2) Microstructure

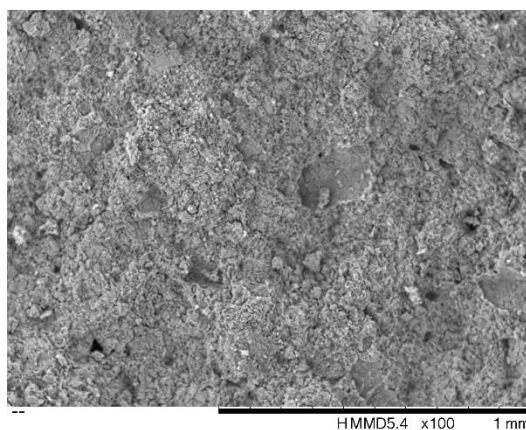
This section studies the morphology of KNO_3 /graphite composite and KNO_3 / SiO_2 composite, as its microstructure plays an important role in physical and thermophysical properties of the FSCPCM. The percentage of KNO_3 used in this section is 60 wt.%, as a higher percentage of KNO_3 could lead to the leakage of the KNO_3 -graphite composite PCM. Figure 39 and Figure 40 show the morphology of KNO_3 /graphite and KNO_3 / SiO_2 composites prepared by two fabrication routes. In Figure 39 (1-a) & (1-b), one can see that KNO_3 / SiO_2 composite with preheating process shows a less porous structure compared with the not-preheated KNO_3 / SiO_2 composite. The pores observed in

not-preheated $\text{KNO}_3/\text{SiO}_2$ composite shows a size up to ~ 4 mm, while only a few pores with a size less than ~ 50 μm can be observed in preheated $\text{KNO}_3/\text{SiO}_2$ composite. Under higher magnification, we can find no KNO_3 particles can be observed due to the infiltration of melted PCM into the interparticle voids, and the SiO_2 particles are bonded closely by the molten salt; see Figure 39 (2-a) and Figure 39 (2-b). Therefore, it can be found that the preheating process has helped the $\text{KNO}_3/\text{SiO}_2$ composite form a denser internal structure. Although the SiO_2 particles are non-porous, the molten KNO_3 can still infiltrate into the interparticle voids of the supporting materials during preheating and contributes to a denser structure.

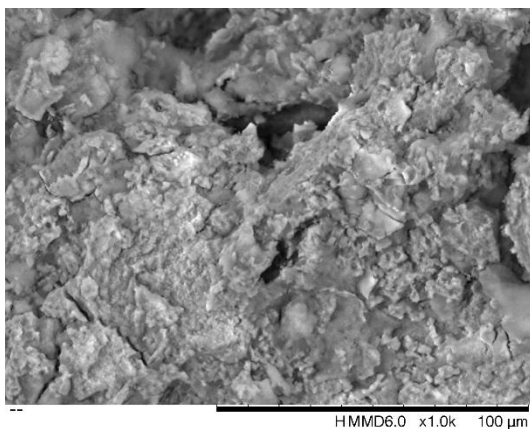
Figure 40 shows the morphology of graphite- KNO_3 composite prepared with and without preheating process. In Figure 40 (1-a) & (1-b), we can see no notable change of the morphology by using preheating process. Under higher magnification, one can see from Figure 40 (2-a) & (2-b) that KNO_3 particles are remained as grains and did not infiltrate into the interparticle voids. The graphite particle and KNO_3 particle are not bonded with each other; see Figure 40 (3-a) & (3-b). It is expected that the melted salt cannot penetrate into the interparticle voids due to the bad wettability with graphite.



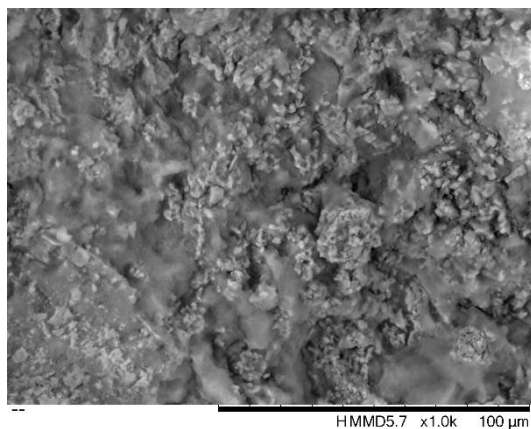
(1-a) SEM image of $\text{SiO}_2\text{-KNO}_3$ sintered pellet without preheating (X100)



(1-b) SEM image of $\text{SiO}_2\text{-KNO}_3$ sintered pellet with preheating (X100)

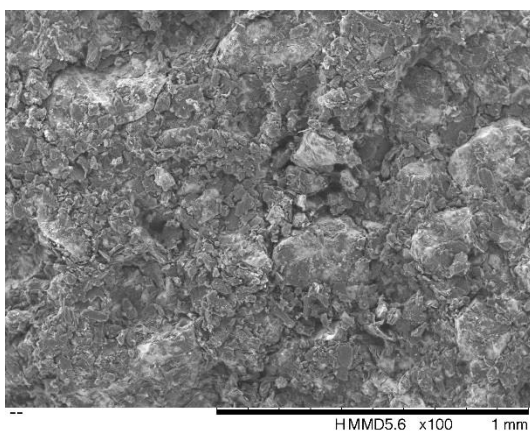


(2-a) SEM image of $\text{SiO}_2\text{-KNO}_3$ sintered pellet without preheating (X1000)

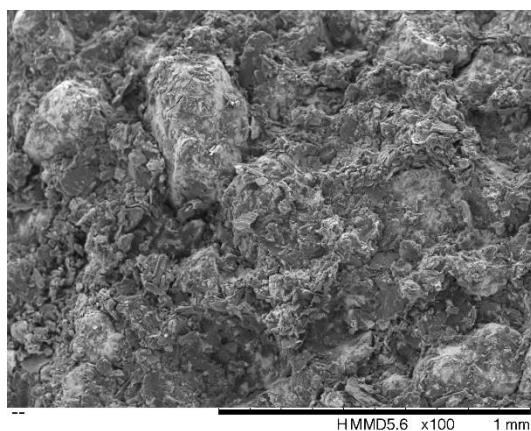


(2-b) SEM image of $\text{SiO}_2\text{-KNO}_3$ sintered pellet with preheating (X1000)

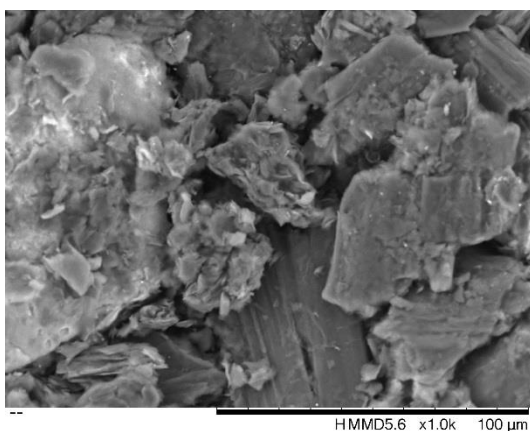
Figure 39 SEM images of sample $\text{SiO}_2\text{-KNO}_3$ with/without preheating



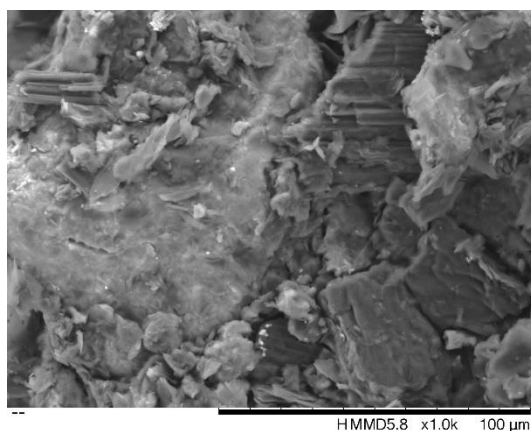
(1-a) SEM image of graphite- KNO_3 sintered pellet without preheating (X100)



(1-b) SEM image of graphite- KNO_3 sintered pellet with preheating (X100)



(2-a) SEM image of graphite- KNO_3 sintered pellet without preheating (X1000)



(2-b) SEM image of graphite- KNO_3 sintered pellet with preheating (X1000)

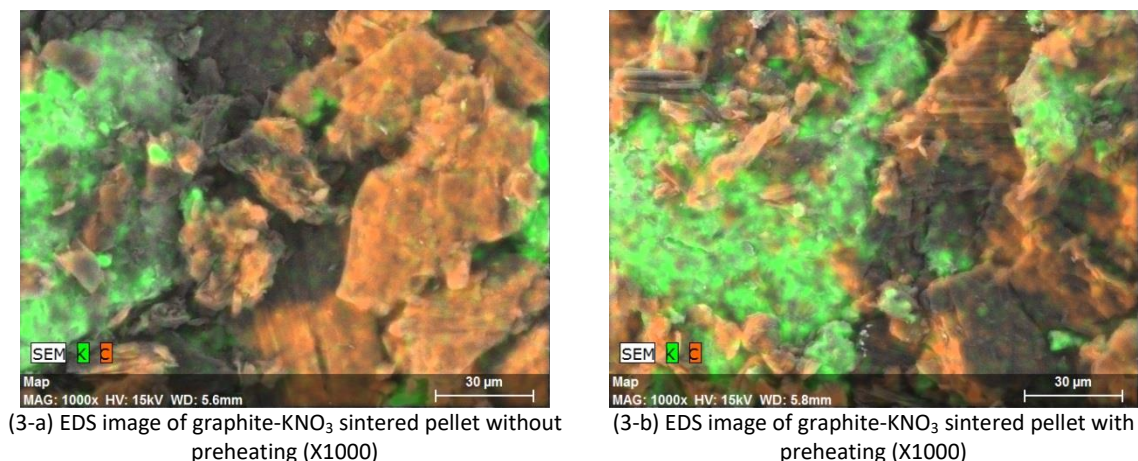


Figure 40 SEM and EDS images of sample graphite-KNO₃ with/without preheating

(3) Density and compressive strength

Figure 41 shows the density of the FSCPCMs prepared by two fabrication routes. One can see that when using graphite as supporting material, there is no notable change in density after using the preheating process. However, for KNO₃/SiO₂ and KNO₃/diatomite composites, there is a significant density increment. Figure 42 shows the compressive strength of the FSCPCM, which reveals the same trend as the density. One can find that the effect of the preheating process on the density and compressive strength of FSCPCMs is also dependent on the wettability between the PCM and the supporting material. A good wettability helps to form a compacted structure and hence results in improved physical properties.

It also can be found that the compressive strength of the graphite/KNO₃ composite is very low compared with other FSCPCMs. This is because of the non-wetting behaviour between graphite and KNO₃ particles, leading to a weak interparticle bonding force and hence a low compressive strength. Another finding from Figure 42 is that the compressive strength enhancement of the SiO₂-KNO₃ composite is higher than that of the diatomite-KNO₃ composite. This is likely due to the majority of molten salt has infiltrated into the interparticle voids rather than absorbed into the natural micropores of diatomite particles. The salt embedded inside the interparticle voids could act

as a binder to hold the structure, resulting in an increment in the rigidity and the compressive strength.

To conclude, it can be found that a good wettability between the liquid and solid phase is essential to obtain property enhancement when using the modified mix-sintering method. However, a porous structure for the supporting material is not essential, as the molten PCM could infiltrate into the interparticle voids during preheating which also contributes to the formation of a dense structure.

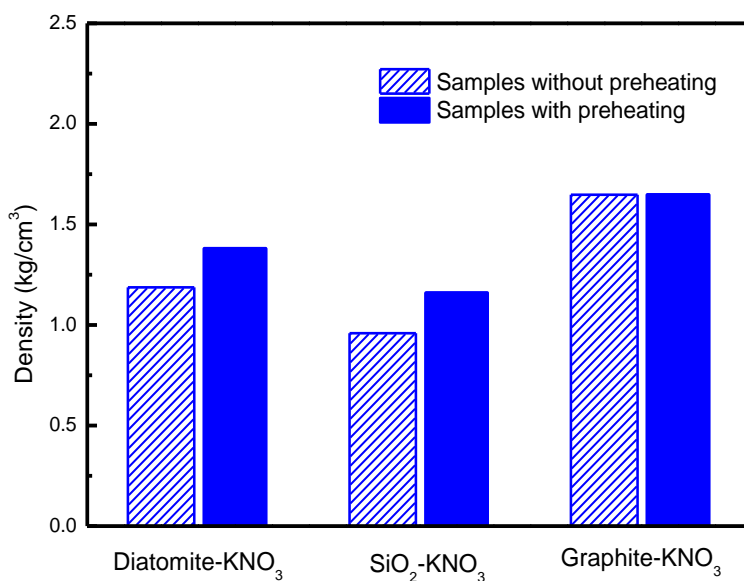


Figure 41 Densities of KNO₃ salt compound with different supporting materials

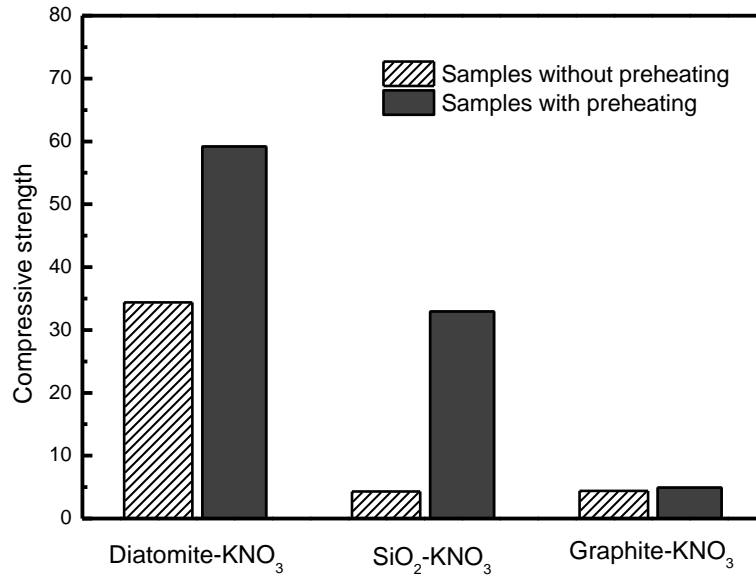


Figure 42 Compressive strength of KNO₃ salt compounded with different supporting materials

4.4 Summary

In this chapter, a modified mix-sintering method with an additional preheating process is proposed and investigated. A diatomite-KNO₃ FSCPCM was prepared by the modified fabrication method and the conventional mix-sintering method. Physical properties, thermal properties and thermal cycling stability of the prepared composites are characterized to investigate the impacts of the preheating process. In terms of the physical properties, it can be found that the improvements for using the modified mix-sintering method are notable. The density has enhanced significantly (~20%), as well as the compressive strength. The porosity has reduced by 8.75% to 9.18%. The less porous microstructure of the preheated sample was also observed by the SEM. In terms of the thermal properties, we found that the preheated sample presents a higher heat capacity, and this leads to a higher energy density for the FSCPCMs with preheating. The thermal conductivity of the preheated FSCPCM has also enhanced by 35.94% to 54.94% due to the reduction in porosity. After

50 times of thermal cycling, the thermal conductivity does not degrade but improves further with an increment from 0.38% to 4.85%. Meanwhile, the microstructure of the FSCPCM remains compacted and homogeneous after thermal cycling. Generally, the FSCPCM prepared by the modified mix-sintering method displays a better internal structure and better thermophysical properties.

The improvement obtained by mix-sintering fabrication method is explained by the microstructure development in the fabrication process. In the preheating process, it was found that the melted PCM had been absorbed into the porous structure of diatomite and also the interparticle voids due to the capillary force. After compression, a dense structure was obtained and this structure remains unchanged after sintering. However, through the conventional fabrication route, the FSCPCM has formed a porous structure after sintering. This is because the melted PCM infiltrate into the small pores preferentially and some large pores have formed at where PCM particles occupied previously. After thermal cycling, the microstructure of the FSCPCM remains unchanged.

Besides, it is found that the wettability between the molten PCM and the supporting materials plays an important role in the structure formation of the FSCPCM. A good wettability helps to form a compacted structure and hence results in improved physical properties. This was verified by the KNO_3 /graphite composite and $\text{KNO}_3/\text{SiO}_2$ composite, which has different wetting behaviour between the molten KNO_3 and the supporting materials. However, a porous structure for the supporting material is not essential, as the molten PCM could infiltrate into the interparticle voids during preheating which also contributes to the formation of a dense structure. This was verified by the KNO_3 /diatomite composite and the $\text{KNO}_3/\text{SiO}_2$ composite.

In summary, the modified fabrication method has been proven to enhance the physical and thermal properties of the FSCPCMs with good wetting behaviour between the PCM and the

supporting material. This modified mix-sintering method could contribute to a better performance of the FSCPCM in practices. Moreover, from the samples being studied, sample N70 presents the best performance in terms of the microstructure, energy storage density and the thermal conductivity.

5 Results and discussions (II): a continuous hot-melt extrusion method – the effects of processing conditions on flow stability and rheological behaviour

5.1 Introduction

Hot-melt extrusion method is an advanced and efficient fabrication method which combines compounding, compression and shaping process in one step. It has advantages of large yield capability due to the continuous fabrication process and automatic operation. Hot-melt extrusion method has been gradually used to prepare polymer-based composite PCM to address the challenge of low scalability of FSCPCM fabrication. However, few studies have revealed the features of the extrusion process. The relationship between the processing parameters and the properties of the composite PCM has not been considered.

In this chapter, a novel HDPE-pentaerythritol (PE)-graphite composite PCM was formulated and firstly extruded by a single screw extruder. The optimal composite formulation was determined by considering the maximum PE particle loadings that can be extruded continuously and steadily, as the higher loading of PE particles could contribute to the higher thermal storage capacity. Effects of different processing parameters on the extrusion stability, rheological behaviour and the exudate morphology were investigated. For instance, the effect of particle size, extrusion speed and processing temperature on the extrusion behaviour were studied. A better understanding of the extrusion behaviour of these materials is essential to obtain a stable extrusion process and for further application of industrial-scale production.

5.2 Fabrication

5.2.1 Sample formulations

A polymer-based FSCPCM was formulated and extruded in this work. HDPE is widely used as the matrix as well as PCM due to its high-temperature stability and low cost. However, the disadvantage of HDPE or to most of the polymers is the low thermal conductivity and the low energy storage capacity. PE (Pentaerythritol) is a kind of polyalcohol that could undergo a solid-solid phase change process associated with the heat energy absorption and release, namely solid-solid PCM. In this work, PE is used as an effective additive to improve the energy storage density of the polymer, as PE presents a much higher latent heat than HDPE. Besides, to address the low thermal conductivity issue of the HDPE, graphite is used as the thermal conductivity enhancers adding into the composite. As graphite does not undergo phase transition during energy charging/discharging processes, the addition of graphite would decrease the total energy density of the composite. Therefore, ~10 wt.% graphite is always being used in the literature [132] [110], which is a trade-off between the increase of thermal conductivity and the loss of energy density. The formulations of the CPCM studied in this work are shown in Table 16.

Table 16 Formulation of the composite PCM for extrusion

Formulations (wt%)	S30	S40	S50	S60
Pentaerythritol (PE)	30	40	50	60
High-density polyethylene (HDPE)	60	50	40	30
Graphite (Cg)	10	10	10	10

PE as the main raw material is received in large granules from the manufacturer, and it needs to be ground before adding to the extruder. This work used a shear mill with different sieves

(1 mm, 0.5mm, 0.25mm, 0.12mm, 0.08mm) to reduce the particle size of PE. Due to the continuous fabrication process of extrusion, a large amount of sample needs to be prepared for fabrication. Each time 1 kg of sample mixture are prepared and added for extrusion. Depending on the consumption rate of the sample, another batch (1 kg) of sample is prepared to top up the feed hopper. Therefore, it is not realistic to control the particle size of PE precisely, hence the particle size is only controlled under a certain size by the sieve. To study particle size distribution, the particle ground under the sieve size of 1 mm, 0.5mm, 0.25mm, 0.12mm are measured and shown in Table 17. $d(0.1)$ means 10 wt.% of the particles have a size below this value, while $d(0.5)$ is also termed as mass median size. In the followed sections, the PE particle sieved under the size of 1mm is termed as PE-1mm. We can see from Table 17 that the particle size is reduced with decreasing sieve size. Besides, the difference between PE-0.25mm and PE-0.12mm is not significant. In the following section, the size effect of PE particles on extrusion behaviour is discussed. In terms of graphite particles, the as-received graphite showing a particle size distribution similar to PE-0.05 mm. As the amount of graphite particles used is small, the size effect of the graphite particle is not considered in this work.

Table 17 Particle size distribution of the PE particles with different size of sieves

Sample (um)	PE-1mm	PE-0.5mm	PE-0.25mm	PE-0.12mm	graphite
d (0.1)	9.822	7.316	4.367	3.523	8.92
d (0.5)	68.133	37.612	18.344	14.188	30.673
d (0.9)	210.551	121.961	67.87	60.6	74.496

5.2.2 Processing conditions

The adequate amount of each component is weighed according to Table 16. Then, the powder is hand-mixed for ~5 minutes to get a uniform mixture before loading into the feed hopper.

In the extrusion process, the material mainly undergoes four regions (shown in Figure 43): 1. materials feeding region, where the materials are fed into the extruder screw channel from the feed hopper by gravity; 2. solid conveying region, where the material is in solid-state and the flow is dragged forward by the frictional of the barrel and screw surfaces; 3. plastination and compression region, where the material is partially melted and the molten phase is accumulated and compressed; 4. melt conveying region, where the flow is completely melted and squeezed through the die to form different shapes. When the melt materials are extruded out from the die dead, the pressure of the flow from upstream should overcome the resistance at the die head. In the extrusion of the HDPE/PE/Cg composite PCM, the extrusion speed and the temperature of the heating zone are controlled. The studied extrusion speeds are 5 rpm, 10 rpm, 15 rpm, 20 rpm, 25 rpm, and 30 rpm. As the extrusion temperature should above the melting point of the polymer ($\sim 133^{\circ}\text{C}$), the studied heating temperatures of the extruder (Zone 1 to 6 are the same; see the place of heating zone 1 to 6 in Figure 22) are 150°C , 160°C , 170°C , 180°C .

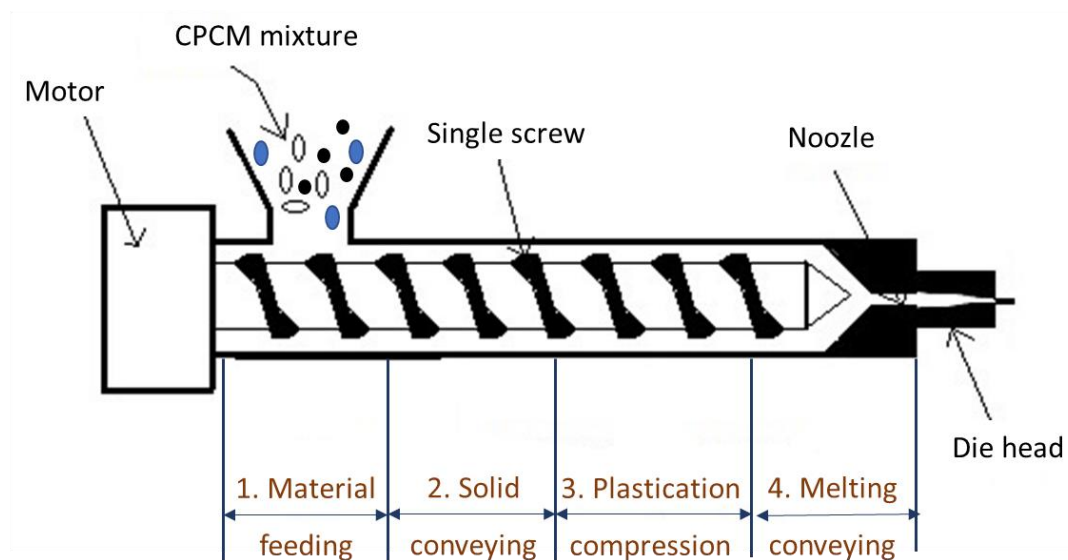


Figure 43 Schematic of the extrusion process

5.2.3 Characterisation methods

To clarify the measurement conditions, test range and the repetitions, the method details are shown in Table 18.

Table 18 Measurement methods and repetitions

Instrument and property	Measurement method	Data acquisition	Sample shape/ amount	Repetitions
Rheometer: Storage/loss modulus	0.628 to 628 rad/s at an amplitude of 1% and a gap of 1mm; 1 L/min air flow.	whole range	~1.5 g	each sample conduct 1 measurement
Extruder (Capillary die): Apparent shear viscosity	1 rpm to maximum rpm at a increasing rate of 1 rpm; N ₂ flow.	acquire 1 result at each rpm	~500 g	each sample conduct 1 measurement

5.2.4 Effect of the mass ratio of the PE fillers on the extrusion and rheological behaviour

5.2.4.1 Extrusion throughput and extrusion stability

(1) Extrusion of neat polymer (HDPE)

Neat HDPE was firstly extruded at 150 °C to understand its extrusion behaviour. Figure 44 displays the pressure profile at the die head when the neat HDPE was extruded at different speeds. The outlet pressure is found to increase with the increasing extrusion speed, and it keeps stable when the extrusion speed remains unchanged. Figure 45 shows the average mass output and pressure at different extrusion speeds. It can be found that the output is almost increasing linearly with the extrusion speed. The outlet pressure also increases with the increasing extrusion speed, but the increment is lower at a higher extrusion speed. For instance, the pressure increment from 5 pm to 10 pm is 8.85 bar, while the pressure increment from 25 pm to 30 pm is only 4.86 bar. This trend agrees with the findings reported by Xiao et al. [165], who also found that the pressure does not increase linearly with the increasing shear rate. This is because the non-Newtonian rheological

behaviour of HDPE, its apparent shear stress the associated pressure drop ($\Delta p = \sigma \cdot (4L/D)$, where Δp represents the pressure drop along the capillary die (MPa), σ represents the apparent shear stress (MPa), L/D is the length-to-diameter ratio of the extruder) does not increase linearly with the shear rate [166]; see the detailed rheological behaviour of HDPE discussed in section 5.2.4.3.

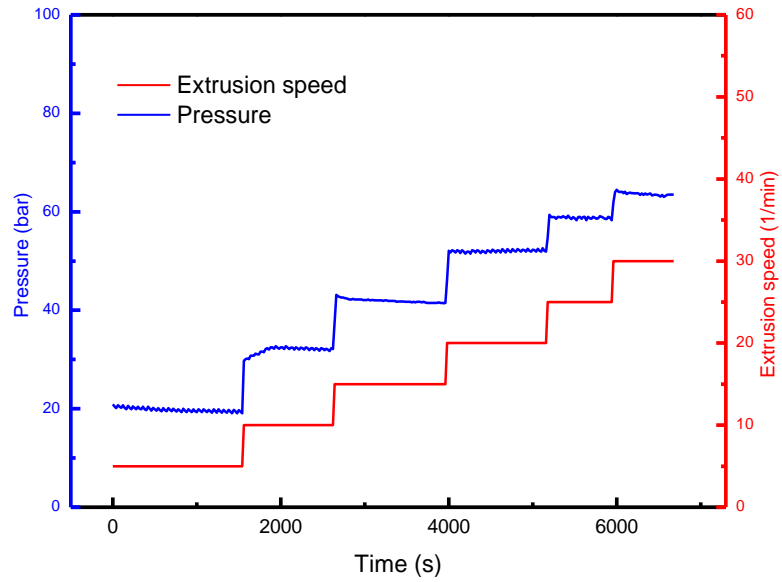


Figure 44 Pressure profile when extruding the neat HDPE at different extrusion speeds

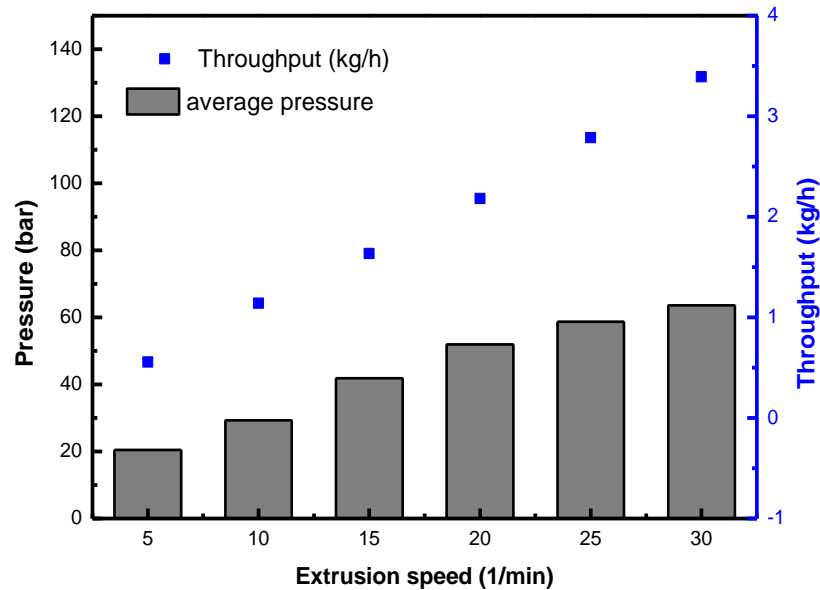
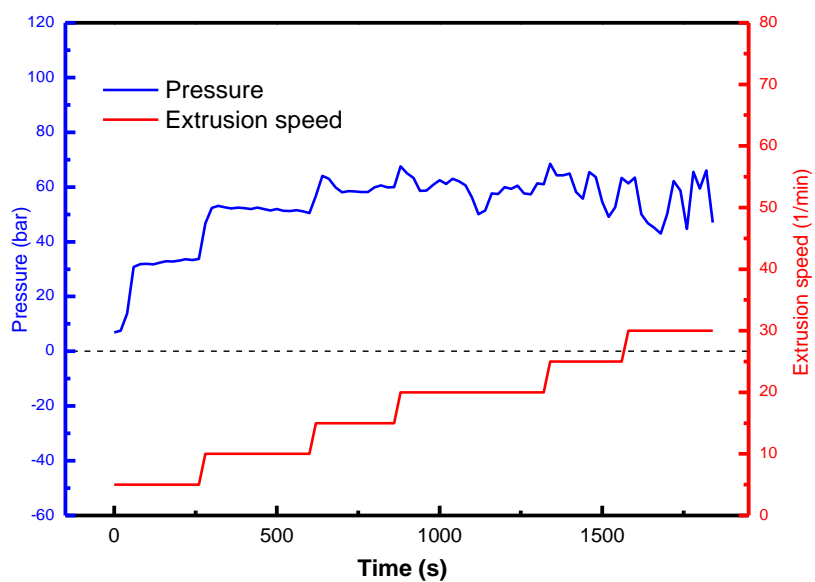


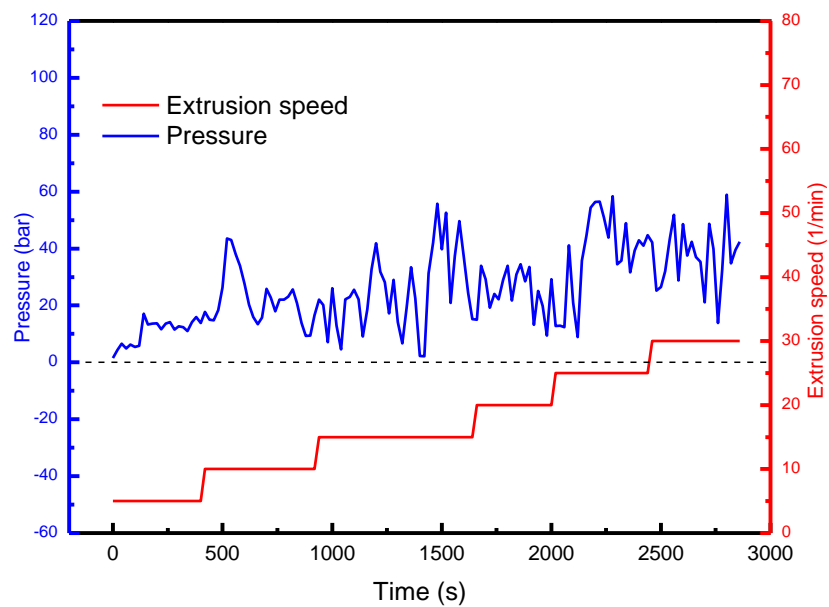
Figure 45 Averaged pressure and output at different extrusion speeds of neat HDPE

(2) Polymer-based FSCPCMs with different percentage of particles fillers

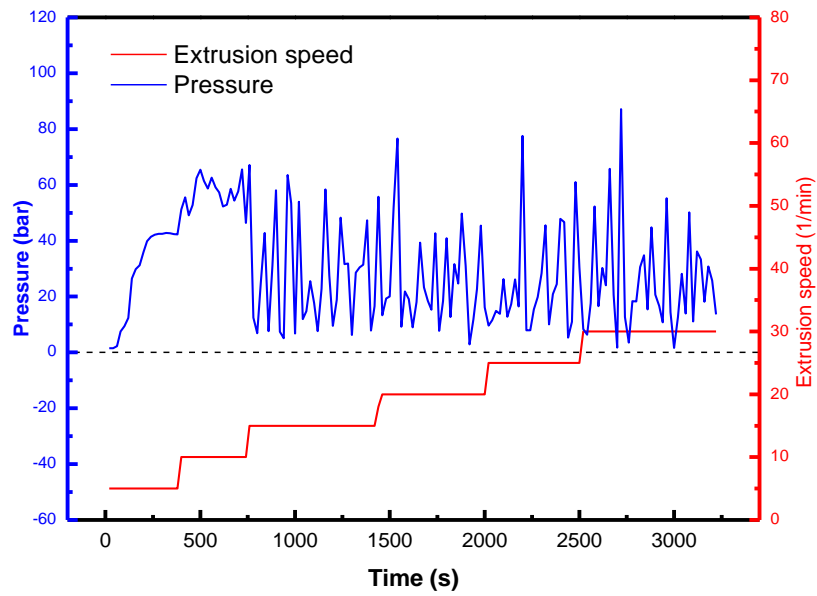
This section is to study the extrusion behaviour of the FSCPCM with different mass ratios of PE. The FSCPCMs are extruded at 150°C with a rate from 5 rpm to 30 rpm. Figure 46 displays the pressure profile of different formulations. One can see that the FSCPCM with 30 wt.% PE fillers (sample S30) shows a stable pressure profile at low extrusion rate. Small irregular pressure fluctuation occurs when rotation speed exceeds 20 rpm. Sample S40 (40 wt.% PE) presents a more pronounced irregular pressure fluctuation than sample S30, and the onset of the instability moves forward to an extrusion rate of 5 rpm. For sample S50 and sample S60, the pressure oscillates cyclically. One can find that the amplitude increases when the amount of PE increases and the frequency of the oscillation increases with increasing extrusion rate for sample S60. Besides, the pressure of sample S60 dropped to almost 0 MPa between each pressure oscillation, indicating no pressure from the upstream to squeeze the material out. This is also observed in practice that no material is extruding out when the flow pressure is 0 MPa. Therefore, the extrusion process is discontinuous when the mass ratio of PE fillers reaches 60 wt.%.



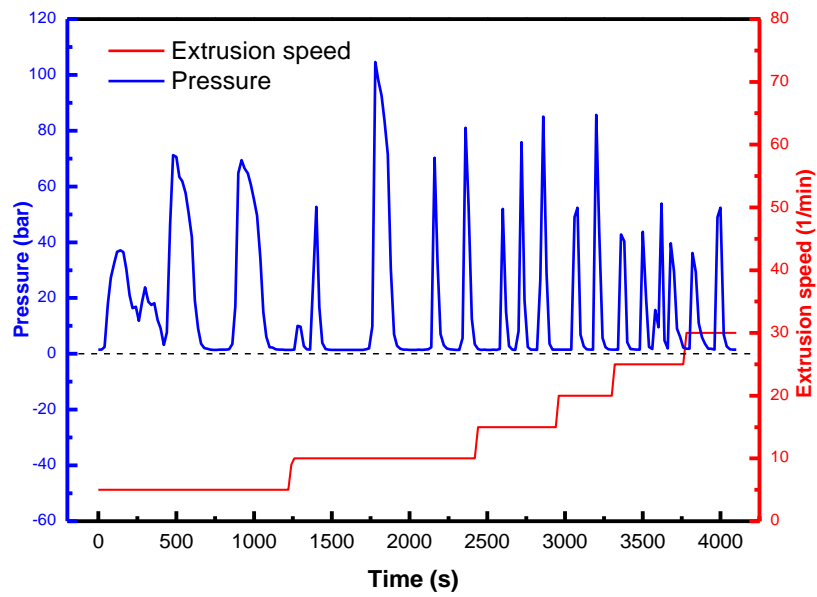
(a) Pressure profile of composite PCM with 30% fillers (sample S30)



(b) Pressure profile of composite PCM with 40% fillers (sample S40)



(c) Pressure profile of composite PCM with 50% fillers (sample S50)



(d) Pressure profile of composite PCM with 60% fillers (sample S60)

Figure 46 Pressure profile when extruding composite PCMs at different extrusion speeds

Mass throughput of the FSCPCM prepared at different extrusion rate was measured and shown in Figure 47. As the throughput of material fluctuates accordingly with the pressure oscillation, the measured throughput was averaged and the fluctuations were reflected by the standard deviations (error bars). One can see from Figure 47 that the throughput is generally increasing with the extrusion rate for most formulations. Besides, the throughput of the FSCPCM is decreasing with the increasing loading percentage of PE. Sample S30 has a similar trend as the neat HDPE when the extrusion speed is less than 20 rpm. With a higher extrusion speed, the throughput of sample S30 increases slower due to the pressure fluctuations (see Figure 46a). Sample S40 and S50 present a lower average throughput than sample S30. Sample S60 displays the lowest average throughput and highest uncertainties due to strong pressure oscillations and discontinuous flow. Besides, the increase of extrusion speed does not promote the mass throughput due to the increased discontinuity at a higher extrusion speed. Therefore, one can find that extrusion instability has a strong negative impact on the throughput and it also causes difficulty in the process control.

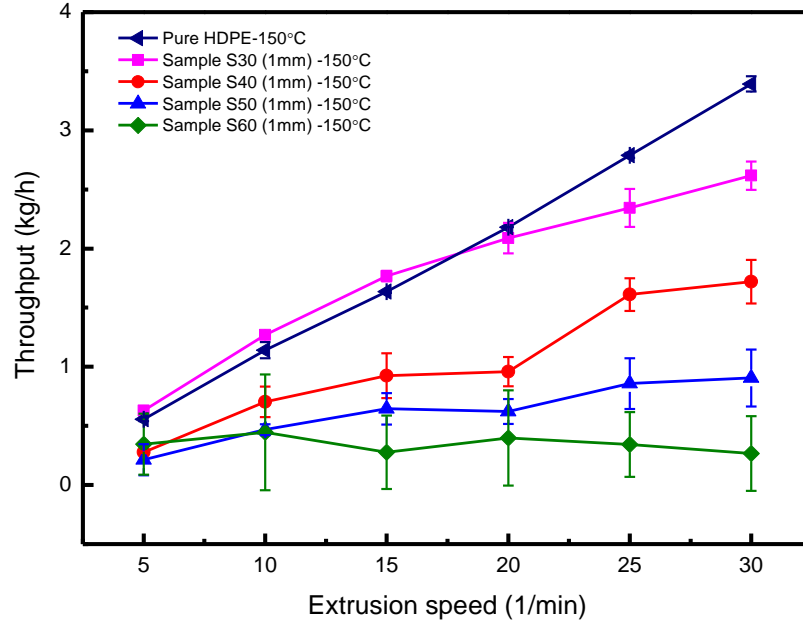


Figure 47 Throughput of the CPCM (S30-S60) at different extrusion rates

5.2.4.2 Surface distortion

(1) Flow instability and surface distortion

From the pressure profile of the extrusion flow, we can find that the extrusion process becomes unstable when its rate exceeds a certain value. The instabilities were often found in polymer melts and plastic composites, e.g. wood plastic composite [167]–[169], and are termed as extrusion defects or melt fractures. The extrusion defects have been reported for over forty years, but these phenomena are still not fully understood and some reasons remain unclear [170]. The extrusion defects always along with observable distortions, either affecting the surface or the volume of the extrudates.

HDPE is a typical linear polymer, unlike branched polymers (eg. LDPE), it often has a discontinuous flow curve (see Figure 48) and three regimes of instabilities with the increasing flow rate: 1) sharkskin defect; 2) oscillating defect or stick-slip defect; 3) smooth or chaotic. Sharkskin

defect is the first instability that occurs during extrusion (Branch I). This defect presents a regular sharkskin distortion on the surface, but no pressure oscillation is observed. This defect often starts with a matt or coarse surface due to small amplitude of sharkskin, and then develops gradually as the flow rate increases. When keep increasing the flow rate above a critical flow rate (Q_1 , g/s), the pressure is no longer stable. The pressure oscillates periodically (between P_1 and P_2 , MPa, see Figure 48) and the flow rate jumped accordingly with the pressure although the imposed flow rate is constant. In the oscillating region, the extrudates alternately present either distorted surface or smooth surface in an oscillation cycle. When the flow rate exceeds the second critical condition (Q_2 , g/s), the pressure becomes stable again (Branch II) but the extrudate is chaotic and may exhibit volume fracture. Some researchers observed that the extrudate may become smooth before it turns to chaotic [170].

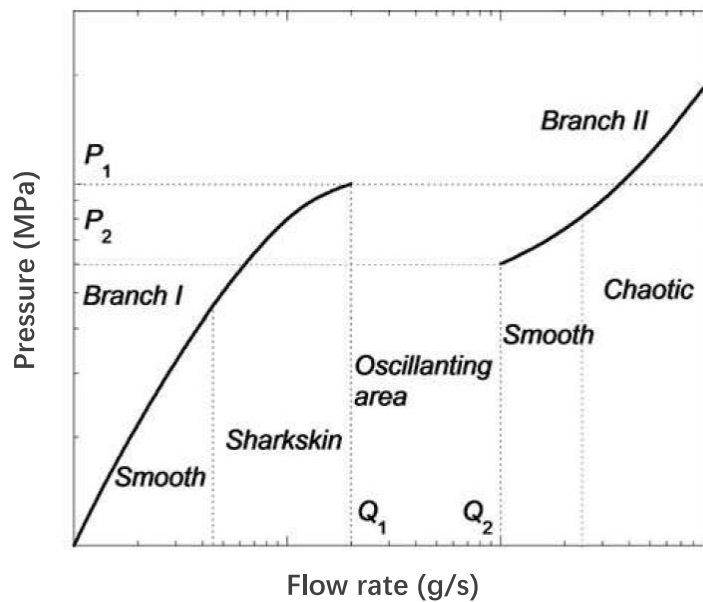







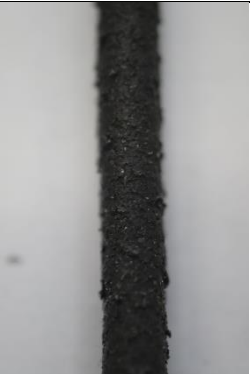






Figure 48 Discontinuous flow curve and characteristic defects of a linear polymer (HDPE) [170]

In terms of the pressure curve of FSCPCM, we can find that most FSCPCMs have undergone stable extrusion at the rate of 5 rpm and then to oscillating extrusion when the rate increases,

excluding sample S60 oscillates from 5 rpm. Surface morphology of the extrudate processed at the lowest rate (5 rpm) and the highest rate (30 rpm) is observed to study the extrusion instabilities; see in Figure 49. The reason for using 5 rpm and 30 rpm to compare is that 5 rpm is the lowest rate which can show the initial surface defects during extrusion, and 30 rpm is the highest rate where the surface defect is fully developed and can be observed in all samples. Sample S30 to S50 all present a consistent appearance morphology at the rate of 5 rpm which in agreement with the stable pressure curve. Sample S30 presents the least distorted surface, no clear signs for instabilities at 5 rpm. When the rate increases to 30 rpm, its surface gets coarser and presents a slight sharkskin defect. Sample S40 and S50 present a typical sharkskin defect with surface tearing at 5 rpm. While at 30 rpm, their surface evolves from the coarse surface or slight sharkskin defect to the severe sharkskin defect, and then back to the surface tearing or slight sharkskin defect periodically. The surface changes regularly along with the pressure fluctuations, indicating the oscillating defect at 30 rpm. Besides, one can find the sharkskin distortion is getting pronounced with the pressure oscillation intensifying: sample S30 presents a slight sharkskin defect, sample S40 and S50 present severe sharkskin defects or “bamboo-like” defects. Sample S60 presents a surface evolution at the rate of 5 rpm. The surface evolution is similar to that of sample S40 at high extrusion speed (30 rpm), so the images are not displayed in Figure 49. When the rate increases to 30 rpm, sample S60 present a volume distortion at the highest pressure fluctuation. The volume distortion is the melt fracture that involves the whole volume of the extrudate, different from surface-related distortion like “sharkskin” [171].

Generally, by the pressure curve and extrudates morphology obtained, two extrusion defects can be identified for the FSCPCMs while increasing the extrusion rate from 5 rpm to 30 rpm: sharkskin defect and oscillating defect. The chaotic regime cannot be reached due to the limitation of the pressure transducer. In the next sections, these instabilities are detailed explained.

Sample S30 (1mm)-150°C			
5 rpm	30 rpm		
 coarse surface	 slight sharkskin	 slight sharkskin	 slight sharkskin
Sample S40 (1mm)-150°C			
5 rpm	30 rpm		
 sharkskin	 sharkskin	 "bamboo-like" defects	 slight sharkskin
Sample S50 (1mm)-150°C			
5 rpm	30 rpm		
 sharkskin	 sharkskin	 "bamboo-like" defects	 slight sharkskin





Sample S60 (1mm)-150°C			
5 rpm	30 rpm		
			
sharkskin (slight sharkskin and severe sharkskin appears alternatively)	sharkskin	volume distortion	slight sharkskin

Figure 49 Surface morphology of different samples at different extrusion rates

(2) Sharkskin defect

Sharkskin defect is the first defect observed in this study. It is also widely observed in the extrusion of linear polymer and wood-plastic composites [167]–[169]. When the sharkskin starts, the surface becomes matt due to small amplitude at the beginning. While the defect is developing, regular waves appear on the surface gradually. The amplitude of the sharkskin varies from a few microns ($\sim 1 \mu\text{m}$) to several micrometres with the increase of flow rate. The onset point of sharkskin often cannot be identified by visual observation, thus several techniques are used to determine the onset of the defect (the critical flow rate), such as microscopy observation, profilometry and image analysing. In this study, we can see that an observable sharkskin defect appears when the slowest extrusion rate (5 rpm) is applied.

The mechanism of the sharkskin has been interpreted since it was discovered. It is now unanimously accepted that the sharkskin defect originates at the exit of the die. One possible

mechanism that accepted by most researchers is: the large elongation stress generated at the die exit due to velocity gradient, giving rise to the rupture of the extrudate surface [170]. Burghilea et al. [172] measured the flow field of the polymer melt at the die exit by laser-Doppler velocimetry (LDV), which experimentally verifies the existence of velocity gradient and elongation stress at the die exit. There are also some other mechanisms proposed by researchers, e.g. the oscillation of the polymer melt along the die wall, and the formation of the vortex at die exit, etc., but these explanations are currently lack of experiment proofs [170].

In terms of the FSCPCM, the sharkskin defect is also attributed to the elongation stress generated at the die exit. The difference between HDPE and the FSCPCM is: the FSCPCM melt consists of a continuous phase (polymer melt) and also a dispersed phase (particle fillers). The addition of PE particles reduces the elongation strength of the polymer melt, as the adhesion force between PE particles and HDPE polymer melt is weaker than the neat polymer (polymer chains are easy to get entangled with each other). When the elongation stress at die exist exceeds the melt strength of the FSCPCM, surface distortion appears. As the melt strength of the FSCPCM gets weaker with an increasing percentage of PE particles, the surface distortion is also getting more pronounced as found in Figure 49.

The schematic diagram showing the development of sharkskin defect is displayed in Figure 50 [173]. When the FSCPCM was extruded through the die, there is a velocity gradient at the cross-section of the die head. The melt adjacent to the wall (arrow 1) moves very slow or stay still, while the melt at the centre (arrow 2) has the highest velocity as shown in Figure 50 (A). Then, the outer layer of the melt (arrow 1) is stretched due to the velocity gradient. Due to the poor adhesion force between the PE particles and the polymer chains, the surface is likely to crack at the interface between the PE particles and the polymer chains when the extension stress exceeds the adhesion

force (as shown in B). Then the cracks grow and propagate on the surface as the melt at the centre is continuously coming out of the die head. Until the stress has been released, the cracks stop propagating (as shown in C) and a helical surface distortion is formed. With the extrusion process ongoing, the extension stress builds up again and a new crack is brewing (arrow 4, as shown in D). To conclude, sharkskin defect happens when the velocity gradient at the cross-section is relatively high and the extension stress exceeds the melt strength.

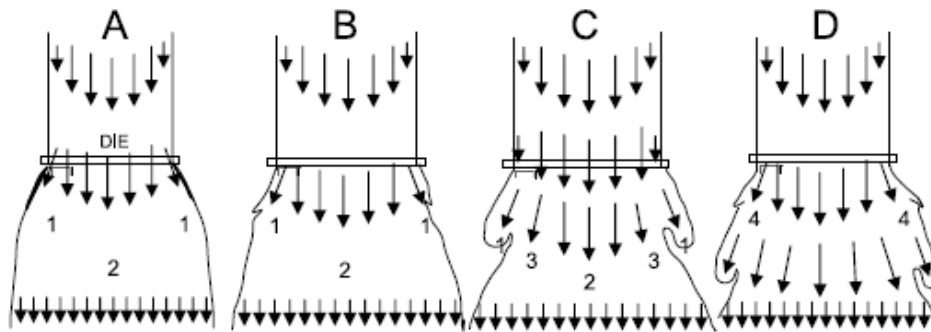


Figure 50 Schematic diagram showing the development of sharkskin defect [173]

(3) Oscillating defect

The second instability observed in the extrusion of FSCPCM is termed as the oscillating defect. In this regime, the pressure oscillates periodically, and the extrudate appears alternately in distorted surface or smooth surface along with the pressure oscillation. Also, the exit flow rate jumps with the pressure oscillation. Figure 51 displays the surface evolution of sample S50 in a single pressure oscillation cycle. One can see the oscillation period is ~ 100 s. At the beginning of the cycle, the pressure increases and the elongation stress accumulated in the compression phase. The surface distortion is getting pronounced due to the accumulated elongation stress. It is also observed that the exit flow rate increased very slightly in the compression phase, but it is always much lower than the imposed flow rate. When the pressure reaches the limit, the exit flow rate suddenly jumps to maximum (far beyond the imposed flow rate), which indicates a transition from the compression

phase to the relaxation phase. In the relaxation phase, the pressure and the exit flow rate decreases gradually, indicating a release of elastic energy [174], [175]. The elongation stress has also been released during the relaxation phase. Subsequently, a smooth surface appears while the pressure is decreasing. When the pressure reduces to the minimum, the exit flow rate jumps back to a minimum and another oscillation cycle begins. The observed oscillating instability and flow discontinuity agree with other findings observed in wood-filled polyethylene melts and neat polyethylene [174]–[177]. However, the period and amplitude of the pressure oscillation varies with different materials and different geometry of the die [169], [178].

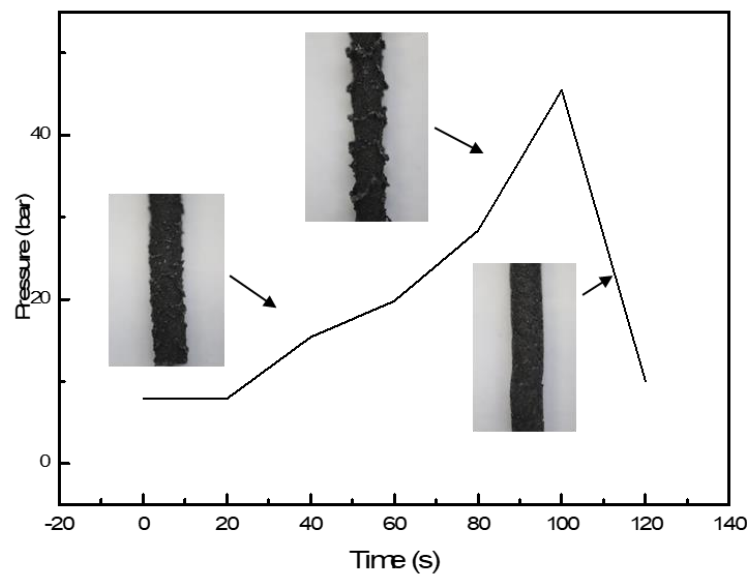


Figure 51 Evolution of the surface in a single pressure for sample S50 (1mm)

The oscillating defect and the discontinuous flow is generally observed in linear polymers. In terms of the mechanism of the oscillating defect, it was first explained by the viscoelastic property of the polymer in 1980. However, this interpretation is unable to explain all the experimental observations. Then, another mechanism is proposed and now accepted by most researchers, which

is the wall slip phenomenon. It is observed that the polymer melt intermittently fails to adhere to the wall surface of the extruder. Figure 52 shows the radial velocity profile changes from steady flow to unsteady flow. Steady flow is normally present at a relatively low extrusion rate, where the polymer chain can stick at the wall surface and the velocity of the melt at the wall surface is zero; see Figure 52 (a). When the shear rate exceeds the maximum static friction force at the wall interface, the polymer chains partially slip from the wall surface; see Figure 52 (b). As a result, the pressure shows small-amplitude oscillation and the surface shows a typical 'sharkskin' distortion. When the shear rate keeps increasing, a whole wall-slip condition occurs at the surface; see Figure 52 (c). The entire polymer chains slip from the surface periodically, which is called 'stick-spurt' flow. The pressure fluctuates significantly according to the periodic change of boundary condition from wall-stick to wall-slip. This fluctuation often along with a large amplitude (ΔP) and a long period (T) of pressure oscillation in this regime. The surface distortion is also more pronounced than 'sharkskin', and sometimes volume distortion or gross fracture is observed at this condition.

In Figure 46 and Figure 49, one can see that the pressure oscillation occurs earlier at a lower flow rate when the PE particle content increases. This indicates the addition of PE particles has contributed to the emergence of the wall-slip phenomenon and also brings forward the flow instability.

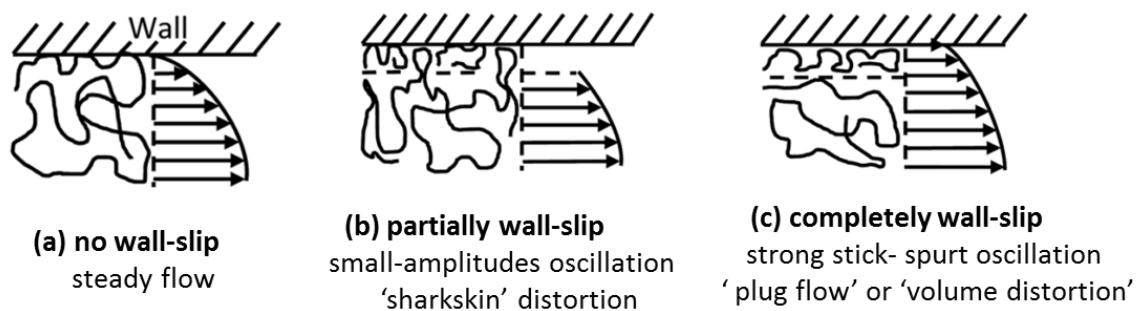


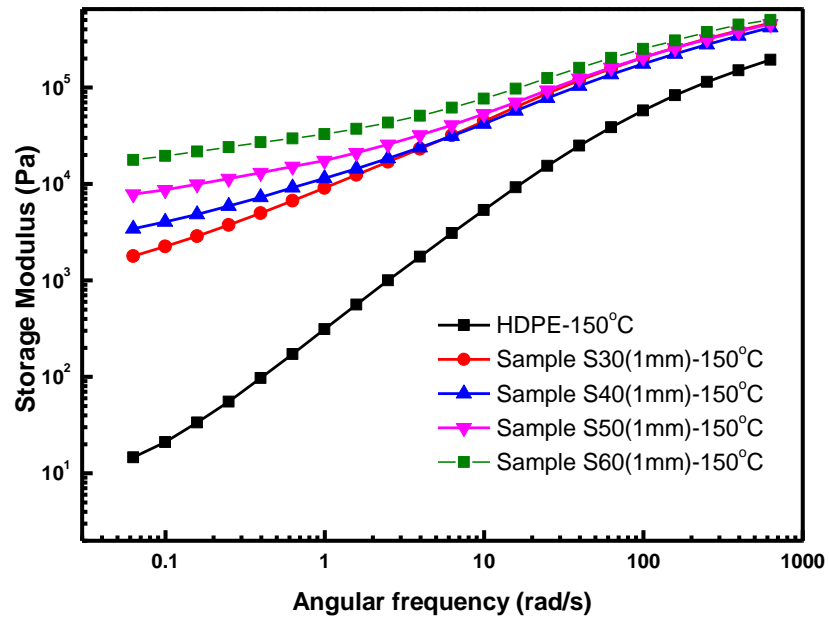
Figure 52 Velocity profile at different boundary conditions [179]

5.2.4.3 *Rheological behaviour*

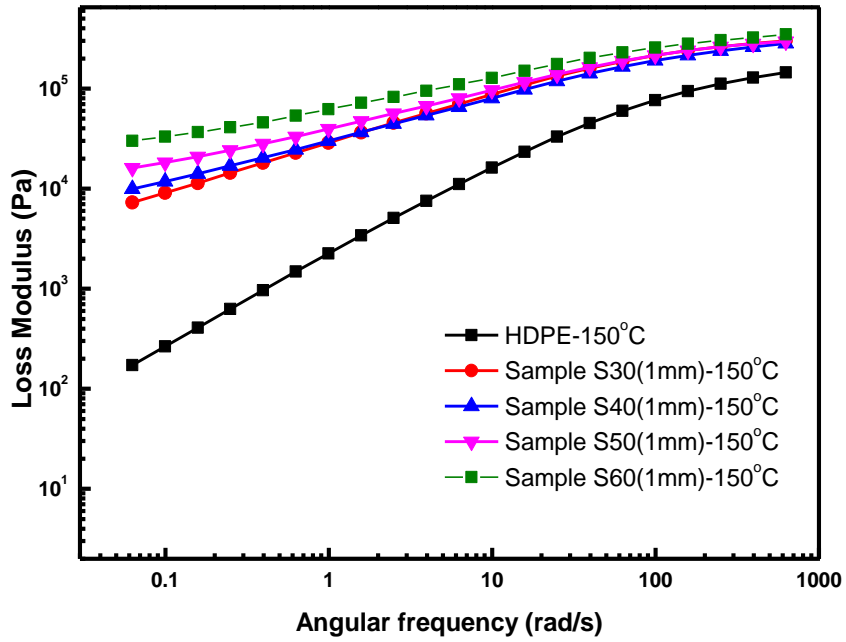
(1) Dynamic oscillatory rheological behaviour

Study the rheology property of the fluid is essential to explain and understand the characteristics of the flow behaviour during extrusion, and also to control the flow instability and surface distortion issues during processing. Polymers are known as viscoelastic fluids. Therefore, a dynamic oscillatory measurement was performed to determine the storage modulus (G') and loss modulus (G'') for the FSCPCM. The storage modulus represents the elastic energy that can be stored, which indicates the elasticity of the fluid. The loss modulus shows the energy that is dissipated as heat, which reflects the viscosity of the fluid. Figure 53 displays the storage moduli and the loss moduli of the neat HDPE and the FSCPCMs (sample S30 to S60). One can find that both the storage moduli and loss moduli increase with the increasing amount of the particle fillers, which agrees with the study for the kenaf fibre/HDPE composites [145] and wood polymer composites [169] [180]. The increment of storage moduli with increasing particle fillers indicates the melt is less compressible. This is attributed to the high rigidity of PE particles. In terms of the loss moduli, the increment of loss moduli with the increasing percentage of particle fillers indicates the increase of the viscosity or the decrease of mobility with the addition of particles. This is because the presence of particle fillers prevents the movement of the polymer. Comparing Figure 53 (a) and Figure 53 (b), one can find that the increment for the loss moduli with an increasing percentage of the particle fillers is not as pronounced as that for the storage moduli. Thus, the loss moduli are less affected by the addition of PE particles compared to the storage moduli. Moreover, one can see that the storage moduli are increasing with the frequency increment, which is a typical characteristic of viscoelastic materials [181]. A low frequency could allow more time for the polymer molecules to rearrange themselves for deformation and result in a low modulus, whereas a high frequency allows less time for molecular rearrangements and result in a higher modulus [182]. Therefore, the higher frequency

dependence of the storage modulus reflects a higher elastic property of the polymer. We can see that the slope of moduli-frequency curve is reducing gradually with increasing particle loadings, indicating a transition from elastomer-like to solid-like behaviour with the addition of particle fillers.



(a) The storage moduli of neat HDPE and the composite PCMs



(b) The loss moduli of neat HDPE and the composite PCMs

Figure 53 Storage and loss moduli of neat HDPE and composite PCMs (S30-S60)

(2) Steady shear viscosity

The elastic and viscous moduli of FSCPCMs with different particle loadings has been investigated by dynamic oscillatory. Besides, the steady shear viscosity (apparent viscosity) is also determined by the capillary rheometry, which is similar to the practical extrusion process. Due to the wall-slip phenomenon, there is an unavoidable uncertainty for the steady shear viscosity. However, this could still provide some guidance to the engineers to understand the flow behaviour in the practical process.

Figure 54 shows the apparent viscosity of the neat HDPE and the FSCPCM. One can observe that the apparent viscosity is increasing with the increment of particle fillers, which agrees with other works [173], [183]. The dependence of viscosity on shear rate presents non-Newtonian

behaviour. The decrease of viscosity with shear rate increment indicates a shear-thinning rheological behaviour for both the FSCPCM and the neat HDPE, and explains why the average pressure of HDPE increases at a lower rate for a higher extrusion speed (see Figure 45, section 5.2.4.1). The shear-thinning behaviour is expected due to the breakdown of particle aggregates and the disentanglements of polymer chains at a high shear rate [184]. Besides, the viscosity-shear rate curve for sample S60 is steeper than that for sample S30 and neat HDPE, indicating that FSCPCM with a higher particle concentration presents a more pronounced shearing-thinning behaviour. This is because it is easier to break down the particles aggregates than to disentangle the polymer chains at high shear rate. Moreover, one can find from the trend that the viscosity at zero shear rate is higher for samples with higher concentrations of the particle filler. In a highly filled polymer composite, the rheological behaviour is affected substantially by the existence of the yield stress which indicates its viscoelastic property. The increase of zero shear viscosity with the increase of particle concentration indicates an increasing resistance to deformation. In other words, the fluid behaves more like a solid, or it has a higher elastic modulus. The increase of zero shear rate is likely attributed to the increase in the bridging and entanglement between the polymer molecules and filler particles. Also, the variation of zero shear rate with increasing particle ratio is consistent with the change of storage modulus discussed in the previous section.

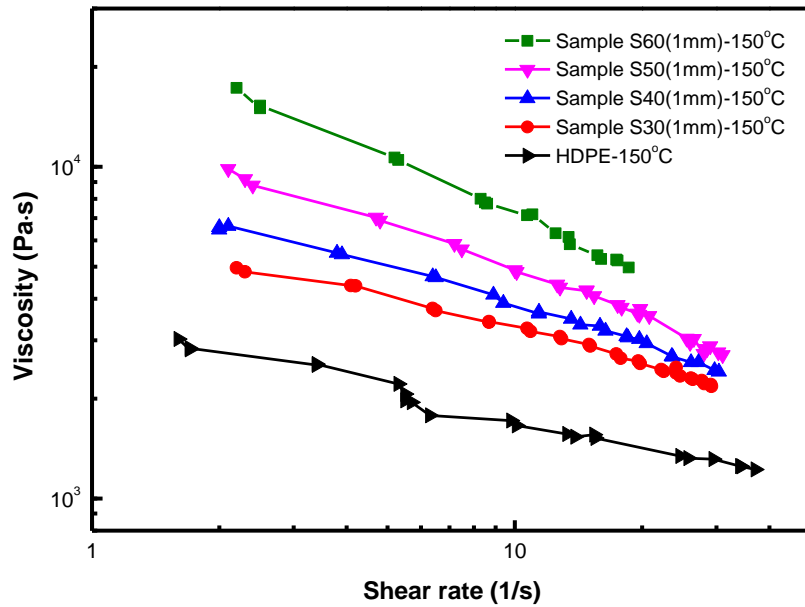


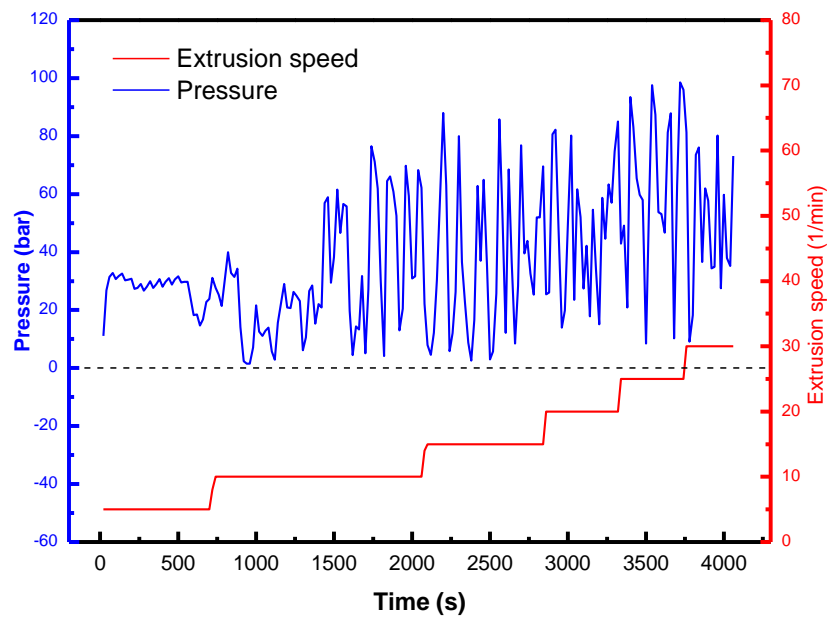
Figure 54 Apparent shear viscosity of the neat HDPE and composite PCMs (S30-S60)

5.2.5 Size effect of particle fillers on the extrusion and rheological behaviour

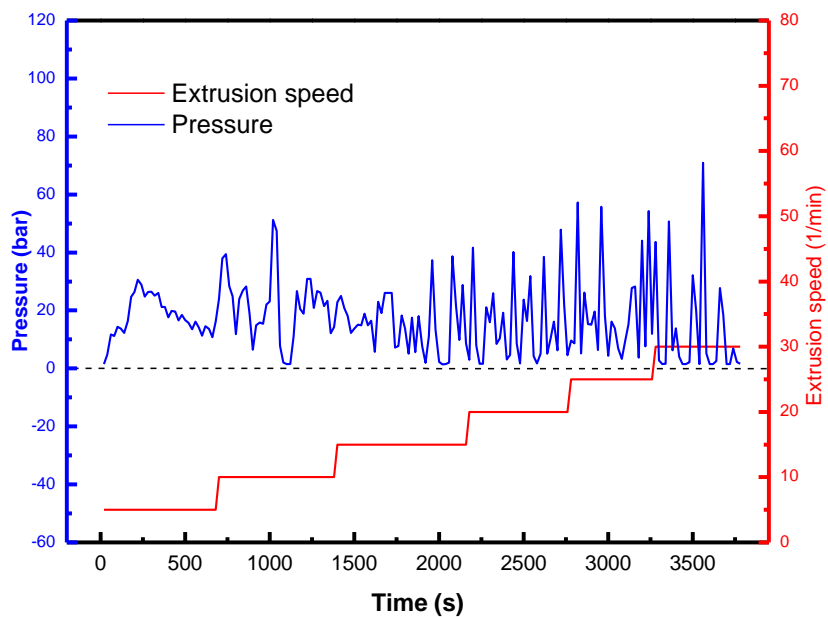
5.2.5.1 Extrusion stability

In this section, sample S50 was selected to study the size effect of PE particles (sieved under the size of 1 mm, 0.5 mm, 0.25 mm, 0.12 mm). The pressure profile for sample S50 with a particle size of 0.5 mm, 0.25 mm, 0.12 mm is displayed in Figure 55, while it is compared with Figure 46 for sample S50-1 mm (in section 5.2.4.1). One can find that sample S50-0.5 mm still presents a pronounced pressure oscillation as sample S50-1 mm. When the particle size reduces to 0.25 mm, the pressure oscillation has been suppressed significantly. However, the instability cannot be further diminished when reduces its particle size to 0.12 mm. This suggests that the pressure oscillation can be suppressed by reducing the particle size, but it cannot be eliminated by that. For sample S50 with different particle sizes, one can find that the onset of regular pressure oscillation always from 10 rpm. This indicates that the decrease of particle size cannot postpone the onset of extrusion

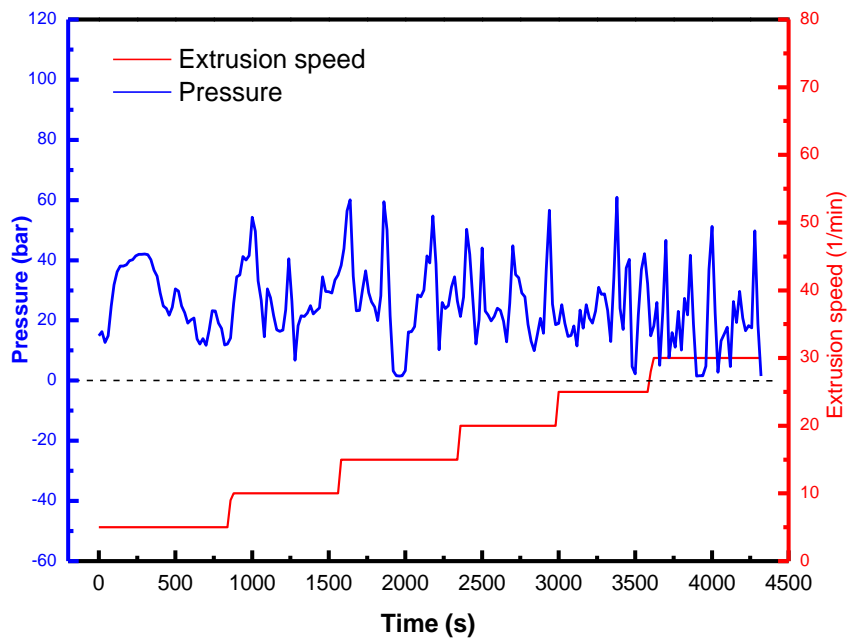
instability, but can suppress the oscillation amplitude to some extent. To understand more about the effect of particle size on extrusion defect, the extrudate morphology is discussed in the next section.



(a) Pressure profile when extruding sample S50 with a particle size of 0.5 mm



(b) Pressure profile when extruding sample S50 with a particle size of 0.25 mm



(c) Pressure profile when extruding sample S50 with a particle size of 0.12 mm

Figure 55 Pressure profile when extruding sample S50 with different sizes of particles





5.2.5.2 *Surface distortion*

Figure 56 displays the surface morphology of sample S50 with different particle size. One can see that all the sample presents a similar surface evolution with the increase of shear rate. It also can be noted that the surface distortion is minished when the particle size is below 0.25 mm. At the extrusion rate of 5 rpm, only slight sharkskin defect (coarse surface) is observed in sample S50-0.25mm and S50-0.12mm. It is regarded that the sharkskin defect is produced due to the elongation stress generated by the velocity gradient exceeds the melt strength of the FSCPCM. For a concentrated polymer-based suspension, a thin layer with lower particle concentration is formed at the die wall [169]. This layer tends to present a low viscosity, and therefore gives rise to a high gradient of velocity at the boundary. Polymer filled with small particles under a constant concentration has a more uniform dispersion of particles, which contributes to a smaller particle concentration difference and the velocity gradient at the die wall. As a result, the elongation stress at die exit decreases with the particle size. This explains the observation found in Figure 56 that the amplitude sharkskin defect is suppressed with the decreasing particle size. However, it also should be noted that the particle-to-particle contact has increased with the decrease of particle size. The increase of particle contacts can give rise to a higher possibility of cracking at the surface due to weak adhesion force between particles. In Figure 56, one can see that minor cracks still exist on the surface for sample S50-0.25mm and S50-0.12mm, which cannot be eliminated by reducing the particle size.

When the extrusion rate increases to 30 rpm, the oscillating defect is observed by the periodic surface evolution and pressure oscillation. In Figure 56, one can find that surface distortion in the oscillating defect regime has generally been suppressed when the particle size is below 0.25 μm . In the oscillating defect regime, the flow pressure is accumulated and released in each oscillation cycle. The accumulation of elongation stress results in a distorted surface. In Figure 55,

the pressure amplitude is reduced with the decreasing particle size, owing to the reduction of wall-slip velocity at the wall surface as found by Hristov et al. [169]. As a result, the distortion is also suppressed while the pressure amplitude is diminished.

To conclude, the surface distortion is generally reduced when the particles size is decreasing. Besides, the surface distortion is affected by several factors, for instance, the interparticle contacts, the pressure oscillation (wall slip phenomena) and the flow velocity gradient. While in different instability regimes, surface distortion is dominated by different factors. For the sharkskin defect, the velocity gradient dominates the amplitude of surface distortion. While for the oscillating defect, the surface distortion is dominated by the amplitude of pressure oscillation.

Sample S50 (1mm)-150°C			
5 rpm	30 rpm		
			
sharkskin	sharkskin	"bamboo-like" defects	coarse surface
Sample S50 (0.5mm)-150°C			
5 rpm	30 rpm		













			
slight sharkskin	sharkskin	"bamboo-like" defects	coarse surface
Sample S50 (0.25mm)-150°C			
5 rpm	30 rpm		
			
slight sharkskin	sharkskin	sharkskin	loss of gloss
Sample S50 (0.12mm)-150°C			
5 rpm	30 rpm		
			
slight sharkskin	slight sharkskin	sharkskin	loss of gloss

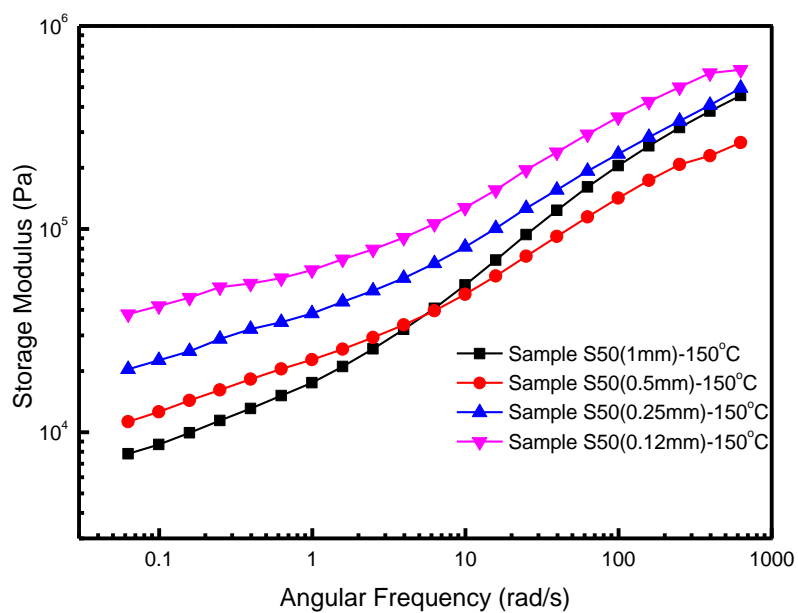
Figure 56 Surface morphology of sample S50 with different particle size

5.2.5.3 *Rheological behaviour*

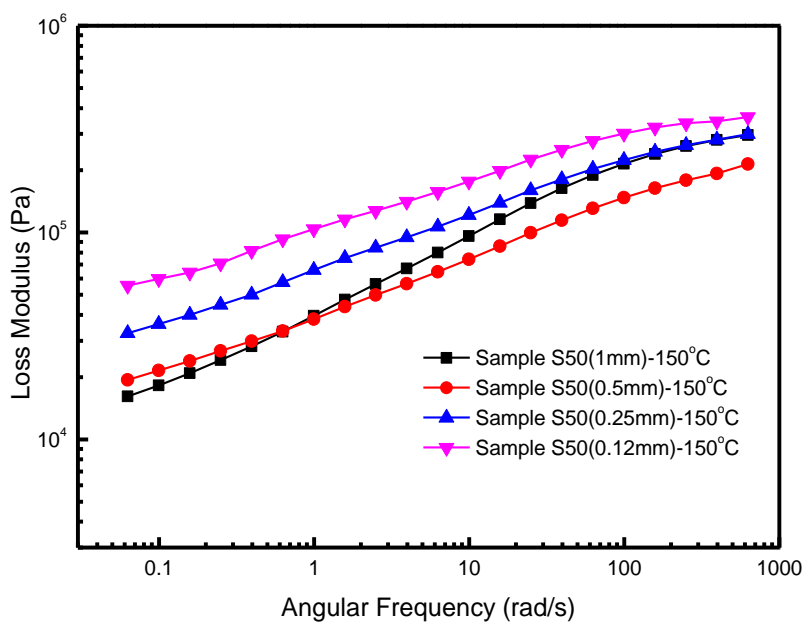
(1) Dynamic oscillatory rheological behaviour

Figure 57 displays the dynamic moduli of sample S50 with different particle size at 150°C. One can see that all the curves are frequency-dependent as discussed in Figure 53. Besides, the effect of particle size is significant on the dynamic moduli. Both the storage and loss moduli are increasing gradually with the decreasing particle size, which is in agreement with other findings [169], [185], [186], [184]. The increase of dynamic moduli is due to the increase of interparticle interactions with decreasing particles. However, they are not increasing consistently with the decreasing particle size [184]. When the particle size decreases to a certain value, fine particles agglomerate into clusters easily. As a result, the interparticle contacts will decrease and gives rise to the reduction of viscosity. In Figure 57, one can find that sample S50-1 mm shows a much steeper flow curve compared with other samples. This indicates that the elasticity dominates the rheological behaviour of sample S50-1mm, as the elastic property is frequency-dependent (section 5.2.4.3). The elastomer-like behaviour of sample S50-1 mm is likely attributed to the decrease of interparticle distance with particle size increase.

In terms of the steady viscosity, samples with different particle size present minor differences, which are within the experimental uncertainty (<5%). Hristov et al. [169] and Li et al. [187] also found that the effect of particle size on the steady shear viscosity is less significant compared to the size effect on the dynamic moduli. This is due to relatively low repeatability for the measurement of steady viscosity. Therefore, the steady viscosity of sample S50 with different particle size is not discussed in this section.



(a) The storage modulus of sample S50 with different particle size



(b) The loss modulus of sample S50 with different particle size

Figure S7 Storage and loss modulus of sample S50 with different particle size

5.2.6 Effect of operation temperature on the extrusion properties and rheological behaviour

5.2.6.1 *Extrusion stability*

To study the effects of processing temperature on the flow behaviour, Figure 58 shows the pressure profile when extruding sample S50 (0.25 mm, 30 rpm) at different processing temperatures (150°C, 160°C, 170°C, 180°C). The maximum operating temperature is set at 180°C to prevent high-temperature degradation during extrusion.

One can see that the pressure fluctuation has been suppressed slightly with the increasing temperature. It is reported that the onset of oscillating defect has been postponed by increasing the processing temperature [171][175]. The oscillating defect onset shifts to a higher shear rate at higher processing temperature leads to the oscillating defect at 30 rpm is not fully developed. Therefore, the pressure oscillation is suppressed with increasing temperature. The temperature-dependent characteristic of the oscillating defect indicates that the slip-stick transition is correlated with the rheological behaviour of the flow at different temperatures, as a result of different behaviour of chain entanglement and disentanglement.

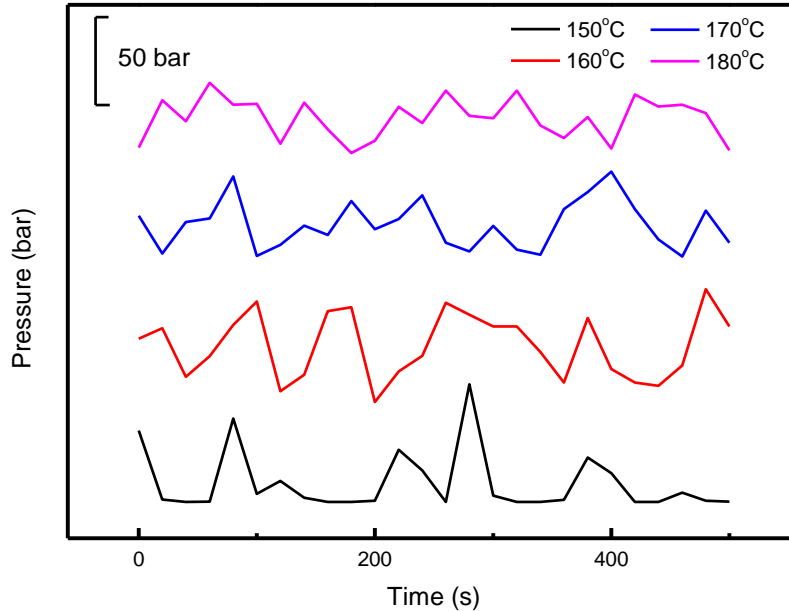










Figure 58 Pressure profile for sample S50 (0.25mm) with different processing temperatures at 30 rpm

1.4.1.1 Surface distortion

The surface morphology of the sample S50-0.25mm extruded at different temperatures (150 °C – 180°C) is displayed in Figure 59. At a low extrusion rate of 5 rpm, where the sharkskin defect is often observed, it can be found that the sharkskin defect has been suppressed with the increasing temperature. The extrudate is observed smooth when the temperature is above 170°C. At a high extrudate of 30 rpm, surface evolution is still observable until the processing temperature increases above 170°C. The extrudates processed at 170°C and 180 °C both present a smooth and glossy surface, and no observable surface distortion is found at low or high extrusion rate. The improvement of the surface morphology at higher temperature is likely attributed to the suppress of pressure oscillation. This finding is consistent with the other works, which reported that both the sharkskin defect [188] and the oscillating defect [175] can be diminished by raising the operating temperature. Besides, Gallos [189] found that a higher temperature allows for better compaction

of the polymer melt, which could enhance the adhesion force between the polymer chains and result in a smoother surface.

Sample S50 (0.25mm)-150°C			
5 rpm	30 rpm		
			
slight sharkskin	slight sharkskin	slight sharkskin	slight sharkskin
Sample S50 (0.25 mm)-160°C			
5 rpm	30 rpm		
			
coarse surface	loss of gloss	slight sharkskin	smooth
Sample S50 (0.25 mm)-170°C			
5 rpm	30 rpm		

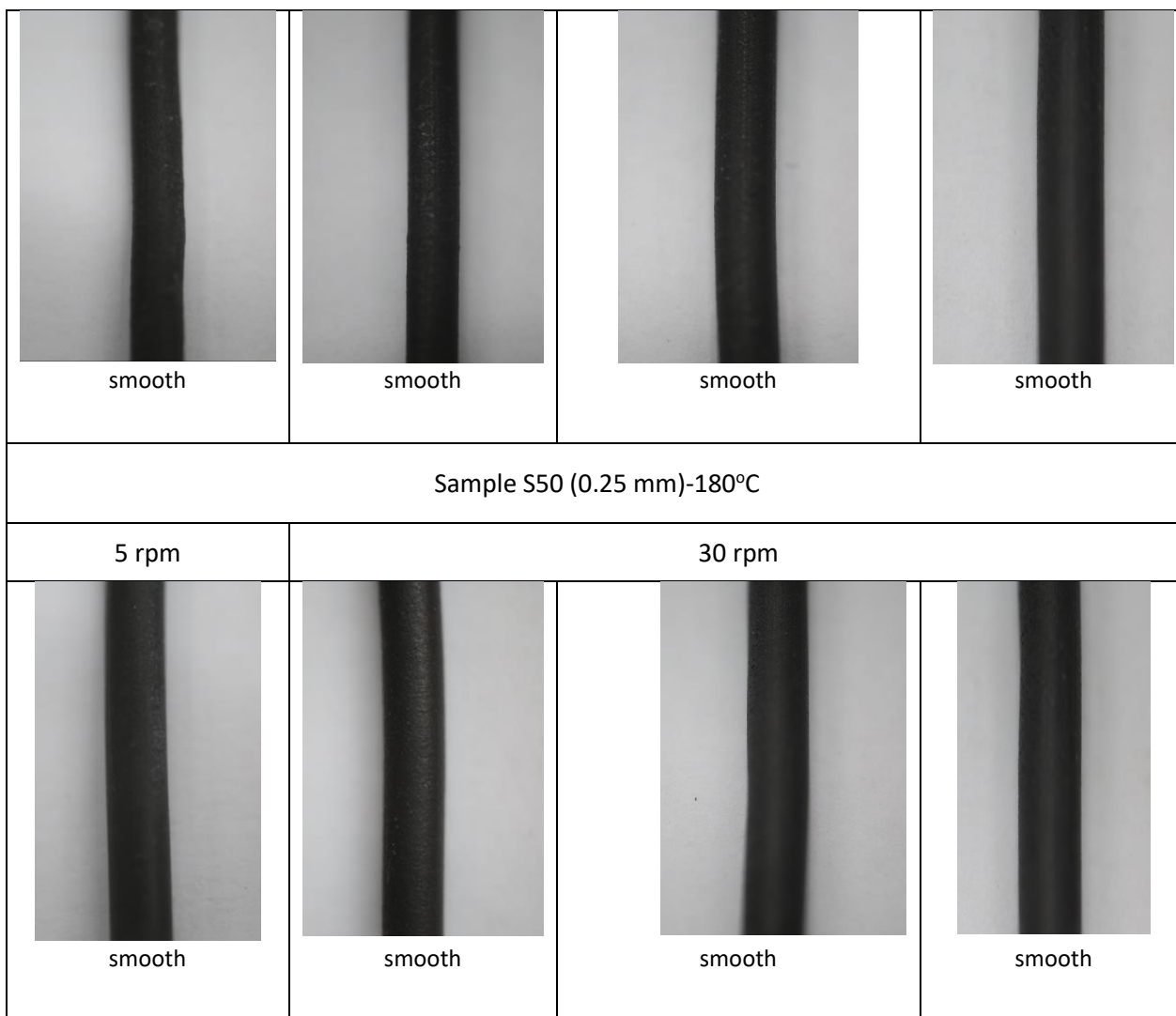


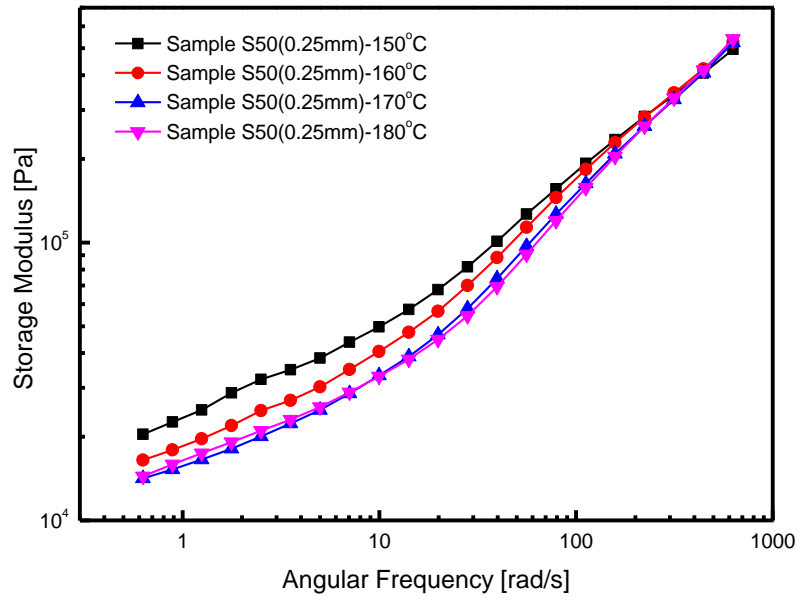
Figure 59 Surface morphology of sample S50 (0.25 mm) at different temperatures

1.4.1.2 Rheological behaviour

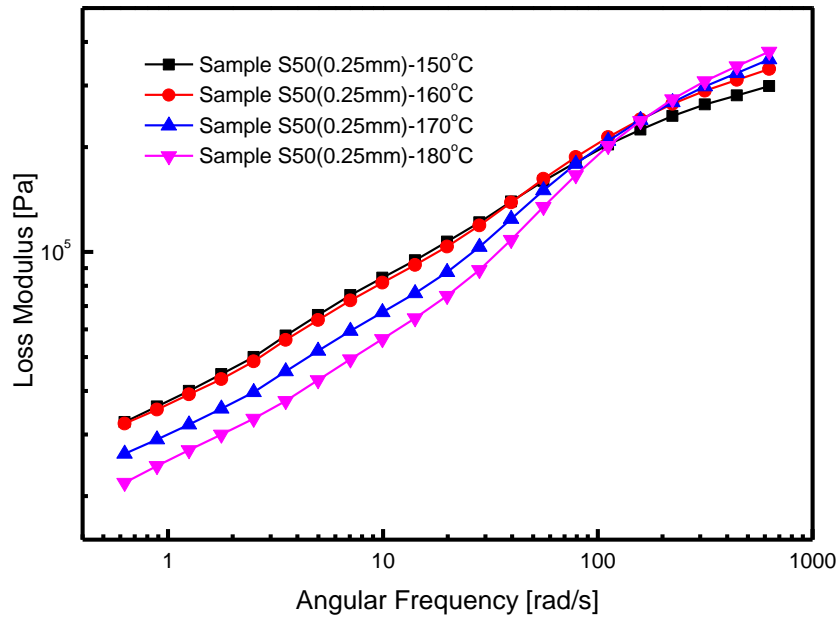
(1) Dynamic oscillatory rheological behaviour

The dynamic moduli of the sample S50-0.25mm at different temperatures are displayed in Figure 60. One can see that the storage modulus (G') decreases with the temperature increase, as polymer melt is easier to entanglement/disentanglement at higher temperatures and hence presents higher compressibility [145], [190]. Meanwhile, the loss modulus is also decreasing with the temperature increase, showing the improved mobility of the polymer melt at high temperatures.

The temperature-dependent characteristic of the dynamic moduli agrees with other studies [191]. Besides, it can be found that the dynamic moduli are more frequency-dependent at high temperatures than at low temperatures. As discussed in section 5.2.4.3, the enhanced frequency-dependent characteristic indicates a more elastomer-like behaviour of the melt at high temperatures.



(a) Storage modulus (G') of sample S50 (0.25 mm) at different temperatures



(b) Storage modulus (G'') of sample S50 (0.25 mm) at different temperatures

Figure 60 Storage and loss moduli of sample S50 (0.25 mm) at different temperatures

(2) Steady shear viscosity

The steady shear viscosity of sample S50-0.25mm at a low temperature (150°C) and a high temperature (180°C) is shown in Figure 61. One can see that the apparent shear viscosity reduced notably when the temperature increased from 150°C to 180°C, which agrees with the dynamic rheological behaviour. Besides, it can be found that the flow presents a shear-thinning behaviour and it is more significant with the increasing temperature. The increase of the shear-thinning behaviour at high temperatures is likely attributed to the breakdown of the interparticle contacts is easier when the viscosity of the polymer matrix is decreased. It is regarded that the reduction of the apparent viscosity is beneficial to practical processes, as the extrusion stress and input mechanical energy can be reduced. Hence, the operating temperature is always set at a high temperature to process the polymer easily [189].

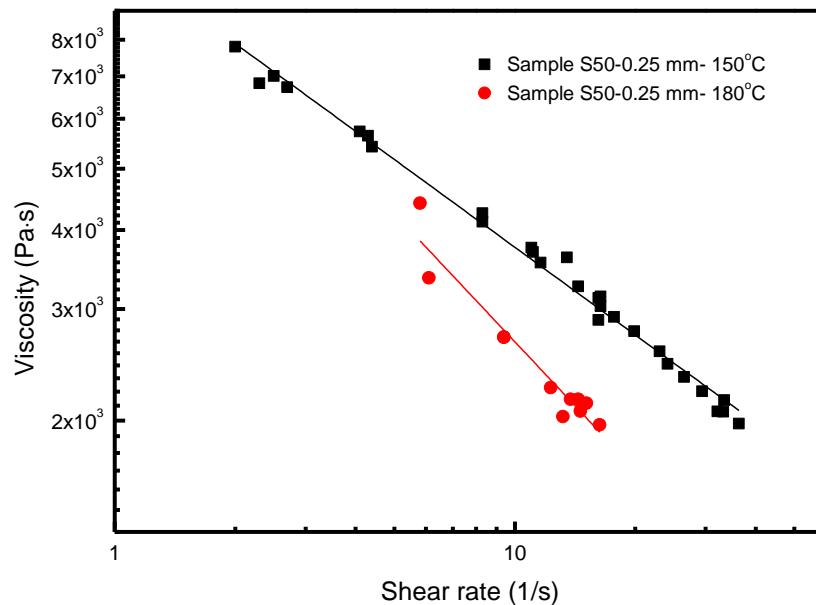


Figure 61 Apparent shear viscosity of composite PCM S50 (0.25 mm) at different temperatures

5.3 Summery

This chapter concerns the use of a continuous extrusion method to prepare a novel PE-HDPE-Cg FSCPCM. The extrusion stability, rheological behaviour and surface morphology of the FSCPCM were studied under different processing conditions, including different particle concentrations, different particle sizes and extrusion temperatures. During the extrusion process of the FSCPCM, two extrusion instabilities were observed in this study: the sharkskin defect and the oscillating defect. These two extrusion instabilities appear due to different mechanisms. In the sharkskin defect regime, the defect originates at the exit of the die when the elongation stress caused by the velocity gradient exceeds the melt strength. Whereas, the oscillating defect is owing to the periodical slip of the polymer chain on the surface. The periodic change of boundary condition from wall-stick to wall-slip results in a discontinuous flow ('stick-spurt' flow) and a cyclic pressure oscillation. The extrudate surface appears alternatively in distorted surface or smooth surface with

the pressure oscillation: in the compression phase, surface distortion intensifies with the accumulated pressure; while in the relaxation phase, the interfacial polymer chains slip on the surface and resulting in a smooth surface.

Study on the impact of particle fillers concentration found that the extrusion defects and surface distortion intensify with the increasing mass ratio of particles. A severe volume distortion and an extremely low throughput were found for the sample S60 due to strong pressure oscillation and discontinuous flow. Hence, sample S50 is regarded as the best formulation feasible for extrusion. The dynamic oscillatory and the steady capillary shear viscosity were studied to understand the viscoelastic property and the rheological behaviour of the FSCPCM. It is found that both the storage and loss moduli increase with the increasing particle fillers, indicating the reduced compressibility and mobility due to the addition of particles. The FSCPCM is also found changed from an elastomer-like flow to a solid-like flow with the addition of particle fillers. Besides, the FSCPCM presents an enhanced shearing-thinning behaviour with a higher particle concentration, which is attributed to a high degree of particles realignment for the concentrated suspension with the increased shear rate.

Different size of the PE fillers also shows a significant impact on extrusion stability and rheological properties. When the particles size reduced from 1 mm to 0.25 mm, the pressure oscillation has been suppressed significantly. However, there is no significant improvement when the particle size further decreased to 0.12 mm. Surface distortion is also found reduced with a small particle size due to the decreased pressure amplitude and velocity gradient. The storage and loss moduli were observed increasing with the decreasing particle sizes, as the reduce of particle size can increase the interparticle interactions and leads to more solid-like behaviour.

It is found that the operating temperature plays an important role in extrusion stability. The development of the oscillating defect is postponed due to the temperature increase. The surface

distortion has been reduced significantly when the temperature is over 170°C, which shows a smooth and glossy surface. The dynamic moduli and the steady shear viscosity of the melt are decreasing with the temperature increase, indicating higher compressibility and mobility at high temperature.

To conclude, the extrusion instabilities can be diminished with the decreasing particle percentage, reducing particle size and the increasing temperature. In this work, sample S50 with a particle size of 0.25mm extruded at 170°C is regarded as the best operational condition, which shows a stabilised process and good surface morphology.

6 Results and discussion (III): a continuous hot-melt extrusion method – the study of structural and thermal properties of the FSCPCM

6.1 Introduction

A novel HDPE-PE-Cg FSCPCM was prepared by a one-step continuous extrusion method previously. In this chapter, the internal structural properties of the prepared FSCPCM were investigated, e.g. particle dispersion, porosity, and the microstructure. An understanding of the internal structure and the heterogeneity of the composite is essential, as these could have a significant effect on its thermal and mechanical properties. Study the correlation between the structural properties and processing parameters can also give feedback to regulate the processing parameters for high-quality products.

Thermal properties of the FSCPCM were also studied, such as the phase change properties, thermal conductivity and thermal stability. Besides, cycling stability of the FSCPCM was investigated by 100 times of thermal cycling. Chemical compatibility between the components was studied to verify the chemical stability of the composite. Study of the thermal property and long-term stability of the FSCPCM is essential before it applied in thermal energy storage.

6.2 Characterisation methods

To clarify the measurement conditions, testing range and repetitions are shown in Table 19.

Table 19 Measurement methods and repetitions

Instruments and Properties	Measurement methods	Data acquisition	Sample shape/ amount	Repetitions
DSC: melting temperature/latent heat/heat capacity	25°C to 200°C; 100 ml/min Air flow. Different heating rates.	whole range.	~10 mg powers.	each sample conduct 3 measurements. averaged form 3 measurements.
LFA: thermal conductivity	25 °C to 120 °C at a heating rate of 5 °C/min; 100 ml/min N ₂ flow.	acquire 6 results at 25°C, 50°C, 75°C, 100°C, 120°C.	tablet: Ø: 13 mm, H: ~2 mm.	each sample conduct 1 measurement. averaged form 6 acquired results
TGA: thermal stability	25 °C to 800 °C at a heating rate of 10 °C/min; 50 ml/min Air or N ₂ flow.	whole range.	~10 mg powers	each sample conduct 1 measurement.
Dilatometer: thermal cycling	1 cycle: a). 100 to 200 °C at a heating rate of 10°C/min; b). maintained at 200 °C for 10 minutes; b). 200 to 100 °C at a cooling rate of 10°C/min. repeat for 100 cycles. N ₂ atmosphere.	/	extrudates: Ø: 4 mm, L: ~20 mm.	sample was characterized after 100 thermal cycles.

6.3 Results and discussion

6.3.1 Structural characteristics

6.3.1.1 *Particle dispersion efficiency*

Particles dispersed in polymers tend to agglomerate due to the entanglement of polymer chains. However, a good dispersion of the particle fillers is vital, as it results in a better mechanical strength of the FSCPCM. It is found that composite bonded through particle-to-polymer interaction is much stronger than particle-to-particle interaction [192]–[194]. Therefore, obtain a good dispersion of the particle fillers is very important.

The ratio of surface-to-volume is an important parameter used to investigate the degree of particle dispersion in a composite. Large particles and aggregates tend to have a small specific surface area. Therefore, a high surface-to-volume ratio indicates a small particle size or a good dispersion. In this section, surface-to-volume ratios of the FSCPCMs prepared at different processing conditions were studied to give feedback to the process regulations. Besides, the particle size distribution is investigated to study the sizes of aggregates.

(1) Image processing by the XRT technique

Different components in the FSCPCM can be identified by the XRT technique according to their density differences. When X-ray is passing through the dense material, the X-ray attenuation is high. Therefore, as shown in Figure 63 (a), components with different densities can be reflected as different greyscales of pixels: pixels with higher greyscale (brighter colour) indicates a higher density, while black pixels indicate the air and voids. A batch of 2-D XRT images taken at different angles can be reconstructed to a 3-D structure (see Figure 62), where we can see a wide range of particles and pores dispersed in the polymer. For quantitative analysis, the 3-D structure is sliced into a batch of cross-section images to count and analysis the pixels. In Figure 63 (a), one can see particles (white pixels), polymer matrix (grey pixels) and voids (black pixels) are in the composite.

Graphite presents a higher density than PE particles, therefore it is represented by brighter pixels than that of PE particles. As to study the particle dispersion, both PE particles and graphite particles are counted for the quantitative analysis. With the cross-section image obtained, the binarizing process is applied under a greyscale threshold. In the binarizing process, one can select certain pixels as objects (white) for analysis and the rest is considered as empty (black). In Figure 63 (b), the particle fillers are selected from the polymer matrix with a higher greyscale threshold (171-255) applied. By calculating the numbers of white and black pixels, size distribution and the surface-to-volume ratio of PE particles can be quantified. In Figure 63 (c), both particles and polymer matrix are selected under a lower greyscale threshold (109-255), which is to characterise the pore-related properties of the composite, such as porosity and pore size distribution.

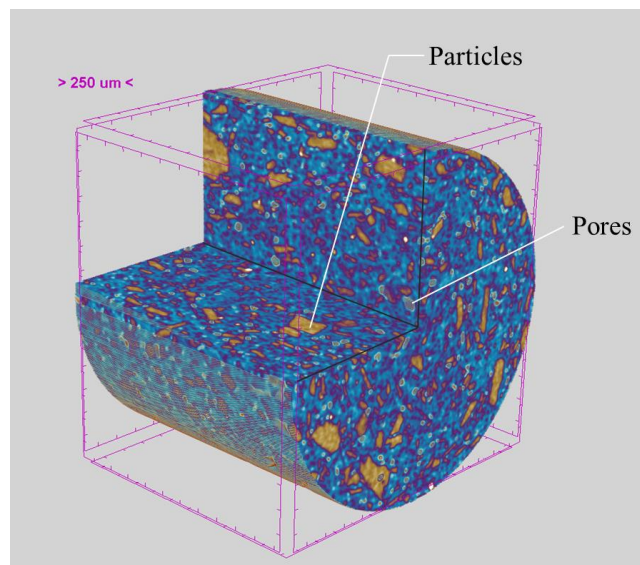


Figure 62 Computed 3-D structure of the FSCPCM

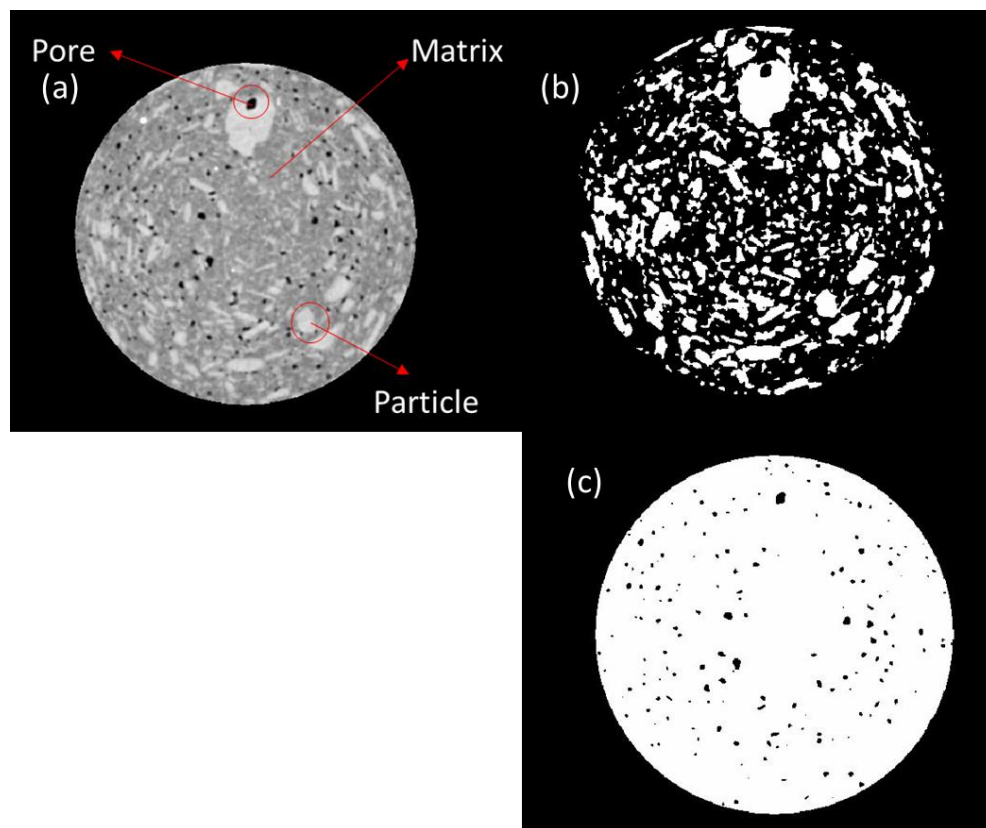


Figure 63 (a) A sliced cross-section image of the specimen, consisting of polymer, particles and pores; (b) and (c) are binarised images correspond to (a) with different greyscale threshold: (b) selects the particles and (c) selects both the particles and the polymer matrix.

(b) Particle dispersion

By studying the surface-to-volume ratio, the particle dispersion efficiency at different extrusion speed can be determined. In Figure 64, one can see that the surface-to-volume ratio of sample S50-0.25mm increases with the extrusion speed until 20 rpm and then starts to decrease. For sample S50-1mm, it shows a lower surface-to-volume ratio compared with sample S50-0.25mm, owing to its larger particle size. Besides, it shows a similar trend as sample S50-0.25mm that the surface-to-volume ratio increases until the rotation speed reaches 25 rpm and then levels off. Hence, it can be found that the particle dispersion efficiency does not increase with the extrusion rate consistently. This is because the increase of extrusion rate can affect the dispersion efficiency in two

different ways: the positive effect is that it can increase the flow velocity and shear stress to enhance the dispersion; the negative effect is that it decreases the residence time of the material in the extruder for mixing. Villmov et al. studied the correlation between the extrusion speed and the residence time for the carbon-filled polycaprolactone [195]. They found that the residence time decreases only 25% - 40% when the extrusion rate increased by 5 times. The residence time and extrusion speed are not changing at the same rate. Therefore, particle dispersion can be enhanced by increasing the extrusion rate but it does not increase consistently. When the negative effect of the reduced residence time outweigh the positive effect of the increased shear stress and flow velocity, particle dispersion will decrease with the extrusion rate increases. In Figure 64, one can also find that the extrusion rate where the surface-to-volume ratio reaches the maximum is different for sample S50-0.25mm and sample S50-1mm, which is attributed to their different rheological behaviour. To obtain a good dispersion, the optimal extrusion rate for sample S50-1mm and sample S50-0.25mm is 25 rpm and 20 rpm, respectively.

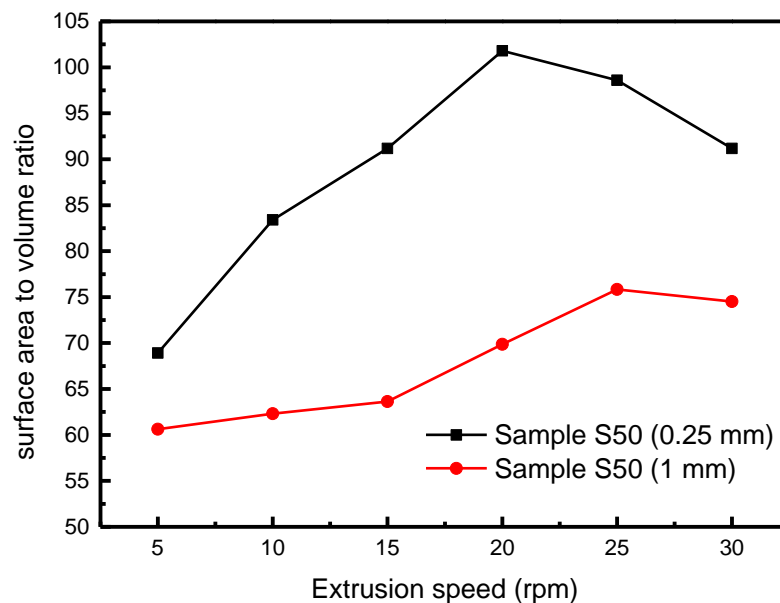


Figure 64 Particle dispersion efficiency at a different extrusion speed

The particle size distribution of sample S50-0.25mm extruded at 5 rpm and 20 rpm are shown in Figure 65. One can see that sample S50-0.25mm with the highest surface-to-volume ratio (20 rpm) mainly consist of small particles below 0.054 mm, which accounts for 85.36% of the total volume. Particles with a size of ~ 0.03 mm show the highest volume percentage, constituting 44.97% of the total volume. Whereas, sample-0.25mm with the lower surface-to-volume ratio (5 rpm) shows a much lower percentage of small particles: particles size below 0.054 mm only accounts for 66.99%. Besides, large particles with a size over 0.2 mm still exist at 5 rpm, but these are not observed at 20 rpm. It is likely that large particles and aggregates are broken into small particles when the extrusion rate increases to 20 rpm.

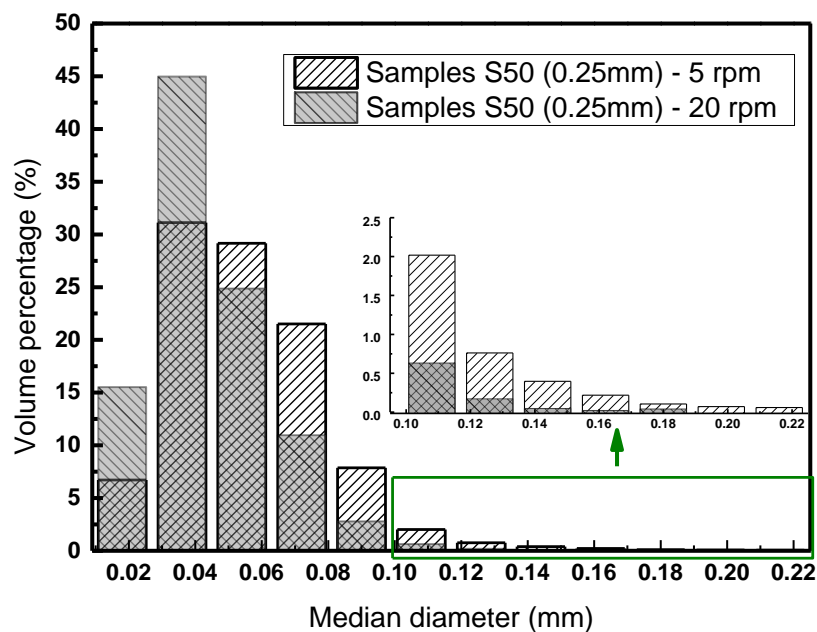


Figure 65 Particle size distribution of sample S50 (0.25 mm) at different extrusion rates

6.3.1.2 Porosity and pore size distribution

During the extrusion process, pores and voids are produced due to the incomplete compaction of the polymer melt and the aggregation of particle fillers. Besides, if one of the

components is volatile, the steam and vapour generated could also produce pores [196]. For the wood-plastic composites, around ~14%-25% of the total volume is occupied by pores and they cannot be eliminated completely [197]. These pores and voids have a direct impact on the structural and mechanical properties of the composite, such as the compressive strength, stiffness and elasticity modulus, etc. It has been revealed that an increase of 1% in porosity can result in a decrease of interlaminar shear strength by ~ 7% [198], [199].

For the FSCPCM, the impact of processing temperature on its porosity has been investigated. Sample S50-0.25mm prepared at 15 rpm was studied and the results are shown in Figure 66. A glance at the cross-section of the composite (insert images) can find that its structure is getting porous with increasing temperature. By the quantitative analysis of XRT, the porosity value can be determined. As the image processing parameters selected can slightly affect the porosity results, all the samples are analysed by identical processing parameters for comparison. Besides, the porosity obtained by XRT technique could vary from different devices slightly, depending on the sensitivity and resolution of the camera.

As displayed in Figure 66, the total porosity has increased from 1.705% to 10.901% when the processing temperature increases from 150°C to 180°C. The increment of porosity with temperature increase is expected caused by the vaporization of PE due to its relatively low thermal stability (see details in section 6.3.2.3). The vapour generated was trapped inside the polymer melt and cannot be removed completely by the extrusion process. From the previous study, we find that raise processing temperature can diminish the extrusion instability and suppress the surface distortion. However, the increased processing temperature could increase the porosity of the extrudate. Therefore, there is a compromise between extrusion instability and internal porosity for fabricating high-quality FSCPCMs.

The pore size distribution of the FSCPCM is shown in Figure 67. One can see that sample extruded at low temperature (150°C) has many small pores, mostly with a size less than 0.1 mm. Pores with a size of ~0.036 mm account for the highest volume percentage. Whereas, the extrudate prepared at 180°C has a larger pore size and a broader pore size distribution. These large pores can also be observed by the cross-section image in Figure 66. Large pores are produced due to a large amount of vapor generated at high temperatures and also the swelling the small pores with temperature increase. The relationship between the extrusion rate and the extrudate porosity was also investigated. However, the impact of the extrusion rate on its porosity is not significant. Hence, the result is not shown in this section.

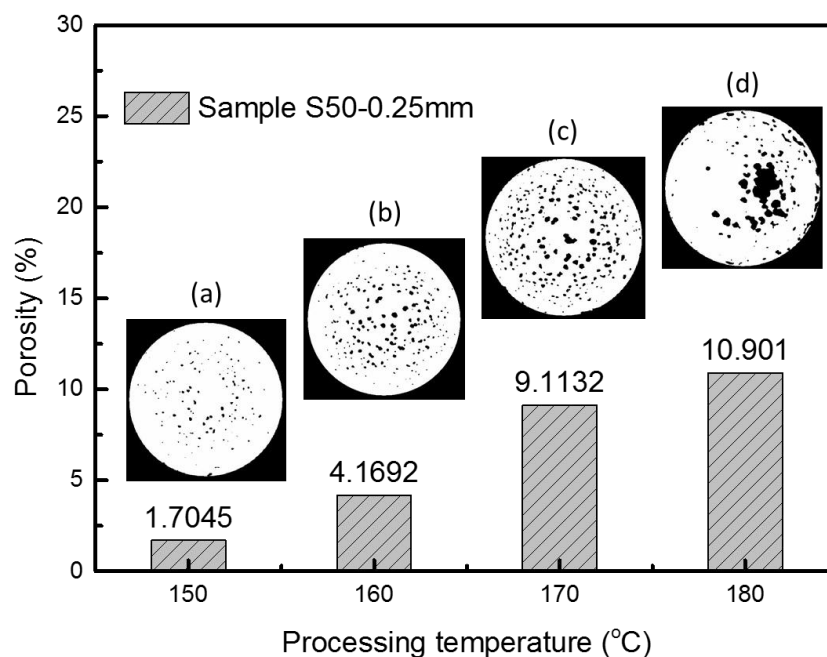


Figure 66 Porosity of Sample S50-0.25mm prepared at different processing temperatures

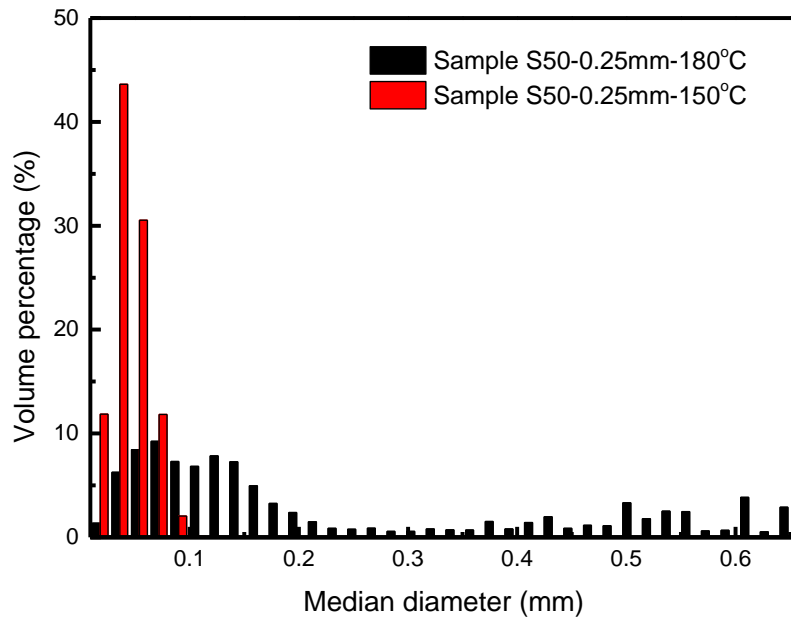


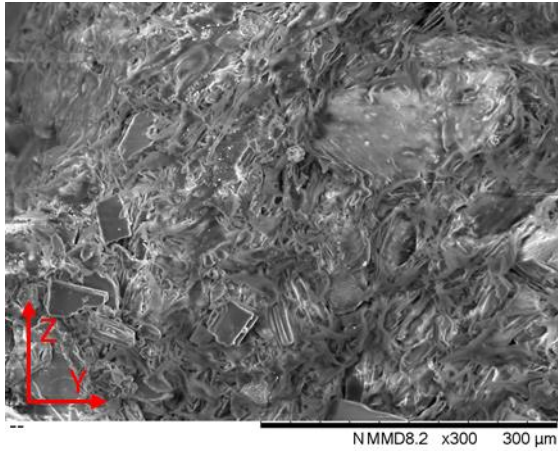
Figure 67 Pore size distribution of Sample S50-0.25mm at 150°C and 180°C

6.3.1.3 Microstructure

Figure 68 shows the SEM images of sample S50 (1mm and 0.25 mm) and sample S30 (1mm) extruded at 150°C and 5 rpm. The X-Y plane displays the surface of the extrudates, while the Z-Y plane represents the cross-section image. Besides, X direction is corresponding to the extrusion direction. One can see from Figure 68 (a) that the HDPE matrix is fibrous and well-compacted in sample S50-1mm. No presence of fibre pulled-out trace was observed, indicating a good interfacial adhesion between the PE particles and HDPE matrix [200]. Samples with smaller particle sizes (Sample S50-0.25 mm) and lower particle content (Sample S50-0.25 mm) also presented a good interfacial bonding; see Figure 68 (c) and (e). In terms of the extrudate surface (X-Y plane), we can see a wave-like rough surface for sample S50-1mm along the extrusion direction. Also, some particles are observed embedded on the surface. With the decrease of particle size and the particle content, the surface becomes smoother. In Figure 68 (f), the surface is less scaly than that of Sample

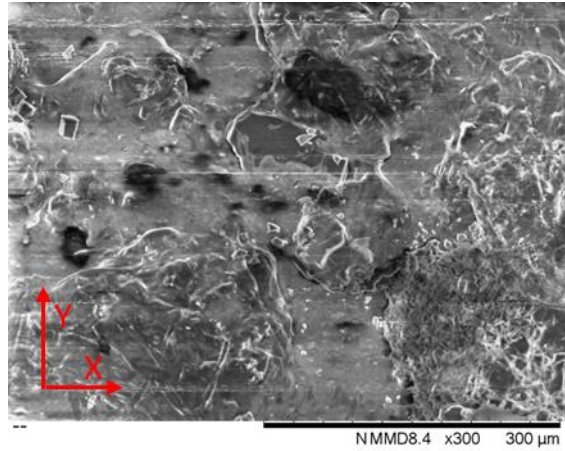
S50-1mm. Generally, from the microstructural study of the extrudate, a good interfacial bond and compaction between the particles and the HDPE matrix can be obtained.

Cross section direction

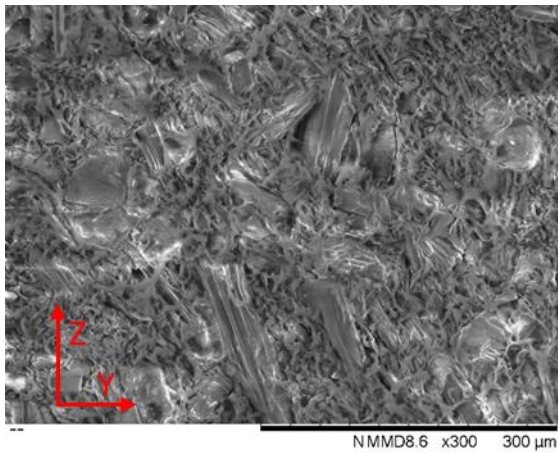


(a) Sample S50 (1 mm) in cross section direction

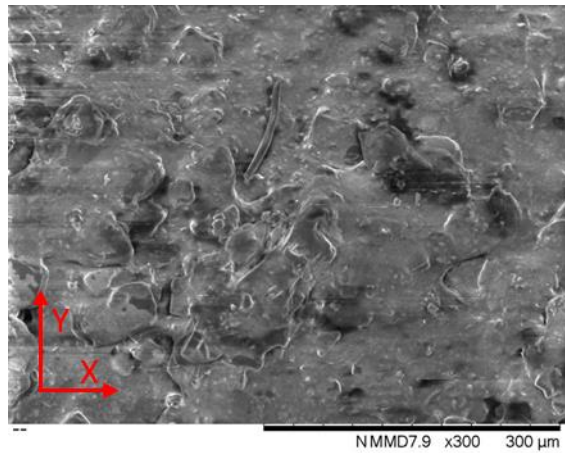
Extrusion direction



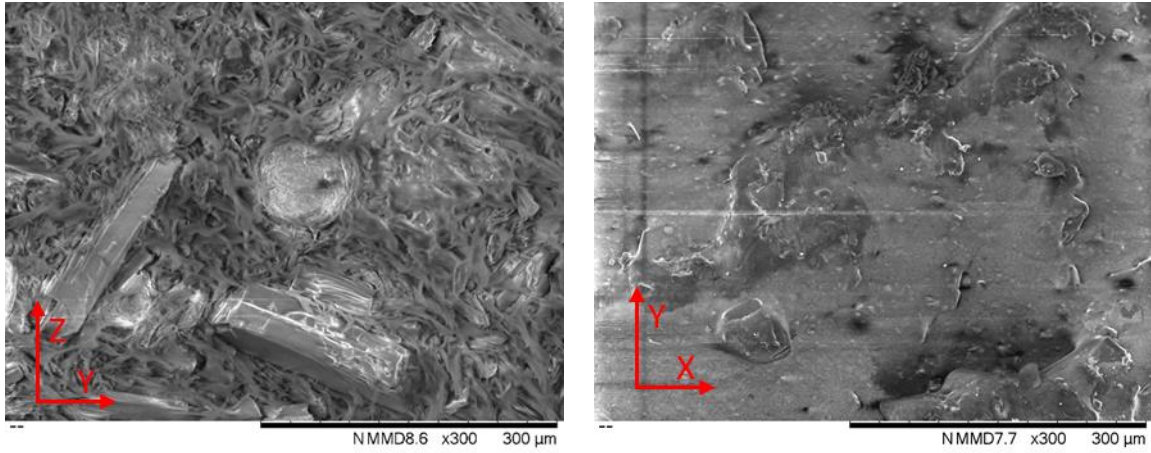
(b) Sample S50 (1 mm) in extrusion direction



(c) Sample S50 (0.25 mm) in cross section direction



(d) Sample S50 (0.25 mm) in extrusion direction



(e) Sample S30 (1 mm) in cross section direction

(f) Sample S30 (1 mm) in extrusion direction

Figure 68 SEM images of sample S30 and S50 in the extrusion direction and cross-section direction (5 rpm)

6.3.2 Thermal properties

6.3.2.1 Phase change parameters and energy density

As for TES applications, the energy storage capacity of the FSCPCM plays a primary role in practical use. Phase change parameters of the FSCPCM measured on DSC at a heating rate of 5 K/min is shown in Figure 69. It can be found that there are two phase-change peaks during the heating/cooling process for all the FSCPCMs. These two peaks are corresponding to the phase transition process of HDPE and PE as seen from Figure 69. HDPE and PE are both PCMs in the FSCPCM. Therefore, this composite displays an advantage in energy storage from 100°C to 200°C, as only 10 wt.% of the composite (graphite) is not PCM. Meanwhile, both HDPE and PE are self-reinforced materials in molten phase. They can keep structure stable when the temperature is over the melting point.

Phase change enthalpies and temperatures of the pure PCMs (HDPE, PE) and the FSCPCMs (sample S30 to S50) are summarized in Table 20. It can be found that the pure HDPE and PE have an endothermic enthalpy of 179.89 kJ/kg and 286.42 kJ/kg at 124.91°C and 185.98 °C respectively. PE presents a higher phase change enthalpy than HDPE, and therefore, composite with a higher

percentage of PE tends to have a higher energy storage capacity. One can find from the total latent heat of the FSCPCM that it decreases with the decreasing PE content. When comparing the melting and solidification temperature of PE and HDPE, a certain degree of supercooling can be found for HDPE and PE. HDPE presents a smaller supercooling degree (6.94 °C) compared with PE (13.78 °C). Even so, the supercooling degree of HDPE and PE are in the acceptable level for high-temperature application.

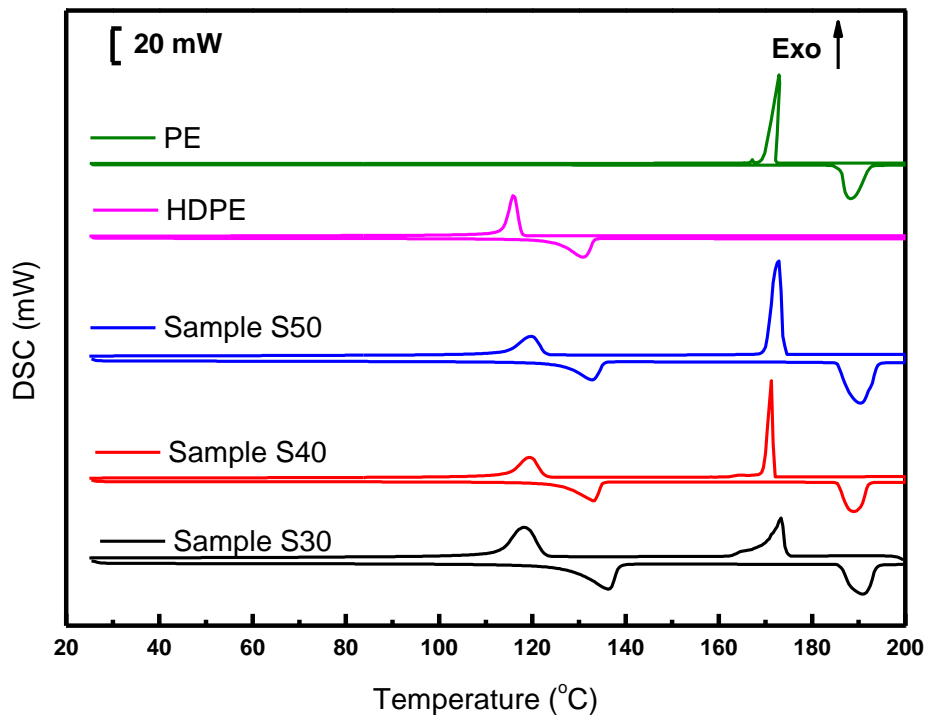


Figure 69 DSC curves of the HDPE-PE-graphite composite PCMs

Table 20 Melting point and latent heat of the composite PCM

Heating (Endothermal process)					
	T₁(°C)	Δ H₁(kJ/kg)	T₂(°C)	Δ H₂(kJ/kg)	Total Δ H (kJ/kg)
HDPE	124.66±0.16	179.89±8.04	-	-	-
PE	-	-	185.98±0.63	286.42±5.21	-
Sample S50	126.17±0.28	73.25±5.45	185.25±0.27	143.97±4.12	217.22±9.48
Sample S40	125.73±0.33	94.92±3.73	185.42±0.21	110.45±3.44	205.37±0.53
Sample S30	127.83±1.02	108.28±2.67	186.07±0.23	86.43±0.51	194.71±2.54
Cooling (Exothermal process)					
HDPE	117.72±0.25	189.94±0.44	-	-	-
PE	-	-	172.20±2.61	262.04±2.86	-
Sample S50	122.91±0.10	73.22±1.46	174.39±0.51	141.9±2.00	215.12±3.38
Sample S40	122.69±0.18	97.08±1.75	172.02±1.81	107.39±0.37	204.47±1.99
Sample S30	122.72±0.04	111.91±0.34	174.61±1.58	84.99±0.40	196.90±0.67

To further study whether the extrusion speed can affect the uniformity of the composite, the FSCPCMs extruded at different speed were studied. Figure 70 and Table 21 shows the phase change temperature and enthalpy of sample S50 extruded at 5 rpm, 15 rpm, 30 rpm, respectively. In terms of the phase change temperature, one can find there is a minor difference (up to 4.22°C) between each sample. Also, the difference in total latent heat is small for the melting process (3.88 kJ/kg), while for the solidification process is larger (14.91 kJ/kg). The difference between the melting process and the solidification process is likely attributed to the crystallisation process is affected by the randomness of the polymer chains when prepared at different extrusion rates. However, this explanation needs to be further studied.

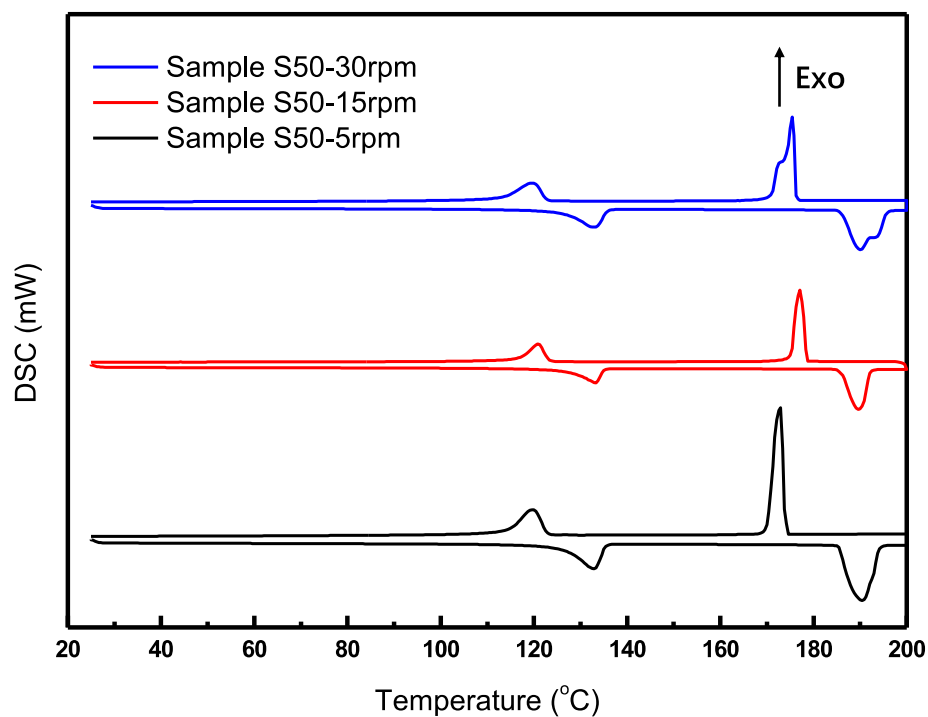


Figure 70 DSC curves of sample S50 at a different extrusion speed

Table 21 Melting point and latent heat of sample S50 at different extrusion speeds with SD

Heating					
Sample S50	T_1 (°C)	ΔH_1 (kJ/kg)	T_2 (°C)	ΔH_2 (kJ/kg)	Total ΔH (kJ/kg)
5 rpm	126.17 ± 0.28	73.25 ± 5.45	185.25 ± 0.27	143.97 ± 4.12	217.22 ± 9.48
15 rpm	127.17 ± 0.25	71.91 ± 2.79	185.81 ± 0.17	142.26 ± 5.01	214.17 ± 6.69
30 rpm	126.57 ± 0.35	70.66 ± 2.10	185.82 ± 0.29	142.68 ± 2.22	213.34 ± 3.01
Cooling					
5 rpm	122.91 ± 0.10	73.22 ± 1.46	174.39 ± 0.51	141.9 ± 2.00	215.12 ± 3.38
15 rpm	123.26 ± 0.06	69.00 ± 2.35	178.61 ± 0.92	140.68 ± 5.06	209.68 ± 7.40
30 rpm	122.68 ± 0.07	61.47 ± 1.20	176.45 ± 1.41	138.74 ± 2.34	200.21 ± 3.40

To examine the effect of heating rate on the results of phase change temperature and latent heat determined by DSC, the measurements were conducted at heating rates from 0.5 K/min to 10 K/min. Figure 71 shows the DSC heat flow curves for different heating rates. One can see that the shape of the peak becomes broader and higher with increasing heating rate. The dependence of DSC thermogram on the heating rate agrees with other studies [201]–[203], which reflects how the thermal hysteresis varies with different heating rates. Table 22 shows the values of onset phase change temperatures and latent heats. In terms of the onset phase change temperatures, one can see it varies slightly with the heating rates. The first onset temperature (T_1) presents a decreasing trend with the increasing heating rate, however the trend of the second onset temperature (T_2) is not significant due to scattered values. The impact of heating rate is explained by many authors [201]–[203], and it is generally accepted that the impact is attributed to the internal thermal gradient inside the PCM. In the DSC measurement, the sensor is located at the bottom of the sample crucible. Due to the temperature gradient inside the sample, the measured temperature is always overestimated while heating and underestimated while cooling. Clearly, a higher heating rate leads to a larger temperature gradient in the sample, hence a more significant hysteresis of the heat flow signal. The dependence of measured phase change behaviour on heating rate is an inherent defect of the dynamic measurement method. Generally, the effect of heating rate on the measured phase change temperatures cannot be avoided completely. For the total latent heat, a slight increase of latent heat with increasing heating rate also can be found. In particular, when the heating rate increased from 5 K/min to 10 K/min, the latent heat increased significantly. The difference of latent heat between heating rate at 5 K/min and 0.5 K/min is minor compared with the experimental deviation (the experimental deviations are very high at 0.5 K/min). Hence, this work used a heating rate of 5 K/min as a compromise which takes account of the time cost and also the small difference in phase change temperatures and latent heat with further decrease in heating rate .

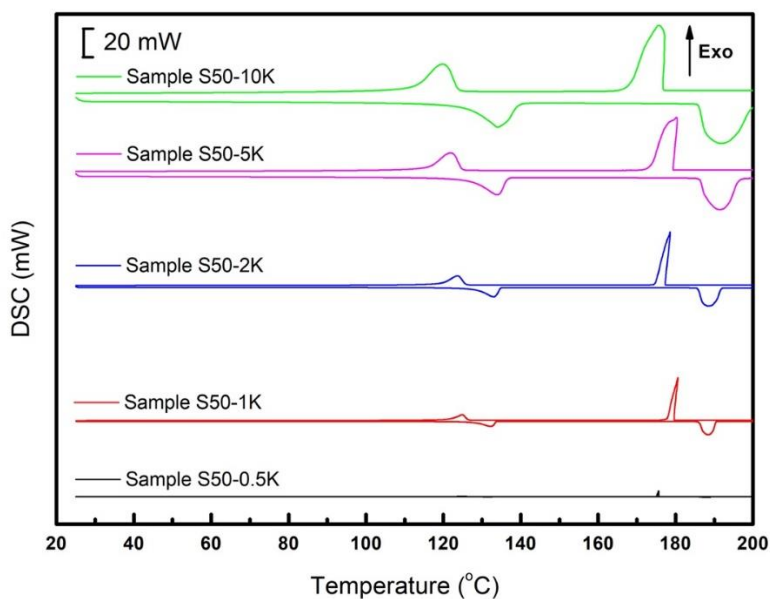


Figure 71 DSC curves of the sample S50 at different heating rate

Table 22 Melting point and latent heat of sample S50 at different heating rates

Heating					
Sample S50	T_1 (°C)	ΔH_1 (kJ/kg)	T_2 (°C)	ΔH_2 (kJ/kg)	Total ΔH (kJ/kg)
0.5 K/min	127.77 ± 0.04	71.83 ± 3.32	186.32 ± 0.33	144.38 ± 6.53	215.93 ± 7.33
1 K/min	127.51 ± 0.04	81.34 ± 0.18	185.28 ± 0.05	134.20 ± 0.59	215.54 ± 0.58
2 K/min	127.20 ± 1.11	80.05 ± 2.84	185.62 ± 0.15	135.63 ± 2.04	215.68 ± 4.77
5 K/min	126.17 ± 0.28	73.25 ± 5.45	185.25 ± 0.27	143.97 ± 4.12	217.22 ± 9.48
10 K/min	126.77 ± 0.24	80.52 ± 1.44	186.16 ± 0.04	143.78 ± 1.64	224.30 ± 3.08
Cooling					
0.5 K/min	126.64 ± 0.13	75.45 ± 10.38	175.78 ± 0.23	131.57 ± 6.74	207.02 ± 17.11
1 K/min	125.63 ± 0.06	79.16 ± 0.59	174.54 ± 0.59	133.69 ± 0.62	212.85 ± 0.98
2 K/min	125.20 ± 0.03	78.30 ± 0.39	175.78 ± 1.13	135.03 ± 1.90	213.33 ± 1.93
5 K/min	122.91 ± 0.10	73.22 ± 1.46	174.39 ± 0.51	141.9 ± 2.00	215.12 ± 3.38
10 K/min	123.37 ± 0.01	86.38 ± 0.50	177.33 ± 1.32	141.44 ± 0.87	227.82 ± 1.35

(2) Specific heat

The specific heat (kJ/(kg·°C)) of FSCPCM at different temperatures is shown in Table 23. One can see the specific heat is increasing with the temperature increase. The specific heat at 125°C is abnormally high compared with other temperatures due to the impact of the phase change process of HDPE (124.91°C). The other points are not affected. Hence, the specific heat at 125°C is discarded. Then, an average of the specific heat in the temperature range of 25 °C to 200°C can be determined. It can be found that the average specific heats for all the FSCPCMs are similar. Besides, the specific heat of the pure HDPE and the PE are shown in Table 23. One can see that HDPE presents a higher specific heat than that of PE. As the prepared FSCPCM is a composite of HDPE, PE, and graphite, its specific heat is moderate compared with that of the HDPE and PE.

Table 23 Specific heat of the composite PCMs

T (°C)	25	50	75	100	125	150	175	200	average
Sample S30	1.06 ±0.47	1.55 ±0.04	1.74 ±0.04	2.04 ±0.04	<u>4.37</u> ±0.29	2.05 ±0.02	2.16 ±0.04	2.36 ±0.04	1.85 ±0.06
Sample S40	1.33 ±0.01	1.46 ±0.00	1.65 ±0.01	1.94 ±0.04	<u>4.71</u> ±0.00	1.99 ±0.02	2.16 ±0.02	2.28 ±0.02	1.83 ±0.01
Sample S50	1.36 ±0.05	1.51 ±0.14	1.68 ±0.12	1.93 ±0.12	<u>3.95</u> ±0.33	2.01 ±0.08	2.20 ±0.10	2.40 ±0.22	1.87 ±0.14
HDPE	-	1.78 ±0.10	2.03 ±0.09	2.55 ±0.09	<u>10.25</u> ±0.24	2.36 ±0.06	2.42 ±0.07	2.41 ±0.16	2.26 ±0.11
PE	-	1.24 ±0.02	1.36 ±0.09	1.45 ±0.15	1.60 ±0.20	1.84 ±0.18	2.12 ±0.19	2.26 ±0.05	1.70 ±0.11

(3) Energy density

The energy density of the FSCPCM can be calculated by Eq. 10 with the phase change enthalpy and specific heat in Table 20 & Table 23 (see details in section 4.3.2.1). According to its phase change temperature, this work considers a working temperature range from 100°C to 200°C.

The specific heat values are fitted in a linear equation as shown in Table 24. It should be noted that the function of heat capacity is fitted based on the experimental results from 100 °C to 200 °C, therefore the fitted function is more precise for the calculation of heat capacity and energy density within this temperature range. By summing the sensible heat stored and the latent heat stored, the total energy density is calculated and displayed in Table 24. One can see from Table 24 that a higher PE loading of the FSCPCM presents a higher energy density. The total energy density has been enhanced by 5.46% when the percentages of PE increased from 30 wt.% to 50 wt.%. For a temperature range of 100 °C to 200 °C, sample S50 presents an extremely high energy storage density (426.17 kJ/kg) in mid-high temperature TES application.

Table 24 Fitting curve of specific heat and calculated energy density

sample	The fitting curve of the C_p (100 °C to 200 °C)	Sensible heat (kJ/kg)	Latent heat (kJ/kg)	total energy density (kJ/kg)
S30	$C_p = 0.00618T + 1.16712$	209.41	194.71	404.12
S40	$C_p = 0.0053T + 1.24291$	203.79	205.37	409.16
S50	$C_p = 0.00559T + 1.25106$	208.95	217.22	426.17

6.3.2.2 Thermal conductivity

The thermal conductivity of the FSCPCMs and pure HDPE are shown in Figure 72. One can see that the thermal conductivity of the FSCPCM is decreasing with the increase of temperature, which shows the same trend as the KNO_3 -diatomite-graphite CPCM. It can be noted that the thermal conductivity of HDPE decreases at the beginning and then starts to increase at 120 °C. This is likely due to the impact of the early phase transition process of HDPE at 117.72 °C (see Table 20), as the phase change process can affect the heat capacity of the material. It is also found by Ghossein et al.

[204] that there is a jump in thermal conductivity when the temperature closes to the melting temperature. Whereas, for the FSCPCMs, the thermal conductivity at 120 °C were not affected by the phase change process, as its onset phase change temperature is ~122 °C.

As displayed in Figure 72, one can see the thermal conductivity of the pure HDPE is much lower than the FSCPCM. Besides, the FSCPCM with a higher PE percentage shows a higher thermal conductivity. Table 25 displays the averaged thermal conductivity and conductivity enhancements. One can see that pure HDPE has an average thermal conductivity of 0.33 W/(m·K), which agrees with the values (~0.39 W/(m·K), ~0.45 W/(m·K)) in literature [205], [206]. The average thermal conductivity of the FSCPCM has been enhanced significantly compared with the HDPE, with an increment up to 26.02% for sample S50. The improvement is due to the addition of graphite, which has an extremely high thermal conductivity of ~209 W/(m·K) [205]. Also, PE content has enhanced the overall thermal conductivity of the composite. It is reported that the thermal conductivity of PE is ~0.53 W/(m·K) to ~0.9 W/(m·K) [207], [208], which is higher than the HDPE. Therefore, the thermal conductivity of the FSCPCM also increases with an increased ratio of PE particles.

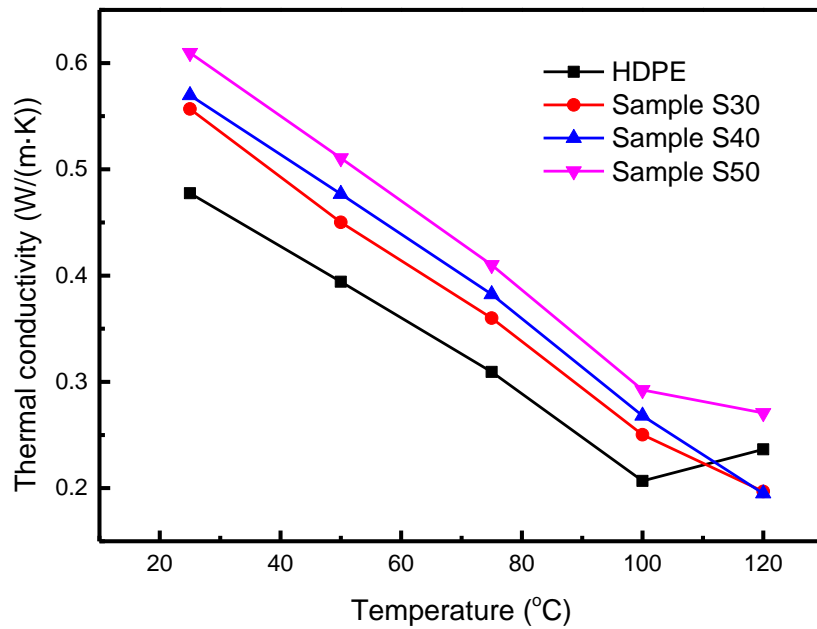


Figure 72 Thermal conductivities of the composite PCMs and HDPE

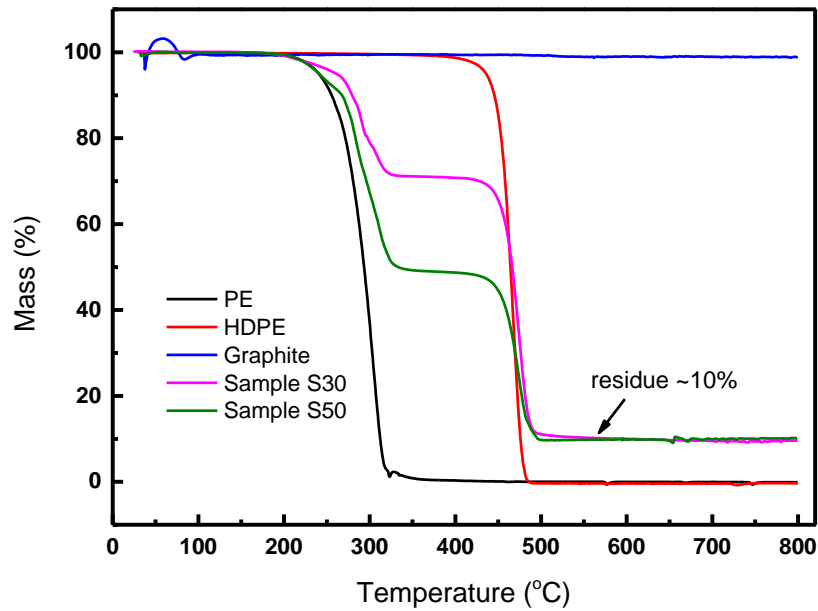
Table 25 Average and enhancement of the thermal conductivity

sample	HDPE	S30	S40	S50
Average (w/(m·K))	0.33±0.01	0.36±0.01	0.38±0.01	0.42±0.01
enhancement	-	9.20%	13.89%	26.02%

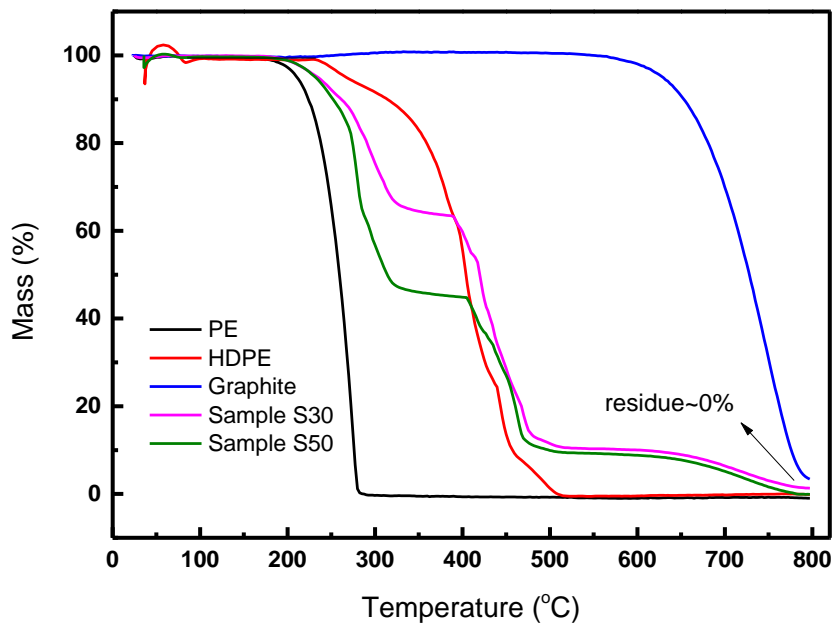
6.3.2.3 Thermal stability

Thermal stability of the FSCPCM in nitrogen and air atmospheres was studied by TGA; see Figure 73. The initial degradation temperature in this work is determined by the point of 5 wt.% weight loss ($T_{5\%}$). Besides, temperature ($T_{100\%}$) of 100 wt.% weight loss and residue weight at 800°C were also shown in Table 26. From Figure 73, one can see graphite presents the highest thermal stability without any degradation in nitrogen and then follows HDPE and PE. In the air atmosphere,

the trend is similar but the graphite was observed degraded at $\sim 750\text{ }^{\circ}\text{C}$ due to oxidization. PE and HDPE decompose both in air and nitrogen atmosphere. In nitrogen, HDPE shows a much higher thermal stability than in air, which is likely due to the combustion of HDPE. However, the decomposition temperature of PE only increased slightly in nitrogen than in air, indicating PE is not sensitive to the oxygen. The FSCPCM displays a two-stage degradation in the nitrogen atmosphere due to the decomposition of PE and HDPE, while also presents a third degradation in air atmosphere due to the oxidization of graphite at $\sim 750\text{ }^{\circ}\text{C}$. From Table 26, one can see that PE and HDPE decomposed completely at 365°C and 485.8°C in nitrogen, and completely decomposed in the air at 285.2°C and 508.7°C . The FSCPCM decomposed completely in the air, but has a residue of $\sim 10\%$ in nitrogen due to the remained graphite. Generally, PE is the least thermally stable component in the FSCPCM (210.8°C), and the working temperature should be controlled below its decomposition temperature. Ideally, usage over $200\text{ }^{\circ}\text{C}$ should be monitored carefully to avoid exceeding the maximum working temperature. Besides, using nitrogen as the working atmosphere is slightly helpful to raise the thermal stability of FSCPCM up to $240.5\text{ }^{\circ}\text{C}$.



(a) TGA curves at N₂ atmosphere



(b) TGA curves at Air atmosphere

Figure 73 TGA curves of the composite PCMs and the components at N₂ and Air atmosphere

Table 26 Thermal degradation properties at N₂ and Air atmosphere

Nitrogen atmosphere			
Sample	T _{5%} (°C)	T _{100%} (°C)	Residue (800°C)
HDPE	435	485.8	0
PE	240.5	365.0	0
Graphite	/	/	100%
S30	261	/	9.66%
S50	240.8	/	10.19%
Air atmosphere			
Sample	T _{5%} (°C)	T _{100%} (°C)	Residue (800°C)
HDPE	267	508.7	0
PE	210.8	285.2	0
Graphite	629.2	/	3.17%
S30	234.6	/	1.29%
S50	232	781.1	0

6.3.3 Thermal cycling stability

6.3.3.1 Latent heat and phase change temperatures

Figure 74 displays the DSC curves of sample S50 after thermal cycling, where one can see its phase change behaviour remains unchanged. Phase change parameters of the FSCPCM after different times of thermal cycle are shown in Table 27. The difference between the cycled sample and the not-cycled sample are also displayed. It can be found that the changes in phase change temperature are minor, which are from -1.37 °C to 3.05 °C. These differences are within the experimental uncertainties (<5%). Therefore, the phase change temperature of FSCPCM is not affected by thermal cycling. In terms of the latent heat, one can observe a slight degradation with increasing times of thermal cycling. It is shown in Table 27 that, the latent heat of the FSCPCM has degraded by -5.72% after 100 times of thermal cycling. This is likely attributed to the degradation of PE, which is the least thermally stable component in the composite from the previous study.

It is reported that other possible PCMs for mid-high temperature thermal energy storage also present a deficiency of cycling stability, such as sugar alcohols (erythritol, D-mannitol, and galactitol) [209] and salt hydrates [210], [211]. Besides, most sugar alcohols and salt hydrates present an extraordinarily high degree of supercooling (can be $\sim 90^\circ\text{C}$) [212], which strongly hinders their application. PE does not present a significant supercooling defect, and it has advantages of cost-effective, non-hazardous, non-corrosive. Also, it has a very high latent energy storage capacity compared with mid-high temperature PCMs. Although degradation was observed, PE still displays an excellent potential for TES applications.

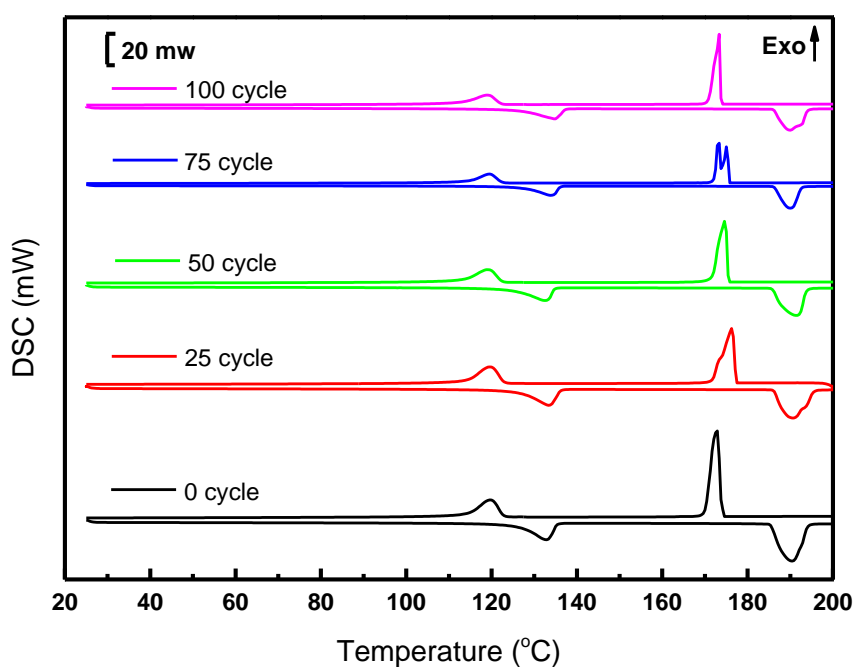


Figure 74 DSC curves of sample S50 after different thermal cycling times

Table 27 Melting point and latent heat of sample S50 after different thermal cycling times

Heating (endothermal)								
	T _{o1} (°C)	Variatio n (%)	Δ H ₁ (kJ/kg)	T _{o2} (°C)	Variatio n (%)	Δ H ₂ (kJ/kg)	Total Δ H (kJ/kg)	Variatio n (%)
0 cycle	126.17 ±0.28	-	73.25 ±5.45	185.25 ±0.27	-	143.97 ±4.12	217.22 ±9.48	-
25 cycles	126.20 ±0.21	0.03	83.55 ±2.01	186.03 ±0.23	0.78	132.07 ±3.02	215.62 ±5.85	-0.74%
50 cycles	124.80 ±0.12	-1.37	76.03 ±1.26	185.71 ±0.19	0.46	132.47 ±1.16	208.50 ±1.86	-4.01%
75 cycles	127.37 ±0.08	1.2	83.33 ±3.22	186.14 ±1.31	0.89	126.72 ±1.89	210.05 ±5.34	-3.30%
100 cycles	126.10 ±0.33	-0.07	78.33 ±2.08	185.98 ±0.15	0.73	126.46 ±1.31	204.79 ±3.68	-5.72%

6.3.3.2 Thermal stability

Figure 75 displays the TGA curves of Sample S50 with and without thermal cycling in the N₂ atmosphere. Mass loss of the first degradation of the FSCPCM represents the decomposition of PE content. One can find that the mass loss has reduced from 50.79% to 44.59%, indicating the percentage of PE content has dropped from 50.79% to 44.59% after 100 times of thermal cycling. Therefore, it confirms that the degradation after thermal cycling is attributed to the loss of PE content. If one considers the latent heat of PE in cycled FSCPCM by its mass ratio, the theoretical enthalpy for 44.59 wt.% PE is calculated to be ~ 127.71 kJ/kg. This value matches well with the latent heat measured by DSC (126.46 kJ/kg). Hence, both TGA and DSC measurements can be used to study the degree of degradation for the FSCPCMs.

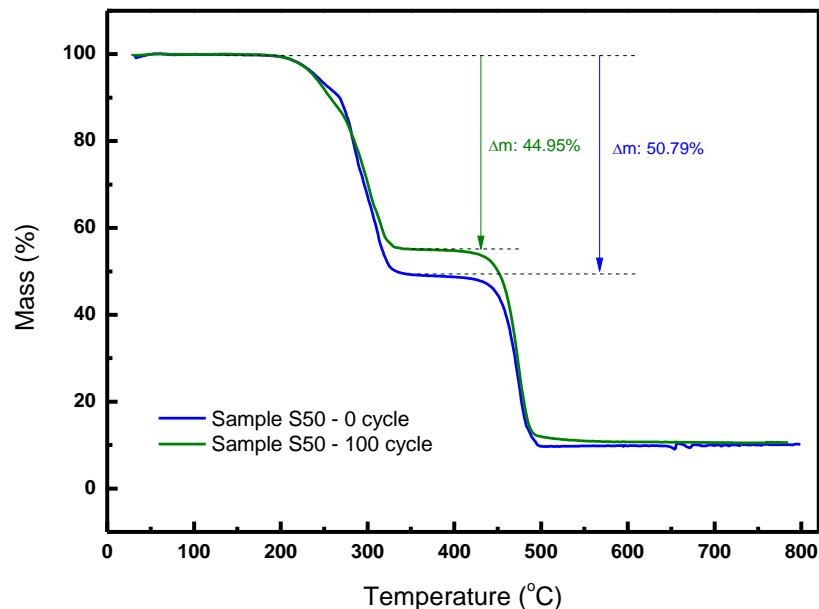


Figure 75 TGA curves of Sample S50 with and without 100 thermal cycles in the N₂ atmosphere

6.3.4 Chemical compatibility

6.3.4.1 Chemical compatibility between components in the FSCPCM

Chemical compatibility between the components in FSCPCM was studied by IR spectroscopy. Figure 76 shows the IR spectra of the components and the FSCPCM. One can see that graphite does not show any characteristic peak as it does not have any functional group. PE spectra display the characteristic peaks for O-H (~3300), -CH₂ (~2930), C-O (~1030) and the CH₂-OH (~1380) group, which agrees with the literature [213]. The IR spectra of HDPE shows the characteristic peaks at ~2912, ~2849, ~1470 and ~720 cm⁻¹ for the -CH₂ stretching, -CH₂ stretching, -CH₂ bending and -CH₂ rocking [131]. After HDPE, PE and graphite are compounded, the FSCPCM spectra show one-to-one position corresponding to each component. No new peak was found for the FSCPCM. Therefore, it can be concluded that the synthesis process of FSCPCM is a physical process and there is no chemical reaction happens. Also, the component in the FSCPCM is chemically compatible with each other.

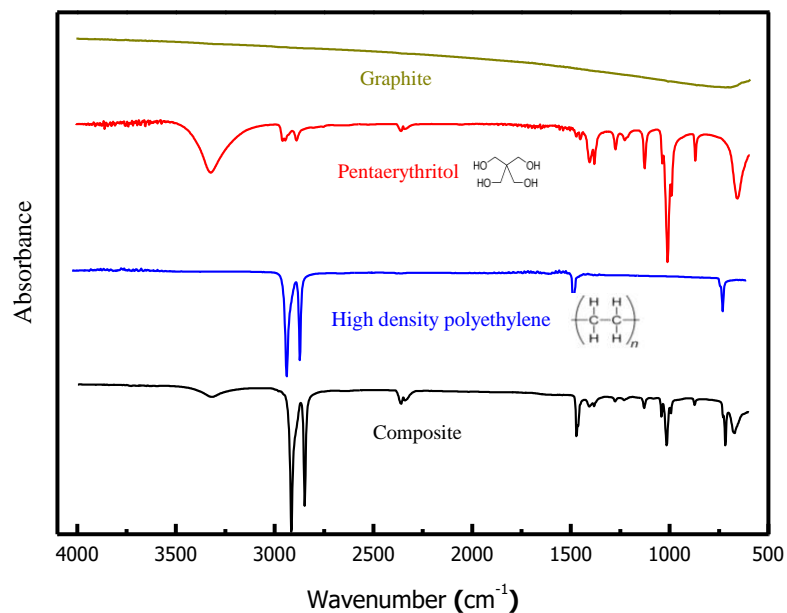


Figure 76 Chemical compatibility between components of the FSCPCM

6.3.4.2 Chemical stability after thermal cycles

Chemical stability the FSCPCM after 100 times of thermal cycling was also investigated. IR spectra of the FSCPCM before and after 100 times of thermal cycling is shown in Figure 77. One can see that the peaks show a one-to-one position corresponding, indicating no new substance generated after thermal cycling. Therefore, good chemical stability of the FSCPCM after thermal cycling can be confirmed.

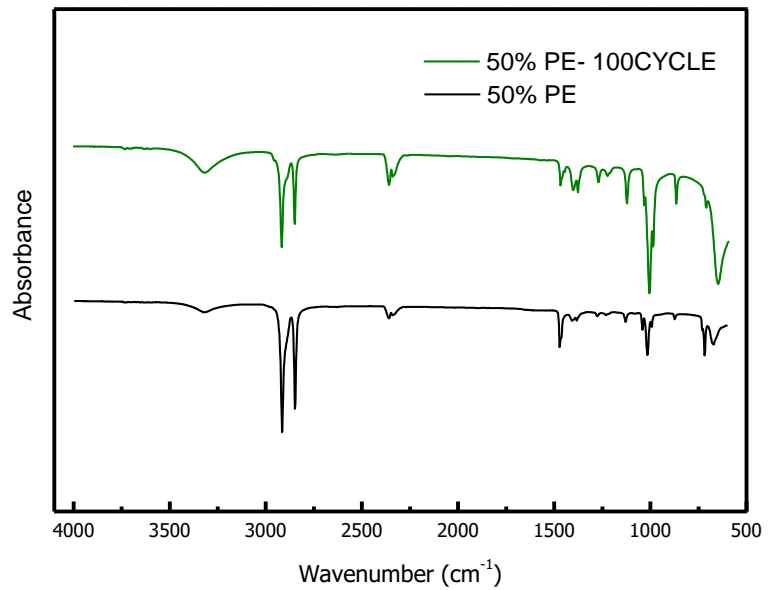


Figure 77 Chemical compatibility of the FSCPCM after thermal cycles

6.4 Summary

This chapter studies the structural properties, thermal properties, thermal cycling stability and chemical stability of the prepared HDPE-PE-Cg FSCPCM. The studied structural properties include particle dispersion efficiency, porosity and microstructure. It is found that the surface-to-volume ratio is increasing with the extrusion speed until a certain value then starts to decrease. The change of surface-to-volume ratio with increasing extrusion speed is the result of two factors: the enhancement of shear stress and the decrease of the mixing time. Hence, when the negative effect of the reduced residence time outweighs the positive effect of the increased shear stress and flow velocity, particle dispersion will decrease with the increasing extrusion rate. The optimal extrusion rate for the best dispersion of sample S50-1mm and sample S50-0.25 mm is 25 rpm and 20 rpm, respectively. Meanwhile, the porosity of FSCPCM shows a trend of increment with the increasing processing temperature. It has increased from 1.705% to 10.901% when the processing temperature increases from 150°C to 180°C. The porosity increment is expected caused by the vaporization of PE for its relatively low thermal stability. Morphology on the cross-section of FSCPCM shows a great interfacial bonding between the PE particles and the HDPE matrix, as no pulled-out trace was observed.

Thermal property study on the FSCPCM includes properties of energy storage capacity, thermal conductivity, and thermal stability. All FSCPCMs have two phase-change peaks during the heating/cooling process, which are corresponding to the phase transition process of HDPE and PE. HDPE and PE are both PCM in the FSCPCM, and they also present a good self-reinforced property to keep structure stable. Hence, this FSCPCM shows great advantages of high energy density, as well as structural stability. Besides, PE presents a higher latent heat storage capacity than HDPE. As a result, sample S50 with the highest PE content shows the most effective energy storage capacity than other FSCPCMs. It is calculated that its total energy density can reach as high as 426.17 kJ/kg,

which presents great potential in mid-high temperature TES applications. The FSCPCM suffers a slight supercooling issue, with a supercooling degree of 6.94 °C and 13.78 °C for HDPE and PE respectively. Compared with some sugar alcohols and salt hydrates for mid-high temperature, this supercooling degree is acceptable and shows an insignificant impact on practical application. The thermal conductivity of FSCPCM was investigated, showing an enhancement of 26.02% for sample S50 compared with the pure HDPE. PE and graphite both show a higher thermal conductivity than HDPE, so they can contribute to a higher overall thermal conductivity of the composite. Study on the thermal stability reveals that PE is the least thermally stable component in the FSCPCM. Therefore, its working temperature should be controlled below the decomposition temperature of PE (210.8 °C). Besides, using nitrogen as the working atmosphere is slightly helpful to raise the thermal stability of FSCPCM up to 240.5 °C.

Long-term stability of the FSCPCM was investigated by 100 times thermal cycling. It shows a slight degradation (-5.72%) in the total latent heat after 100 times of thermal cycling. The DSC and TGA measurements both reveal that degradation is attributed to the loss of PE content. However, degradation after thermal cycling is also observed in sugar alcohols and salt hydrates, which are regarded as promising candidates for mid-high temperature TES application. Therefore, the FSCPCM still displays an excellent potential for TES application for its advantages of cost-effective, non-hazardous, non-corrosive.

Chemical compatibility of the FSCPCM was investigated by IR, showing that no chemical reaction was observed between the components. After 100 times of thermal cycling, the materials are still chemically compatible.

7 Conclusions and future work

7.1 Conclusions

This work focuses on investigating advanced manufacturing technologies, aiming to prepare large-scaleable high-performance FSCPCMs at a low cost. Also, this work is to understand how the manufacturing process affects the FSCPCM structures and hence their properties. The studied manufacturing methods include a modified mix-sintering method and a continuous hot-melt extrusion method. The modified mix-sintering method is integrated with a preheating process. The impact of adding the preheating process on the thermal and physical properties of FSCPCM is studied by comparing with the conventional fabrication route. The microstructure development of the preheated FSCPCM is also explained in this work. Besides, the criteria for using the modified mix-sintering method to produce high-quality products are investigated and verified. For the hot-extrusion method, a novel HDPE-pentaerythritol (PE)-graphite FSCPCM was firstly extruded by a single-screw extruder. Effects of different processing parameters on the extrusion stability and rheological behaviour were studied. The internal structure of extrudates was also correlated with the processing parameters. Finally, thermal properties and thermal cycling stability were investigated for the novel FSCPCM. The main outcomes of this work are summarized in the following points:

1. The modified mix-sintering method with a preheating process integrated is proved to improve the physical and thermal properties of the diatomite-KNO₃ FSCPCM effectively. The modified mix-sintering method contributes to a denser structure of the FSCPCM with density increased by ~20% and the porosity reduced by ~9.18%. The thermal conductivity has also enhanced by 54.94% due to the reduction of air trapped inside the composite.

2. The melted PCM (salt KNO_3) was found being absorbed into the porous structure of diatomite as well as the interparticle voids during the preheating process, which results in a less porous structure of the CPCM after compression and sintering. The microstructure of the sintered CPCM remains unchanged after repeated thermal cycling.
3. A good wettability between the liquid and solid phase was found to be an essential criterion to obtain high-quality FSCPCMs by applying the preheating process. However, a porous structure of the supporting materials is not an essential condition. This was verified by comparing with a graphite- KNO_3 composite and a SiO_2 - KNO_3 composite.
4. Hot-melt extrusion method is a continuous and easy-controllable manufacturing method which is able to prepare CPCMs in a large scale (~ 1 - ~ 2.5 kg/h). This method has significantly improved the productivity of the CPCM.
5. Two extrusion instabilities were observed during the process: sharkskin defect and oscillating defect. These extrusion instabilities were found suppressed with decreasing particle percentages, decreasing particle size, and increasing processing temperature. The flow instability normally occurs when the extrusion rate (shear rate) exceeds a critical value.
6. A periodic surface distortion was found evolving with the periodic pressure oscillation, alternatively in smooth surface and distorted surface: in the compression phase, surface distortion intensifies with the accumulated pressure; while in the relaxation phase, the interfacial polymer chains slip on the surface and resulting in a smooth surface.

7. The viscoelastic property of FSCPCM was found affected by the particle contents, particle size and temperature. The dynamic moduli were found increased with the increasing particle content, decreasing particle sizes, and decreasing processing temperature. Besides, the FSCPCM presents a Non-Newtonian rheological behaviour with shearing-thinning.
8. The structural properties of the extrudates were correlated with the processing parameters. The particle dispersion increases with the extrusion speed until a certain value before it starts to decrease. This is because the particle dispersion is affected both by the shear stress and the mixing time, with the former increasing with increasing extrusion speed and the latter showing the opposite trend. Besides, the porosity of the extrudate was found increasing with the increasing processing temperature due to vaporization of PE.
9. The extruded FSCPCM could be a promising TES material for the mid-high temperature application, with an extremely high energy density (426.17 kJ/kg) from 100 °C to 200 °C. Study on thermal cycling stability shows a slight decrease in the latent heat by 5.72% after sample S50 being cycled for 100 times. The maximum thermally stable temperature of the FSCPCM is ~210°C in the air due to the less thermally stable component of PE.

7.2 Future work

This work has obtained some results which help to develop the manufacturing technology for FSCPCMs. However, some of the works can be further investigated or expanded. The recommendations for future work are:

1. Impacts of manufacturing method and processing parameters on the thermophysical properties and the microstructure of prepared FSCPCM are investigated in this work. More studies could be conducted in the future to build up a database about the linkage between the processing parameters and the properties of material. In the end, the manufacturing method and parameters can be selected and designed easily by the requirements of materials properties.
2. Modified mix-sintering fabrication method has been demonstrated to be an effective method to improve the thermophysical properties of the FSCPCM. Besides, good wetting behaviour is essential to obtain high-quality products by applying the preheating process. In this work, we discussed FSCPCMs consisting of two components, whether wettable or not wettable with each other. FSCPCMs which are composed of more than two components have not been investigated. Especially when the wettable component and the non-wettable component are coexisted in the FSCPCM, whether the preheating process is effective can be a very interesting topic.
3. This work has successfully applied the hot-melt extrusion method to prepare a polymer-based FSCPCM. However, it is necessary to expand the species of the CPCM that can be processed by the extruder. The ceramic-based CPCM is a promising candidate to be extruded in future, as there is an existed industrial process that uses ram extruder for brick shaping. However, this type of material can not be extruded by the single-screw extruder that we used in this work.
4. Wall-slip phenomenon was found to have a significant impact on the flow instability. However, the wall-slip phenomenon is a sophisticated topic that has not been revealed thoroughly. A better understanding of the wall-slip phenomenon is helpful for the

control of flow instability. Therefore, it is necessary to study the underlying physics of the wall-slip phenomenon.

5. The prepared FSCPCMs present excellent energy storage properties in a small amount (~g) measuring by the lab instruments. However, for future application, these materials have to be demonstrated in a much larger scale in practice. Therefore, investigating the thermal performance of the FSCPCMs in test rigs is recommended in future to verify their feasibility in practical applications.

References

- [1] "GECO 2019." [Online]. Available: <https://www.iea.org/geco/>. [Accessed: 07-May-2019].
- [2] L. Miró, J. Gasia, and L. F. Cabeza, "Thermal energy storage (TES) for industrial waste heat (IWH) recovery: A review," *Appl. Energy*, vol. 179, pp. 284–301, Oct. 2016.
- [3] B. Zalba, J. M. Marín, L. F. Cabeza, and H. Mehling, "Review on thermal energy storage with phase change: materials, heat transfer analysis and applications," *Appl. Therm. Eng.*, vol. 23, no. 3, pp. 251–283, Feb. 2003.
- [4] *The Power of Change*. Washington, D.C.: National Academies Press, 2016.
- [5] J. Gustavsson, "Energy Storage Technology Comparison-A knowledge guide to simplify selection of energy storage technology."
- [6] T.-T. Nguyen, V. Martin, A. Malmquist, and C. A. S. Silva, "A review on technology maturity of small scale energy storage technologies ★."
- [7] P. G. Taylor, R. Bolton, D. Stone, and P. Upham, "Developing pathways for energy storage in the UK using a coevolutionary framework," *Energy Policy*, vol. 63, pp. 230–243, Dec. 2013.
- [8] Z. Ge *et al.*, "Thermal energy storage: Challenges and the role of particle technology," *Particuology*, vol. 15, pp. 2–8, 2014.
- [9] N. R. Jankowski and F. P. McCluskey, "A review of phase change materials for vehicle component thermal buffering," *Appl. Energy*, vol. 113, pp. 1525–1561, Jan. 2014.
- [10] B. Copertaro Advisor and P. Principi, "UNIVERSITÀ POLITECNICA DELLE MARCHE CORSO DI DOTTORATO DI RICERCA IN SCIENZE DELLA VITA E DELL'AMBIENTE CURRICULUM IN

PROTEZIONE CIVILE ED AMBIENTALE Phase Change Materials (PCMs): an Opportunity for Energy Saving in the Cold Chain.”

- [11] S. M. Hasnain, “Review on sustainable thermal energy storage technologies, part I: Heat storage materials and techniques,” *Energy Convers. Manag.*, vol. 39, no. 11, pp. 1127–1138, Aug. 1998.
- [12] “Evidence Gathering: Thermal Energy Storage (TES) Technologies Evidence Gathering: Thermal Energy Storage (TES) Technologies Acknowledgements,” 2016.
- [13] R. Baetens, B. Petter Jelle, and A. Gustavsen, “Phase change materials for building applications: A state-of-the-art review,” *Energy Build.*, vol. 42, no. 7491, pp. 1361–1368, 2010.
- [14] M. M. Farid and X. D. Chen, “Domestic electrical space heating with heat storage,” 1999.
- [15] Y. Shin, D.-I. Yoo, and K. Son, “Development of thermoregulating textile materials with microencapsulated phase change materials (PCM). II. Preparation and application of PCM microcapsules,” *J. Appl. Polym. Sci.*, vol. 96, no. 6, pp. 2005–2010, Jun. 2005.
- [16] S. S. Mostafavi Tehrani, Y. Shoraka, K. Nithyanandam, and R. A. Taylor, “Cyclic performance of cascaded and multi-layered solid-PCM shell-and-tube thermal energy storage systems: A case study of the 19.9 MWe Gemasolar CSP plant,” *Appl. Energy*, vol. 228, pp. 240–253, Oct. 2018.
- [17] T. Nomura, N. Okinaka, and T. Akiyama, “Technology of Latent Heat Storage for High Temperature Application: A Review,” *ISIJ Int.*, vol. 50, no. 9, pp. 1229–1239, 2010.

- [18] M. M. Farid, A. M. Khudhair, S. A. K. Razack, and S. Al-Hallaj, "A review on phase change energy storage: materials and applications," *Energy Convers. Manag.*, vol. 45, no. 9, pp. 1597–1615, 2004.
- [19] A. M. Khudhair and M. M. Farid, "A review on energy conservation in building applications with thermal storage by latent heat using phase change materials," *Energy Convers. Manag.*, vol. 45, no. 2, pp. 263–275, 2004.
- [20] Z. Ge *et al.*, "Thermal energy storage: Challenges and the role of particle technology," *Particuology*, vol. 15, pp. 2–8, Aug. 2014.
- [21] A. Abhat, "LOW TEMPERATURE LATENT HEAT THERMAL ENERGY STORAGE: HEAT STORAGE MATERIALS," vol. 10, no. 4, pp. 313–332.
- [22] B. Zalba, J. M. Marín, L. F. Cabeza, and H. Mehling, "Review on thermal energy storage with phase change: materials, heat transfer analysis and applications," *Appl. Therm. Eng.*, vol. 23, no. 3, pp. 251–283, Feb. 2003.
- [23] P. Zhang, X. Xiao, and Z. W. Ma, "A review of the composite phase change materials: Fabrication, characterization, mathematical modeling and application to performance enhancement," *Appl. Energy*, vol. 165, pp. 472–510, Mar. 2016.
- [24] S. Kuravi, J. Trahan, D. Y. Goswami, M. M. Rahman, and E. K. Stefanakos, "Thermal energy storage technologies and systems for concentrating solar power plants," *Prog. Energy Combust. Sci.*, vol. 39, pp. 285–319, 2013.
- [25] E. B. Jebasingh, "Effects of various types of graphite on the thermal conductivity and energy storage properties of ternary eutectic fatty acid-based composite as phase change material," *Renewables Wind. Water, Sol.*, vol. 3, no. 1, p. 8, Dec. 2016.

- [26] A. Lázaro, B. Zalba, M. Bobi, C. Castellón, and L. F. Cabeza, "Experimental study on phase change materials and plastics compatibility," *AIChE J.*, vol. 52, no. 2, pp. 804–808, Feb. 2006.
- [27] G. Diarce, I. Gandarias, Campos-Celador, A. García-Romero, and U. J. Griesser, "Eutectic mixtures of sugar alcohols for thermal energy storage in the 50-90°C temperature range," *Sol. Energy Mater. Sol. Cells*, vol. 134, pp. 215–226, 2015.
- [28] G. Leng, H. Navarr, G. Wellio, C. Li, Y. Huang, and Y. Zhao, "Design of composite materials / devices for thermal storage – A critical review," pp. 1–56.
- [29] M. Duquesne, A. Godin, E. P. Del Barrio, and F. Achchaq, "Crystal growth kinetics of sugar alcohols as phase change materials for thermal energy storage," *Energy Procedia*, vol. 139, pp. 315–321, 2017.
- [30] R. Liu, F. Zhang, W. Su, H. Zhao, and C. Wang, "Impregnation of porous mullite with Na₂SO₄ phase change material for thermal energy storage," *Sol. Energy Mater. Sol. Cells*, vol. 134, pp. 268–274, Mar. 2015.
- [31] I. Sarbu, C. Sebarchievici, I. Sarbu, and C. Sebarchievici, "A Comprehensive Review of Thermal Energy Storage," *Sustainability*, vol. 10, no. 2, p. 191, Jan. 2018.
- [32] Z. Ge, F. Ye, and Y. Ding, "Composite Materials for Thermal Energy Storage: Enhancing Performance through Microstructures," *ChemSusChem*, vol. 7, no. 5, pp. 1318–1325, May 2014.
- [33] M. Li, Z. Wu, and H. Kao, "Study on preparation and thermal properties of binary fatty acid/diatomite shape-stabilized phase change materials," *Sol. Energy Mater. Sol. Cells*, vol. 95, no. 8, pp. 2412–2416, Aug. 2011.

- [34] J. Temuujin, K. Okada, and K. J. D. MacKenzie, "Preparation of porous silica from vermiculite by selective leaching," *Appl. Clay Sci.*, vol. 22, no. 4, pp. 187–195, 2003.
- [35] B. Xu, H. Ma, Z. Lu, and Z. Li, "Paraffin/expanded vermiculite composite phase change material as aggregate for developing lightweight thermal energy storage cement-based composites," *Appl. Energy*, vol. 160, pp. 358–367, Dec. 2015.
- [36] P. Lv, C. Liu, and Z. Rao, "Review on clay mineral-based form-stable phase change materials: Preparation, characterization and applications," *Renew. Sustain. Energy Rev.*, vol. 68, pp. 707–726, Feb. 2017.
- [37] A. Sari, A. Karaipekli, and C. Alkan, "Preparation, characterization and thermal properties of lauric acid/expanded perlite as novel form-stable composite phase change material," *Chem. Eng. J.*, vol. 155, pp. 899–904, 2009.
- [38] Y. Qin *et al.*, "Sodium sulfate-diatomite composite materials for high temperature thermal energy storage," *Powder Technol.*, vol. 282, pp. 37–42, 2015.
- [39] T. Nomura, N. Okinaka, and T. Akiyama, "Impregnation of porous material with phase change material for thermal energy storage," *Mater. Chem. Phys.*, vol. 115, pp. 846–850, 2009.
- [40] F. Ye, Z. Ge, Y. Ding, and J. Yang, "Multi-walled carbon nanotubes added to Na₂CO₃/MgO composites for thermal energy storage," *Particuology*, 2014.
- [41] A. Sari, "Fabrication and thermal characterization of kaolin-based composite phase change materials for latent heat storage in buildings," *Energy Build.*, vol. 96, pp. 193–200, Jun. 2015.
- [42] Z. Ge, F. Ye, and Y. Ding, "Composite materials for thermal energy storage: enhancing performance through microstructures," *ChemSusChem*, 2014.

- [43] Z. Ge, F. Ye, H. Cao, G. Leng, and Y. Qin, "Carbonate-salt-based composite materials for medium- and high-temperature thermal energy storage," *Particuology*, vol. 15, pp. 77–81, Aug. 2014.
- [44] F. Jiang *et al.*, "Diatomite-based porous ceramics with high apparent porosity: Pore structure modification using calcium carbonate," *Ceram. Int.*, vol. 45, no. 5, pp. 6085–6092, Apr. 2019.
- [45] T. Qian, J. Li, X. Min, Y. Deng, W. Guan, and L. Ning, "Diatomite: A promising natural candidate as carrier material for low, middle and high temperature phase change material," *Energy Convers. Manag.*, vol. 98, pp. 34–45, 2015.
- [46] T. Qian, J. Li, and Y. Deng, "Pore structure modified diatomite-supported PEG composites for thermal energy storage," *Sci. Rep.*, vol. 6, no. 1, p. 32392, Oct. 2016.
- [47] Y. Deng, J. Li, T. Qian, W. Guan, and X. Wang, "Preparation and Characterization of KNO₃/diatomite Shape-stabilized Composite Phase Change Material for High Temperature Thermal Energy Storage," *J. Mater. Sci. Technol.*, vol. c, no. 2, pp. 1–6, 2016.
- [48] G. Xu *et al.*, "Sodium nitrate – Diatomite composite materials for thermal energy storage," *Sol. Energy*, vol. 146, pp. 494–502, 2017.
- [49] Y. Qin, X. Yu, G. H. Leng, L. Zhang, and Y. L. Ding, "Effect of diatomite content on diatomite matrix based composite phase change thermal storage material," 2014.
- [50] Q. Zhang, H. Wang, Z. Ling, X. Fang, and Z. Zhang, "RT100/expand graphite composite phase change material with excellent structure stability, photo-thermal performance and good thermal reliability," 2015.

- [51] Y. Wu and T. Wang, "Hydrated salts/expanded graphite composite with high thermal conductivity as a shape-stabilized phase change material for thermal energy storage," *Energy Convers. Manag.*, vol. 101, pp. 164–171, 2015.
- [52] P. Mantilla Gilart, Á. Yedra Martínez, M. González Barriuso, and C. Manteca Martínez, "Development of PCM/carbon-based composite materials," *Sol. Energy Mater. Sol. Cells*, vol. 107, pp. 205–211, 2012.
- [53] T. Y. Choi, D. Poulikakos, J. Tharian, and U. Sennhauser, "Measurement of thermal conductivity of individual multiwalled carbon nanotubes by the 3- ω method," *Appl. Phys. Lett.*, vol. 87, no. 1, p. 013108, Jul. 2005.
- [54] J. Xiang and L. T. Drzal, "Investigation of exfoliated graphite nanoplatelets (xGnP) in improving thermal conductivity of paraffin wax-based phase change material," *Sol. Energy Mater. Sol. Cells*, vol. 95, no. 7, pp. 1811–1818, Jul. 2011.
- [55] Y. B. Cai, Q. F. Wei, D. F. Shao, Y. Hu, L. Song, and W. D. Gao, "Magnesium hydroxide and microencapsulated red phosphorus synergistic flame retardant form stable phase change materials based on HDPE/EVA/OMT nanocomposites/paraffin compounds," *J. Energy Inst.*, vol. 82, no. 1, pp. 28–36, Mar. 2009.
- [56] A. S. Sari, K. Kaygusuz, "High Density Polyethylene/Paraffin Composites as Form-stable Phase Change Material for Thermal Energy Storage."
- [57] A. Sari, "Form-stable paraffin/high density polyethylene composites as solid–liquid phase change material for thermal energy storage: preparation and thermal properties," *Energy Convers. Manag.*, vol. 45, pp. 2033–2042, 2004.

- [58] Y. Cai, Y. Hu, L. Song, Y. Tang, ... R. Y.-J. of A., and undefined 2006, "Flammability and thermal properties of high density polyethylene/paraffin hybrid as a form-stable phase change material," *Wiley Online Libr.*
- [59] Y. Cai, L. Song, Q. He, D. Yang, and Y. Hu, "Preparation, thermal and flammability properties of a novel form-stable phase change materials based on high density polyethylene/poly(ethylene-co-vinyl acetate)/organophilic montmorillonite nanocomposites/paraffin compounds," 2008.
- [60] F. Chen and M. P. Wolcott, "Miscibility studies of paraffin/polyethylene blends as form - stable phase change materials," *Eur. Polym. J.*, vol. 52, pp. 44–52, 2014.
- [61] X. Lv, Q. Yuan, C. Bai, X. Huang, and L. Lei, "A phenomenological description of moisture capacity of iron ores," *Particuology*, vol. 10, no. 6, pp. 692–698, Dec. 2012.
- [62] X. Li, J. G. Sanjayan, and J. L. Wilson, "Fabrication and stability of form-stable diatomite/paraffin phase change material composites," *Energy Build.*, vol. 76, pp. 284–294, Jun. 2014.
- [63] M. Li, Z. Wu, and H. Kao, "Study on preparation and thermal properties of binary fatty acid/diatomite shape-stabilized phase change materials," *Sol. Energy Mater. Sol. Cells*, vol. 95, pp. 2412–2416, 2011.
- [64] T. Qian, J. Li, H. Ma, and J. Yang, "Adjustable thermal property of polyethylene glycol/diatomite shape-stabilized composite phase change material," *Polym. Compos.*, vol. 37, no. 3, pp. 854–860, Mar. 2016.

- [65] Y. Konuklu, O. Ersoy, and O. Gokce, "Easy and industrially applicable impregnation process for preparation of diatomite-based phase change material nanocomposites for thermal energy storage," *Appl. Therm. Eng.*, vol. 91, pp. 759–766, Dec. 2015.
- [66] Z.-J. Duan *et al.*, "CaCl₂·6H₂O/Expanded graphite composite as form-stable phase change materials for thermal energy storage," 2013.
- [67] G. Fang, H. Li, Z. Chen, and X. Liu, "Preparation and characterization of stearic acid/expanded graphite composites as thermal energy storage materials," *Energy*, vol. 35, pp. 4622–4626, 2010.
- [68] Z. Huang, X. Gao, T. Xu, Y. Fang, and Z. Zhang, "Thermal property measurement and heat storage analysis of LiNO₃/KCl – expanded graphite composite phase change material," *Appl. Energy*, vol. 115, pp. 265–271, Feb. 2014.
- [69] H. Li, X. Liu, and G.-Y. Fang, "Synthesis and characteristics of form-stable n-octadecane/expanded graphite composite phase change materials," *Appl Phys A*, vol. 100, pp. 1143–1148, 2010.
- [70] Z. Ling, J. Chen, T. Xu, X. Fang, X. Gao, and Z. Zhang, "Thermal conductivity of an organic phase change material/expanded graphite composite across the phase change temperature range and a novel thermal conductivity model," *Energy Convers. Manag.*, vol. 102, pp. 202–208, 2015.
- [71] P. Mantilla Gilart, Á. Yedra Martínez, M. González Barriuso, and C. Manteca Martínez, "Development of PCM/carbon-based composite materials," *Sol. Energy Mater. Sol. Cells*, vol. 107, pp. 205–211, Dec. 2012.

- [72] S. Kim and L. T. Drzal, "High latent heat storage and high thermal conductive phase change materials using exfoliated graphite nanoplatelets," 2008.
- [73] Z. Lu, B. Xu, J. Zhang, Y. Zhu, G. Sun, and Z. Li, "Preparation and characterization of expanded perlite/paraffin composite as form-stable phase change material," *Sol. ENERGY*, vol. 108, pp. 460–466, 2014.
- [74] R. Li, J. Zhu, W. Zhou, X. Cheng, and Y. Li, "Thermal properties of sodium nitrate-expanded vermiculite form-stable composite phase change materials," 2016.
- [75] A. Hussain, I. H. Abidi, C. Y. Tso, K. C. Chan, Z. Luo, and C. Y. H. Chao, "Thermal management of lithium ion batteries using graphene coated nickel foam saturated with phase change materials," *Int. J. Therm. Sci.*, vol. 124, pp. 23–35, Feb. 2018.
- [76] Y. Cai *et al.*, "Flexible cellulose acetate nano-felts absorbed with capric–myristic–stearic acid ternary eutectic mixture as form-stable phase-change materials for thermal energy storage/retrieval," *J. Therm. Anal. Calorim.*, vol. 128, no. 2, pp. 661–673, May 2017.
- [77] T. Qian, J. Li, W. Feng, and H. Nian, "Enhanced thermal conductivity of form-stable phase change composite with single-walled carbon nanotubes for thermal energy storage," *Sci. Rep.*, vol. 7, no. 1, p. 44710, Apr. 2017.
- [78] Y. Cai *et al.*, "Influences of expanded graphite on structural morphology and thermal performance of composite phase change materials consisting of fatty acid eutectics and electrospun PA6 nanofibrous mats," 2013.
- [79] H. Ji *et al.*, "Enhanced thermal conductivity of phase change materials with ultrathin-graphite foams for thermal energy storage," *Energy Environ. Sci.*, vol. 7, no. 3, pp. 1185–1192, Feb. 2014.

- [80] Z. Wang, • Xianyong Zhang, S. Jia, Y. Zhu, • Ligui Chen, and • Lei Fu, "Influences of dynamic impregnating on morphologies and thermal properties of polyethylene glycol-based composite as shape-stabilized PCMs."
- [81] A. Sar&&, C. Alkan, A. Biçer, and C. Bilgin, "Latent heat energy storage characteristics of building composites of bentonite clay and pumice sand with different organic PCMs," *Int. J. Energy Res.*, vol. 38, no. 11, pp. 1478–1491, Sep. 2014.
- [82] Y. Zhong *et al.*, "Heat transfer enhancement of paraffin wax using compressed expanded natural graphite for thermal energy storage," *Carbon N. Y.*, vol. 48, pp. 300–304, 2009.
- [83] S. Karaman, A. Karaipekli, A. Sarı, and A. Biçer, "Polyethylene glycol (PEG)/diatomite composite as a novel form-stable phase change material for thermal energy storage," *Sol. Energy Mater. Sol. Cells*, vol. 95, no. 7, pp. 1647–1653, Jul. 2011.
- [84] A. M. Goitandia, G. Beobide, E. Aranzabe, and A. Aranzabe, "Development of content-stable phase change composites by infiltration into inorganic porous supports," *Sol. Energy Mater. Sol. Cells*, vol. 134, pp. 318–328, Mar. 2015.
- [85] D. Zhang, J. Zhou, K. Wu, and Z. Li, "Granular phase changing composites for thermal energy storage," *Sol. Energy*, vol. 78, no. 3, pp. 471–480, Mar. 2005.
- [86] S. Ramakrishnan, X. Wang, J. Sanjayan, and J. Wilson, "Assessing the feasibility of integrating form-stable phase change material composites with cementitious composites and prevention of PCM leakage," *Mater. Lett.*, vol. 192, pp. 88–91, Apr. 2017.
- [87] X. Zhang *et al.*, "Shape-stabilized composite phase change materials with high thermal conductivity based on stearic acid and modified expanded vermiculite," *Renew. Energy*, vol. 112, pp. 113–123, Nov. 2017.

- [88] Y. Li, J. Li, W. Feng, X. Wang, and H. Nian, "Design and Preparation of the Phase Change Materials Paraffin/ Porous Al₂O₃ @Graphite Foams with Enhanced Heat Storage Capacity and Thermal Conductivity," 2017.
- [89] A. Karaipekli and A. Sari, "Development and thermal performance of pumice/organic PCM/gypsum composite plasters for thermal energy storage in buildings," *Sol. Energy Mater. Sol. Cells*, vol. 149, pp. 19–28, May 2016.
- [90] X. Min *et al.*, "Enhanced thermal properties of novel shape-stabilized PEG composite phase change materials with radial mesoporous silica sphere for thermal energy storage," *Sci. Rep.*, vol. 5, no. 1, p. 12964, Oct. 2015.
- [91] Y. Li, B. Guo, G. Huang, S. Kubo, and P. Shu, "Characterization and thermal performance of nitrate mixture/SiC ceramic honeycomb composite phase change materials for thermal energy storage," *Appl. Therm. Eng.*, vol. 81, pp. 193–197, Apr. 2015.
- [92] Y. Galazutdinova, M. Vega, M. Grágeda, L. F. Cabeza, and S. Ushak, "Preparation and characterization of an inorganic magnesium chloride/nitrate/graphite composite for low temperature energy storage," *Sol. Energy Mater. Sol. Cells*, vol. 175, pp. 60–70, Feb. 2018.
- [93] A. Karaipekli and A. Sari, "Capric–myristic acid/vermiculite composite as form-stable phase change material for thermal energy storage," 2008.
- [94] C. Li, H. Yu, Y. Song, and M. Zhao, "Synthesis and characterization of PEG/ZSM-5 composite phase change materials for latent heat storage," *Renew. Energy*, vol. 121, pp. 45–52, Jun. 2018.

- [95] L. Zhong, X. Zhang, Y. Luan, G. Wang, Y. Feng, and D. Feng, "Preparation and thermal properties of porous heterogeneous composite phase change materials based on molten salts/expanded graphite," 2014.
- [96] J. Gao *et al.*, "Enhanced Thermal Properties of Novel Latent Heat Thermal Storage Material Through Confinement of Stearic Acid in Meso-Structured Onion-Like Silica," *JOM*, vol. 69, no. 12, pp. 2785–2790, Dec. 2017.
- [97] Y. Feng, R. Wei, Z. Huang, X. Zhang, and G. Wang, "Thermal properties of lauric acid filled in carbon nanotubes as shape-stabilized phase change materials," *Phys. Chem. Chem. Phys.*, vol. 20, no. 11, pp. 7772–7780, Mar. 2018.
- [98] D. A. Vasco, C. Salinas-Lira, I. Barra-Reyes, and D. M. Elustondo, "Kinematic characterization of the pressure-dependent PCM impregnation process for radiata pine wood samples," *Eur. J. Wood Wood Prod.*, vol. 76, pp. 1461–1469, 2018.
- [99] W. G. Alshaer, M. A. Rady, S. A. Nada, E. Palomo Del Barrio, and A. Sommer, "An experimental investigation of using carbon foam–PCM–MWCNTs composite materials for thermal management of electronic devices under pulsed power modes," *Heat Mass Transf.*, vol. 53, no. 2, pp. 569–579, Feb. 2017.
- [100] S. Pincemin, R. Olives, X. Py, and M. Christ, "Highly conductive composites made of phase change materials and graphite for thermal storage," *Sol. Energy Mater. Sol. Cells*, vol. 92, no. 6, pp. 603–613, Jun. 2008.
- [101] T. D. Claar, E. T. Ong, and R. J. Petri, "Composite salt/ceramic media for thermal energy storage applications," *Proc., Intersoc. Energy Convers. Eng. Conf.; (United States)*, vol. 4, 1982.

- [102] R. J. Petri, T. D. Claar, and E. T. Ong, "High-temperature salt/ceramic thermal storage phase-change media," *Proc., Intersoc. Energy Convers. Eng. Conf.; (United States)*, vol. 4, 1983.
- [103] R. J. Petri, E. T. Ong, and L. G. Marianowski, "High-temperature composite thermal energy storage for industrial applications." 1985.
- [104] A. Glück, R. Tamme, H. Kalfa, C. Streuber, and T. Weichert, "Development and Testing of Advanced TES Materials for Solar Central Receiver Plants," 1991.
- [105] E. Hame, U. Taut, and Y. Grob, "Salt ceramic thermal energy storage for solar thermal central receiver plants," *Proc. Sol. World Congr.*, 1991.
- [106] N. Gokon, D. Nakano, S. Inuta, and T. Kodama, "High-temperature carbonate/MgO composite materials as thermal storage media for double-walled solar reformer tubes," *Sol. Energy*, vol. 82, no. 12, pp. 1145–1153, 2008.
- [107] Q. Yu *et al.*, "A novel low-temperature fabrication approach of composite phase change materials for high temperature thermal energy storage," *Appl. Energy*, vol. 237, pp. 367–377, Mar. 2019.
- [108] Z. Jiang *et al.*, "Form-stable LiNO₃–NaNO₃–KNO₃–Ca(NO₃)₂/calcium silicate composite phase change material (PCM) for mid-low temperature thermal energy storage," *Energy Convers. Manag.*, vol. 106, no. 3, pp. 165–172, 2015.
- [109] J. Liu *et al.*, "Next generation materials for thermal interface and high density energy storage applications via liquid phase sintering," in *2009 11th Electronics Packaging Technology Conference*, 2009, pp. 506–511.

- [110] G. Xu *et al.*, "Sodium nitrate – Diatomite composite materials for thermal energy storage," *Sol. Energy*, vol. 146, pp. 494–502, Apr. 2017.
- [111] G. Leng *et al.*, "Micro encapsulated & form-stable phase change materials for high temperature thermal energy storage," *Appl. Energy*, vol. 217, pp. 212–220, May 2018.
- [112] Y. Deng, J. Li, T. Qian, W. Guan, and X. Wang, "Preparation and Characterization of KNO₃/Diatomite Shape-Stabilized Composite Phase Change Material for High Temperature Thermal Energy Storage," *J. Mater. Sci. Technol.*, vol. 33, no. 2, pp. 198–203, Feb. 2017.
- [113] Z. Acem, J. Lopez, and E. Palomo Del Barrio, "KNO₃/NaNO₃ – Graphite materials for thermal energy storage at high temperature: Part I. – Elaboration methods and thermal properties," *Appl. Therm. Eng.*, vol. 30, no. 13, pp. 1580–1585, Sep. 2010.
- [114] R. Tammer, "Energy storage for direct steam solar power plants," 2008.
- [115] J. Liu, M. Xie, Z. Ling, X. Fang, and Z. Zhang, "Novel MgCl₂-KCl/expanded graphite/graphite paper composite phase change blocks with high thermal conductivity and large latent heat," *Sol. Energy*, vol. 159, pp. 226–233, Jan. 2018.
- [116] Y. Ren, C. Xu, M. Yuan, F. Ye, X. Ju, and X. Du, "Ca(NO₃)₂-NaNO₃/expanded graphite composite as a novel shape-stable phase change material for mid- to high-temperature thermal energy storage," *Energy Convers. Manag.*, vol. 163, pp. 50–58, May 2018.
- [117] Malek, Y. Pan, and S. Al-Hallaj, "Selective Laser Sintering of Phase Change Materials for Thermal Energy Storage Applications," *Procedia Manuf.*, vol. 10, pp. 851–865, Jan. 2017.
- [118] Z. Jiang *et al.*, "A Form Stable Composite Phase Change Material for Thermal Energy Storage Applications over 700 °C," *Appl. Sci.*, vol. 9, no. 5, p. 814, Feb. 2019.

- [119] F. Ye and Z. Ge, "Multi-walled carbon nanotubes added to Na₂CO₃/MgO composites for thermal energy storage," *Particuology*, vol. 15, pp. 56–60, 2014.
- [120] N. Gokon, D. Nakano, S. Inuta, and T. Kodama, "High-temperature carbonate/MgO composite materials as thermal storage media for double-walled solar reformer tubes," *Sol. Energy*, vol. 82, no. 12, pp. 1145–1153, Dec. 2008.
- [121] C. Li *et al.*, "MgO based composite phase change materials for thermal energy storage: The effects of MgO particle density and size on microstructural characteristics as well as thermophysical and mechanical properties," *Appl. Energy*, vol. 250, pp. 81–91, Sep. 2019.
- [122] C. Li, Q. Li, and Y. Ding, "Investigation on the thermal performance of a high temperature packed bed thermal energy storage system containing carbonate salt based composite phase change materials," *Appl. Energy*, vol. 247, pp. 374–388, Aug. 2019.
- [123] C. Li *et al.*, "Carbonate salt based composite phase change materials for medium and high temperature thermal energy storage: A microstructural study," *Sol. Energy Mater. Sol. Cells*, vol. 196, pp. 25–35, Jul. 2019.
- [124] N. M. E, "Thermal properties of a novel medium temperature thermal energy storage composite based on sodium nitrate as phase change material."
- [125] G. Leng, G. Qiao, G. Xu, T. Vidal, and Y. Ding, "Erythritol-Vermiculite form-stable phase change materials for thermal energy storage," *Energy Procedia*, vol. 142, pp. 3363–3368, Dec. 2017.
- [126] Y. Jiang, Y. Sun, R. D. Jacob, F. Bruno, and S. Li, "Novel Na₂SO₄-NaCl-ceramic composites as high temperature phase change materials for solar thermal power plants (Part I)," *Sol. Energy Mater. Sol. Cells*, vol. 178, pp. 74–83, May 2018.

- [127] Z. Ge, F. Ye, and Y. Ding, "Composite Materials for Thermal Energy Storage: Enhancing Performance through Microstructures," *ChemSusChem*, vol. 7, no. 5, pp. 1318–1325, May 2014.
- [128] C. Li *et al.*, "Wettability of eutectic NaLiCO₃ salt on magnesium oxide substrates at 778 K," *Appl. Surf. Sci.*, vol. 442, pp. 148–155, Jun. 2018.
- [129] K. S. Do, C. Aktay, · R Tamme, and · H Müller-Steinhagen, "Thermal Conductivity of High-Temperature Multicomponent Materials with Phase Change," *Int J Thermophys*, vol. 29, pp. 678–692, 2008.
- [130] H. Blackmore, "A dictionary of London gunmakers 1350-1850," 1986.
- [131] M. Mu, P. A. M. Basheer, W. Sha, Y. Bai, and T. McNally, "Shape stabilised phase change materials based on a high melt viscosity HDPE and paraffin waxes," *Appl. Energy*, vol. 162, pp. 68–82, Jan. 2016.
- [132] M. A. AlMaadeed, S. Labidi, I. Krupa, and M. Karkri, "Effect of expanded graphite on the phase change materials of high density polyethylene/wax blends," *Thermochim. Acta*, vol. 600, pp. 35–44, Jan. 2015.
- [133] Y. Tang, Y. Jia, G. Alva, X. Huang, and G. Fang, "Synthesis, characterization and properties of palmitic acid/high density polyethylene/graphene nanoplatelets composites as form-stable phase change materials," *Sol. Energy Mater. Sol. Cells*, vol. 155, pp. 421–429, Oct. 2016.
- [134] Y. Tang, Y. Lin, Y. Jia, and G. Fang, "Improved thermal properties of stearyl alcohol/high density polyethylene/expanded graphite composite phase change materials for building thermal energy storage," *Energy Build.*, vol. 153, pp. 41–49, Oct. 2017.

- [135] P. Zhang, Y. Hu, L. Song, J. Ni, W. Xing, and J. Wang, "Effect of expanded graphite on properties of high-density polyethylene/ paraffin composite with intumescent flame retardant as a shape-stabilized phase change material," 2009.
- [136] T. Benjamin Freeman and T. Benjamin, "Shape-Stabilization of PCM/HDPE Composites with 3D-Printing Applications for Battery Thermal Management Scholarly Commons Citation," 2018.
- [137] G. D. Estep, "The influence of extrusion processing and formulation on form-stable phase change material," 2010.
- [138] Y. Cai *et al.*, "Flammability and thermal properties of high density polyethylene/paraffin hybrid as a form-stable phase change material," *J. Appl. Polym. Sci.*, vol. 99, no. 4, pp. 1320–1327, Feb. 2006.
- [139] F. Chen and M. Wolcott, "Polyethylene/paraffin binary composites for phase change material energy storage in building: A morphology, thermal properties, and paraffin leakage study," *Sol. Energy Mater. Sol. Cells*, vol. 137, pp. 79–85, Jun. 2015.
- [140] Y. P. Zhang, K. P. Lin, R. Yang, H. F. Di, and Y. Jiang, "Preparation, thermal performance and application of shape-stabilized PCM in energy efficient buildings," *Energy Build.*, vol. 38, no. 10, pp. 1262–1269, Oct. 2006.
- [141] X. Guo, S. Zhang, and J. Cao, "An energy-efficient composite by using expanded graphite stabilized paraffin as phase change material," *Compos. Part A Appl. Sci. Manuf.*, vol. 107, pp. 83–93, Apr. 2018.
- [142] "Thermodynamics of Polymer Blends."

- [143] P. A. McGuire, S. Blackburn, and E. M. Holt, "An X-ray micro-computed tomography study of agglomerate breakdown during the extrusion of ceramic pastes," *Chem. Eng. Sci.*, vol. 62, pp. 6451–6456, 2007.
- [144] H. Potente, S. Krawinkel, M. Bastian, M. Stephan, and P. Pötschke, "Investigation of the melting behavior and morphology development of polymer blends in the melting zone of twin-screw extruders," *J. Appl. Polym. Sci.*, vol. 82, no. 8, pp. 1986–2002, Nov. 2001.
- [145] F. M. Salleh, A. Hassan, R. Yahya, and A. D. Azzahari, "Effects of extrusion temperature on the rheological, dynamic mechanical and tensile properties of kenaf fiber/HDPE composites," *Compos. PART B*, vol. 58, pp. 259–266, 2014.
- [146] C. Chen, L. Wang, and Y. Huang, "Electrospinning of thermo-regulating ultrafine fibers based on polyethylene glycol/cellulose acetate composite," *Polymer (Guildf)*, vol. 48, no. 18, pp. 5202–5207, Aug. 2007.
- [147] J. T. Mccann, M. Marquez, and Y. Xia, "Melt Coaxial Electrospinning: A Versatile Method for the Encapsulation of Solid Materials and Fabrication of Phase Change Nanofibers," *NANO Lett.*, vol. 6, 2006.
- [148] A. SarÄ±, C. Alkan, A. Karaipekli, and O. Uzun, "Poly(ethylene glycol)/poly(methyl methacrylate) blends as novel form-stable phase-change materials for thermal energy storage," *J. Appl. Polym. Sci.*, p. n/a-n/a, 2009.
- [149] B. Tang, C. Wu, M. Qiu, X. Zhang, and S. Zhang, "PEG/SiO₂/Al₂O₃ hybrid form-stable phase change materials with enhanced thermal conductivity," 2014.
- [150] A. E. Danks, S. R. Hall, and Z. Schnepf, "The evolution of 'sol-gel' chemistry as a technique for materials synthesis," *Mater. Horizons*, vol. 3, no. 2, pp. 91–112, Mar. 2016.

- [151] Q. Guo and T. Wang, "Influence of SiO₂ pore structure on phase change enthalpy of shape-stabilized polyethylene glycol/silica composites."
- [152] B. Tang, J. Cui, Y. Wang, C. Jia, and S. Zhang, "Facile synthesis and performances of PEG/SiO₂ composite form-stable phase change materials," *Sol. Energy*, vol. 97, pp. 484–492, 2013.
- [153] F. Jurado-Lasso, N. Jurado-Lasso, J. Ortiz, and J. F. Jurado, "Thermal dielectric and Raman studies on the KNO₃ compound high-temperature region," *DYNA*, vol. 83, no. 198, p. 244, Sep. 2016.
- [154] T. Qian, J. Li, X. Min, Y. Deng, W. Guan, and L. Ning, "Diatomite: A promising natural candidate as carrier material for low, middle and high temperature phase change material," *Energy Convers. Manag.*, vol. 98, pp. 34–45, 2015.
- [155] R. K. Sharma, P. Ganesan, V. V. Tyagi, H. S. C. Metselaar, and S. C. Sandaran, "Developments in organic solid-liquid phase change materials and their applications in thermal energy storage," *Energy Convers. Manag.*, vol. 95, pp. 193–228, 2015.
- [156] W. U. Jianfeng *et al.*, "Molten Salts/Ceramic-Foam Matrix Composites by Melt Infiltration Method as Energy Storage Material," *J. Wuhan Univ. Technoloty-Mater. Sci. Ed*, 2009.
- [157] J. S. Hwang, K. J. Lin, and C. Tien, "Measurement of heat capacity by fitting the whole temperature response of a heat-pulse calorimeter," *Rev. Sci. Instrum.*, vol. 68, no. 1, pp. 94–101, Jan. 1997.
- [158] F. M. Etzler and J. J. Connors, "Structural Transitions in Vicinal Water: Pore Size and Temperature Dependence of the Heat Capacity of Water in Small Pores," 1991.

- [159] F. E.-J. of C. and I. Science and undefined 1983, "A statistical thermodynamic model for water near solid interfaces," *Elsevier*.
- [160] T. Bauer, D. Laing, U. Kröner, and R. Tamme, "Sodium nitrate for high temperature latent heat storage," 2009.
- [161] C. Li *et al.*, "Heat transfer of composite phase change material modules containing a eutectic carbonate salt for medium and high temperature thermal energy storage applications," *Appl. Energy*, vol. 238, pp. 1074–1083, Mar. 2019.
- [162] R. M and German, *Liquid Phase Sintering*, vol. 53, no. 9. 2013.
- [163] M. C. PHILLIPS and A. C. RIDDIFORD, "Temperature Dependence of Contact Angles," *Nature*, 1965.
- [164] J. D. Bernardin, I. Mudawar, C. B. Walsh, and E. I. Franses, "Contact angle temperature dependence for water droplets on practical aluminum surfaces," *Int. J. Heat Mass Transf.*, 1997.
- [165] K. Xiao and C. Tzoganakis, "An experimental study of single-screw extrusion of HDPE-wood composites," *Adv. Polym. Technol.*, vol. 29, no. 3, pp. 197–218, Sep. 2010.
- [166] M. Ansari, E. Mitsoulis, and S. G. Hatzikiriakos, "Capillary extrusion and swell of a HDPE melt exhibiting slip," *Adv. Polym. Technol.*, 2013.
- [167] H. Münstedt, M. Schmidt, and E. Wassner, "Stick and slip phenomena during extrusion of polyethylene melts as investigated by laser-Doppler velocimetry," *Cit. J. Rheol.*, vol. 44, p. 413, 2000.
- [168] S. G. Hatzikiriakos, "Wall slip of molten polymers," *Progress in Polymer Science (Oxford)*. 2012.

- [169] V. Hristov and J. Vlachopoulos, "Effects of polymer molecular weight and filler particle size on flow behavior of wood polymer composites," *Polym. Compos.*, vol. 29, no. 8, pp. 831–839, Aug. 2008.
- [170] B. Vergnes, "Extrusion defects and flow instabilities of molten polymers," *International Polymer Processing*, vol. 30, no. 1. Carl Hanser Verlag, pp. 3–28, 01-Mar-2015.
- [171] J.-F. Agassant *et al.*, "Polymer Processing Extrusion Instabilities and Methods for their Elimination or Minimisation," 2006.
- [172] T. I. Burghilea, H. J. Griess, and H. Münstedt, "Comparative investigations of surface instabilities ('sharkskin') of a linear and a long-chain branched polyethylene," 2010.
- [173] V. Hristov, "Melt flow instabilities of wood polymer composites," *Compos. Interfaces*, 2009.
- [174] S. Mueller, E. W. Llewellyn, and H. M. Mader, "The rheology of suspensions of solid particles," *Proc. R. Soc. A Math. Phys. Eng. Sci.*, vol. 466, no. 2116, pp. 1201–1228, Apr. 2010.
- [175] L. Carrino, S. Ciliberto, G. Giorleo, and U. Prisco, "Effect of Filler Content and Temperature on Steady-State Shear Flow of Wood/High Density Polyethylene Composites."
- [176] N. Minagawa and J. L. White, "The Influence of Titanium Dioxide on the Rheological and Extrusion Properties of Polymer Melts," 1976.
- [177] J. Cai, M. Jia, P. Xue, Y. Ding, and X. Zhou, "The Effect of Processing Conditions on the Mechanical Properties and Morphology of Self-Reinforced Wood-Polymer Composite."
- [178] S. G. Hatzikiriakos and J. M. Dealy, "Role of slip and fracture in the oscillating flow of HDPE in a capillary," *Cit. J. Rheol.*, vol. 36, p. 845, 1992.

- [179] H. Hu *et al.*, "Entrance pressure instability of LLDPE and its composites," *RSC Adv.*, vol. 6, no. 85, pp. 81703–81711, Aug. 2016.
- [180] K. X. Celgard, C. Tzoganakis, and K. Xiao, "Rheological Properties of HDPE-Wood Composites," 2003.
- [181] C. W. Macosko, *Rheology : principles, measurements, and applications*. VCH, 1994.
- [182] G. W. Radebaugh, S. R. Babu, and J. N. Bondi, "Characterization of the viscoelastic properties of compacted pharmaceutical powders by a novel nondestructive technique," *Int. J. Pharm.*, vol. 57, no. 2, pp. 95–105, Dec. 1989.
- [183] M. A. Osman, A. Atallah, T. Schweizer, and H. Christian, "Particle-particle and particle-matrix interactions in calcite filled high-density polyethylene-steady shear," 2004.
- [184] G. Guo, Y. H. Lee, G. M. Rizvi, and C. B. Park, "Influence of wood fiber size on extrusion foaming of wood fiber/HDPE composites," *J. Appl. Polym. Sci.*, vol. 107, no. 6, pp. 3505–3511, Mar. 2008.
- [185] J.-F. O. Le Meins, P. Moldenaers, and J. Mewis, "Suspensions in Polymer Melts. 1. Effect of Particle Size on the Shear Flow Behavior," 2002.
- [186] V. Hristov, E. Takács, and J. Vlachopoulos, "Surface tearing and wall slip phenomena in extrusion of highly filled HDPE/wood flour composites," *Polym. Eng. Sci.*, vol. 46, no. 9, pp. 1204–1214, Sep. 2006.
- [187] T. Q. Li and M. P. Wolcott, "Rheology of wood plastics melt. Part 1. Capillary rheometry of HDPE filled with maple," *Polym. Eng. Sci.*, 2005.

- [188] E. Miller and J. P. Rothstein, "Control of the sharkskin instability in the extrusion of polymer melts using induced temperature gradients," *Rheol. Acta*, vol. 44, no. 2, pp. 160–173, Dec. 2004.
- [189] A. Gallos, G. Paës, F. Allais, and J. Beaugrand, "Lignocellulosic fibers: A critical review of the extrusion process for enhancement of the properties of natural fiber composites," *RSC Advances*, vol. 7, no. 55. Royal Society of Chemistry, pp. 34638–34654, 2017.
- [190] Z. Liang, P. Pan, B. Zhu, T. Dong, and Y. Inoue, "Mechanical and thermal properties of poly(butylene succinate)/plant fiber biodegradable composite," *J. Appl. Polym. Sci.*, 2010.
- [191] P. Shahi *et al.*, "Morphological Analysis of Foamed HDPE/LLDPE Blends by X-ray Micro-Tomography: Effect of Blending, Mixing Intensity and Foaming Temperature," 2017.
- [192] H. Bouafif, A. Koubaa, P. Perré, and A. Cloutier, "EFFECTS OF FIBRE CHARACTERISTICS ON THE PHYSICAL AND MECHANICAL PROPERTIES OF WOOD PLASTIC COMPOSITES."
- [193] D. J. Valles-Rosales, L. C. Méndez-González, L. A. Rodríguez-Picon, A. Del Valle-Carrasco, and H. A. Alodan, "WOOD CHILE PEPPERS STALKS-PLASTIC COMPOSITE PRODUCTION," *Cienc. y Tecnol.*, vol. 18, no. 1, pp. 179–190, 2016.
- [194] D. J. Gardner, Y. Han, and L. Wang, "Wood–Plastic Composite Technology," *Curr. For. Reports*, vol. 1, no. 3, pp. 139–150, Sep. 2015.
- [195] T. Villmow, B. Kretzschmar, and P. Pötschke, "Influence of screw configuration, residence time, and specific mechanical energy in twin-screw extrusion of polycaprolactone/multi-walled carbon nanotube composites," 2010.

- [196] C. Stefano Trillo and D. Tutore Ing Valentina Mazzanti Ing Francesco Mollica, "Università degli Studi di Ferrara DOTTORATO DI RICERCA IN "SCIENZE DELL'INGEGNERIA; Rheology of Wood Polymer Composites," 2012.
- [197] A. A. Andrey Askadskii, Tatyana Matseevich, "Structure and Properties of Wood-Polymer Composites (WPC)." [Online]. Available: https://books.google.co.uk/books?id=bB-NDwAAQBAJ&pg=PA157&lpg=PA157&dq=WPC+without+any+pores.&source=bl&ots=RbSafpbAHT&sig=ACfU3U3EZ-UpvYP__AEtw7LrRXdefl7y-Q&hl=zh-CN&sa=X&ved=2ahUKEwj9vfCU0drkAhUyrXEKHQseCZsQ6AEwAHoECACQAQ#v=onepage&q=WPC without any. [Accessed: 18-Sep-2019].
- [198] J. Kastner, B. Plank, D. Salaberger, and J. Sekelja, "Defect and Porosity Determination of Fibre Reinforced Polymers by X-ray Computed Tomography," 2010.
- [199] E. A. Birt and R. A. Smith, "A review of NDE methods for porosity measurement in fibre-reinforced polymer composites," *Insight - Non-Destructive Test. Cond. Monit.*, vol. 46, no. 11, pp. 681–686, Nov. 2004.
- [200] U. del Bío Bío Chile Poletto and M. Poletto, "Polypropylene-based wood-plastic composites: effect of using a coupling agent derived from a renewable resource," *Cienc. y Tecnol.*, vol. 19, no. 3, pp. 265–272, 2017.
- [201] C. Castellón, E. Günther, H. Mehling, S. Hiebler, and L. F. Cabeza, "Determination of the enthalpy of PCM as a function of temperature using a heat-flux DSC-A study of different measurement procedures and their accuracy," *Int. J. Energy Res.*, vol. 32, no. 13, pp. 1258–1265, Oct. 2008.

- [202] R. M. Saeed, J. Paul Schlegel, C. H. Castano Giraldo, J. P. Schlegel, C. Castano, and R. Sawafta, "Uncertainty of Thermal Characterization of Phase Change Material by Differential Scanning Calorimetry Analysis Thermal Energy Storage View project CO2 Recycling View project 58 PUBLICATIONS 487 CITATIONS SEE PROFILE," 2016.
- [203] T. Kousksou, A. Jamil, K. El Omari, Y. Zeraouli, and Y. Le Guer, "Effect of heating rate and sample geometry on the apparent specific heat capacity: DSC applications," *Thermochim. Acta*, vol. 519, no. 1–2, pp. 59–64, May 2011.
- [204] R. M. Al Ghossein, M. S. Hossain, and J. M. Khodadadi, "Experimental determination of temperature-dependent thermal conductivity of solid eicosane-based silver nanostructure-enhanced phase change materials for thermal energy storage," *Int. J. Heat Mass Transf.*, vol. 107, pp. 697–711, Apr. 2017.
- [205] C.-M. Ye, B.-Q. Shentu, and Z.-X. Weng, "Thermal conductivity of high density polyethylene filled with graphite," *J. Appl. Polym. Sci.*, vol. 101, no. 6, pp. 3806–3810, Sep. 2006.
- [206] Q. Wang, J. Gao, R. Wang, and Z. Hua, "Mechanical and rheological properties of HDPE/graphite composite with enhanced thermal conductivity," *Polym. Compos.*, vol. 22, no. 1, pp. 97–103, Feb. 2001.
- [207] J. Song, J. Ma, F. Li, Y. Chen, Y. D.-2015 I. F. on, and undefined 2015, "Experimental Analysis on Phase-Change Heat Storage Materials PG and PE," *atlantis-press.com*.
- [208] B. Feng, J. Tu, J.-W. Sun, L.-W. Fan, and Y. Zeng, "A molecular dynamics study of the effects of crystalline structure transition on the thermal conductivity of pentaerythritol as a solid-solid phase change material," *Int. J. Heat Mass Transf.*, vol. 141, pp. 789–798, Oct. 2019.

- [209] A. Solé, H. Neumann, S. Niedermaier, I. Martorell, P. Schossig, and L. F. Cabeza, "Stability of sugar alcohols as PCM for thermal energy storage," *Sol. Energy Mater. Sol. Cells*, vol. 126, pp. 125–134, 2014.
- [210] M. K. Rathod and J. Banerjee, "Thermal stability of phase change materials used in latent heat energy storage systems: A review," *Renewable and Sustainable Energy Reviews*, vol. 18. Pergamon, pp. 246–258, 01-Feb-2013.
- [211] Z. Khan, Z. Khan, and A. Ghafoor, "A review of performance enhancement of PCM based latent heat storage system within the context of materials, thermal stability and compatibility," *Energy Conversion and Management*, vol. 115. Elsevier Ltd, pp. 132–158, 01-May-2016.
- [212] Y. Wang, S. Li, T. Zhang, D. Zhang, and H. Ji, "Supercooling suppression and thermal behavior improvement of erythritol as phase change material for thermal energy storage," 2017.
- [213] P. Hu, P.-P. Zhao, Y. Jin, and Z.-S. Chen, "Experimental study on solid-solid phase change properties of pentaerythritol (PE)/nano-AlN composite for thermal storage," 2014.